UNIVERSIDADE FEDERAL DO PARANÁ

EDUARDO DE MIO

IMPROVEMENTS ON NUMERICAL MODELING OF AN ATYPICAL PETROLEUM SYSTEMS IN PARNAÍBA BASIN, NE BRAZIL:

INTEGRATION OF ORGANIC-INORGANIC THERMAL INDICATORS BASED ON VITRINITE REFLECTANCE AND ILLITE CRYSTALLINITY AND ESTABLISHMENT OF CUSTOMIZED KINETIC SCHEME

CURITIBA

2025

UNIVERSIDADE FEDERAL DO PARANÁ

EDUARDO DE MIO

IMPROVEMENTS ON NUMERICAL MODELING OF AN ATYPICAL PETROLEUM SYSTEMS IN PARNAÍBA BASIN, NE BRAZIL:

INTEGRATION OF ORGANIC-INORGANIC THERMAL INDICATORS BASED ON VITRINITE REFLECTANCE AND ILLITE CRYSTALLINITY AND ESTABLISHMENT OF CUSTOMIZED KINETIC SCHEME

Tese apresentada como requisito parcial à obtenção de título de Doutor em Geologia.ao Programa de Pós-Graduação em Geologia, com área de concentração em Geologia Exploratória e ênfase em Análise de Bacias, no Setor de Ciências da Terra, na Universidade Federal do Paraná,

Orientador:

Prof. Dr. Leonardo Fadel Cury

Co – Orientadores:

Profa. Dra. Anelize Manuela Banhiuk Rumbelsperger
Dr. Nilo das Chagas Azambuja Filho

CURITIBA

2025

FICHA CATALOGRÁFICA

DADOS INTERNACIONAIS DE CATALOGAÇÃO NA PUBLICAÇÃO (CIP)
UNIVERSIDADE FEDERAL DO PARANÁ
SISTEMA DE BIBLIOTECAS – BIBLIOTECA DE CIÊNCIA E TECNOLOGIA

Mio, Eduardo de
Improvements on numerical modeling of an atypical petroleum systems in Parnaíba basin, NE Brazil: integration of organic-inorganic thermal indicators based on vitrinite reflectance and illite crystallinity and establishment of customized kinetic scheme / Eduardo de Mio. – Curitiba, 2025.
1 recurso on-line : PDF.

Tese (Doutorado) - Universidade Federal do Paraná, Setor de Ciências da Terra, Programa de Pós-Graduação em Geologia.

Orientador: Leonardo Fadel Cury
Coorientadores: Anelize Manuela Banhiuk Rumbelsperger; Nilo das Chagas Azambuja Filho

1. Campos petrolíferos – Parnaíba, Rio (PI e MA). Bacia do. 2. Sistemas de controle. 3. Calibração. I. Universidade Federal do Paraná. II. Programa de Pós-Graduação em Geologia. III. Cury, Leonardo Fadel. IV. Rumbelsperger, Anelize Manuela Banhiuk. V. Azambuja Filho, Nilo das Chagas. VI. Título.

Bibliotecário: Elias Barbosa da Silva CRB-9/1894

MINISTÉRIO DA EDUCAÇÃO
SETOR DE CIENCIAS DA TERRA
UNIVERSIDADE FEDERAL DO PARANÁ
PRÓ-REITORIA DE PÓS-GRADUAÇÃO
PROGRAMA DE PÓS-GRADUAÇÃO GEOLOGIA 40001016028P5

TERMO DE APROVAÇÃO

Os membros da Banca Examinadora designada pelo Colegiado do Programa de Pós-Graduação GEOLOGIA da Universidade Federal do Paraná foram convocados para realizar a arguição da tese de Doutorado de **EDUARDO DE MIO**, intitulada: **IMPROVEMENTS ON NUMERICAL MODELING OF AN ATYPICAL PETROLEUM SYSTEMS IN PARNAÍBA BASIN, NE BRAZIL: Integration of Organic-Inorganic Thermal Indicators Based on Vitrinite Reflectance and Illite Crystallinity and establishment of Customized Kinetic Scheme**, sob orientação do Prof. Dr. LEONARDO FADEL CURY, que após terem inquirido o aluno e realizada a avaliação do trabalho, são de parecer pela sua APROVAÇÃO no rito de defesa.

A outorga do título de doutor está sujeita à homologação pelo colegiado, ao atendimento de todas as indicações e correções solicitadas pela banca e ao pleno atendimento das demandas regimentais do Programa de Pós-Graduação.

CURITIBA, 15 de Agosto de 2025.

Assinatura Eletrônica
19/08/2025 10:42:10.0
LEONARDO FADEL CURY
Presidente da Banca Examinadora

Assinatura Eletrônica
20/08/2025 09:15:16.0
FÉLIX THADEU TEIXEIRA GONÇALVES
Avaliador Externo (CONSULTORIA E SERVICOS DE GEOLOGIA LTDA)

Assinatura Eletrônica
21/08/2025 15:49:21.0
FERNANDO FARIAS VESELY
Avaliador Interno (UNIVERSIDADE FEDERAL DO PARANÁ)

Assinatura Eletrônica
27/08/2025 11:22:47.0
FERNANDO SANTOS CORRÊA
Avaliador Externo (TOTALENERGIES)

Assinatura Eletrônica
19/08/2025 14:23:41.0
ALMÉRIO BARROS FRANÇA
Avaliador Interno (UNIVERSIDADE FEDERAL DO PARANÁ)

“Happiness is real only when shared”

Christopher McCandless’s reading of Henry Thoreau’s philosophy

“A felicidade só é real se for compartilhada”

Releitura de Christopher McCandless para a obra de Henry Thoreau]

DEDICATION

I dedicate this research to my family — first and foremost to my mother, who has always encouraged me and been my inspiration. I also dedicate it to my wife, Eliandra, who has supported me from the beginning and embraced this project with me; to my son Aleksei, who surprised us in the middle of the process and has always been by my side during the preparation of my qualification; to our beloved dog, Tobi; and to my son NiKola, who is expected to arrive around the time of this doctoral examination. I extend this dedication to my brother João, my sister-in-law Sol, and my nephew Giovanni, who have always supported and encouraged me, offering essential help even from a distance. Finally, I dedicate this work in memoriam to my nephew Gabriel and my stepfather Amauri, who would have been proud to be part of this achievement— and to our beloved and much-missed dogs, Myke and Sophie.

DEDICATÓRIA

Dedico este trabalho de pesquisa à minha família, primeiramente à minha mãe, que sempre me incentivou e foi minha inspiração. Dedico à minha esposa Eliandra, que sempre me apoiou e abraçou conjuntamente este projeto, ao meu filho Aleksei, que nos surpreendeu no meio do processo, e que me esteve sempre ao meu lado na elaboração da qualificação, junto com nosso querido cão Tobi, e ao meu filho Nikola, que deve chegar junto com a defesa do doutorado. Dedico também ao meu irmão João e minha cunhada Sol e ao meu sobrinho Giovanni, que sempre me apoiaram e incentivaram, dando um suporte essencial mesmo de longe.

Dedico ainda In Memorian ao meu sobrinho Gabriel e meu padrasto Amauri, que se orgulhariam de fazer parte de mais essa conquista, e aos nossos amados e saudosos cães Myke e Sophie.

ACKNOWLEDGEMENTS

To my family, for their unwavering support, affection, and constant presence throughout these intense four years of study. To my mother, Iraci, a true pillar in my life and a continuous source of strength. To my wife, Eliandra, a tireless partner whose presence always — on easy days and difficult ones — was essential for my perseverance. To my sons, Aleksei and Nikola, whose very existence inspires me every day to become a better person. To Tobi, for his silent companionship, and to our beloved Pomeranians, Myke and Sophie, who, despite their size, filled our days with joy and balance throughout this journey — and whose absence now only makes it clearer how special they were.

To ENEVA, as an institution, for embracing this project from the very beginning. I am especially grateful to my director, Frederico Miranda, and my manager, Diogo Michelon, whose vision and support were crucial in turning an idea into reality. You became friends and colleagues who believed in this path since our very first conversation, back at the beginning of 2021 — a decisive moment, when this work was reinvented and rewritten at the eleventh hour, with courage and commitment on both sides.

To my university colleague, professional partner, dear friend, and advisor, Prof. Dr. Leonardo Fadel Cury, for his firm yet generous guidance, and for the academic freedom he always granted me. Our meetings, which often went beyond the scope of science and took place over productive barbecues at his home, served as the setting for decisive discussions. I also thank his wife, our dear dentist, Dr. Lariessa, always warm and kind, whose presence made those moments even more special and to our dear “Little John”.

To my co-advisors, Prof. Dr. Anelise Bahniuk and Dr. Nilo Azambuja, my sincere thanks for your patience, dedication, and constant availability. Even during periods of introspection and absence on my part, you remained present with valuable contributions and relevant discussions.

To my colleagues at LAMIR, especially Lari and Zito, thank you very much for your essential help in defining the main lines of investigation of this research. Your generosity in sharing knowledge and your patience in teaching me the fundamentals were key to starting this journey with greater confidence.

To my fellow graduate students with whom I had the privilege of interacting during this new phase at UFPR — whether in courses, joint projects, or our daily routine at LAMIR — my sincere gratitude. Every exchange and conversation enriched this academic experience.

To the Centro de Investigaciones Geológicas at the Universidad Nacional de La Plata (CIG UNLP) — especially Prof. Dr. Daniel Poiré and my colleague Luis Vigiani (Pocho) from the X-ray laboratory technical team — thank you for the warm welcome and deep technical exchange during the week I spent in Argentina as part of the LAMIR/UFPR – UNLP collaboration.

To the Exploration Geology team at ENEVA, a group I have the pleasure of leading technically, my deep appreciation for your professionalism, partnership, and genuine support. To the team formed by Manu, Guga, Henrique, Floripa, Roque, Fernando, and Julianna — thank you for your constant support, especially during my absences to focus on writing this thesis. Without you, this stage would have been even more difficult.

To my colleagues at ENEVA who became friends and partners in this journey, my heartfelt thanks for embracing this project from the beginning. Your technical contributions, unwavering support, rich discussions, teamwork, participation in publications, figure preparation, reviews, and above all, encouragement and friendship, were fundamental. I mention here, at the risk of forgetting someone: Henrique, Fernando, Lilian, Marcia, Beto, Nane, Caio, David, Padoves, Cassia, Lelê, Rafa, Roma, among others. A special thanks to my management colleagues and friends Pati, Carlinhos, and Vini, who took part in the job load during this period — I am deeply grateful.

To my friends and colleagues from undergraduate studies and profession — professors, doctors, academic partners, sports teammates, and life companions who remained close during these past few years: Cozó and Vera, PS and Dog, Kaluan, Ju, Igor, Bebó, Tuti, Dodô, Ale, Gilson, Gustavo, Camila, Wagnão, Mari, Fabi, Maiô, Bá, Cris, Jô, Gaúcho, Barbara, Barrados, Ângela, Roger, Negro, Max, Mari Cal, Rave, Alemão, Wally, Pitu, Ana, Ju, Zb, Max, Mari, Fabinho and many others. Each one of you played a unique role in this journey.

To the friends who live academia with passion and inspire me with their enthusiasm and dedication to science — and who are true references in their fields: Caesar, Bruno, Jose Margotta, Juliana, Ceará, Max — thank you for walking with me in this path of discovery and learning.

And finally, to a few professors who, during the now distant years of my undergraduate studies (1995–2000) and my master's (2003–2005), left a lasting mark on my academic formation: Sidnei, Eleonora, Augustinho, Paulo Soares, Gianinni, Mario Assine, and Chang. Your lectures and examples planted seeds that are now blooming in this doctoral journey. I would not be here had I not met you. My most sincere thanks.

AGRADECIMENTOS

À minha família, pelo apoio inabalável, carinho e presença constante ao longo destes quatro intensos anos de estudo. À minha mãe, Iraci, um verdadeiro pilar em minha vida e fonte permanente de força. À minha esposa, Eliandra, companheira incansável, cuja presença em todos os momentos — nos dias fáceis e difíceis — foi essencial para que eu persistisse. Aos meus filhos, Aleksei e Nikola, cuja existência me inspira todos os dias a ser uma pessoa melhor. Ao Tobi, por sua companhia silenciosa, e aos nossos queridos pomerânios, Myke e Sophie, que, apesar de pequenos, encheram nossos dias com alegria e equilíbrio ao longo desta jornada — e cuja ausência agora só evidencia ainda mais o quanto foram especiais.

À ENEVA, enquanto instituição, por ter abraçado este projeto desde o princípio. Agradeço especialmente ao meu diretor, Frederico Miranda, e ao meu gerente, Diogo Michelon, cuja visão e apoio foram cruciais para transformar uma ideia em realidade. Vocês se tornaram colegas e amgos que acreditaram nesse caminho desde a nossa primeira conversa, no início de 2021 — um momento decisivo, em que este projeto foi reinventado e reescrito no apagar das luzes, com coragem e comprometimento de ambas as partes.

Ao meu colega de universidade, parceiro de profissão, amigo querido e orientador, Prof. Dr. Leonardo Fadel Cury, por sua orientação firme e generosa, e pela liberdade acadêmica que sempre me concedeu. Nossos encontros, muitas vezes indo além do campo da ciência e ocorrendo em churrascos produtivos em sua casa, serviram como palco de discussões decisivas. Também agradeço à sua esposa, nossa querida dentista, Dra. Lariessa, sempre acolhedora e gentil e ao querido Joãozinho, cuja presença tornou esses momentos ainda mais especiais.

Aos meus coorientadores, Profa. Dra. Anelise Bahniuk e Dr. Nilo Azambuja, minha sincera gratidão pela paciência, dedicação e constante disponibilidade. Mesmo durante períodos de introspecção e ausência da minha parte, vocês sempre estiveram presentes com incentivo, contribuições valiosas e discussões relevantes.

Aos colegas do LAMIR, em especial à Lari e ao Zito, muito obrigado pela ajuda essencial na definição das principais linhas de investigação desta pesquisa. Sua generosidade em compartilhar conhecimento e a paciência em me ensinar os fundamentos foram fundamentais para que eu pudesse iniciar essa caminhada com mais confiança.

Aos colegas da pós-graduação com quem tive o privilégio de conviver nesta nova fase na UFPR — seja em disciplinas, projetos conjuntos ou na convivência diária no LAMIR — meu sincero agradecimento. Cada troca e cada conversa enriqueceram esta experiência acadêmica.

Ao Centro de Investigaciones Geológicas da Universidad Nacional de La Plata – CIG UNLP –, especialmente ao Prof. Dr. Daniel Poiré e ao colega Luis Vigiani (Pocho), do grupo técnico do laboratório

de Raios X, pela calorosa recepção e profunda troca técnica durante a semana que passei na Argentina como parte da colaboração LAMIR/UFPR – UNLP.

Ao time de Geologia da Exploração da ENEVA, grupo que tenho o prazer de coordenar tecnicamente, minha profunda gratidão pelo profissionalismo, parceria e apoio genuíno. À equipe formada por Manu, Guga, Henrique, Floripa, Roque, Fernando e Julianna, muito obrigado pelo suporte constante, especialmente durante minhas ausências para me dedicar à redação desta tese. Sem vocês, esta etapa teria sido ainda mais difícil.

Aos colegas da ENEVA que se tornaram amigos e parceiros nesta jornada, meu sincero agradecimento por abraçarem este projeto desde o início. Suas contribuições técnicas, apoio irrestrito, discussões ricas, trabalho em equipe, participação em publicações, elaboração de figuras, revisões e, acima de tudo, incentivo e amizade foram fundamentais. Cito alguns aqui, certo do risco de esquecer alguém: Henrique, Fernando, Lilian, Marcia, Beto, Nane, Caio, David, Padoves, Cassia, Lelê, Rafa, Roma, entre outros. Um agradecimento especial aos colegas de gestão e amigos Pati, Carlinhos e Vini, que assumiram parte da carga durante esse período — sou profundamente grato.

Aos amigos e colegas da graduação, de trabalho — professores, doutores, parceiros na academia, nos esportes e na vida — que estiveram por perto nesses últimos anos: Cozó, Vera, PS e Dog, Kaluan, Ju, Igor, Bebó, Tuti, Dodô, Ale, Gilson, Gustavo, Camila, Wagnão, Mari, Fabi, Maiô, Bá, Cris, Jô, Gaúcho, Barbara, Barrados, Ângela, Roger, Negro, Max, Mari, Cal, Rave, Alemão, Wally, Pitu, Ana, Ju, Zb, Max, Mari, Fabinho e muitos outros. Cada um teve um papel único nesta trajetória.

Aos amigos que vivem a academia com paixão e me inspiram com seu entusiasmo e dedicação à ciência — e que são referências em suas áreas — Caesar, Bruno, Jose Margotta, Juliana, Ceará, Max — obrigado por seguirem comigo nesta caminhada de descobertas e aprendizado.

E, por fim, a alguns professores que, nos já distantes tempos da graduação (1995–2000) e do mestrado (2003–2005), deixaram uma marca profunda na minha formação: Sidnei, Eleonora, Augustinho, Paulo Soares, Gianinni, Mario Assine e Chang. Suas aulas e seus exemplos plantaram sementes que agora florescem neste doutorado. Eu não estaria aqui se não os tivesse conhecido. Meu mais sincero obrigado

RESUMO

A Bacia do Parnaíba, localizada no nordeste do Brasil, é uma bacia intra-cratônica, multifásica, de idade Paleozoica, que contém inúmeros campos de gás natural, gerados na Formação Pimenteiras, do Devoniano, um sistema petrolífero atípico, onde a maturação da rocha fonte e os mecanismos de formação de trapas são causados pelo Evento Magmático do Atlântico Central (CAMP), de idade Neo Triássica. A modelagem numérica de sistemas petrolíferos em ambientes atípicos é um processo desafiador devido ao número de variáveis adicionais e desconhecidas que precisam ser modeladas. As incertezas relacionadas à idade e sequência das intrusões magmáticas, às propriedades térmicas do magma, à escassez e qualidade dos parâmetros orgânicos de calibração térmica e ausência de esquemas cinéticos adequados podem levar a previsões incorretas sobre a transformação das rochas geradoras, bem como na estimativa de fase e composição das acumulações de hidrocarbonetos modeladas. Esta tese apresenta resultados inovadores em três linhas principais de pesquisa: 1) Aquisição de novos dados orgânicos e geoquímicos, como carbono orgânico total (TOC), pirólise e vitrinita dos níveis enriquecidos em matéria orgânica da Formação Pimenteiras; 2) Estabelecimento de um esquema cinético composicional específico para a rocha geradora da Formação Pimenteiras e subsequente implementação no simulador numérico 3D de sistemas petrolíferos 3) Estudo das variações da cristalização da ilita (índice de Kubler) ao longo do perfil de três poços da bacia, com o objetivo de entender o impacto do calor devido às intrusões magmáticas sobre os minerais argilosos, utilizando um extenso conjunto de dados de difração de raios-X. Os resultados dos dados geoquímicos demonstram o impacto das intrusões de soleiras de diabásio sobre o perfil de maturação, levando a valores de reflectância de vitrinita acima de 5% de Ro, no campo de sobre maturação, também mostrando uma importante redução nos valores de TOC. A escassez de partículas de vitrinita e a ampla gama de maturidade indicam a dificuldade de usar a reflectância de vitrinita como um único indicador da maturação da rocha geradora. Os resultados cinéticos mostraram uma distribuição estreita da energia de ativação (entre 50-56 kcal/mol), em linha com uma estrutura homogênea do querogênio. A análise do pirolisados corrobora com a deposição de matéria orgânica algal/bacteriana em um ambiente predominantemente marinho, de querogênio do Tipo II. A implementação do esquema cinético no simulador numérico e a comparação com um esquema cinético análogo, de uma rocha geradora Devoniana da América do Norte (Woodford Shale), mostrou diferenças de -66,6%, -19,5% e -0,8%, respectivamente, para os ORL's A, B e C, nas massas de petróleo geradas, indicando um efeito substancial do esquema cinético nas previsões da modelagem numérica. A análise dos dados de difração de raios-X na fração argila, com ênfase na decomposição do pico 10A, permitiu a individualização das fases de moscovita/mica detríticas das fases de ilita neo formadas pelo metamorfismo de contato. O Índice de Kubler (largura total no máximo de largura – FWHM, na sigla em inglês), medido no pico associado à ilita, mostrou uma correlação consistente com a reflectância de vitrinita, permitindo a melhoria na calibração térmica dos modelos numéricos

Palavras-Chave: Sistemas Petrolíferos Atípicos, Esquema Cinético Composicional, Modelagem de Sistemas Petrolíferos, Calibração Térmica, Cristalinidade da Ilita

ABSTRACT

The Parnaíba Basin, located in northeastern Brazil, is an intra-cratonic, multi-phase Paleozoic basin that hosts a considerable number of natural gas fields sourced from the Devonian Pimenteiras Formation. It is an atypical petroleum system, where source rock maturation and trap formation mechanisms are driven by the Central Atlantic Magmatic Event (CAMP), which occurred during the Late Triassic. Numerical modeling of petroleum systems in such atypical environments is a challenging process due to the numerous additional unknown variables that must be accounted for. Uncertainties related to the timing and age of magmatic intrusions, thermal properties of the magma, the scarcity and quality of organic thermal calibration parameters, and appropriate kinetic schemes can lead to inaccurate predictions of source rock transformation as well as the phase and composition of predicted hydrocarbon accumulations. This thesis presents novel results in three main areas of research: 1) Acquisition of a new dataset of organic geochemical parameters, such as total organic carbon (TOC), pyrolysis data, and vitrinite reflectance, from the organic-rich layers (ORLs) of the Pimenteiras Formation; 2) The establishment of a specific compositional kinetic scheme for the Pimenteiras Formation source rock and its implementation into a 3D petroleum system modeling (PSM) simulator; and; 3) The investigation of illite crystallinity variations (Kübler Index) across profiles from three wells in the basin, to investigate and understand the impact of magmatic heating on clay minerals, using an extensive dataset of X-ray diffraction (XRD) data. The geochemical data reveals the impact of magmatic sill intrusions on the maturation profiles, resulting in vitrinite reflectance values exceeding 5% of Ro, entering the overmature range, and showing significant reductions in TOC values. The scarcity of vitrinite particles and the wide thermal maturity range highlight the limitations of using vitrinite reflectance as a sole thermal maturity proxy. The kinetic analysis revealed a narrow activation energy distribution (between 50–56 kcal/mol), consistent with a homogeneous kerogen structure. Pyrolysate analysis supports the deposition of algal/bacterial organic matter in a dominantly marine, Type II kerogen environment. The implementation of the new kinetic scheme into the numerical simulator and its comparison with a North American Devonian source rock analogue (the Woodford Shale) showed differences of -66.6%, -19.5%, and -0.8% in generated petroleum masses for ORLs A, B, and C, respectively, indicating the substantial impact of the kinetic scheme on PSM predictions. XRD analysis of the clay fraction, focusing on the decomposition of the 10Å peak, enabled the differentiation between detrital muscovite/mica and newly formed illite phases. The Kübler Index (full width at half maximum—FWHM), measured from the decomposed illite peak, showed a consistent correlation with vitrinite reflectance, enhancing the thermal calibration of numerical models.

Keywords: Atypical Petroleum Systems; Compositional Kinetic Scheme; Petroleum System Modeling; Thermal Calibration; Illite Crystallinity.

SUMMARY

1. INTRODUCTION 1

1.1. OBJECTIVES, HYPOTHESES AND EXPECTED PRODUCTS 3

1.2. AVAILABLE DATASET TO THE RESEARCH PROJECT 6

2. THEORETICAL FOUNDATION 7

2.1. GEOLOGICAL BACKGROUND OF PARNAÍBA BASIN 7

2.1.1. Tectonic evolution and structural framework 7

2.1.2. Stratigraphic Framework 11

2.1.2.1. The Meso-Devonian Eo-Carboniferous Sequence 12

2.1.3. The atypical petroleum system of the Parnaíba basin 16

2.2. PETROLEUM SYSTEMS NUMERICAL MODELING 20

2.2.1. Short history, principles, and process on petroleum systems numerical modeling 20

2.2.2. Structure of a model and modeling steps 25

2.2.3. Transport Processes 28

2.2.4. Thermal calculations and calibrations 29

2.2.4.1. Heat Transfer - Steady State and Transient Effect 31

2.2.4.2. Thermal Rock Properties – Thermal Conductivity and Specific Heat Capacity 31

2.2.4.3. Radiogenic Heating 32

2.2.4.4. Three-Dimensional Heat Flow Equations 33

2.2.4.5. Magmatic Intrusions 34

2.2.4.6. Organic and inorganic calibration tools in PSM 35

2.2.5. Challenges in atypical Petroleum Systems Modeling 44

2.2.6. Kinetic of Organic Matter Transformation 46

2.3. X-RAY DIFFRACTOMETRY 48

2.3.1. X-Ray Diffractometry 48

2.3.1.1. The Illite Crystallinity and the Kubler Index 49

3. DATASET AND METHODOLOGY 53

3.1. Analysis of Reflectance of Vitrinite 53

3.2. Definition of compositional kinetic scheme from pimenteiras source rock and implementation on petromod 54
3.3. X-Ray diffraction analysis 58
3.4. Spectral decomposition of illite peaks on XRD data 63
3.5. Petroleum systems modeling 65
4. RESULTS 71
4.1. Vitrinite Reflectance Analysis 71
4.2. Organofacies, Compositional Kinetics and Phase Behavior Results 75
4.3. XRD Analysis, Kubler Index and Esquevin Index Results 81
4.4. Petroleum System Modeling Results 89
4.4.1. Impacts of PSM results due to implementation of compositional kinetics scheme for Pimenteiras Formation 89
4.4.2. Smectite to Illite calculation in PSM Models 91
5. DISCUSSION 94
5.1. The characterization of organofacies and the implication of the kinetic parameters on the Pimenteiras Formation. 94
5.2. The implementation of the Pimenteiras kinetics and the comparison of modeling results with the Woodford Shale kinetics. 96
5.3. The use of Kubler Index from decomposed Illite fraction as support of the reflectance of vitrinite in the atypical petroleum systems modeling. 104
5.4. Analysis of Esquevin index results versus Kubler Index, the Anchimetamorphic zone and Epizone characterization at the analyzed wells. 113
5.5. Correlation between Kubler Index and Vitrinite and the Anchimetamorphic zone and Epizone characterization at the analyzed wells. 116
6. SCIENTIFIC CONTRIBUTIONS 121
7. CONCLUSIONS AND FINAL REMARKS 124
REFERENCES 128
8. APPENDIX A – 1D PSM Input Tables 135
9. APPENDIX B – DRX Decomposition Charts 136

FIGURE 1 – WORKFLOW OF IMPROVEMENTS IN PETROLEUM SYSTEM MODELING SUBJECT OF THIS RESEARCH. IN ORANGE THE MAIN CHALLENGES TO BE ADDRESSED ARE PRESENTED AND IN GREEN THE RESEARCH TOPICS IN THE FORM OF TOPICS INVESTIGATED DURING WORK. THE DARK GREEN ITEMS, WITH RELEVANT SCIENTIFIC IMPACT, BECAME THE PAPERS TO BE PUBLISHED. 3
FIGURE 2 – GEOLOGICAL MAP OF THE PARNAÍBA BASIN, SHOWING THE OCCURRENCE OF THE GEOLOGICAL UNITS, THEIR AGES AND THE DISTRIBUTION OF WELLS AND EXPLORATORY BLOCKS ALONG THE BASIN. 8
FIGURE 3 – PALEOTECTONIC MAP OF PRE-SILURIAN BASEMENT OF PARNAÍBA BASIN PROPOSED BY PORTO ET AL., 2022 AND USED AS REFERENCE IN THIS STUDY. 10
FIGURE 4 – STRATIGRAPHIC CHART OF THE PARNAÍBA BASIN BY VAZ ET AL., 2007....11
FIGURE 5- HIGH RESOLUTION SEQUENCE STRATIGRAPHY, SYSTEM TRACS, STRATIGRAPHIC SURFACES AND FACIES SUCCESSIONS FROM THE UPPER PART OF ITAIM, PIMENTEIRAS AND LOWER PART OF CABEÇAS FORMATIONS, ACCORDING TO YOUNG, (2006).....14
FIGURE 6 – STRATIGRAPHIC CROSS SECTION ALONG PARNAÍBA BASIN SHOWING THE CORRELATION BETWEEN KEY WELLS FERRAZ ET AL. (2017).....15
FIGURE 7 – TYPE SECTION OF TRANSGRESSIVE SYSTEM TRACT CORRESPONDING TO THE LOWER PORTION OF PIMENTEIRAS FORMATION, OBJECT OF THIS STUDY, ACCORDING TO FERRAZ ET AL., (2017).....15
FIGURE 8 – TYPE SECTION OF THE HIGH STAND SYSTEM TRACT (HST/TSNA) CORRESPONDING TO THE UPPER PART OF THE PIMENTEIRAS FORMATION ACCORDING TO FERRAZ ET AL., (2017) 16
FIGURE 9 – SCHEMATIC CROSS SECTION ALONG PARNAÍBA BASIN SHOWING THE INFLUENCE OF INTRUSIVE DIABASE SILLS ON THE PETROLEUM SYSTEM ALONG PARNAÍBA BASIN. MIRANDA (2014).....19
FIGURE 10 – ACCUMULATION MODELS FOR ATYPICAL GENERATION AND TRAPPING OF HYDROCARBONS IN THE PARNAÍBA BASIN. MIRANDA (2014).....19
FIGURE 11 – 2D PETROLEUM SYSTEM MODELING LINE (E-W) ALONG THE PARNAÍBA BASIN SHOWING THE PRESENT-DAY FINGERPRINT OF THE THERMAL STRESS CAUSED BY THE MAGMATISM (MIO, 2022).....20
FIGURE 12 – EVOLUTION OF A SEDIMENTARY BASIN, FROM THE INITIAL DEPOSITION (T = T0) TO THE BASIN CONFIGURATION OBSERVED TODAY (T = TX). PARAMETERS SUCH AS TEMPERATURE, ARE CHANGING CONTINUOUSLY IN EACH SEDIMENTARY UNIT ACCORDING TO THE IMPROVEMENT IN DEPTH OF BURIAL (ADAPTED FROM TISSOT & WELTE, 1984).....23
FIGURE 13 – CONCEPTUAL FLOW OF TWO-DIMENSIONAL BASIN MODELING AS PROPOSED BY UNGERER ET AL., (1990) WITH THE ADVANCE ON TWO-PHASES FLUID FLOW AND THE POSSIBILITIES OF COUPLED THERMAL CALCULATION WITH SINGLE-PHASE FLUID FLOW AND MATURATION CALCULATIONS. IN GREEN, THE INPUT FILES AND PARAMETERS IN YELLOW THE CALCULATION MODULES AND IN LIGHT RED THE OUTPUTS OF EACH MODULE OF CALCULATION AND THE ARROWS INDICATES INTERACTIONS AMONG THE STEPS OF CALCULATIONS. 24
FIGURE 14 – MAIN GEOLOGICAL PROCESSES ON BASIN MODELING HANTSCHEL; KAUERAUF (2009). THE OUTPUTS OF THE BASIN MODELS, WITH A SCENARIO OF TEMPERATURE AND

PRESSURES ALONG THE TIME, SERVED AS THE BASIS FOR MODELLING OF OTHER GEOLOGICAL AND PHYSICAL PROCESSES SUCH AS MINERAL TRANSFORMATION, MODELLING OF HYDROCARBON CONTAMINANTS AND CARBON DIOXIDE STORAGE.....25
FIGURE 15 – MAIN REQUIREMENTS FOR A BASIN MODEL, INCLUDING: A) THE INITIAL GEOMETRIES; B) MODEL FILLING WITH FACIES AND PROPERTIES; C) MODEL DEFINITION AND MESHING, WITH ATTRIBUTION OF AGES, RESERVOIRS AND SOURCE ROCKS PROPERTIES, PALEO GEOMETRIES, PALEO BATHYMETRIES AND EROSIONS, AND D) BOUNDARY CONDITIONS OF THE MAPS, AS THE SURFACE-TO-SEDIMENT TEMPERATURE INTERFACE (SWI) AND HEAT FLOW AT THE BASE OF THE BASIN, THAT CAN BE FROM DIRECT MAPS OR INFERRED FROM ANOTHER INFORMATION (PALEO BATHYMETRIES, CRUSTAL STRETCHING MAPS ETC.). BASED ON HANTSCHEL AND KAUERAUF (2009). 27
FIGURE 16 – BASIN MODELING PROCESS STEPS, DESCRIBING THE CALIBRATION PROCESS (A), THE SIMULATION STEP (B) AND THE RESULTS AND POST-PROCESSING PROCESS (C). 27
FIGURE 17 – EXAMPLE OF EXTRACTION OF BASIN MODELING RESULTS ALONG THE TIME. CROSS SECTION IN DIP DIRECTION IN PELOTAS BASIN, BRAZILIAN SOUTH ATLANTIC MARGIN, SHOWING THE EVOLUTION OF OVERPRESSURE IN TWO DIFFERENT SCENARIOS, IN A) THE EVOLUTION OF OVERPRESSURE WITHOUT THE CONTRIBUTION OF HYDROCARBON GENERATION; B) THE EVOLUTION OF OVERPRESSURE WITH COUPLED CALCULATION OF MATURITY AND HYDROCARBON GENERATION. (KIA AND MIO, (2022).....28
FIGURE 18 -FUNDAMENTALS PHYSICAL TRANSPORT LAWS AND THEIR VARIABLES. HANTSCHEL AND KAUERAUF (2009). 29
FIGURE 19 – BOUNDARY VALUE PROBLEM FOR A HEAT FLOW ANALYSIS (A) OF THE LITHOSPHERE AND (B) IN THE SEDIMENTS HANTSCHEL AND KAUERAUF (2009). 30
FIGURE 20 – INTRUSION MODEL AND THE DEFAULT VALUES PRESENTED BY DELANEY (1988) IN A FORTRAN 77 ROUTINE FOR CALCULATION. APUD (HANTSCHEL AND KAUERAUF, 2009) 34
FIGURE 21 – COMPOSITION OF DISSEMINATED ORGANIC MATTER IN SEDIMENTARY ROCKS. ADAPTED FROM TISSOT AND WELTE (1984). FROM THE INITIAL TOC, PART OF CARBON IS THE KEROGEN, WHICH IS INSOLUBLE IN ORGANIC SOLVENTS AND PART IS THE BITUMEN (HC´S ALREADY GENERATED), COMPOSED OF AROMATICS AND SATURATED HC´S AND NSO.....36
FIGURE 22 - VAN KREVELEN DIAGRAM SHOWING THE EVOLUTION PATH OF THE MAIN KEROGEN TYPES, ACCORDING TO THE RATIOS OF H/C VS O/C (TISSOT AND WELTE, 1984). 37
FIGURE 23 – GEOCHEMICAL FRACTIONATION OF ORGANIC MATTER(HANTSCHEL AND KAUERAUF, 2009). 38
FIGURE 24 – KINETIC PARAMETERS FOR THE TRANSFORMATION OF VITRINITE AS DESCRIBED BY SWEENEY AND BURNHAM (1990), RIGHT, AND LARTER (1988), LEFT.....39
FIGURE 25 – SOME OF PROPOSED LIMITS FOR THE "MATURITY WINDOWS" OF SOURCE ROCKS BASED ON THE VALUES OF REFLECTANCE OF VITRINITE (%RO), IN A, THE LIMITS PROPOSED IN THE EASY RO MODEL FROM SWEENEY & BURNHAM., (1990), DETAILING THE OIL WINDOWS, AND IN B, THE LIMITS PRESENTED BY TISSOT; WELTE (1984), WITH SOME VARIATIONS, ESPECIALLY IN OIL ZONES, WITH THE VARIATION OF THE KEROGEN TYPE.....40
FIGURE 26 – EXAMPLE OF THERMAL CALIBRATION USE BOTTOM HOLE TEMPERATURE (BHT) AND VITRINITE REFLECTANCE DATA DO FIT THE PETROLEUM SYSTEM MODEL IN ULTRADEEP SETTINGS IN FOZ DO AMAZONAS BASIN, BRAZIL CANELAS (2020). 41

FIGURE 27 – MATURITY PROFILE OF PARNAÍBA BASIN BASED ON TMAX AND VITRINITE REFLECTANCE DATA (%RO). IN A THE BURIAL TREND OF MATURITY, USING TMAX DATA CONVERTED TO VITRINITE. IN B THE THERMAL EFFECT OF THE MAGMATISM IN THE VITRINITE REFLECTANCE, CHANGING THE BURIAL TREND, LEADING THE VITRINITE TO REACH THE OVERMATURE WINDOW MIO ET AL. (2023). 42
FIGURE 28 – COMPOSITION OF I/S IN THE SHALE NEAR TO AN INTRUSIVE BASALT DIKE IN COLORADO. THE POINTS WERE DEFINED USING X-RAY DIFFRACTOMETRY AND THE CURVE IS CALCULATED USING THE KINETIC MODEL EQUATION FROM PYTTE; REYNOLDS (1988). 44
FIGURE 29 – MAIN CHALLENGES IN MODELING ATYPICAL PETROLEUM SYSTEMS, THE IMPACT IN THE RESULTS AND THE PROPOSED ACTION ITEMS TO BE ADDRESSED TO SOLVE THE PROBLEMS MIO ET AL. (2023).....45
FIGURE 30 – GENERAL SCHEME OF THE EVOLUTION OF THE ORGANIC MATTER, FROM DEPOSITION TO METAMORPHISM, ABRAKASA ET AL. (2022) ADAPTED FROM TISSOT AND WELTE (1984). 47
FIGURE 31 – REGRESSION LINES AND EQUATIONS FROM THE RELATIONSHIP BETWEEN KUBLER INDEX OR ICII (ILLITE CRYSTALLINITY INDEX) AND PERCENT OF VITRINITE REFLECTANCE FROM THE DATA PRESENTED BY FREY & ROBINSON, (1999) AND MÄHLMANN AND FREY (2012).....52
FIGURE 32 - LOCATION OF 3D, 2D AND 1D PSM MODELS USED IN THIS STUDY. 3D SPM MODEL 01 AND 02, THE E-W LINE OF 2D PSM MODEL, AND THE 1D PSM MODELS WELL A, B AND C. ADDITIONALLY, THE LOCATION OF WELL B AND D WHICH WERE THE SELECTED WELLS TO PERFORM THE STUDY OF COMPOSITIONAL KINETICS OF THE PIMENTEIRAS FORMATION IS SHOWN. 53
FIGURE 33 – PHOTOMOSAIC OF SAMPLE SELECTION FOR COMPOSITIONAL KINETIC ANALYSIS. A) BOX WITH CUTTINGS OF PIMENTEIRAS FORMATION AT THE WELL 1- PA-1-MA; B) SET OF SAMPLES SELECTED INSIDE OF EACH ORGANIC RICH INTERVAL OF THE PIMENTEIRAS FM. (A, B, C AND D); C) DETAIL OF THE SELECTED SAMPLE AT LEVEL A OF THE PIMENTEIRAS FORMATION, ONE OF THE SELECTED SAMPLES FOR KINETIC STUDY. 55
FIGURE 34 - BULK KINETIC PARAMETERS FOR THREE SAMPLES BASED ON SLOW HEATING RATES (0.7; 2.0; 5.0K/MIN) USING DISCRETE MODELS. THE SAMPLE 20189 (CENTER) WAS THE SAMPLE SELECTED FOR PHASEKINETICS. IT IS A SAMPLE OF 2077 M (PIMENTEIRAS SR A) FROM WELL B. 57
FIGURE 35 - PHOTOMOSAIC OF CLAY FRACTION SAMPLE PREPARATION AND ANALYSES AT CIG – UNPL LABORATORIES, LA PLATA, ARGENTINA. A – DIFFRACTOMER PHILLIPS XPERT PRO; B - SAMPLE CRUSHING AND HOMOGENIZATION; C - DECANTATION IN TUBES; D – PIPETTING AND GLASS BASE MOUNTING OF NATURAL CLAY PLATE; E – SAMPLES IN THE OVEN FOR TWO HOURS HEATING AT 550°C; F – DRIED NATURAL CLAY FRACTION BEFORE ANALYSIS; G – INTERFACE OF PHILLIPS XPERT PRO EQUIPMENT DURING MEASURING PROCESS. 59
FIGURE 36 - USGS CLAY MINERAL IDENTIFICATION FLOW DIAGRAM FOR 10Â PHASE.....63
FIGURE 37 – PROCESS OF DECOMPOSITION OF X-RAY DIFFRACTOGRAM INTO DECOMPXR SOFTWARE AND INTERPRETATION OF POSSIBLE CLAY MINERAL PHASES. A) MICA-LIKE OR MUSCOVITE PHASE; B) AND C) ADDITION OF ILLITE PHASES; D) CHLORITE PHASE; E)

Talc/Pyrophyllite and F) Final interpretation with insertion of a broad FWHM peak to correct background. 64
Figure 38 – Example of use of KI converted to %Ro and the comparison with measured %Ro along the interval of the Pimenteiras Formation at the well A, showing the preliminary results. Green triangles represent the first KI (converted to %Ro) measure at Highscore Plus Software@, the purple and yellow diamonds represent the KI (converted to %Ro) from decomposition at DecompRX software. The illite phase (yellow diamonds - authigenic formed) match with the measured vitrinite reflectance (red circles) while the detrital muscovite phases (purple diamonds) present a higher crystallinity. Conversion from KI to %Ro was performed using Mählmann and Frey (2012). 65
Figure 39 – Workflow of 3D Model Construction. A) Location of the two three-dimensional models and the 1D PSM models; B) seismic coverage at the 3D PSM Model 01; C) Example of a 2D seismic interpretation; D) Seismic acoustic impedance; E) Acoustic impedance from well analysis; F) Seismic acoustic impedance populated into the 3D geological model and G) Acoustic impedance into the 3D model from seismic plus well analysis 66
Figure 40 - 2D PSM Model. A) Depth converted seismic section (E-W Direction) with the interpretation of main horizons and faults; B) Petromod 2D PSM Model highlighting the Meso-Devonian/Eo Carboniferous sequence and the atypical petroleum system: 1) Diabase intrusive sill; 2) Poti Formation; 3) Longá Formation; 4) Cabeças Formation, 5) Pimenteiras Formation and 6) Itaim Formation. 68
Figure 41 – 1D PSM Model (Well A) showing the present-day temperature, calibrated with bottom hole temperature data (A), and the burial history graphs for temperature (B) and vitrinite reflectance (C), using the Sweeney and Burnham (1990) model. 70
Figure 42 – Examples of vitrinite reflectance measurements procedure in two good quality samples. In the left, Well A at 1968 m, with 32 measures of primary vitrinite: In the right, Well C, 1917 m, with 27 measures of primary vitrinite. 72
Figure 43 - Examples of vitrinite reflectance measurements procedure in two low quality samples. In the left, Well B at 2061 m, with 11 measures of primary vitrinite with high dispersion in the values: In the right, Well A, 2064 m, with five measures of primary vitrinite, showing the challenge in finding good quality measurements in some of the samples. 72
Figure 44 2D PSM Model. (A) Depth converted seismic section (E-W Direction) with the interpretation of main horizons and faults; (B) Petromod 2D PSM Model highlighting the Meso-Devonian/Eo Carboniferous sequence and the atypical petroleum system: 1) Diabase intrusive sill; 2) Poti Formation; 3) Longá Formation; 4) Cabeças Formation, 5) Pimenteiras Formation and 6) Itaim Formation. (C) Calculated Vitrinite reflectance along the 2D Model, indicating the position of the wells 01 and 02 and the samples 20170 and 20189, with the geochemical and maturity parameters used to selection for phase kinetics. VR*

values were initially calculated using TMax Jarvie et al. (2001) and later were compared with vitrinite, grapholite and bitumen reflectance. 74
Figure 45 – Compositional scheme for the black oil (A), two components (B), four components (C) and fourteen components (D) for the sample 20189, from the Pimenteiras Formation source rock interval A in Well B, at 2277 m. 78
Figure 46 – Compositional scheme for the black oil (A), two components (B), four components (C) and fourteen components (D) for the sample 20170, from the Pimenteiras Formation source rock interval C in Well D, at 2034 m. 78
Figure 47 - Organofacies, kinetics and phase behavior for samples 20189 (ORL A – Well B) and 20170 (ORL C – Well D) showing the petroleum type of samples into the gas/condensate field (A – Horsfield (1989a)), the narrow distribution of activation energies for samples 20189 and 20170, between 50 to 60 kcal/mol (B), and the impact of these petroleum type and kinetic parameters on phase composition (C). 79
Figure 48 Kinetic Results A) Comparison of transformation ratio curves between the Pimenteiras Formation and Woodford Shale, calculating using heating rates of 3k/My (Devonian from USA/Canada – Hantschel and Kauerauf 2009). B) Bulk kinetic curves for several samples from Pimenteiras Formation showing a narrow interval of activation energies (between 55 to 60 kcal/mol); Comparison of four compounds kinetic schemes for: C) Woodford Shale; D) Pimenteiras level C; and E) Pimenteiras level A.....80
Figure 49 - Semi quantitative results from total powder and clay fractions from well A samples. Legend for total powder fraction: Qz= quartz, K Felds= K Feldspars, Plag= Plagioclase, Ca= Calcite, Dol= Dolomite, Sid= Siderite, Py= Pyrite, Pf= Pyrophyllite, Oth= Others, Clay= Clay. Legend for clay fraction: I/M= Illite or Mica, I/S Interstratified Illite-Smectite, Sm= Smectite, Cl= Chlorite, K= Kaolinite. 86
Figure 50 - Semi quantitative results from total powder and clay fractions from well B samples. Legend for total powder fraction: Qz= quartz, K Felds= K Feldspars, Plag= Plagioclase, Ca= Calcite, Dol= Dolomite, Sid= Siderite, Py= Pyrite, Pf= Pyrophyllite, Oth= Others, Clay= Clay. Legend for clay fraction: I/M= Illite or Mica, I/S Interstratified Illite-Smectite, Sm= Smectite, Cl= Chlorite, K= Kaolinite. 87
Figure 51 - Semi quantitative results from total powder and clay fractions from well C samples. . Legend for total powder fraction: Qz= quartz, K Felds= K Feldspars, Plag= Plagioclase, Ca= Calcite, Py= Pyrite, Pf= Pyrophyllite, Oth= Others, Clay= Clay. Legend for clay fraction: I/M= Illite or Mica, I/S Interstratified Illite-Smectite, Sm= smectite, Cl= Chlorite, K= Kaolinite. 88
Figure 52 – Implementation of kinetic parameters of the Pimenteiras formation into 2D PSM. A) Impacts on hydrocarbon composition prediction in a 2D model ran with Woodford Shale Kinetic (left), and Pimenteiras Formation Kinetic (right) with composition close to the PVT data from the fields (adapted from Lopes and Mio, 2023). B) Impact in hydrocarbon column height and composition of expected

ACCUMULATIONS IN THE PSM 2D MODEL IN THE NORTHERN PART OF THE PARNAÍBA BASIN (FIGURE 32), ADAPTED FROM MIO ET AL., (2023). 90
FIGURE 53 – IMPACT OF THE USE OF DISTINCT KINETICS SCHEME ON **TRANSFORMATION RATIO** OF SOURCE ROCK IN THE 3D PSM (MODEL 01). UPPER LINE: USING THE NEW KINETIC PARAMETERS FOR THE PIMENTEIRAS FORMATION AND THE IMPACT AT SR LEVEL A (LEFT), SR LEVEL B (MIDDLE) AND SR LEVEL C (RIGHT); LOWER LINE USING CLASSICAL WOODFORD SHALE KINETICS FROM PETROMOD LIBRARY. 91
FIGURE 54 – PERCENT OF SMECTITE TO ILLITE CONVERSION ALONG THE THREE STUDIED WELLS, PERFORMED THROUGH 1D PSM IN PETROMOD@ USING THE SIXTH ORDER KINETICS SCHEME PROPOSED BY PYTTE AND REYNOLDS (1988). THE WHOLE PIMENTEIRAS FORMATION IS INSIDE A RANGE OF MORE THAN 80% OF I/S CONVERSION RATE.....93
FIGURE 55 – 3D PSM MODEL 01 WITH THE CALCULATION OF PERCENT FOR SMECTITE TO ILLITE TRANSFORMATION (PYTTE AND REYNOLDS, (1988) AND THE REFLECTANCE OF VITRINITE (EASY %RO).....93
FIGURE 56 - EXPERIMENTAL DESIGN OF THE 3D PETROLEUM SYSTEM MODELING SIMULATIONS SHOWING THE GEOLOGICAL MODEL USED (LEFT), THE THREE-DIMENSIONAL RESULT OF THE PREDICTED VITRINITE REFLECTANCE (CENTER) AND THE DETAIL OF THE WELL 01 ORL´S A, B AND C, COUPLED WITH THERMAL CALIBRATION USING VITRINITE DATA AND ILLITE CRYSTALLITE INDEX. EXPERIMENTS A AND B EMPLOYED DIFFERENT KINETICS ASSIGNMENTS AS DESCRIBED IN THE TEXT, AND THEIR RESULTS WERE COMPARED.....97
FIGURE 57 - SIMULATION RESULTS OF GENERATION MASS OF OIL + GAS (BULK GENERATION) IN THE 3D PSM. UPPER LINE: USING THE NEW KINETIC PARAMETERS FOR THE PIMENTEIRAS FORMATION AND THE IMPACT AT ORL A (LEFT), ORL B (MIDDLE) AND ORL C (RIGHT); LOWER LINE USING WOODFORD SHALE KINETICS FROM PETROMOD LIBRARY (HANTSCHEL AND KAUERAUF, 2009).....101
FIGURE 58 - - SIMULATION RESULTS OF GENERATION MASS OF OIL IN THE 3D PSM. UPPER LINE: USING THE NEW KINETIC PARAMETERS FOR PIMENTEIRAS FORMATION AND THE IMPACT AT ORL A (LEFT), ORL B (MIDDLE) AND ORL C (RIGHT); LOWER LINE USING WOODFORD SHALE KINETICS FROM PETROMOD LIBRARY (HANTSCHEL AND KAUERAUF, 2009). 102
FIGURE 59 - SIMULATION RESULTS OF GENERATION MASS OF GAS IN THE 3D PSM. UPPER LINE: USING THE NEW KINETIC PARAMETERS FOR PIMENTEIRAS FORMATION AND THE IMPACT AT ORL A (LEFT), ORL B (MIDDLE) AND ORL C (RIGHT); LOWER LINE USING WOODFORD SHALE KINETICS FROM PETROMOD LIBRARY (HANTSCHEL AND KAUERAUF, 2009). 103
FIGURE 60 - CORRELATION BETWEEN MEASURED VITRINITE (RED POINTS), SIMULATION RESULTS OF REFLECTANCE OF VITRINITE (SMALL CONTINUOUS POINTS AND LINE) AND THE EQUIVALENT REFLECTANCE OF VITRINITE FROM KUBLER INDEX FROM ILLITE (YELLOW DIAMONDS) AND MUSCOVITE (PURPLE DIAMONDS) FRACTIONS AT WELL A. AT THE TOP RIGHT THE SUMMARY DIFFRACTOGRAM OF THE DECOMPOSED PHASES RESULTS FROM 66 SAMPLES ANALYZED107
FIGURE 61 - CORRELATION BETWEEN MEASURED VITRINITE AND SIMULATION RESULTS OF REFLECTANCE OF VITRINITE (LEFT), PERCENT OF ILLITE TO SMECTITE TRANSFORMATION (CENTER) AND PRESENT DAY AND MAXIMUM PAST TEMPERATURES FROM 1D MODELLING (RIGHT), AT WELL A. 108

FIGURE 62 – CORRELATION BETWEEN MEASURED VITRINITE (RED POINTS), SIMULATION RESULTS OF REFLECTANCE OF VITRINITE (SMALL CONTINUOUS POINTS AND LINE) AND THE EQUIVALENT REFLECTANCE OF VITRINITE FROM KUBLER INDEX FROM ILLITE (YELLOW DIAMONDS) AND MUSCOVITE (PURPLE DIAMONDS) FRACTIONS AT WELL B. AT THE TOP RIGHT THE SUMMARY DIFFRACTOGRAM (PRELIMINARY RESULTS FROM 13 SAMPLES) OF THE DECOMPOSED PHASES RESULTS FROM 66 SAMPLES ANALYZED. 109
FIGURE 63 -CORRELATION BETWEEN MEASURED VITRINITE AND SIMULATION RESULTS OF REFLECTANCE OF VITRINITE (LEFT), PERCENT OF ILLITE TO SMECTITE TRANSFORMATION (CENTER) AND PRESENT DAY AND MAXIMUM PAST TEMPERATURES FROM 1D MODELLING (RIGTH), AT THE WELL B.....110
FIGURE 64 - CORRELATION BETWEEN MEASURED VITRINITE (RED POINTS), SIMULATION RESULTS OF REFLECTANCE OF VITRINITE (SMALL CONTINUOUS POINTS AND LINE) AND THE EQUIVALENT REFLECTANCE OF VITRINITE FROM KUBLER INDEX FROM ILLITE (YELLOW DIAMONDS) AND MUSCOVITE (PURPLE DIAMONDS) FRACTIONS AT WELL C. AT THE TOP RIGHT THE SUMMARY DIFFRACTOGRAM (PRELIMINARY RESULTS FROM 14 SAMPLES) OF THE DECOMPOSED PHASES RESULTS FROM 66 SAMPLES ANALYZED. 111
FIGURE 65 - CORRELATION BETWEEN MEASURED VITRINITE AND SIMULATION RESULTS OF REFLECTANCE OF VITRINITE (LEFT), PERCENT OF ILLITE TO SMECTITE TRANSFORMATION (CENTER) AND PRESENT DAY AND MAXIMUM PAST TEMPERATURES FROM 1D MODELLING (RIGTH), AT THE WELL C.....112
FIGURE 66 – PLOT OF CRYSTALLINITY (KUBLER INDEX) VS CHEMISTRY OF ILLITE (ESQUEVIN INDEX) FROM WELLS A (TOP), B (CENTER) AND C (BOTTOM) 115
FIGURE 67 – COMPARISON BETWEEN KI VS ESQUEVIN INDEX PLOTS WITH VERTICAL PROFILES OF MATURITY AND SMECTITE-TO-ILLITE CONVERSION, AT THE WELLS A, B AND C.....116
FIGURE 68 – CORRELATION BETWEEN 37 PAIRS OF MEASURED VITRINITE REFLECTANCE AND KÜBLER INDEX (KI) MEASURED FOR ILLITE (YELLOW) AND MUSCOVITE (PURPLE) PHASES. THE RESULTS ARE COMPARED WITH THE PAIRS OF KI-RO FROM FREY AND ROBINSON (1999) E MÄHLMANN AND FREY (2012) REFERENCE POINTS AND THEIR RESPECTIVE CORRELATION USING AN EXPONENTIAL REGRESSION. 118
FIGURE 69 – PLOT OF 37 PAIRS OF MEASURED VITRINITE REFLECTANCE AND KÜBLER INDEX (KI) MEASURED FOR ILLITE (YELLOW) AND MUSCOVITE (PURPLE) PHASES INTO THE PATHWAY OF DIAGENESIS-METAMORPHISM PROPOSED BY FERREIRO MÄHLMANN ET AL. (2024) FOR REGIONAL METAMORPHISM IN THE ALPS, SHOWING THE ILLITE PHASE DATA MATCH INSIDE THE RANGE OF OROGENIC DIAGENESIS-METAMORPHISM, WHILE THE MUSCOVITE PHASE DATA DID NOT MATCH, INDICATING A DETRITAL ORIGIN.....120

TABLE 1 – APPROXIMATE TIMES AT TEMPERATURE EXCEEDING 90% OF THE PEAK VALUES FOR ARGILLACEOUS ROCKS CONTAINING I/S WITH 80% OF ILLITE. 43
TABLE 2 – SAMPLES USED IN THE X-RAY DIFFRACTION ANALYSIS WITH INDICATION OF THE DEPTHS, FORMATION, SOURCE OF SAMPLES AND LABORATORIES USED IN THE STUDY 62
TABLE 3 - EXAMPLE OF INPUT TABLE OF 1D PSM MODEL (WELL A) WITH THE WELL TOPS/HORIZONS, STRATIGRAPHIC AGES, DEPTH, AND THICKNESS. THE EVENT TYPE DISCRIMINATES AGAINST DEPOSITION, HIATUS AND INTRUSIONS. THE TOTAL INTRUSIVE THICKNESS IN THIS WELL IS 260 M. 69
TABLE 4 – MEASURED VALUES OF VITRINITE REFLECTANCE (%RO, %RO MIN AND %RO MAX) AND VISUAL ANALYSIS OF KEROGEN ON 54 SAMPLES AT THE WELLS A, B AND C. ALG. = ALGINITE; ESP. = ESPORINITE; RES. = RESINITE; CUT. = CUTINITE; LIPTDR. = LIPTODETRINITE; VITR. = VITRINITE; INERT. = INERTINITE; BIT. – BITUMEN AND CONT. = CONTAMINANTS 73
TABLE 5 - FOUR COMPONENTS COMPOSITIONAL SCHEME TABLE FOR THE SAMPLE 20189, FROM THE PIMENTEIRAS FORMATION SOURCE ROCK INTERVAL A IN WELL 01, AT 2277 M SHOWING THE ENERGY OF ACTIVATION VALUES IN KCAL/MOL VERSUS THE PERCENTUAL AMOUNT OF EACH COMPOUND. 75
TABLE 6 - FOUR COMPONENTS COMPOSITIONAL SCHEME TABLE FOR THE SAMPLE 20170, FROM THE PIMENTEIRAS FORMATION SOURCE ROCK INTERVAL C IN WELL 02, AT 2034 M SHOWING THE ENERGY OF ACTIVATION VALUES IN KCAL/MOL VERSUS THE PERCENTUAL AMOUNT OF EACH COMPOUND. 76
TABLE 7 - RESULTS OF KUBLER INDEX FOR ILLITE AND MUSCOVITE PHASE AT DECOMPOSED PEAKS MEASURED AT NATURAL CLAY FRACTION, CONVERSION FROM KI TO EQUIVALENT %RO, INTENSITY MEASURED AT 10Â AND % Â PEAKS AND ESQUEVIN INDEX FOR THE 207 SAMPLES ANALYZED AT WELLS A, B AND C. 84
TABLE 8 - DIFFERENCES IN 3D PSM SIMULATIONS RESULTS USING THE WOODFORD SHALE AND PIMENTEIRAS KINETIC SCHEMES FOR TRANSFORMATION RATIO, GENERATED MASSES OF OIL AND GAS AND OIL+GAS (BULK) FOR THE ORGANIC RICH LEVELS A, B AND C OF THE PIMENTEIRAS FORMATION, PARNAÍBA BASIN. VALUES ARE PRESENTED IN MILLION OF TONS FOR THE WHOLE AREA OF THE 3D PSM (169 SQKM) AND IN TONS PER SQUARE KILOMETER. TRANSFORMATION RATIO IS EXPRESSED AS THE AVERAGE ALONG THE WHOLE MODEL (100X100 M CELL SIZE – TOTALIZING 17100 CELLS PER INTERVAL). 100

TABLE 9 – PAIRS OF MEASURED REFLECTANCE OF VITRINITE AND KUBLER INDEX FROM ILLITE AND MUSCOVITE DECOMPOSED PHASES, AT THE WELLS A, B AND C.....117
TABLE 10 INPUT TABLE OF 1 PSM MODEL FOR WELL B WITH THE WELL TOPS/HORIZONS, STRATIGRAPHIC AGES, DEPTH, AND THICKNESS. THE EVENT TYPE DISCRIMINATES AMONG DEPOSITION, HIATUS AND INTRUSIONS. THE TOTAL INTRUSIVE THICKNESS IN THIS WELL IS 371 M. 135

Equation 1 - Thermal conductivity equation. 30
Equation 2 – Heat production rates (Qr) due to radiogenic production according to Rybach (1973), using the individual concentration (C) of Uranium (U), Thorium (Th) and Potassium (K). 32
Equation 3 – Age correction of Uranium (U) contribution for the heat production rate (Hantschel and Kauerauf, 2009) 32
Equation 4 - Age correction of Thorium (Th) contribution for the heat production rate (Hantschel and Kauerauf, 2009) 33
Equation 5 - Age correction of Potassium (K) contribution for the heat production rate (Hantschel and Kauerauf, 2009) 33
Equation 6 – Transport type differential equation of multi-dimensional heat transfer Hantschel; Kauerauf (2009) 33
Equation 7 – First Arrhenius Order Kinetic (or temperature dependence of reaction rates), relative to the pore fluid activity ratio K/Na. Pytte and Reynolds (1988). 43
Equation 8 - Fifth order kinetic parameters for equation for the Smectite to Illite transformation from Pytte and Reynolds (1988), after Pytte (1982) and Reynolds (1980), apud Pytte and Reynolds (1988). 43

List of Acronyms

FWHM = Full Width at Half of Maximum Intensity

HC(s) – Hydrocarbon(s)

I/S = Illite to Smectite Ratio

O.M. = Organic Matter

ORL(s) = Organic Rich Level(s)

PSM – Petroleum System Numerical Modelling

QEMScan® - Quantitative evaluation of minerals by scanning electron microscopy.

TOC – Total Organic Carbon

SWI – Sediment to water interface temperature (Boundary condition in basin modeling)

XRD – X-Ray Diffractometry

1. INTRODUCTION

The numerical modelling of sedimentary basins evolution and the petroleum generation, expulsion, and migration, so called petroleum system modeling (PSM), has been extensively used since early 1980´s and was classic developed for typical petroleum systems, where the source rock maturation is mainly driven by the interaction between sediment burial and basal heat flow.

The Parnaíba basin, the subject of this research, is an intra-cratonic, muti-phasic Paleozoic basin, situated in the NE of Brazil. In this basin the main petroleum system occurs into the Meso-Devonian Eo-Carboniferous sequence, where the main source rock is the Meso/Eodevonian Pimenteiras Formation and the main reservoirs are the Cabeças (Meso/Eodevonian) and Poti (Mississipian) formations. Although, the source rock maturation and trap formation mechanisms differ significantly from the typical petroleum system due to the occurrence of two important magmatic events during the basin evolution, the Central Atlantic Magmatic Event (CAMP), during Neo Triassic and the Paraná-Etendeka Magmatic Event, Eo Cretaceous in age. Both events are well described and characterized along the basin, through geological, geochemical, and geochronological data.

Magmatism, especially the CAMP event, is responsible for the triggering source rock thermal maturation due to the massive intrusion of magmatic sills into the Pimenteiras Formation and the intensive thermal stress produced by the magmatism. The formation of hydrocarbon traps in the Cabeças and Poti formations is due to the magmatic intrusion of diabase sills into these units, and the timing of hydrocarbon generation and migration and the synchronism in the trap filling is strongly controlled by the magmatism. The combination of the factors described above led to classifying this petroleum system as atypical.

The challenges in PSM within the atypical petroleum systems may include, but are not restricted to:

- Thermal calibration of the models: The main paleothermometer in PSM, the index of vitrinite reflectance (%Ro) did not capture the full range of paleo temperatures, which reached more than 400 °C in the past, the common ranges

of metamorphic rocks.

- Specific kinetic parameters for source rock transformation: kinetic models from analogous basin and/or ages will not correctly describe the thermal transformation of the kerogen and a specific kinetic scheme is mandatory.
- Timing of trap formation and hydrocarbon generation, expulsion, and trapping: high resolution geochronological data (TIMS U/Pb in zircon – Resolution > 20 k years) are required to be precisely set up the input parameters in the model and geochemical composition of the magmatic rocks must be used to determine the thermal properties of the magma.
- Thermal parameters of magmatic intrusion such as liquid temperatures, thermal conductivity, heat capacity and crystallization heat of magma.
- Uncertainties in models of tectonic evolution of intracratonic basins and the consequent heat flow model associated with this process.

Numerical modeling of atypical petroleum systems requires the integration of organic and inorganic geochemical data, geochronological data and the incorporation of additional paleothermometers as support to fine tune of the physical process, leading to more accurate results and predictions.

The mind map presented in Figure 1 shows some of the main challenges listed above, highlighting the thermal calibration process and the correct addressing of hydrocarbon maturity and generation. In the workflow, the main investigation lines performed in this research are presented.

This research aims to achieve the expected improvements in modeling process, such as the definition of specific kinetic parameters for kerogen to petroleum transformation and the enhancement of the calibration process with the use of inorganic calibration parameters as support of classical vitrinite reflectance.

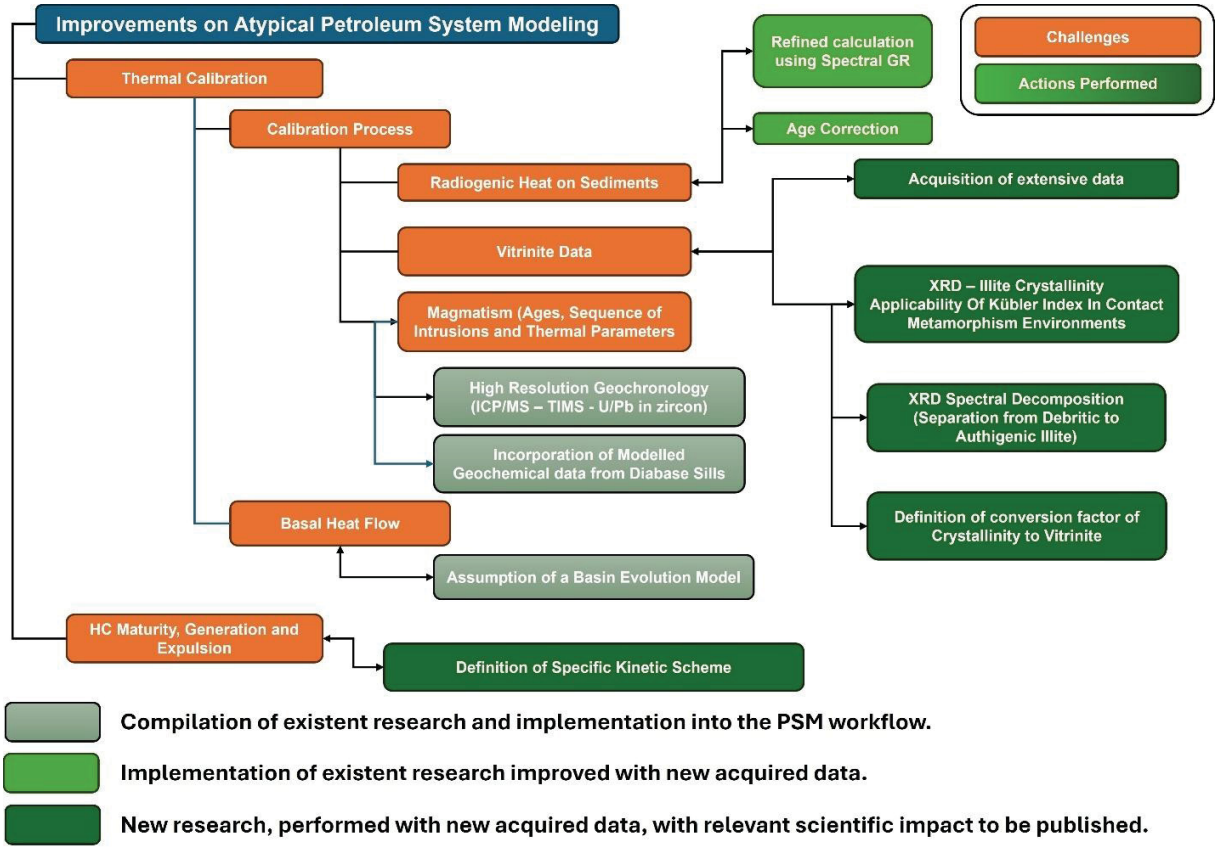

Figure 1 – Workflow of improvements in Petroleum System modeling subject of this research. In orange the main challenges to be addressed are presented and in green the research topics in the form of topics investigated during work. The dark green items, with relevant scientific impact, became the papers to be published.

1.1. OBJECTIVES, HYPOTHESES AND EXPECTED PRODUCTS

The main goal of this thesis is:

To improve the petroleum system modeling process on the atypical petroleum system of the Parnaíba Basin, reducing the number of uncertainties throughout fixing some of them with already available investigations and robust new research. This improvement will produce more accurate predictions of the petroleum systems of this basin and to enable to reproduced this method in other similar geologic contexts.

The aim is to achieve the statement described above through attaining some specific objectives, such as:

1) to establish a specific compositional kinetic scheme of organic matter transformation for the Devonian Pimenteiras Formation and to test the impacts on the petroleum system numerical modeling, compared with default kinetics (software library).

2) to understand the effects and the extent of the contact metamorphism caused by the intrusion of the massive diabase sills within of the Meso-Devonian Eo-Carboniferous sequence, in the Parnaíba Basin using a couple of inorganic and organic thermal indicators.

3) to use and to present extensive newly acquired data that supports the interpretations and the statements

The main hypotheses investigated in this research are:

- The use of generic kinetic parameters, such as those available in commercial numerical simulator packages, are not enough accurate to represent the transformation of organic matter in petroleum in the Parnaíba Basin, and the definition of a specific kinetic scheme is mandatory to accurate predictions of hydrocarbon generation.
- The thermal stress caused by magmatic intrusion led the Meso-Devonian Eo-Carboniferous sediments into the classic ranges of anchimetamorphism or even epizone zone due to temperatures stretching up to 450 °C in the past, during the CAMP magmatic event.
- This range of thermal stress will cause a transformation in clay mineral, including smectite-illite transformation, and this effect can be measured.
- The relationship between vitrinite reflectance and the crystallinity of clay minerals (Kubler Index, e.g.) may vary in environments affected by severe contact metamorphism compared to regional tectonic settings, due to kinetic factors. Therefore, classical relationships should be reviewed before applying them.

The main products available at the end of this research are:

- New compositional kinetic scheme for kerogen transformation of the Pimenteiras Formation organic-rich levels, as well as implementation and tests of this scheme in 3D petroleum system numerical modeling simulator.
- Establishment of a consistent inorganic paleo thermometer to be used in addition to vitrinite reflectance in zones with high thermal stress as well as in zones with absence or scarcity of vitrinite data (eg, Deep marine environments or formations older than the Devonian). The most likely candidate is the Illite Crystallinity Index (Kübler Index) refined by the spectral decomposition on DRX data to separate authigenic from detrital contributions.
- Discussion over the classical relationship between the Kübler Index and Vitrinite Reflectance and the proposal of a specific KI-Ro relationship for severe contact metamorphism environments.
- **Paper 01:** Compositional Kinetic Scheme for the selected organic-rich levels in the Pimenteiras Formation, Devonian of the Parnaíba Basin – Implications for Atypical Petroleum Systems Modeling.

  Status in September 2025: Submitted to Marine and Petroleum Geology in April 2025 – Peer Review
- **Paper 02:** The integration of Kubler Index and vitrinite reflectance as thermal calibration parameters in the numerical modelling of the atypical petroleum system of the Pimenteiras Formation, Devonian of the Parnaíba Basin, NE – Brazil

  Status in September 2025: Authors Revision

1.2. AVAILABLE DATASET TO THE RESEARCH PROJECT

The data available for use in this research are part of the data acquired by ENEVA in their exploratory campaign in the Parnaiba Basin, and includes seismic and well data, confidential in their origin. The company allowed the author to use and publish the dataset presented here. Some names and exact locations of the data may differ from the originals to maintain the confidentiality of the original information without impact on the research results.

The specific dataset available for this study includes, but is not restricted to:

- 03 Exploratory/Appraisal wells including:
  - ✓ Wells Stratigraphic Tops;
  - ✓ Wireline Logs (Including spectral gamma ray log);
  - ✓ 54 Analysis of TOC, Pyrolysis and Vitrinite Reflectance;
- 203 Analysis of X-Ray Diffraction (DRX) in whole rock and clay fraction (natural, glycol and heated);
- 18 Analysis of X-Ray Fluorescence (FRX);
- Compositional Kinetic Scheme Study for the Pimenteiras Formation (levels A and C), including new vitrinite reflectance data, from 2 key Wildcat/Appraisal wells in the northern part of the Parnaíba Basin.
- Two sets of 3D Petroleum System Models performed in Petromod, including results of temperature, pressure and source rock maturity in the present and along basin evolution.
- One Set of 2D Petroleum System Modeling – E-W Regional Cross-Section
- Three sets of 1D Petroleum System Models performed in Petromod in the selected wells.

2. THEORETICAL FOUNDATION

In this chapter, the main theoretical aspects of this work will be detailed, involving the geological background of the Parnaíba Basin, the area of this study, including the tectonic evolution and structural framework of the basin basement, the stratigraphic framework with the geological record and the stratigraphic interval of interest, the Meso Devonian/Eo-Carboniferous sequence.

A detailed description of the atypical petroleum system is also presented with emphasis in the Pimenteiras Formation, the main source rock interval in the basin, and the focus of the analytical program and interpretations performed here.

As support for the hypotheses testing, the petroleum system numerical modeling process is described, including topics as classical inputs, calibration process and kinetic parameters for kerogen to hydrocarbon transformation are discussed.

By the end, the X-Ray diffraction technique is presented and the methods to achieve the paleo thermal stress through the study of illite crystallinity are discussed, including the Kubler Index and the peak deconvolution techniques.

2.1. GEOLOGICAL BACKGROUND OF PARNAÍBA BASIN

2.1.1. Tectonic evolution and structural framework

The Parnaiba Basin is an intra cratonic, multi-phasic Paleozoic and Phanerozoic basin, characterized by a volcano sedimentary filling, located in the northeast portion of Brazil (Figure 2). The geology of the basin was intensely studied throughout the decades for several authors and there are some hypotheses on the mechanisms of basin formation and evolution. One of the main hypotheses is that the initial subsidence of the basin was triggered by the extensional collapse during the stabilization of the South American Platform during Brazilian-Pan African Orogeny (Almeida and Carneiro, 2004, Brito Neves et al. 1984, Cordani et al. 2003). An evolution process from a rift a basin towards an intra cratonic sag was postulated by Oliveira and Mohriak (2003) and seismic evidence of

deeper horsts and grabens, below the Paleozoic sequence were showed by Miranda et al. (2018), although this lower sequence of siliciclastic rocks, below the pre Silurian unconformity, was characterized by Porto et al. (2018) and Porto et al., 2022, as Ediacaran to Lower Cambrian in age and represents the Riachão Basin.

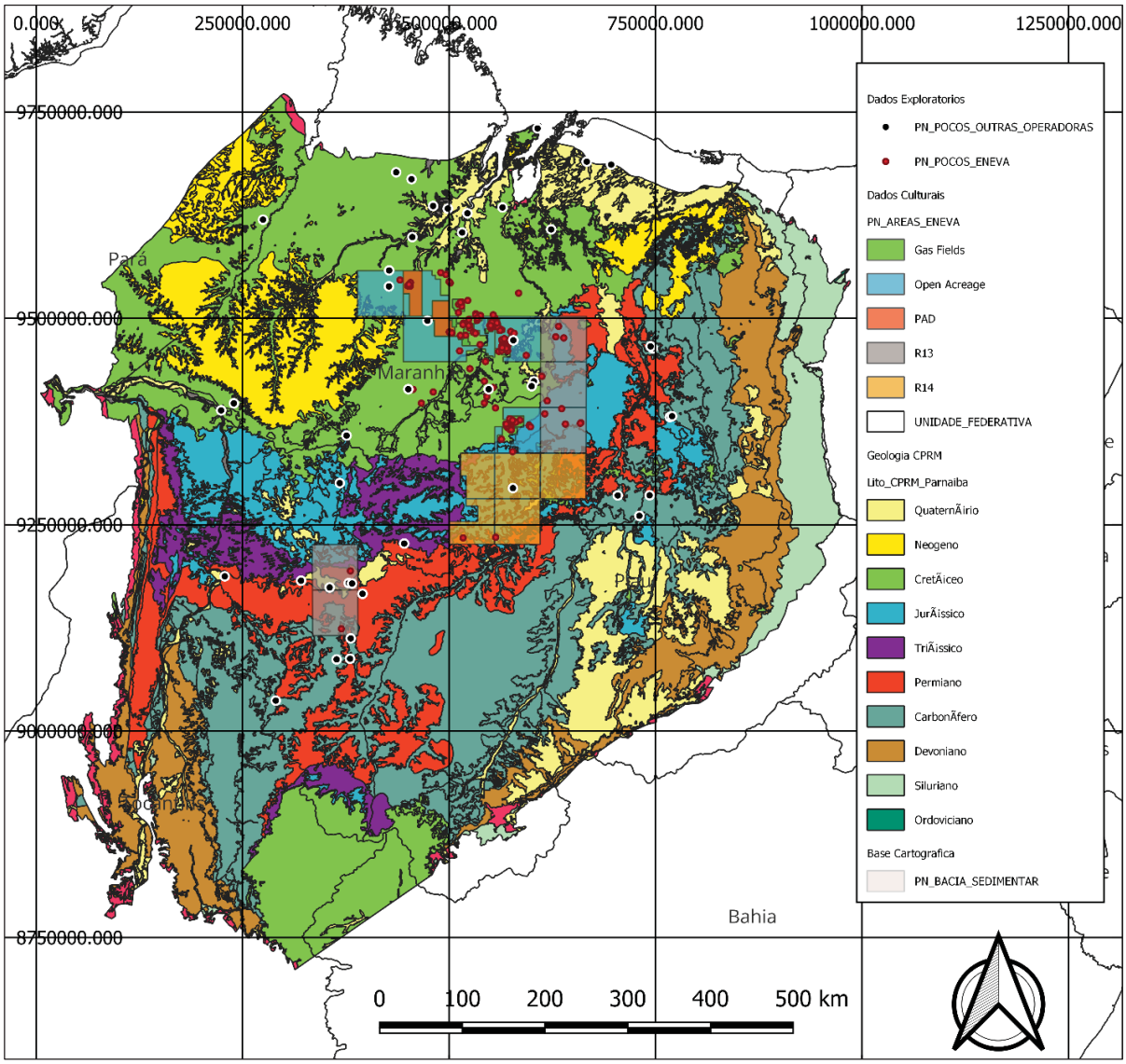

Figure 2 – Geological Map of the Parnaíba Basin, showing the occurrence of the geological units, their ages and the distribution of wells and exploratory blocks along the basin.

Several authors have recently integrated airborne gravity and magnetic data with surface geology and subsurface data, including wells, reflection seismic and deep refraction seismic to understand the structure and composition of the basement beneath

the basin as well as to understand the basin evolution mechanisms. It is possible to highlight the paper from Daly et al. (2014) describing the internal crustal structure through the analysis of deep seismic profile and pointed out that there is no seismic evidence of crustal stretching or crustal thinning. Tozer et al (2017) have studied the crustal structure and the gravity anomalies beneath the basin. Michelon (2020) characterized through seismic mapping and structural interpretation, the magmatism in subsurface, detailed the main tectonic events fingerprinted in the basin and presented a volumetric estimation of the magmatism inside of the basin. These authors also proposed some of the major crustal boundaries which are supported by airborne gravity and magnetic data. Interpretation carried out by de Castro et al., 2014. Soares et al., 2018 through the acquisition and interpretation of a wide-angle reflection-refraction profile (WARR) along the basin investigates the crustal thickness and Moho reflection without recognize an expressive lithosphere-driven process related to the basin implementation.

The most comprehensive study carried out to understanding the Parnaiba Basin formation is described in detail in Tozer et al., 2017 and Watts et al., 2018. These two papers present a detailed study of gravity anomalies, crustal modelling, flexural back-stripping, and the comparison of these with a viscous-elastic flexural modelling of deep buried loads in the basement of the Parnaíba Basin are presented. These authors propose an initial load of a dense material in the base of lower crust as the main driven mechanism of basin generation and evolution and they present the main evidences of this process as: 1) offset of sedimentary sequences over the basement; 2) the residual gravity anomalies at the center of the basin; 3) constant rates of sediment deposition (through the analysis of back stripping curves) 4) comparison of flexural model with back stripping subsidence curves and, 5) Comparison with analogous intra cratonic basins of Congo (Cuvette Centrale) and Michigan basins. This interpretation and the subsequent consequences are adopted in the present study, if the basin evolution did not experienced crustal and/or lithospheric thinning with the absence of thermal anomalies derived from these processes.

The state of art of the Parnaíba Basin basement framework knowledge is summarized in the work from Porto et al., 2022, who presented the tectonic-structural framework of the basin basement (Figure 3) using seismic interpretation and gravity

modeling constrained by crustal thickness map, well data and integration with a compilation of recent geophysical studies (de Castro et al., 2014; Porto et al., 2018; Tozer et al., 2017 and Watts et al., 2018).They present a scenario with a complex collisional tectonic setting, including two main Pre-Brazilian orogeny crustal blocks (Amazonian-West Africa and Central African Blocks) surrounded by the Brazilian Orogeny mobile belts, contradicting older ideas of an stable cratonic block beneath the basin. Another relevant contribution is the description and modeling of mid-crustal reflection as a remanent paleo suture zone, with impact on lithosphere density and one of the possible driving mechanisms for the basin formation.

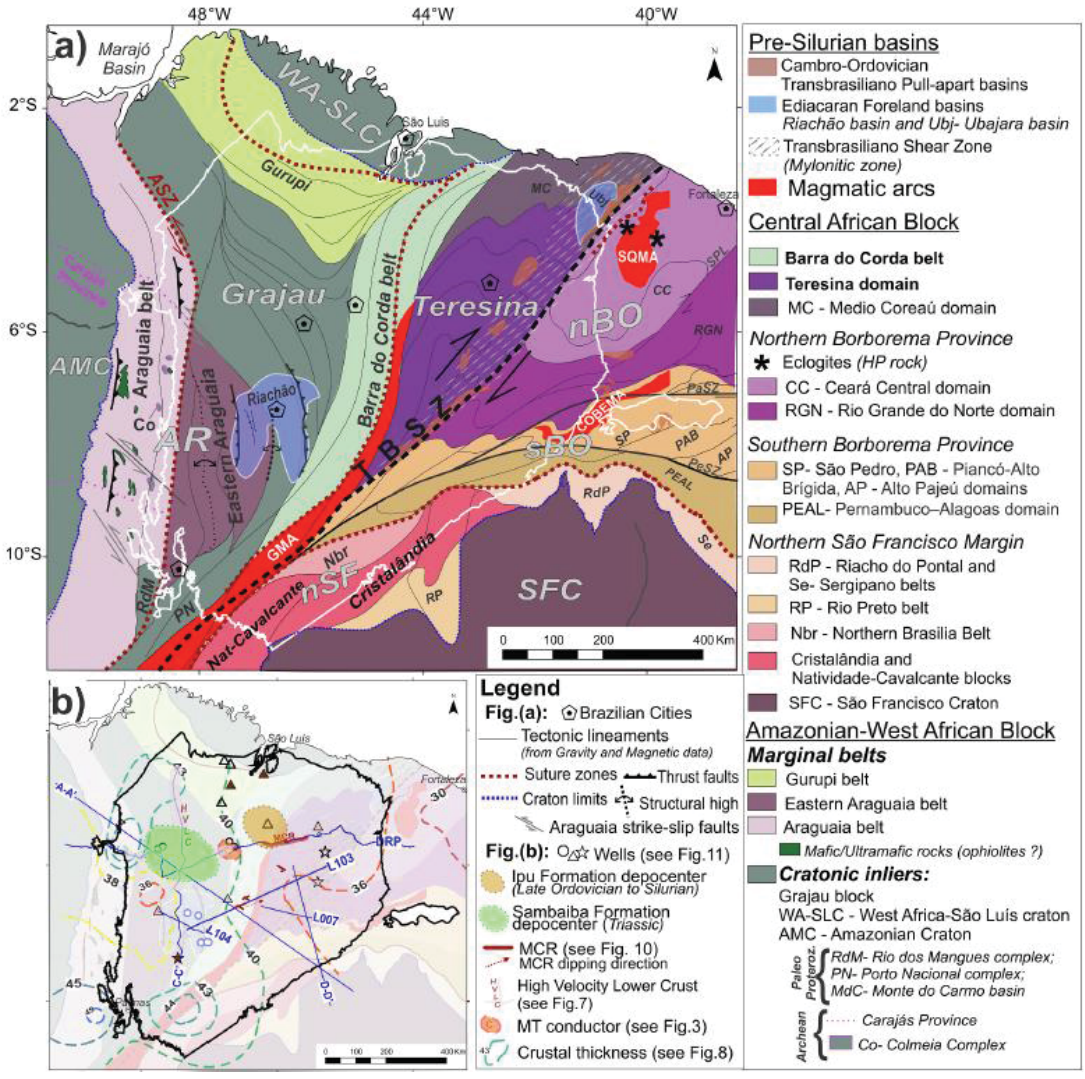

Figure 3 – Paleotectonic map of Pre-Silurian basement of Parnaíba Basin proposed by Porto et al., 2022 and used as reference in this study.

2.1.2. Stratigraphic Framework

The basin stratigraphy is based on surface and subsurface efforts driven by oil and gas exploration and was detailed by Della Fávera (1990), Góes et al. (1990); Góes and Feijó (1994), Young (2006) and Vaz et al. (2007). Those authors described four Paleozoic and two Mesozoic sedimentary sequences, and assuming the multi-phased character of the basin. Lately, Barbosa et al. (2016), Ferraz et al. (2017), and Cruz et al. (2019) detailed, respectively, the Neo-Carboniferous/Eo -Triassic, Meso Devonian/Eo - Carboniferous and Silurian sequences in the light of the sequence stratigraphy. The stratigraphic chart of the Parnaíba Basin, adopted in this study is presented in Figure 4, Vaz et al. (2007).

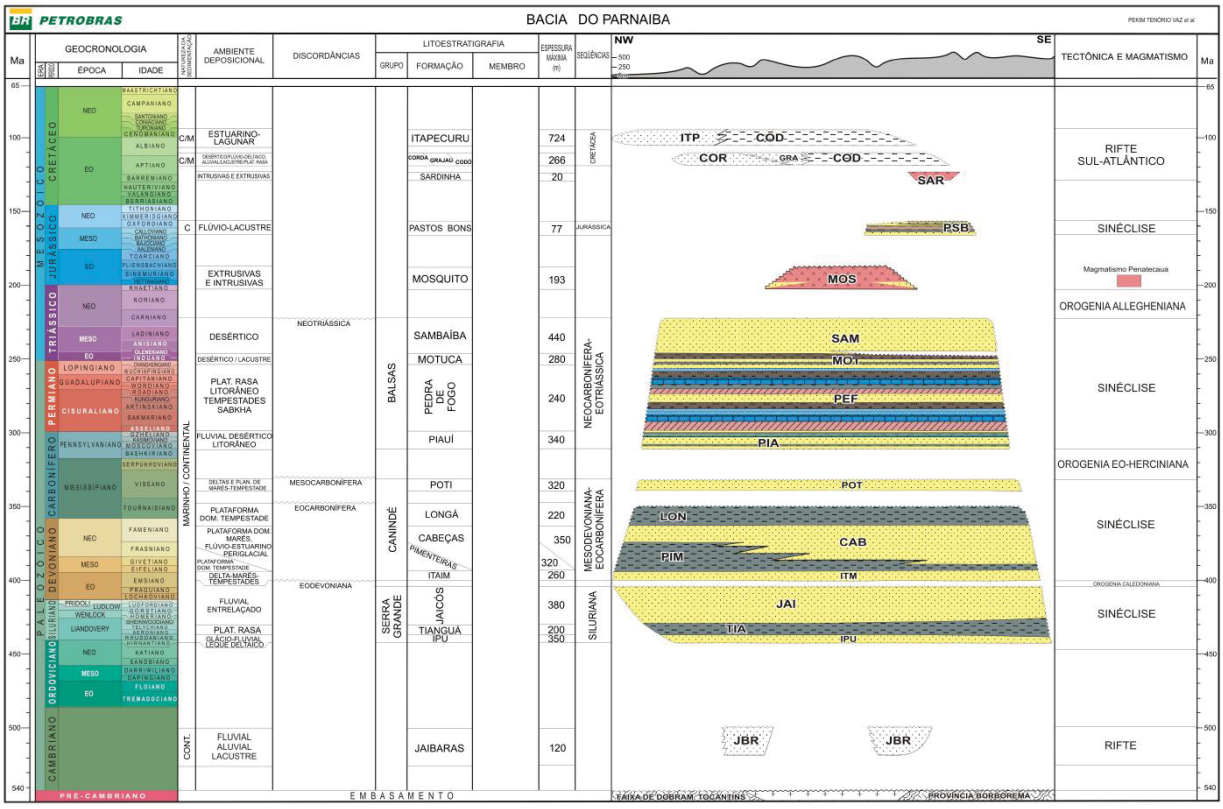

Figure 4 – Stratigraphic chart of the Parnaíba Basin by Vaz et al., 2007.

2.1.2.1. The Meso-Devonian Eo-Carboniferous Sequence

The Meso Devonian/Eo-Carboniferous sequence, represented in the stratigraphic chart (Vaz et al., 2007, Figure 4) as Canindé Group, includes from the base to the top the Itaim, Pimenteiras, Cabeças, Longá and Poti formations (Lithostratigraphic Classification) and it is the sequence that play the leading role in the hydrocarbon occurrences and includes the potential source rocks and reservoirs. The stratigraphic record may reach maximum stacked thickness of 1450 m.

The Meso Devonian/Eo-Carboniferous sequence is widely distributed along the basin and the main outcrop area is located on the eastern border of the basin. It is deposited over the silurian sequence and separated by this basal unit by the eo - Devonian unconformity. There is an internal unconformity (eo - Carboniferous Unconformity) separating the Poti formation from the basal units. The upper limit of the neo Carboniferous - eo Triassic sequence is through the meso Carboniferous Unconformity Vaz et al. (2007).

From the point of view of sequence stratigraphy, focused on the Meso Devonian/Eo-Carboniferous sequence is important to highlight the papers from Young, (2006) who studied in detail the Pimenteiras Formation and Ferraz et al., (2017) describing the whole sequence.

Young, (2006), using core data from 13 wells in the east border defined nine sequences, comprising two regressive-transgressive cycles into de Pimenteiras Formation, deposited in a shallow shelf environment with storm and deltaic influence (Figure 5).

Miranda, (2014) recognized 8 microfacies using thin section analysis and compositional analysis using DRX, FRX and QEMScan® and describe similarity with the seven facies successions detailed by Young (2006).

Ferraz et al., (2017) defined two depositional sequences (SEQ1 and SEQ2 - Figure 5). The basal sequence (SEQ1, Figure 5) begins with a low stand system tract (LST/TSNB) with progradation parasequences deposited under deltaic systems under

influence of storm, and capped at the top by the maximum regressive surface (MRS/SRM1). The transgressive system tract (TST) is characterized by shallow shelf mudstones with progradation stacking followed by the high stand system tract (HST) where mudstones and sandstones were deposited in shelf and fluvial-estuarine peri glacial deposits, limited at the top by the maximum transgression surface (MFS/STM1). The SEQ2 is an LST/TST entirely deposited in shelf environment, and at the top, there is a partially eroded record of a HST, cut by the Meso-Carboniferous unconformity.

The Pimenteiras Formation, object of this study, is represented by the transgressive system tract (TST - basal portion of the formation) and the high stand system tract (HST/TSNA - upper portion) of the SEQ1 (Ferraz et al., 2017 - Figure 5).

The TST (Figure 6 and Figure 7), as the basal portion of the formation, is characterized by two parasequences, with an aggradational to retrogradational stacking, with deposition of shelf shales intercalated with few lenses of sandstones, indicating a storm facies contribution. The gamma ray increases towards the top of the formation, reaching up to 150 API at the level of the maximum transgressive surface (MTS/STM1 - Ferraz et al., 2017).

The HST (Figure 8), is characterized by the progradational stacking of parasequences, culminating at the top with the Neodevonian unconformity, the limit between Cabeças and Longá formations Ferraz et al. (2017).

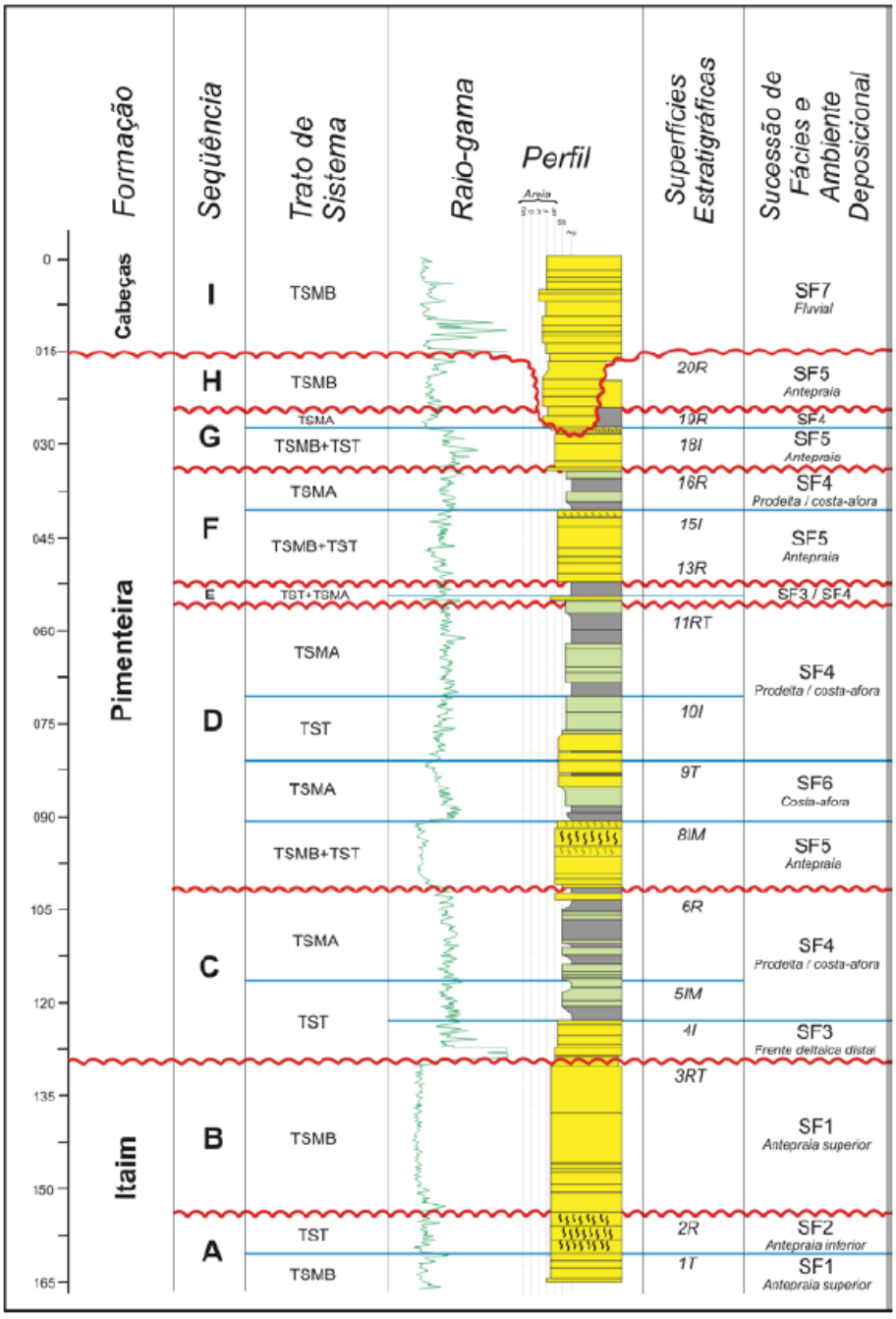

Figure 5- High resolution sequence stratigraphy, system tracs, stratigraphic surfaces and facies successions from the upper part of Itaim, Pimenteiras and lower part of Cabeças formations, according to Young, (2006).

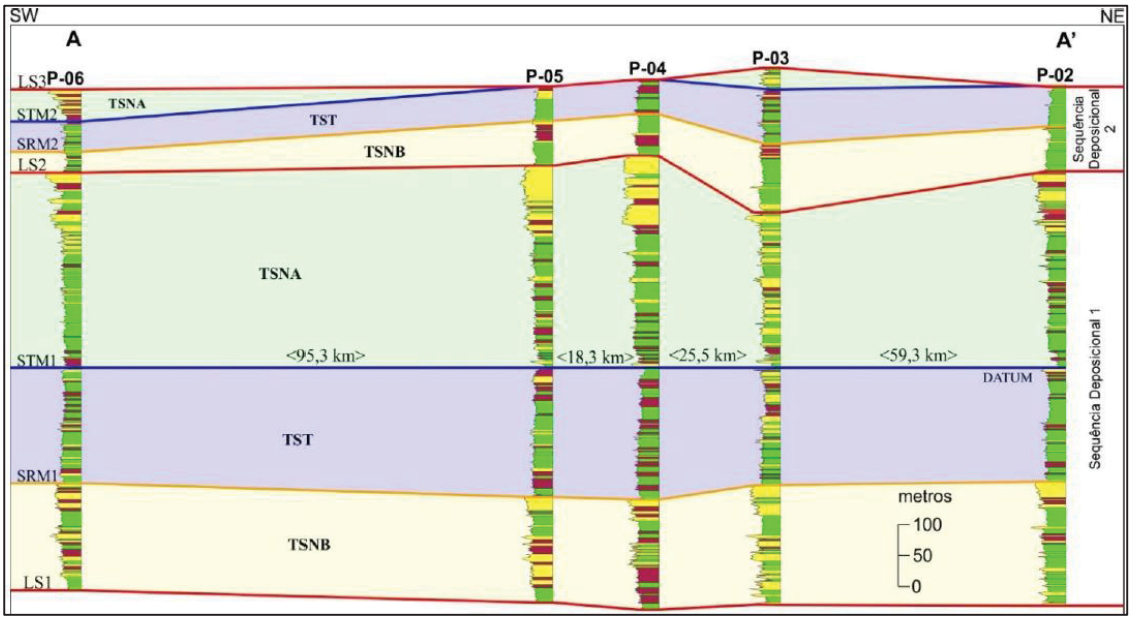

Figure 6 – Stratigraphic cross section along Parnaíba Basin showing the correlation between key wells Ferraz et al. (2017).

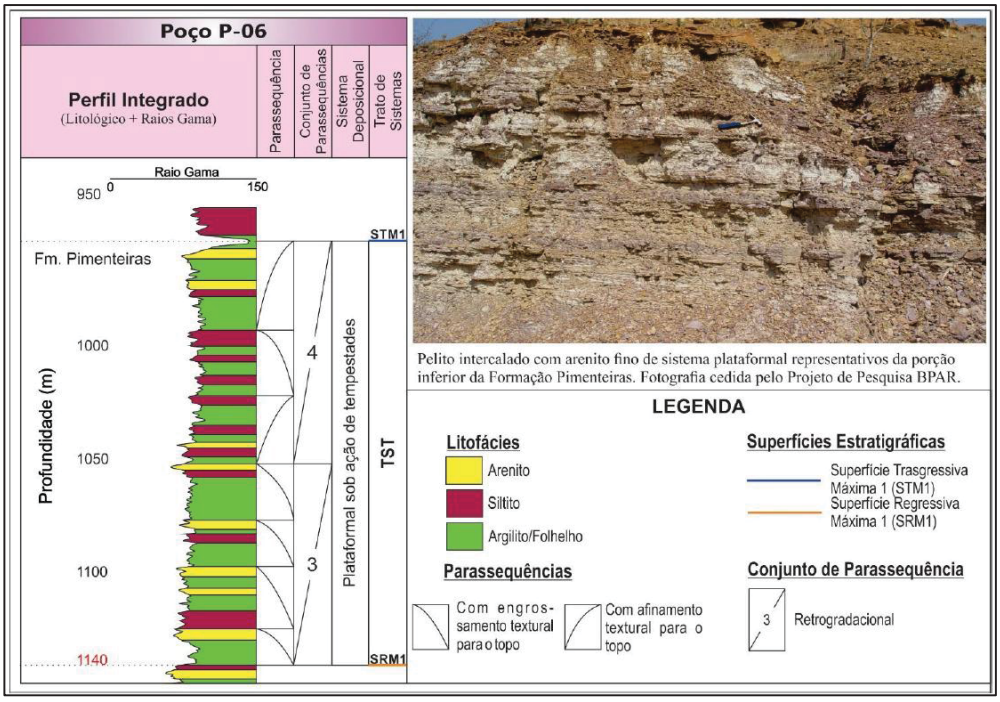

Figure 7 – Type section of Transgressive System Tract corresponding to the lower portion of Pimenteiras formation, object of this study, according to FERRAZ et al., (2017).

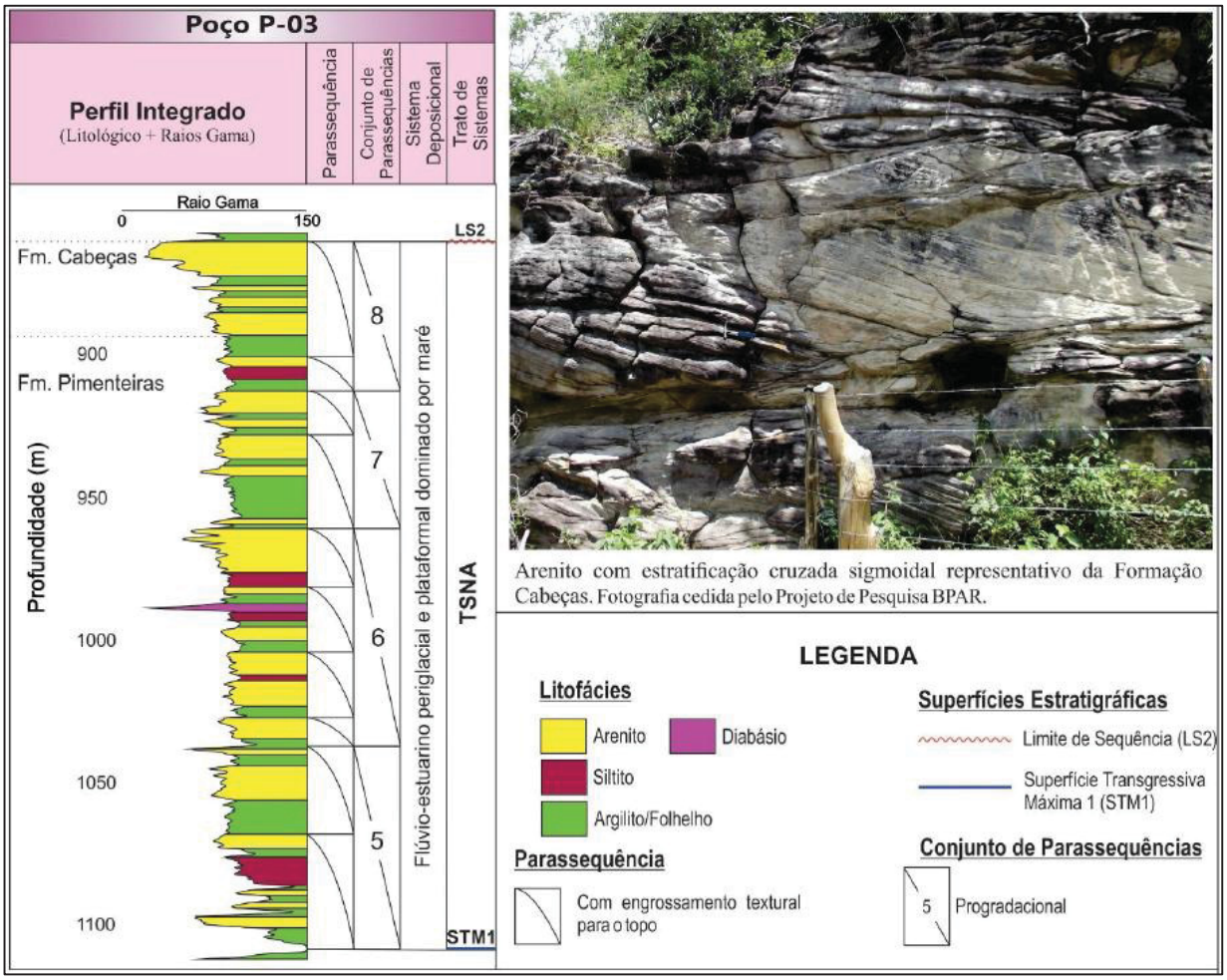

Figure 8 – Type section of the High Stand System Tract (HST/TSNA) corresponding to the upper part of the Pimenteiras formation according to Ferraz et al., (2017) .

2.1.3. The atypical petroleum system of the Parnaíba basin

The atypical petroleum system was initially described in the Parnaiba Basin by Rodrigues (1995), Eiras and Wanderley Filho, 2003 and later detailed by Miranda et al., 2018, and it is mainly characterized by the influence of igneous intrusions of Jurassic magmatism, which affects the source rock maturation (Pimenteiras Formation), in the formation of the structural traps and the sealing capacity as well as the generation of migration pathways due to instantaneous generation under high pressure.

The depletion of TOC and the effect thermal alteration of diabases on the host rocks was qualitatively described by Rodrigues (1995). Miranda (2014), using well logs, side well cores, X-Ray Diffractometry and *QEMScan*® data have quantified those effects on the organic rich black shales of the Pimenteiras formation and the effects of diabase intrusions and the results of contact metamorphism, including formation of hornfels, development of organic porosity and micro-fracturing in shales.

Miranda et al., 2018 describe in detail the elements and the processes of the atypical petroleum system into the Parnaiba basin, with a description of the main source rocks, reservoirs and sealing units and the effects of the thermal stress in hydrocarbon generation, the effects in reservoir obliteration and the mechanism of formation of a extensive four-way closure traps (Figure 9). The authors also describe at least five model of accumulations related to atypical petroleum systems (Figure 10), highlighting the effects of the magmatism on each of the petroleum system elements, source rock, trap, seal, and reservoir.

Heilbron et al., 2018 characterized through geochemical and geochronological data one magmatic event of Cambrian age, and other three magmatic pulses, associated with CAMP magmatic event (Lower Jurassic), the Parana-Etendeka (Lower Cretaceous) and South Atlantic breakup respectively. All those events are potential candidates to trigger hydrocarbon generation or remobilization.

Significant alteration of the reservoir quality was also observed by Lopes, (2019) who described the effects of thermal alteration in reservoirs of Cabeças and Poti formations. The author studied the authigenic mineralization caused by hydrothermal fluids due to magmatism and estimates through chlorite geothermometry that the rocks reached two temperature plateaus of 150 °C and 250 °C and the analysis of stable isotopes of C and O in calcite and S in pyrite indicates a magmatic source of the fluids. The process of rock and fluid interaction leads to reservoir quality depletion according to the author.

Michelon (2020) characterized magmatism in subsurface through seismic mapping and structural interpretation, detailed the main tectonic events fingerprinted in the basin and presented a volumetric estimation of the magmatism within the basin. A high-

resolution U-Pb (ICP-MS and TIMS) was performed and confirm CAMP age magmatism inside of Poti (Meso Devonian/Eo-Carboniferous sequence)and Tianguá (Silurian sequence) formations, although the extensive subsurface geochemical data was not able to distinguish CAMP and Paraná-Etendeka magmatic events.

Aragão, (2020) using well data and one dimensional PSM evaluated the effects of magmatic intrusions inside of the Pimenteiras Formation and noted the impact on the maturation, generation ad expulsion mass of hydrocarbons in different intrusion contexts. The author described the relationship between the thickness and position of the intrusion in the maturation of source rock and TOC depletion, caused by the consumption of organic matter in hydrocarbon generation during the magmatic event. Another relevant observation was the sensibility of the modeling results to the age and synchronism among multiple intrusion, adding a challenge in thermal calibration process.

Mio (2022) described low-grade metamorphism in the argillaceous materials near the source rock and suggested the possibility of use as thermal calibration data. The author also demonstrates the effects of diabase sills intrusions on the results of petroleum system modeling in 2D lines along distinct domains in the the basin (Figure *11*) and the evidence on the spectral gamma ray log data of the total organic carbon (TOC) consumption close to the diabase sill intrusion.

Mio et al. 2023 described similar effects noted by Aragão, 2020 and Mio, 2022, using three dimensional PSM in the northern part of the basin and showed the initial results of using illite crystallinity (Kubler Index - Kubler (1964)) as a calibration parameter in the modeling of atypical petroleum system in the Parnaíba Basin.

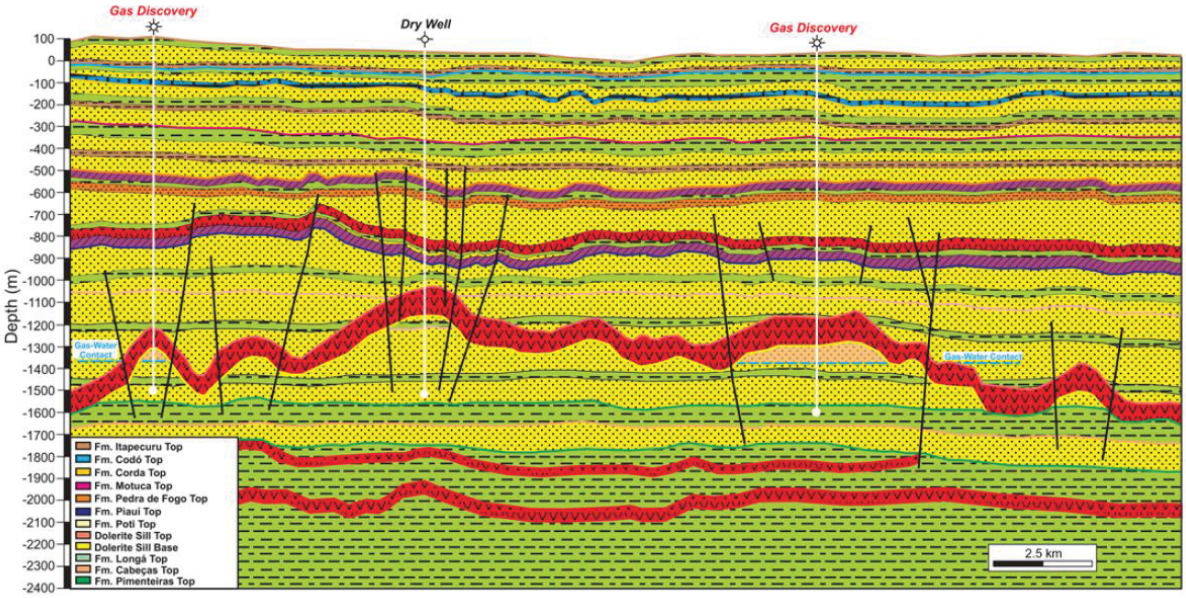

Figure 9 – Schematic cross section along Parnaíba basin showing the influence of intrusive diabase sills on the petroleum system along Parnaíba Basin. Miranda (2014).

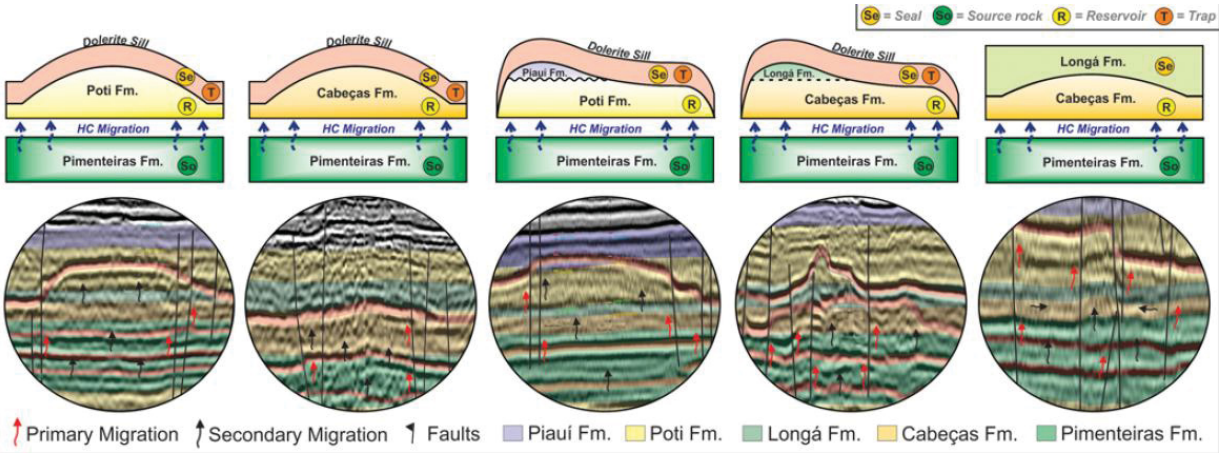

Figure 10 – Accumulation models for atypical generation and trapping of hydrocarbons in the Parnaíba Basin. Miranda (2014)

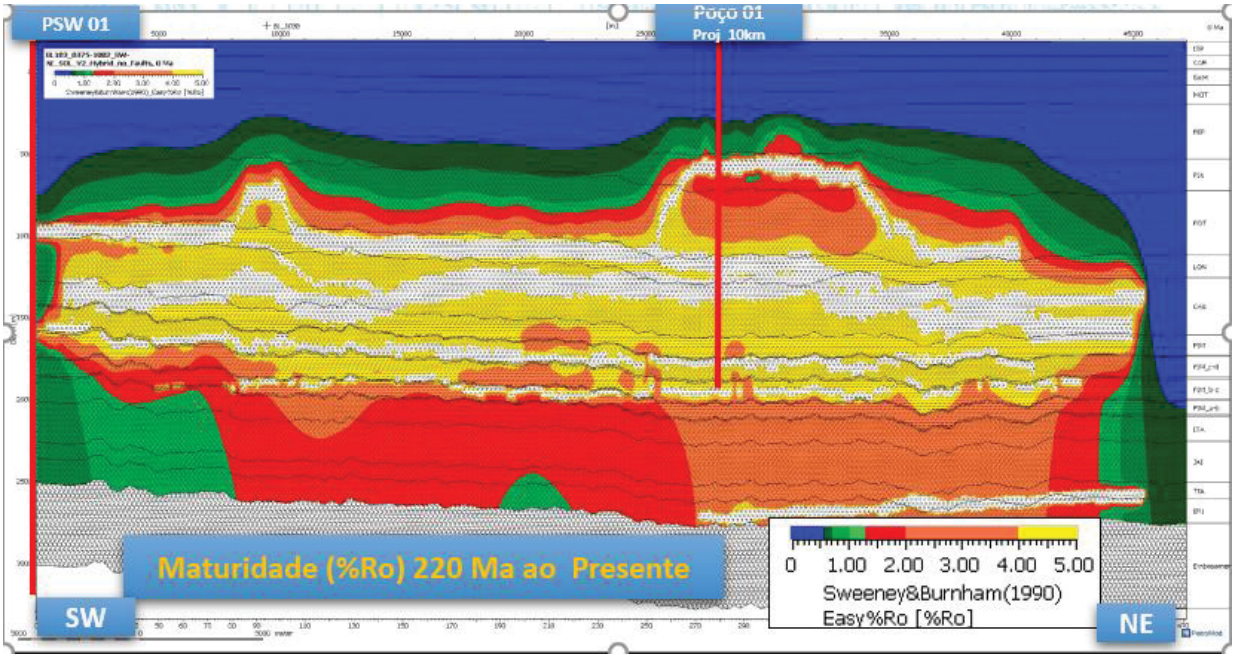

Figure 11 – 2D Petroleum System modeling line (E-W) along the Parnaíba basin showing the present-day fingerprint of the thermal stress caused by the magmatism (Mio, 2022).

2.2. PETROLEUM SYSTEMS NUMERICAL MODELING

2.2.1. Short history, principles, and process on petroleum systems numerical modeling

Petroleum Systems Modeling (PSM) is a modern statement for the “Basin Modeling” term, adopted in the early 1970´s to describe the quantitative modeling of geological processes in sedimentary basins on geological timescales Hantschel and Kauerauf (2009).

The term is not only used to describe the modeling of sediment related processes (heat and pore water flow modeling, sediment compaction and temperature-controlled chemistry of hydrocarbon generation), but also to describe crustal modeling and mantle processes as well as mass transport processes (Allen and Allen, 2005, Turcotte and Schubert, 1982).

Several textbooks described in detail the processes of basin evolution and petroleum generation, from de organic matter deposition to hydrocarbon preservation at

the trap, and the books from Tissot and Welte (1984), Turcotte and Schubert, (2002), Allen and Allen, (2005), Peters et al., (2005) and Hantschel and Kauerauf, (2009) presents the complete description of the main principles and process defined by Magoon and Beaumont (1998), who defined in their classic paper “Petroleum Systems” the processes and elements need to petroleum an accumulation occurs.

One of the most comprehensive works is the book published in 1984 by Bernard Tissot and Dietrich Welte, named “*Petroleum formation and occurrence*” where the authors in the preface of the second edition (1984) stated the importance of the numerical modeling and the need for computational support to perform the calculations and to achieve what they call the “Age of true quantification in the geosciences”:

“It is evident that computer modeling is here to stay and may very well revolutionize the field. The computer can be used as an experimental tool to test geological ideas and hypotheses whenever it is possible to provide adequate software for normally very complicated geological processes. The enormous advantages offered by computer simulation of geological processes are that no physical or physicochemical principles are violated and that for the first time the geological time factor, always measured in millions of years rather than in decades, can be handled with high-speed computers with large memories. Thus, the age of true quantification in the geosciences has arrived. We believe that this computer aided, quantitative approach will have an economic and intellectual impact on the petroleum industry, mainly on exploration” Bernard P. Tissot & Dietrich H. Welte, 1984

The authors presented at that time some of the processes they believe to be mandatory to be modelled to achieve the understanding of basin evolution: the behavior of temperature, porosity, pressure and thermal conductivity along the basin´s evolution and continuous burial (Figure 12). It is important to highlight that these two authors were the precursors of the two main schools in basin modeling, the Institute Français du Pétrole (IFP) and the University of Aachen in Germany, the first on responsible for the development of Genex™ and Temis™ basin modeling suites, and the second one for the development of Petromod™.

The development of numerical modeling can be divided into three distinct phases:

- Phase 01 - beginning in the early 1980´s, with the development of 1D temperature and pressure modules, solving simultaneously two unknows, the hydraulic head (pore pressure) and the temperature, both in function of time and distance (Yukler et al., 1979). Some assumptions were made at this time, as: a) Darcy law is valid; b) fluid and heat flow takes place only vertically (1D); c) geothermal gradient in the only source of heating and, d) heat is distributed by conduction and forced convection (fluid flow).

- Phase 02 – During the early 1990´s, based in the publication of Ungerer et al., (1990) with refinements in fluid flow of three components (water, liquid petroleum and gas) and the application of Darcy allowed the calculation all relevant processes of fluid flow accumulation and seal break through. The Figure 13 the conceptual calculation process idealized by Ungerer et al., (1990) is showed, with the improvements in multi-phasic flow and the possibilities of coupled calculations between the modules, in advance of the previous 1D possibilities.

- Phase 03 – After 1998 with the refinement of calculation and the improvements in computational capacity a new generation of basin modeling was developed and the main advances were the full 3D calculations of heat and pore pressure, as well as the three phasic Darcy fluid flow. The high computational demands to full Darcy calculations lead to the development of alternative migration engines such as flowpath, invasion percolation and hybrid models, where Darcy law is applied in low permeability facies and simple flowpath equations are applied into high permeability facies Hantschel and Kauerauf, (2009). This third phase is also characterized by the implementation of multi-component kinetics and PVT (pressure - volume - temperature) phase calculations, leading to more accurate subsurface phase predictions.

By the end of the 1990´s, the main basin modeling or petroleum system modeling packages have already solved the main problems in geological processes involving basin evolution over time (Figure 14). In the last decades, since the engines or calculators were ready, a significant number of additional processes were implemented into the basin simulators, since the time-temperature-pressure relationship can be easily calculated and handled. It includes several possibilities of kinetically controlled processes such as kerogen to hydrocarbon conversion, mineral transformation (diagenetic process, quartz overgrowth, illitization, thermal sulfur reduction e.g), modeling of contaminants (CO2, N, He) and biogenically petroleum generation. Kinetically controlled processes such as biomarkers and apatite fission track predictions have been also incorporated into the basin modeling routines.

At the time of this work, the main promising utilization to the basin simulators is the modeling and prediction on the Carbon Capture, Utilization and Storage (CCUS) workflows. Is there an important effort in technology development to take advantage of existent simulators on those flows.

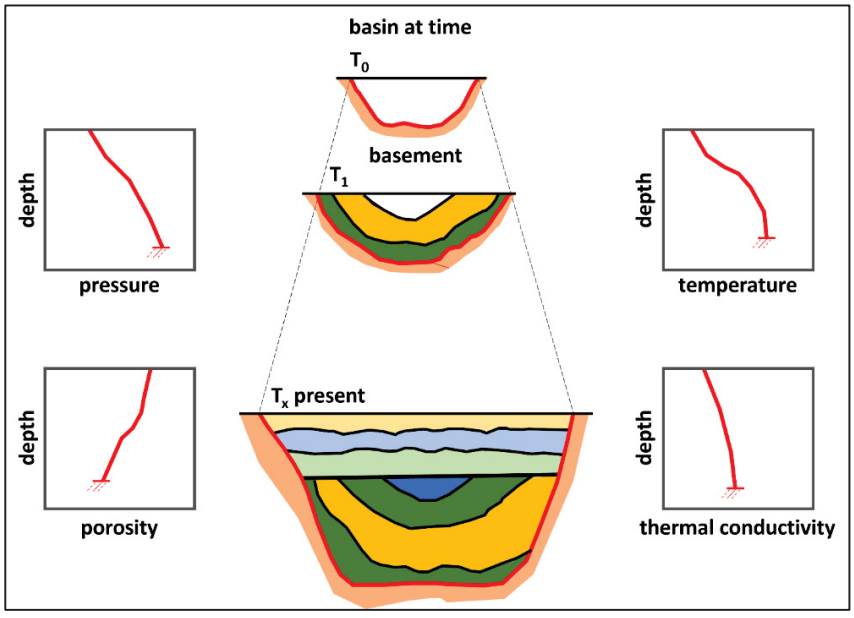

Figure 12 – Evolution of a sedimentary basin, from the initial deposition (t = t0) to the basin configuration observed today (t = tx). Parameters such as temperature, are changing continuously in each sedimentary unit according to the improvement in depth of burial *(adapted from Tissot & Welte, 1984)*.

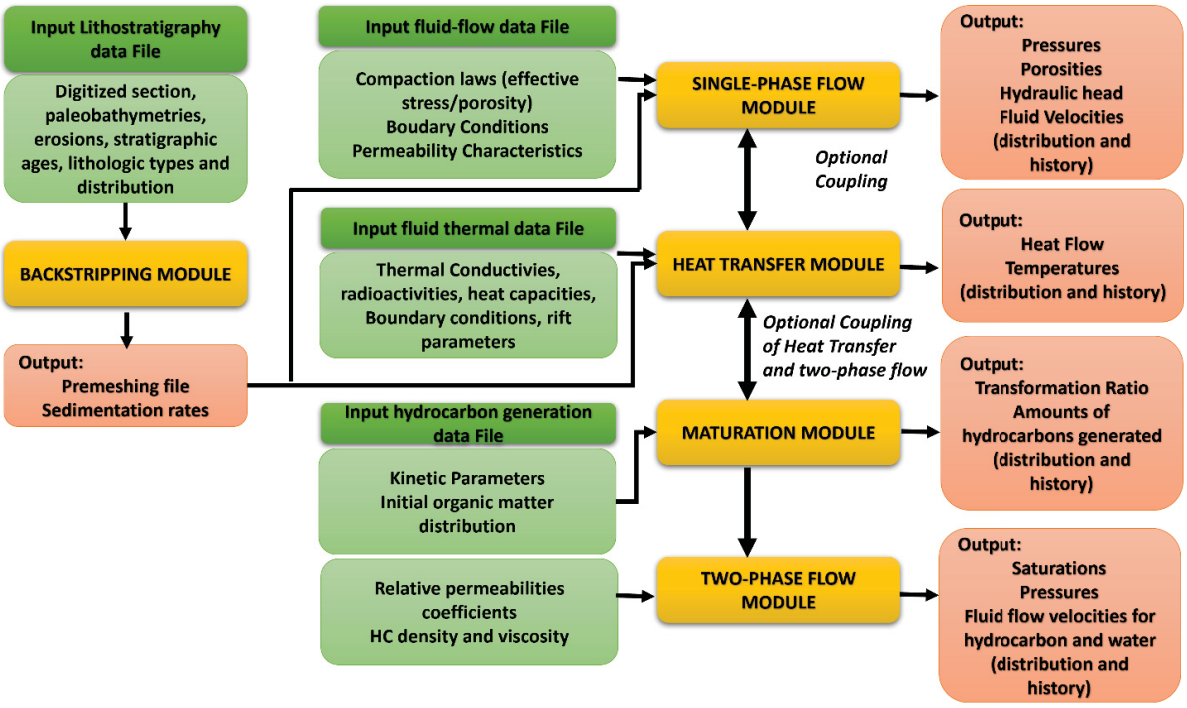

Figure 13 – Conceptual flow of two-dimensional basin modeling as proposed by Ungerer et al., (1990) with the advance on two-phases fluid flow and the possibilities of coupled thermal calculation with single-phase fluid flow and maturation calculations. In green, the input files and parameters in yellow the calculation modules and in light red the outputs of each module of calculation and the arrows indicates interactions among the steps of calculations.

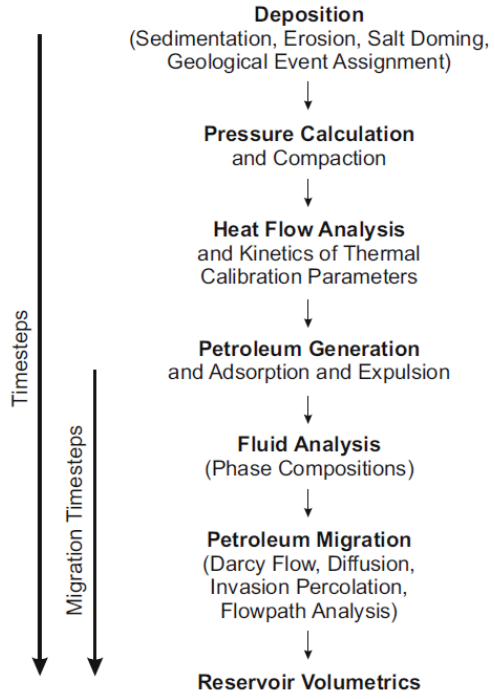

Figure 14 – Main geological processes on basin modeling Hantschel; Kauerauf (2009). The outputs of the basin models, with a scenario of temperature and pressures along the time, served as the basis for modelling of other geological and physical processes such as mineral transformation, modelling of hydrocarbon contaminants and carbon dioxide storage.

2.2.2. Structure of a model and modeling steps

The process to build a basin or petroleum system model consists of the collection of distinct geological information, including crustal and tectonic data, stratigraphic filling and depositional system, global climates, paleo geography and paleo geomorphology information (Hantschel and Kauerauf, 2009, Tissot and Welte, 1984).

The main initial structure of a model encompasses four main steps (Figure 15):

- Geometry of the model at the present day: stratigraphic tops (1D), seismic horizons (2D) or seismic maps (3D models).
- Model filling: The facies may be set for each stratigraphic unit, being single facies or a mixing of facies, a single value (1D), varying along the section (2D) or along the map (3D Models).

- Model Parameters Definition and meshing: Definition of initial meshing size and internal sub layering, definition of age of stratigraphic units, definition of the source rock and reservoirs intervals and their properties (thickness, richness and distribution), definition of past geometry parameters such as paleo bathymetry, paleo thickness, uplifts and erosions (applicable for 1D, 2D and 3D models).
- Definition of Boundary Conditions: definition of the bottom and top conditions of the model, including the basal heat flow and the sediment to water temperature interface (SWI) at the top of the model, at the present and along the model evolution. It can be set using direct values or using different approaches and assumptions to achieve these values.

The subsequent phases of the modeling process include calibration, simulation, results analysis, and post-processing.

The calibration phase is performed after initial geometrical forward simulations, normally ran using the modules of three-dimensional simulation of temperature and pressure, without generation and migration calculations activated (in 1D models the calibration process includes generation, since it is not a time-consuming problem – in 2D model the third-dimension ins given by the finite elements dimension, orthogonal to the modeled section). The calibration consists of the comparing calculated data with measured data (Figure 16 - a) of temperature, pressure, porosity and vitrinite reflectance, not restricted to these parameters.

Since the model presents a satisfactory calibration quality, the full simulations can be performed (Figure 16 - a) and the results of temperature, pressure, porosity, maturation, HC expulsion and migration, HC saturation, composition and phase (not restricted to that) become available (Figure 16 – b and c), at the present and during the time of basin evolution (Figure 17).

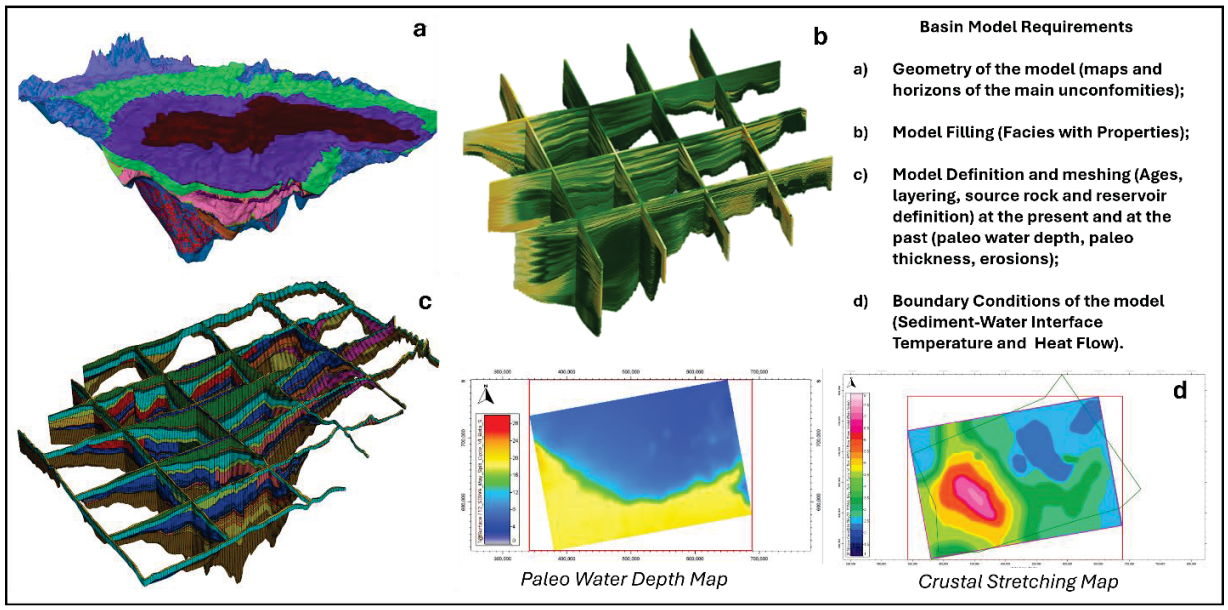

Figure 15 – Main requirements for a basin model, including: a) the initial geometries; b) model filling with facies and properties; c) model definition and meshing, with attribution of ages, reservoirs and source rocks properties, paleo geometries, paleo bathymetries and erosions, and d) boundary conditions of the maps, as the surface-to-sediment temperature interface (SWI) and heat flow at the base of the basin, that can be from direct maps or inferred from another information (paleo bathymetries, crustal stretching maps etc.). Based on Hantschel and Kauerauf (2009).

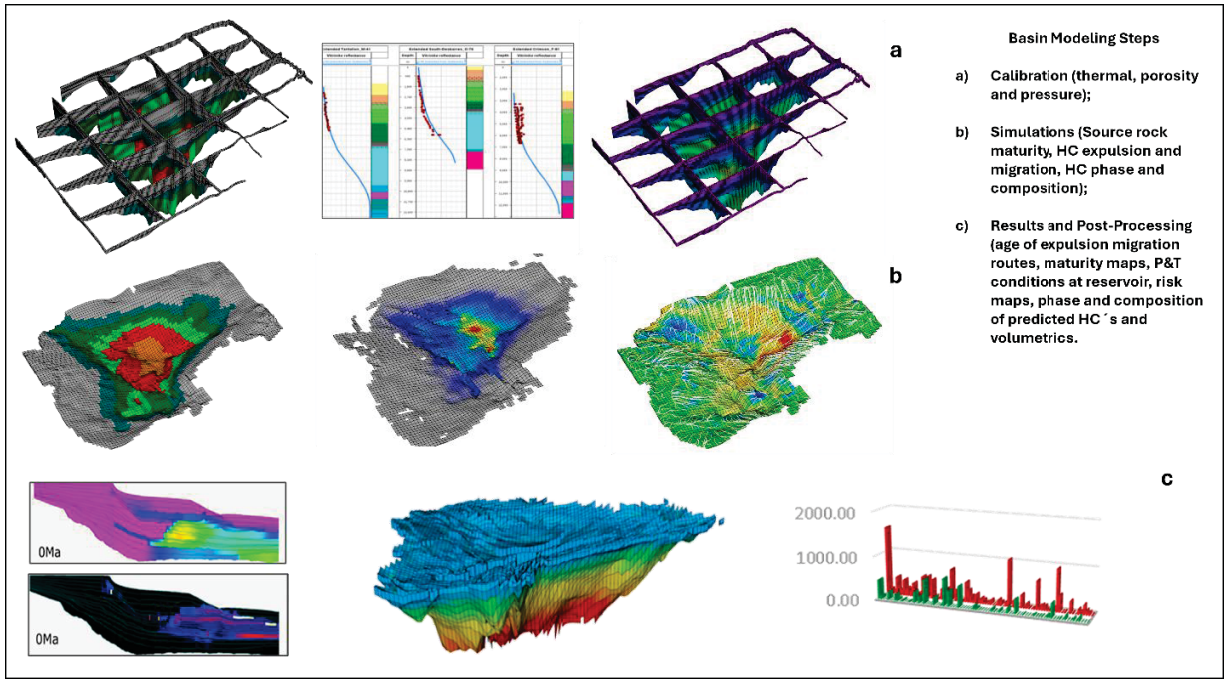

Figure 16 – Basin modeling process steps, describing the calibration process (a), the simulation step (b) and the results and post-processing process (c).

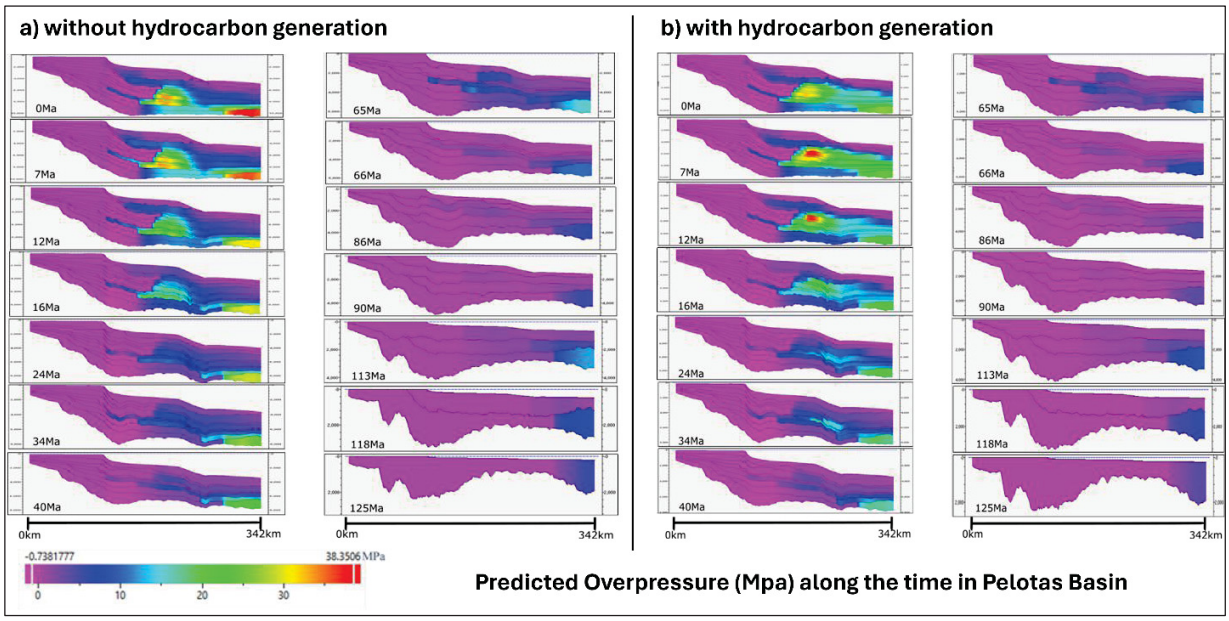

Figure 17 – Example of extraction of basin modeling results along the time. Cross section in dip direction in Pelotas Basin, Brazilian South Atlantic Margin, showing the evolution of overpressure in two different scenarios, in a) the evolution of overpressure without the contribution of hydrocarbon generation; b) the evolution of overpressure with coupled calculation of maturity and hydrocarbon generation. (Kia and Mio, (2022).

2.2.3. Transport Processes

The main physical processes involved in basin modeling, and which were described as the basis of basin models by Tissot and Welte, (1984) and Ungerer et al., (1990), the heat flow, pore pressure, compaction, Darcy flow migration process and diffusion are transport process (Hantschel and Kauerauf, 2009). They can be described, derived, and formulated in a similar way in math and the core problem is the interaction between two initial quantities, the state variable and the flow variable (Figure 18). The calculation of influence of a flow variable acting from any location on any other neighboring location is the main part of the mathematical formulation and it is given by the flow equation. For each transport process there is a material property that can be directly measured or estimated.

State variable	Flow variable	Flow equation	Material property
Temperature T	Heat flow $\mathbf{q}$	$\mathbf{q} = -\boldsymbol{\lambda} \cdot \operatorname{grad} T$	Thermal conductivity $\boldsymbol{\lambda}$
Pressure p	Water flow $\mathbf{v}_w$	$\mathbf{v}_w = -\frac{\mathbf{k}}{\nu} \cdot \operatorname{grad}(p - \rho g z)$	Permeability $\mathbf{k}$ and viscosity ν
Fluid potential u_p	Fluid flow $\mathbf{v}_p$	$\mathbf{v}_p = -\frac{\mathbf{k} k_{rp}}{\nu_p} \cdot \operatorname{grad} u_p$	Relative perm. $\mathbf{k}k_{rp}$ and viscosities ν_p
Concentration c	Diffusion flux $\mathbf{J}$	$\mathbf{J} = -D \operatorname{grad} c$	Diffusion coeff. D

Figure 18 -Fundamentals Physical Transport Laws and their variables. Hantschel and Kauerauf (2009).

2.2.4. Thermal calculations and calibrations

Considering the flow equations presented in the Figure 18 the heat flow and the temperature are the basic variables for the heat conduction, where temperature is the state variable and heat flow is the corresponding flow variable. For a given difference of temperature between points A and B, (or gradient) a heat flow is generated. The heat flow decreases the temperature difference. The heat flow is controlled by the bulk thermal conductivity (thermal conductivity of rock matrix + fluids) and the response of temperature is the function of the heat capacity of the rock or mineral (Hantschel and Kauerauf, 2009).

A mass balance (or energy) scheme can be used to formulate the boundary conditions to calculate the development of both, state and flow variables through time. The practical solution (inside of the simulator e.g.) requires the discretization of the space in cells and the construction and inversion of a large matrix. The matrix elements represent the change in state variable (change in temperature) caused by the flow (heat flow) between two neighboring cells. The number of cells is the number of unknown, and the solution of the matrix gives a solution vector (temperature inside of each cell). The number of cells impact directly on the computational requirements and the expended time in calculations in exponentially dependent of the number of cells and therefore the resolution of the model (Hantschel and Kauerauf, 2009).

The heat can be transferred in three different ways, conduction, convection, and radiation (Hantschel and Kauerauf, 2009, Turcotte and Schubert, 2002). The magnitude, orientation, and the distribution of the heat flow in the base of sediments into a sedimentary basin is determined by the crustal and mantellic process (Allen and Allen, 2005, Hantschel and Kauerauf, 2009). The sources of internal heat derived from two main mechanisms, the internal earth cooling and the radiogenetic heat production, with contributions of 17% and 83% respectively, according to Turcotte and Schubert (2002).

The heat flow analysis into sedimentary basin can be divided into two distinct problems (Figure 19), the crustal model to calculate the heat influx at the base of the basin and a second heat flow into the sediments itself, in the two cases the boundary conditions are stablished in the base and in the top of the calculation, normally expressed as temperatures, and the heat flow is function of the transfer of these temperature through the rocks and sediments with distinct thermal conductivities and heat capacities (Hantschel and Kauerauf, 2009). The Equation 1 explains the basic equation of heat flow, where q is the heat flow or heat flux, k is the thermal conductivity of the rocks or sediments and ∇T is the thermal gradient between two points of calculation.

$$q = -k.\nabla T$$

Equation 1 - Thermal conductivity equation.

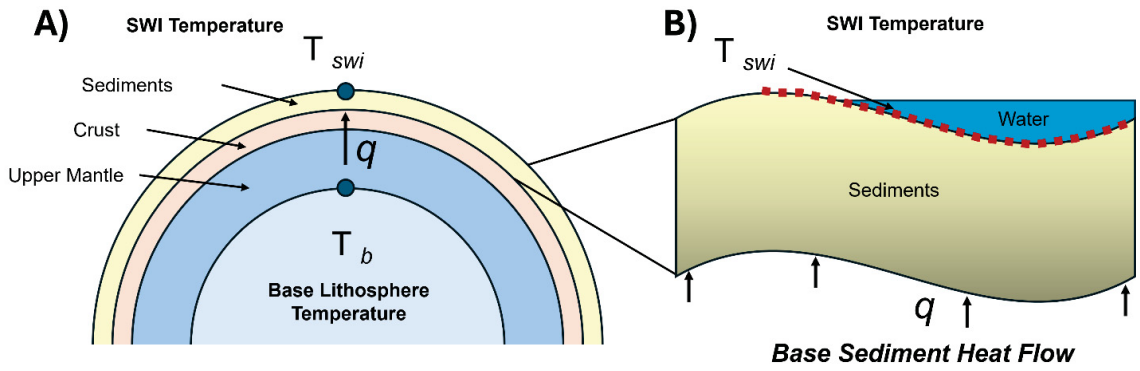

Figure 19 – Boundary value problem for a heat flow analysis (A) of the lithosphere and (B) in the sediments Hantschel and Kauerauf (2009).

2.2.4.1. Heat Transfer - Steady State and Transient Effect

The heat transfer, based on the Equation 1, is the simple calculation of one directional heat flow, without interaction between the convection, radioactive heat and changes in the geometry, thermal conductivity, and heat capacity along the time. This type of calculation is so called steady state calculations and was extensively applied in solving one-dimensional models in the recent past (Hantschel and Kauerauf, 2009).

However, the most complex geological problems involve all the variables described above, and the basin modeling process deals with the variation in thickness along the time, and some thermal properties as thermal conductivity and heat capacity that are temperature dependent. Variations of basal heat flow, the insertion of intrusions into the model and the changes in porosity and compaction lead the thermal calculation to be performed using transient effect into the calculations, which will accommodate this variation into the differential equations to perform the calculation (Hantschel and Kauerauf, 2009, Turcotte and Schubert, 2002).

2.2.4.2. Thermal Rock Properties – Thermal Conductivity and Specific Heat Capacity

The most relevant thermal properties of rocks and sediments in PSM are the thermal conductivity and the specific heat capacity.

Thermal conductivity is the ability of a material to conduct heat, and in rocks and sediments, it can be a complex mixture of different types of minerals, the pore space and the consequent amount of fluid and the nature of the fluids filling the porous space. The thermal conductivity is a temperature-dependent property, and it can vary widely. There are some well-stablished models to handle thermal conductivity variations such as Sekiguchi-Waples Model (Sekiguchi, 1984, apud Hantschel and Kauerauf, 2009) model and Linear Model (Hantschel and Kauerauf, 2009).

The heat capacity is an intrinsic property, the ratio of an infinitesimal amount of heat to be absorbed by a body with the increase of the temperature and the specific heat capacity is the same property at a given unit of mass. The specific heat capacity is therefore the storage capacity for heat energy per unit mass.

The ratio of heat capacity to thermal conductivity is a measure of the transient effect (Hantschel and Kauerauf, 2009).

Like thermal conductivity, the specific heat capacity is temperature dependent, and there are some models to describe the behavior of this property with temperature variation, as Waples Model, Pore Fluid functions and Linear dependency models.

2.2.4.3. Radiogenic Heating

The natural decay of radioactive elements such as Uranium (U), Thorium (Th) and Potassium (K) produces a strong contribution in the internal heat flow (Turcotte and Schubert, 2002). The contribution of mantle and crustal rock are function of the composition and ages of those rocks and in sediments is also function of the porosity since it is a volumetric response.

The common way to estimate the contribution in the sediments is the calculation of the radiogenic heat is to use the gamma ray or spectral gamma ray to calculate the bulk (Buecker and Rybach, 1996) and individual contribution of each of the radio isotope (Rybach, 1973) in the heat flow.

$$Qr\ (uW/m3)\ =\ 0.00001\ \rho\ (kg/m^3) * (9.52C_U\ + 2.56C_{Th} + 3.48C_K)$$

Equation 2 – Heat production rates (*Qr*) due to radiogenic production according to Rybach (1973), using the individual concentration (*C*) of Uranium (*U*), Thorium (*Th*) and Potassium (*K*).

Correction of heat production rates including the age of the rocks were proposed by Hantschel and Kauerauf, (2009), calculating the radioactive decay of each element along geological age, through the equations below, where Xp is the contribution of the element (U, Th and K) in the past and t is time:

$$U_p = U^*(1 + 2{,}77^{-4}\, t - 7.82^{-8}\, t^2 + 4.53^{-12}\, t^3)$$

Equation 3 – Age correction of Uranium (U) contribution for the heat production rate (Hantschel and Kauerauf, 2009).

$$Th_p = Th\ exp\ (0.00005_t)$$

Equation 4 - Age correction of Thorium (Th) contribution for the heat production rate (Hantschel and Kauerauf, 2009).

$$K_p = K\ exp\ (0.00005_t)$$

Equation 5 - Age correction of Potassium (K) contribution for the heat production rate (Hantschel and Kauerauf, 2009).

2.2.4.4. Three-Dimensional Heat Flow Equations

The three-dimensional heat flow calculation takes in account the internal input and output energy balance in a given unit of mass, due to the temperature variations plus the radiogenic heat contribution and the convection. It is performed using transform type differential equations, with temperature as the field variable and the heat flow as the transport variable, in the form of Equation 1, where ∇, ρ and c are bulk thermal conductivity, bulk density and bulk heat capacity tensors, $\rho_c\ c_p$ and v_p are the pore fluid vectors of density heat capacity and velocity, and Qr is the bulk radiogenic heat production.

$$\rho c \frac{dT}{dt} - \nabla.\lambda.\nabla \mathrm{T} = \rho_c c_p \nabla.\left(v_p T\right) + Q_r$$

Equation 6 – Transport type differential equation of multi-dimensional heat transfer Hantschel; Kauerauf (2009).

Since the modern simulators are based on one finite elements method, even in a 1D model there is a third dimensional calculation and the multi-dimensional heat transfer calculation including transient effect can be performed.

2.2.4.5. Magmatic Intrusions

An important process in the thermal calculations in the sedimentary basin history is the contribution of the heating due to the magmatic intrusions. Instead of fact of short duration of the heating source, the instantaneous temperatures can reach values extremely higher, triggering processes as thermal maturity of source rocks (Eiras and Wanderley Filho, 2003; Miranda et al., 2018), impact in vitrinite maturity, (Hantschel and Kauerauf, 2009, Tissot and Welte, 1984) as well as inorganic transformation in clay minerals (Lopes, 2019, Mio et al., 2023, Pytte, 1982, Pytte and Reynolds, 1988).

The modeling of igneous intrusions in PSM is performed by assuming an inner boundary of temperature in the center of the intrusive body at the time of the intrusion, and some magma properties such as intrusion and solidus temperature, crystallization heat and magma density (Delaney, 1988 apud Hantschel and Kauerauf, 2009).

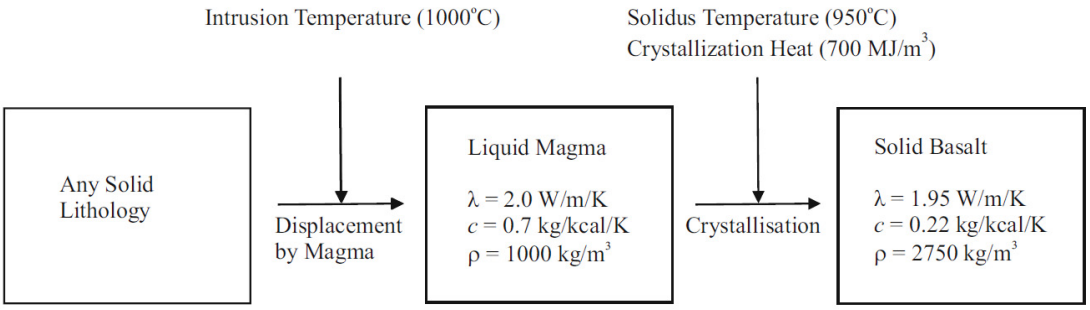

Figure 20 – Intrusion model and the default values presented by Delaney (1988) in a Fortran 77 routine for calculation. Apud (Hantschel and Kauerauf, 2009)

2.2.4.6. Organic and inorganic calibration tools in PSM

In this chapter, the most common organic calibration tool, the reflectance of vitrinite as well as the alternative illite to smectite calibration model are presented

2.2.4.6.1. Kerogen, Kerogen Types and Vitrinite Reflectance

The most important and common organic paleo thermometer, extensively used in the oil and gas industry as the main tool in recognizing the thermal fingerprint in potential source rocks is the vitrinite, and this maceral is part of the material called kerogen (Hantschel and Kauerauf, 2009).

Kerogen can be defined as the fraction of organic matter (Total Organic Carbon – TOC) in sediments or sedimentary rocks that is insoluble in organic solvents, whereas bitumen is the part that can be dissolved in those organic solvents (Figure 21). The kerogens can be divided into three main types according to the they path evolution in the H/C and O/C Van Krevelen diagram, (Figure 22) Tissot and Welte (1984):

- Type I – With typically high H/C originally ratio, mainly constituted by aliphatic chains with few aromatic nuclei, they present high potential of oil and gas generation. The main source is algal lipids by microbial activity.
- Type II – With more aromatic and naphthenic rings and intermediate to high H/C ratio (less than Type I kerogens) and good potential for oil and gas generation. Usually related to marine deposition in reduction environments, locally can present important sulfur contends.
- Type III – Contain mostly condensed polyaromatics and oxygenated functional groups with minor aliphatic chains. The O/C ratio is higher than types I and II while the H/C decreases substantially. The potential for oil is low although it can generate considerable amounts of gas in the higher degree of thermal evolution. The organic matter is mostly derived from terrestrial higher plants.

Residual kerogen can also be present in sediments, and it is constituted by reworked, oxidized or inertinitic materials with no hydrocarbon potential, characterized as dead carbon in TOC analysis.

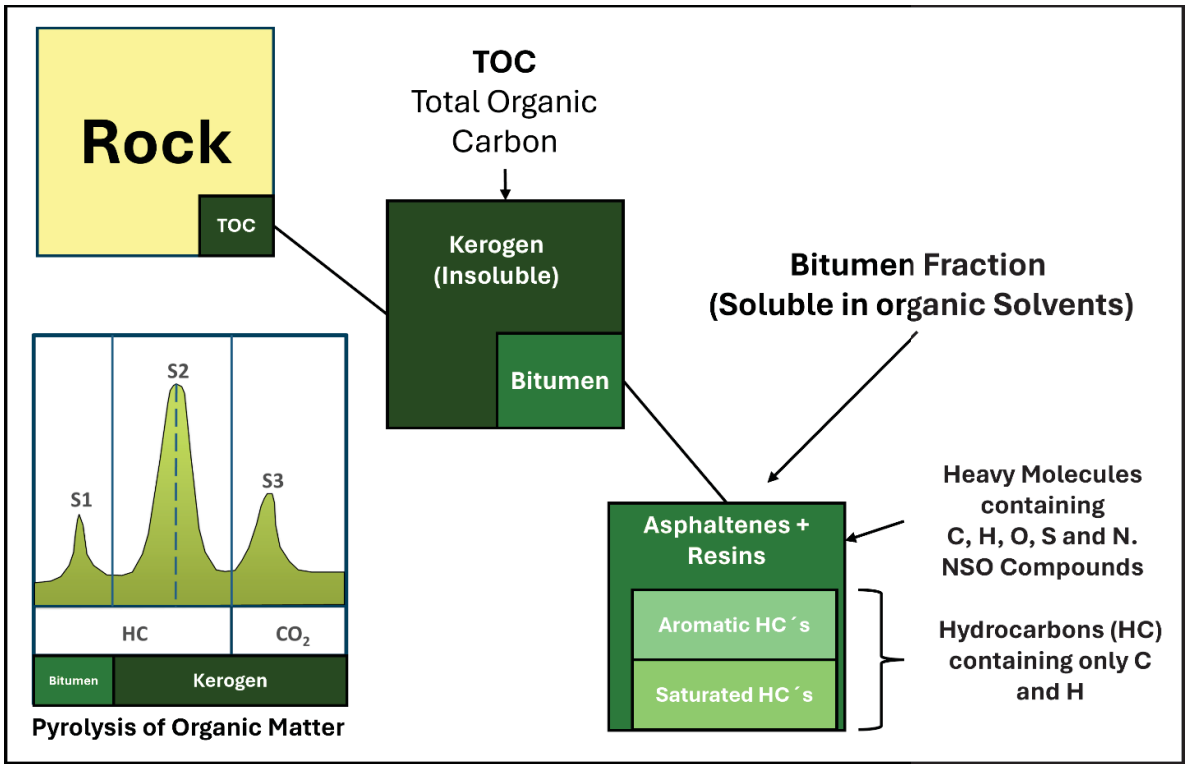

Figure 21 – Composition of disseminated organic matter in sedimentary rocks. Adapted from Tissot and Welte (1984). From the initial TOC, part of carbon is the kerogen, which is insoluble in organic solvents and part is the bitumen (HC´s already generated), composed of aromatics and saturated HC´s and NSO.

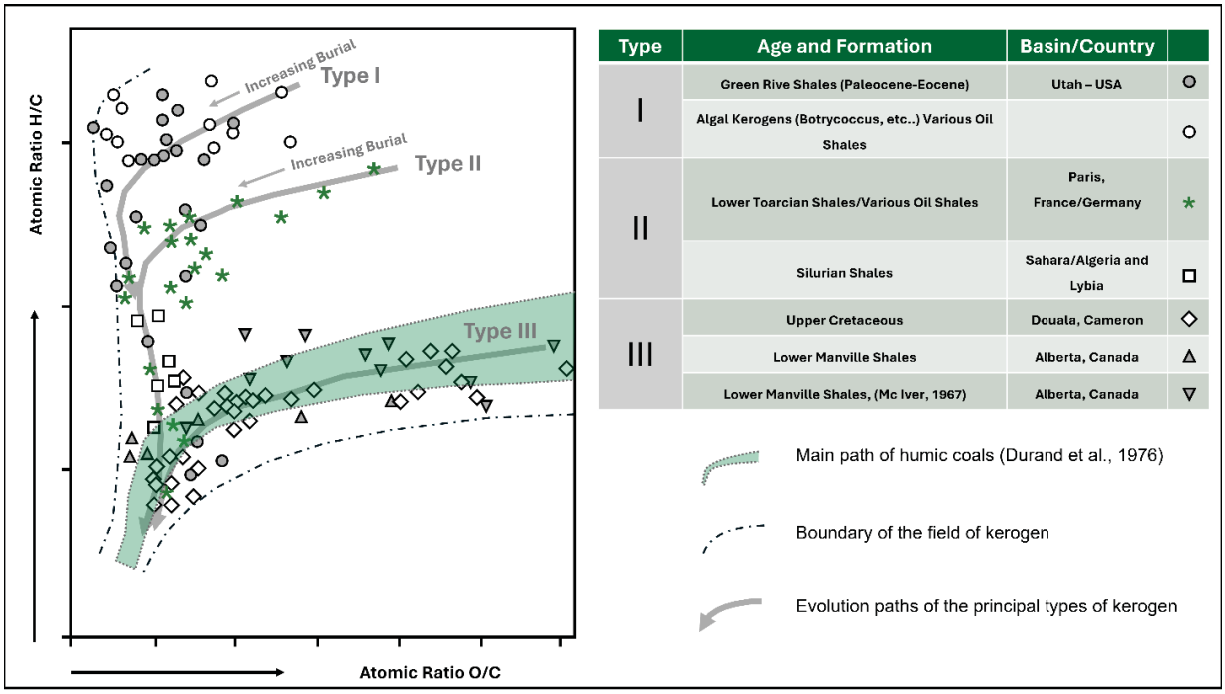

Type	Age and Formation	Basin/Country	
I	Green Rive Shales (Paleocene-Eocene)	Utah – USA	○
	Algal Kerogens (Botrycoccus, etc..) Various Oil Shales		○
II	Lower Toarcian Shales/Various Oil Shales	Paris, France/Germany	*
	Silurian Shales	Sahara/Algeria and Lybia	□
III	Upper Cretaceous	Dcuala, Cameron	◇
	Lower Manville Shales	Alberta, Canada	△
	Lower Manville Shales, (Mc Iver, 1967)	Alberta, Canada	▽

Figure 22 - Van Krevelen Diagram showing the evolution path of the main kerogen types, according to the ratios of H/C vs O/C (Tissot and Welte, 1984).

Vitrinite is part of coal material, which is originally sourced in the sedimentary basins from terrestrial input of higher plants. It is considered the best parameters to define coalification stages (Tissot and Welte, 1984) and widely used thermal maturation indicator in maceral in coal, coaly particles, or dispersed organic matter (Hantschel and Kauerauf, 2009). In the Figure 23, is shown an schematic division of organic matter in sediments, where vitrinite is part of kerogen, the portion which is insoluble in organic solvents and since it has meant a terrestrial input it is expected to be found in different depositional environments where source rocks are being deposited.

The measurement of reflectance of vitrinite particles (formally known as percent of Ro) is performed at microscope, in a polished thin section, and the relationship between the reflectance values with the increase of thermal maturity was widely investigated (Tissot and Welte, 1984) and some ranges of thermal maturity, so called maturity windows, where proposed, from peat stage (%Ro = 0,25) until anthracite (%Ro = 4,5). Some kinetic models were proposed to describe the thermal transformation of vitrinite and the most widely used are Waples (1980), Larter (1988) and Sweeney and Burnham., (1990).

The Sweeney & Burnham (1990) is the kinetic model most used and implemented in all modern simulators. This model described four main reactions that occurs during thermal evolution of vitrinite, the elimination of water, carbon dioxide, methane and higher hydrocarbons, and a simplified model (Easy Ro) is the kinetic parameters incorporating all these processes. Figure 24 shows the Easy Ro kinetic parameters and the comparison with a similar model proposed by Larter (1988).

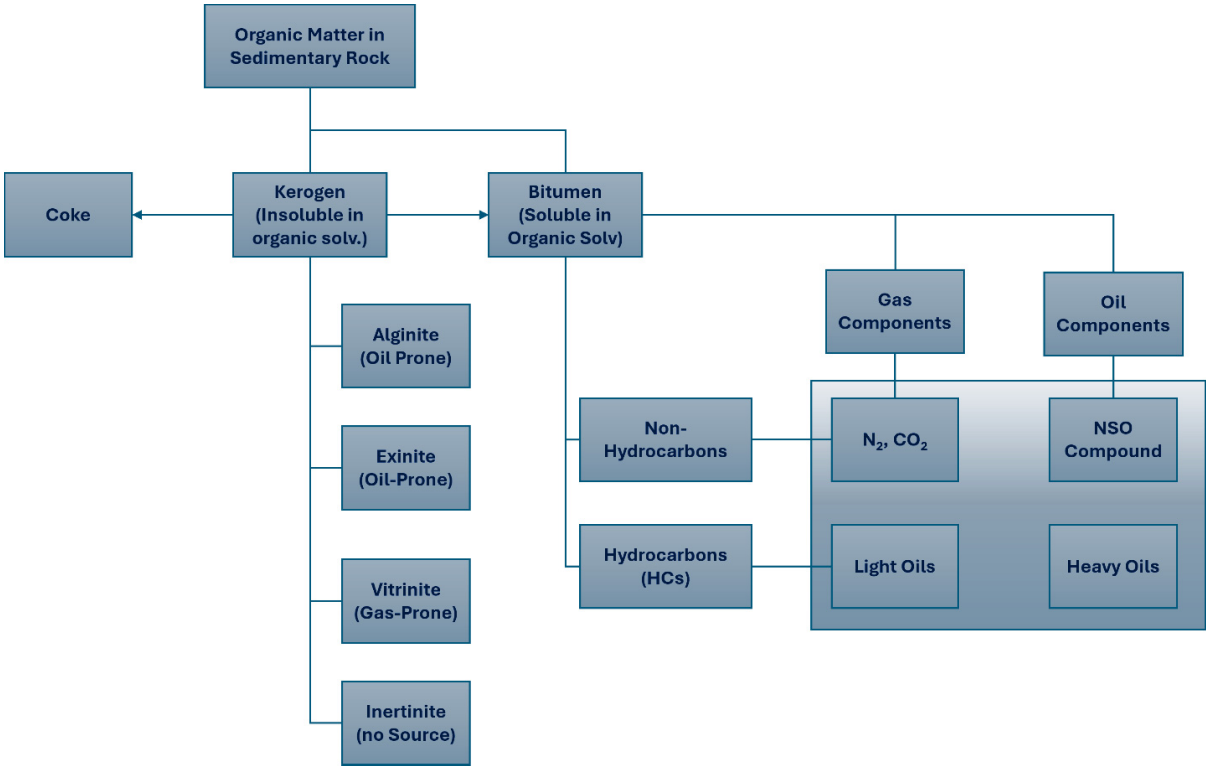

Figure 23 – Geochemical fractionation of organic matter*(Hantschel and Kauerauf, 2009)*.

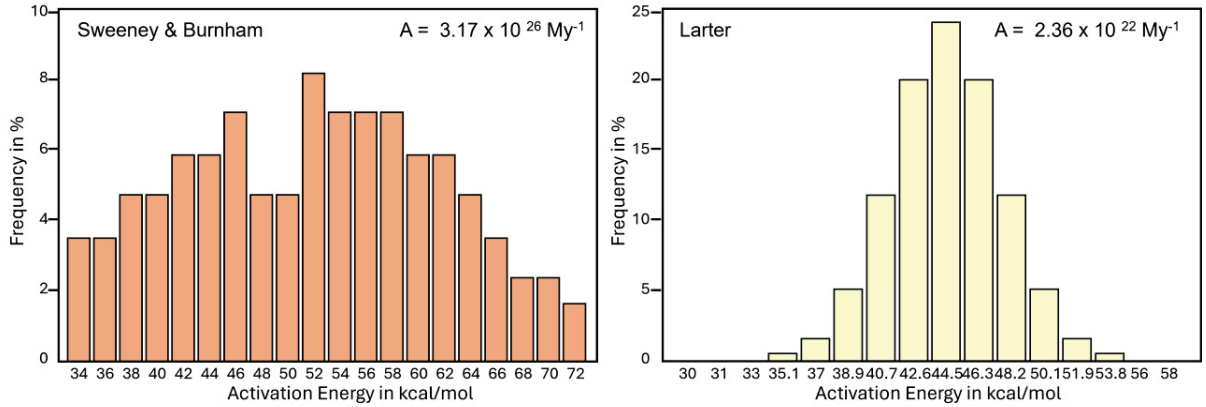

Figure 24 – Kinetic parameters for the transformation of vitrinite as described by Sweeney and Burnham (1990), right, and Larter (1988), left.

The kinetic of vitrinite reflectance during the thermal transformation can be used to estimate the degree of thermal transformation of the kerogen, and can give a good indication of the thermal status of a given source rock, although, since the kerogen is a complex mixture of organic matter particles, including alginite, exinite, vitrinite e.g. and the transformation of each of these compounds in petroleum depends on specific kinetic reaction, the use of a vitrinite scale of measurement might present important differences between the thermal status and the expected products of the reactions. The Figure 25 shows an example of these variations, in the A, the limits of maturity windows proposed in the Easy Ro model (Hantschel and Kauerauf, 2009; Sweeney and Burnham 1990) and in B the limits presented by Tissot and Welte, (1984). There are some agreements on the immature zone and in the wet gas/dry gas zones, although into the oil zone there are different proposals since it depends on the type of organic matter, as demonstrated by Tissot and Welte (1984), analyzing different types of kerogens with distinct limits between maturity windows.

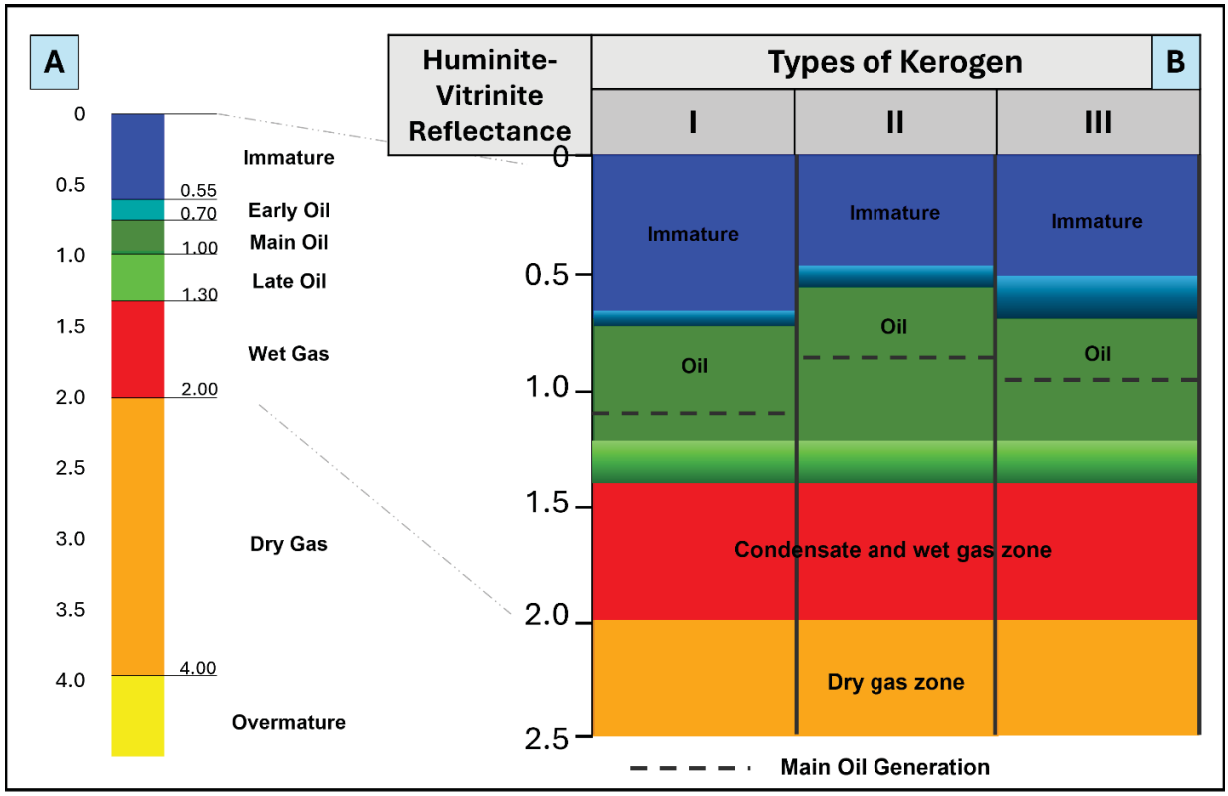

Figure 25 – Some of proposed limits for the “maturity windows” of source rocks based on the values of reflectance of vitrinite (%Ro), in A, the limits proposed in the Easy Ro model from *Sweeney & Burnham., (1990)*, detailing the oil windows, and in B, the limits presented by Tissot; Welte (1984), with some variations, especially in oil zones, with the variation of the kerogen type.

The use of vitrinite reflectance as calibration tool in petroleum system modeling consists in the comparison of the measured vitrinite data points with the curve calculated by the simulator using some of the kinetical model described above. This comparison allows the review of thermal models in the present and during the basin evolution to achieve the best fit between the observed and modelled data. In the Figure 26 an example of fitting of measured data from bottom hole temperature (BHT) and modelled temperatures as well as the fitting of vitrinite data from a set of wells with the model using Easy Ro vitrinite calculation (Canelas, 2020).

Although, when the source rock is submitted to high thermal stress due to the intrusion of magmatic bodies, in atypical petroleum systems as in the Parnaíba Basin (Lopes, 2019, Mio et al. 2023, Miranda et al. 2018), the values of reflectance can exceed the maximum calculated in the models and reach the overmature status (4% Ro), putting additional challenge in the use for calibration. In the Figure 27 - A, using around 5500 data

of pyrolysis, from 60 wells, converted to vitrinite reflectance using the Jarvie et al., (2001) method, is possible to recognize a linear trend of maturity increasing with the depth, relative to the burial of the basin. These data, with S2 values greater than 2 mgHC/gRock, showing an increasing straight trend in subsurface, reaching at 3500 m of burial (basin depocenter depth) values around 0.6 %Ro.

In Figure 27 - B, using 214 data of measured vitrinite, from 26 wells it is possible to see the impact of thermal stress on vitrinite, and the challenge in defining any burial trend based on this data.

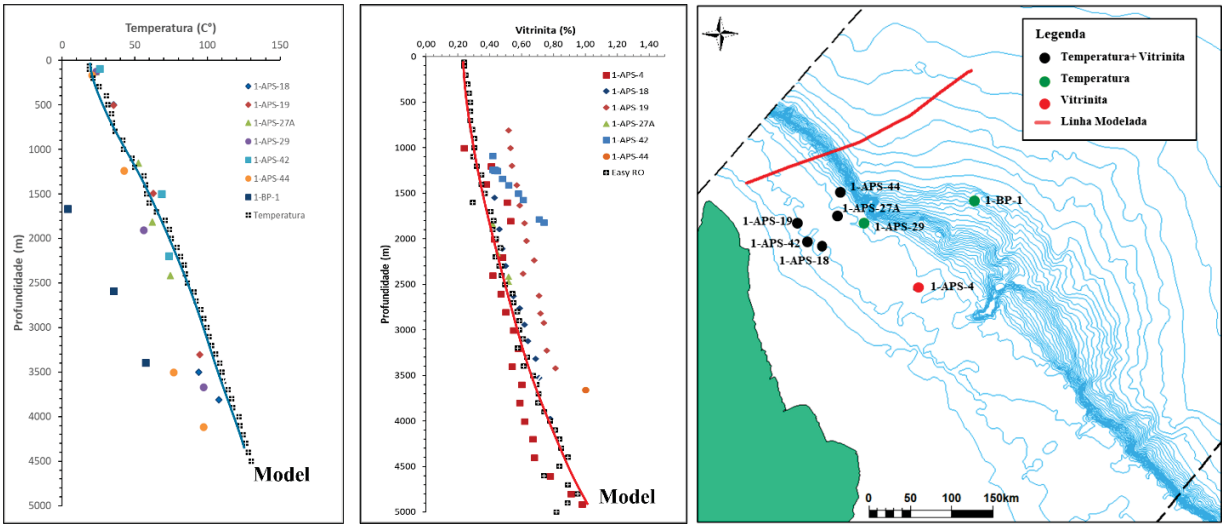

Figure 26 – Example of thermal calibration use bottom hole temperature (BHT) and vitrinite reflectance data do fit the petroleum system model in ultradeep settings in Foz do Amazonas basin, Brazil Canelas (2020).

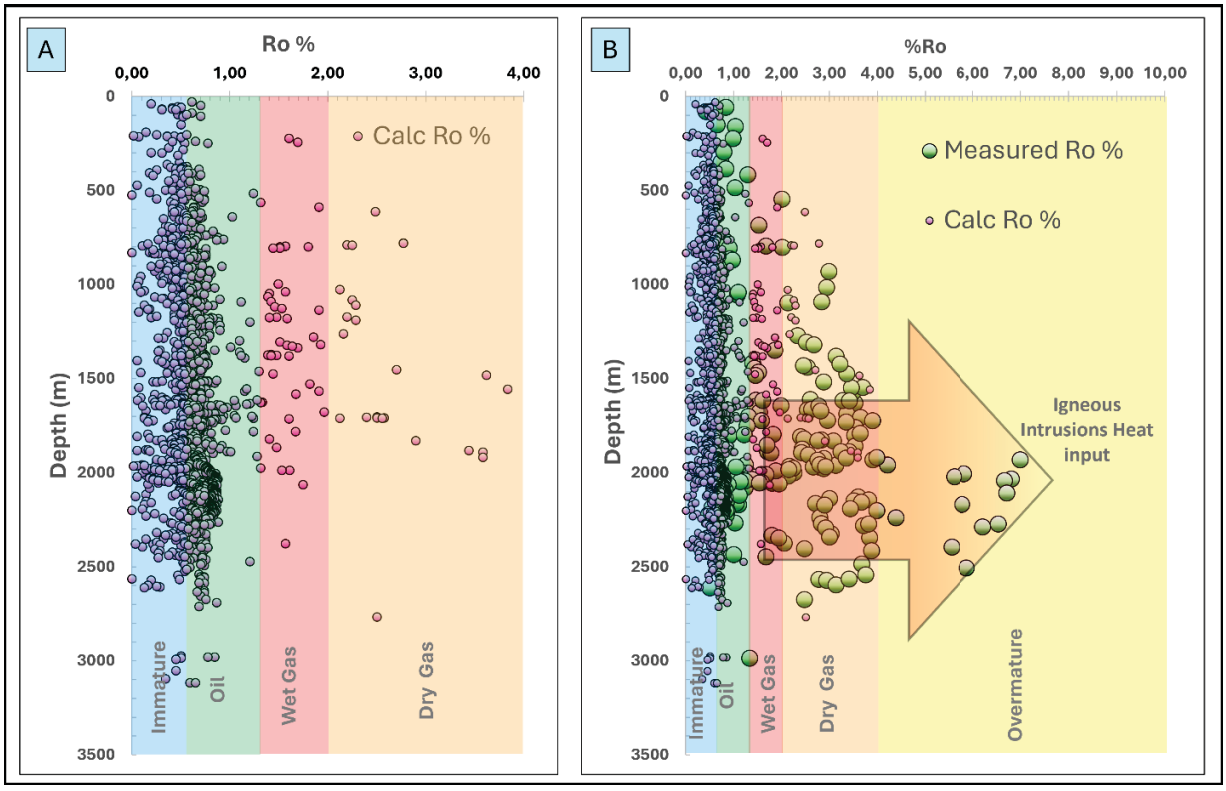

Figure 27 – Maturity profile of Parnaíba Basin based on TMax and Vitrinite Reflectance data (%Ro). In A the burial trend of maturity, using TMax data converted to vitrinite. In B the thermal effect of the magmatism in the vitrinite reflectance, changing the burial trend, leading the vitrinite to reach the overmature window Mio et al. (2023).

2.2.4.6.2. Smectite to Illite transformation calibration models

The Smectite/Illite transformation was studied by several authors (Dutta, 1986, Pytte, 1982, Pytte and Reynolds, 1988) in different ranges of time and temperature and there is an agreement that the process of transformation is kinetically controlled rather than equilibrium factors (Pytte and Reynolds, 1988). These authors presented a synthesis of those studies (Table 1) and highlighted the higher temperatures and faster transformation times of contact metamorphism in this process.

Pytte & Reynolds, (1988) presented the kinetic formulation for Smectite to Illite transformation based on the study of contact metamorphism in shales intruded by basalts sills in Colorado, USA (Pytte, 1982 apud Pytte and Reynolds, 1988), where it is clear the variation in I/S ratio with the proximity of the intrusion (Figure 28). The kinetic formulation

includes a first order kinetic, related to the pore-fluid ratio of K/Na (Equation 7), and a fifth order kinetic relative to the mole fraction of the smectite (Equation 8). The final kinetic is a sixth order kinetical scheme, that can be easily implemented into the basin modeling simulators to calculate the thermal effects of both, burial, and intrusion, in the smectite to illite transformation. This scheme is implemented into the Petromod simulator together with another kinetical scheme defined by Dutta (1986).

In the Equation 7, k is the rate of reaction, A is frequency factor, and U ins activation energy for a given R (gas constant) and T (Temperature in Kelvin). In the Equation 8, -dS/dt is the rate of transformation of initial contend of smectite, S is the molar fraction of smectite, K/Na is the ratio of those components in the reaction products and the exponents a and b means the order of the kinetics. Values of a and b were tested for the variations of time and temperature presented in the Table 1 and the best fit was a = 5 and b = 1 for A values of 5,6 x 107 s-1 and U = 33.2 kcal/mol. The application of this kinetic parameters in real data is presented in the Figure 28.

$$k = A \exp\ (-\frac{U}{RT})$$

Equation 7 – First Arrhenius Order Kinetic (or temperature dependence of reaction rates), relative to the pore fluid activity ratio K/Na. Pytte and Reynolds (1988).

$$-\frac{dS}{dt} = S^a\ (\frac{K}{Na})^b\ \text{A} \exp\ (-\frac{U}{RT})$$

Equation 8 - Fifth order kinetic parameters for equation for the Smectite to Illite transformation from Pytte and Reynolds (1988), after Pytte (1982) and Reynolds (1980), *apud* Pytte and Reynolds (1988).

Approximate time	Estimated peak temperature (°C)	Geological conditions	Reference
10 yr	250	Contact metamorphism	Reynolds (1981)
10,000 yr	150	Hydrothermal well	Jennings and Thompson (1986)
1 my	127	Burial diagenesis	Perry and Hower (1972)
10 my	100	Burial diagenesis	Perry and Hower (1972)
300 my	70	Burial diagenesis	Środoń and Eberl (1984)
450 my	70	K-Bentonite	Huff and Turkmenoglu (1981)

Table 1 – Approximate times at temperature exceeding 90% of the peak values for argillaceous rocks containing I/S with 80% of illite.

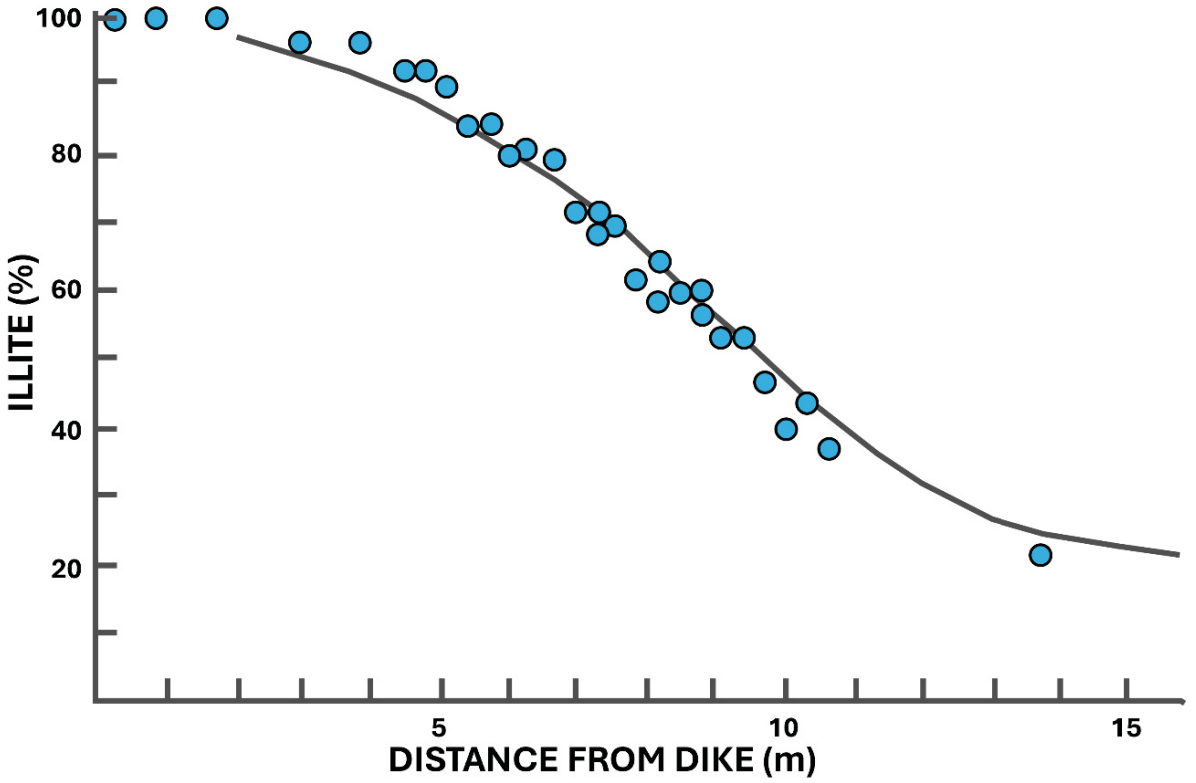

Figure 28 – Composition of I/S in the shale near to an intrusive basalt dike in Colorado. The points were defined using X-ray diffractometry and the curve is calculated using the kinetic model equation from Pytte; Reynolds (1988).

2.2.5. Challenges in atypical Petroleum Systems Modeling

The atypical petroleum systems, in the sense as described by Eiras and Wanderley Filho (2003) and Miranda et al. (2018) presents some key characteristics that point to some challenges in the numerical modeling process.

Magmatism introduces uncertainties in the ages of the intrusions as well as in the magma composition (Michelon, 2020), and these parameters are essential to the accurate thermal definition of the model and the calibration process. The sequence of the intrusion along the sedimentary column can drastically change the timing of hydrocarbon generation and trap filling (Aragão, 2020).

The reservoir quality can be obliterated by authigenic and contact metamorphism processes by quartz overgrowth and/or clay mineral developments into the pore space (Lopes, 2019; Miranda et al. 2018).

In terms of source rocks, the processes related to thermal stress can trigger the hydrocarbon generation and primary migration from source rock (Miranda, 2014 and Rodrigues, 1995).

In terms of thermal calibration, considering the source rocks are Devonian in ages Vaz et al., (2007) in the Paleozoic Brazilian basins and the fact the organic rich intervals are related with marine environments, normally associated with transgressive surfaces and maximum flooding surfaces (Ferraz et al, 2017, Rodrigues, 1995), the scarcity of the vitrinite particles is expected, due to small availability of superior plants at this age and the distal depositional environmental itself. It points to an important challenge in thermal calibration of the models in the past, and the support of external paleo thermometers can bring accuracy on the modeling process (Mio, 2022). A list of some of main challenges, the impact of these challenges on the modeling results, as well as the required actions to turn around those problems was proposed by Mio et al. (2023), and shown in the Figure 29.

CHALLENGES	IMPACT ON RESULTS	ACTIONS
Thermal Properties of the Magma	Wrong thermal prediction; Challenging Calibration; Low power of prediction on thermal and fluids prediction	Magma & Rock Physical-Chemical Properties Modeling of Thermal Properties
Age and Sequence of the intrusions	Wrong Thermal Prediction; Timing of trap filling (Problems in Synchronism); Migration barriers (Shadow Zone).	High Resolution Geochronology using U-Pb TIMS on zircon - Resolution around 20 ky;
Scarcity of Calibration Data (Absence of Vitrinite, High Thermally Altered Vitrinite)	Wrong thermal prediction; Challenging Calibration; Absence of calibration data in some high mature intervals.	Improvement on data acquisition Selection of new labs Development of Alternative calibration data (XRD Illite Crystallinity Index)
Fluid Predictivity/SR Kinetics	Inaccurate phase and composition prediction Inaccurate HC columns predictions Inaccurate fluid properties prediction	Acquisition of specific Kinetic for Parnaíba Devonian Shales Phase Kinetics

Figure 29 – Main challenges in modeling atypical petroleum systems, the impact in the results and the proposed action items to be addressed to solve the problems Mio et al. (2023).

2.2.6. Kinetic of Organic Matter Transformation

The maturation of kerogen and its transformation into hydrocarbons can be quantified through chemical kinetics parameters, using mass balance of generated compounds (Hantschel and Kauerauf, 2009). The measurement of the quantities of generated compounds according to the controlled increase of temperature experiments allow to determine the number of reactants and products, define the reactivity distributions, and establish the Arrhenius type of frequency factor and activation energies needed to reaction occur. The rate of reactions is defined by using different heating rates, and the inversion of different pairs of transformation ratio led to different pairs of frequency factors (A) and activation energy (E), as described in Equation 7. (Hantschel and Kauerauf, 2009).

The transformation ratio of organic matter or the converted mass fraction of initial reactant, is normally described as a first order kinetic equation (Equation 7), assuming a linear dependency of reactant conversion. The temperature dependency of the rate of the reaction is described as an Arrhenius law with two parameters A and E. Frequency factor A is the frequency at which molecules will be transformed and the activation energy E represents the energy needed to initiate the reaction (Equation 7).

The initial research developed to understand the process of transformation from organic matter into kerogen (diagenesis), the subsequent degradation of the kerogen to oil and gas (catagenesis) and cracking compounds into dry gas (metagenesis) was fully described by Tissot and Welte (1984), Figure 30. Those authors also conducted experimental processes of heating the kerogen to obtain and measure the generated compounds with the available methods to define the initial parameters to compare artificial laboratory results with natural processes. They also review the previous results of artificial maturation of Toarcian shales from Paris Basin with results of vitrinite reflectance and defined the initial relationships of time-dependence from transformation, the initial elementary composition changes in O and H.

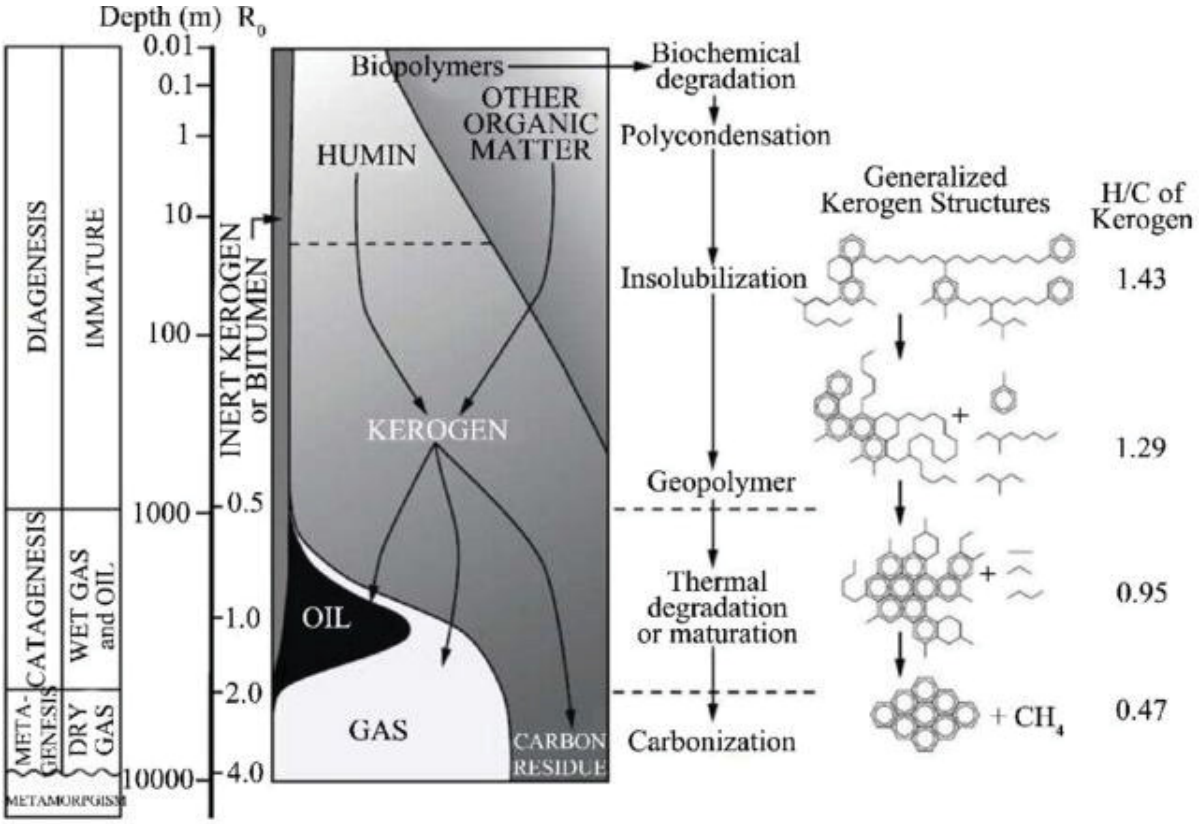

Figure 30 – General Scheme of the evolution of the organic matter, from deposition to metamorphism, Abrakasa et al. (2022) adapted from Tissot and Welte (1984).

After this initial approach, this field of science experienced a series of developments, incluiding: time and temperature dependence in the petroleum formation (Waples, 1980); primary cracking of four classes of hydrocarbons (Espitalié et al. 1988); kerogen classification and pyrolysis gas chromatography (Horsfield, 1989 and 1990); bulk kinetics of oil generation Ungerer et al. (1990); kinetic model for vitrinite reflectance (Larter, 1988; Sweeney and Burnhan, 1990); the thermal evolution of oils (Behar et al. 1991); kinetic modelling of kerogen and oil cracking in a closed pyrolysis system (Behar et al. 1992); bulk oil generation and expulsion, along with kerogens changes (Sweeney et al. 1995); cracking comparisons between thermal cracking in open and closed pyrolysis systems and multi-compounds kinetics (Behar et al. 1997); fourteen compound kinetics and hydrocarbon phase prediction (Di Primio and Horsfield, 2006).

A large variety of kinetics models, from bulk to multi-compositional schemes was compiled and presented in Hantschel and Kauerauf (2009), covering a wide range of geological ages, from Devonian to Cenozoic, and different geological environments from

type I lacustrine to Type III terrestrial organic matter. Those schemes covered bulk kinetics (Sweeney and Burnham, 1990, Tegelaar and Noble, 1994), multi component kinetics for four compounds (Ungerer et al. 1990), nine compounds (Vandenbroucke et al. 1999) and fourteen compounds (Di Primio and Horsfield, 2006). Most of these, bulk and compositional schemes, are available in commercial numerical simulator packages.

2.3. X-RAY DIFFRACTOMETRY

2.3.1. X-Ray Diffractometry

X-ray diffraction (XRD) is a non-destructive analytical technique widely used for material characterization, particularly in studying physical properties such as phase composition, crystal structure, and preferred orientation of powdered or clay fraction samples. It is a fundamental methodology in various fields, including materials science, geosciences, and engineering, enabling precise identification of crystalline compounds and monitoring of structural transformations (Cullity and Stock 2001).

X-rays are electromagnetic radiation, analogous to visible light waves, but with significantly shorter wavelengths — ranging approximately from 10 nanometers to 10 picometers. These wavelengths lie between the ultraviolet and gamma-ray regions of the electromagnetic spectrum. Due to this characteristic, X-rays possess high energy and significant penetrating power, making them particularly effective in analyzing solid materials (Giacovazzo et al. 2002).

X-ray radiation, also known as Röntgen radiation, is generated when accelerated electrons collide with a metallic target, typically composed of copper or molybdenum. Upon interacting with the crystalline structures of materials, X-rays undergo diffraction, producing specific patterns that can be recorded and interpreted using appropriate detectors. These diffraction patterns are unique to each crystalline substance, allowing for qualitative and, in many cases, quantitative identification of the constituents present in the analyzed sample (Silva, 2012).

In the field of mineralogy, X-ray diffraction plays a crucial role in mineral identification and the investigation of geological processes. It is particularly useful in characterizing clay minerals, oxides, sulfides, and silicates in rock, soil, and sediment samples. XRD enables differentiation of polymorphs with distinct crystalline structures—such as kaolinite and dickite — and identification of mineralogical alterations associated with weathering, diagenesis, and metamorphism. Additionally, it is applied in the evaluation of mineral deposits, monitoring stability in tailings dams, and research on critical minerals for industrial and technological applications (Peters and Ward, 2010).

The analytical methodology of XRD can vary depending on the sample´s granulometric fraction. For total powder analysis, the sample is dried, homogenized, and ground to achieve a particle size of less than 0.074 mm (200 mesh), then compacted into appropriate holders for direct reading. The clay fraction (<2 μm) requires physicochemical pretreatments such as dispersion, sedimentation, and, in some cases, removal of organic matter and iron oxides. After separation, the clay fraction is mounted on oriented glass slides, allowing the identification of lamellar minerals based on the position and intensity of diffraction peaks, before and after thermal treatments or solvation with ethylene glycol. These procedures enhance the sensitivity and resolution of mineralogical identification (Moore and Reynolds, 1997).

Typical applications of X-ray diffraction also include the investigation of ceramic and semiconductor materials, as well as soil analysis in environmental and geotechnical studies. Furthermore, XRD is employed in the pharmaceutical industry for quality control of drugs and identification of crystalline polymorphs that may affect the bioavailability of active ingredients. In summary, X-ray diffraction is an indispensable tool in structural material analysis, providing detailed information with high reliability without compromising the physical integrity of the examined samples.

2.3.1.1. The Illite Crystallinity and the Kubler Index

The Kübler Index (KI) was introduced by Bernard Kübler in the 1960s as a quantitative parameter to evaluate the crystallinity of illite group minerals, primarily in clay fractions. Prior to this, mineralogical studies of clays were largely qualitative, making it

challenging to establish consistent criteria for assessing metamorphic grades, especially under low-temperature conditions. Kübler's pioneering work revolutionized this approach by linking the width of the 10 Å basal reflection line (*d*001) observed in X-ray diffraction (XRD) patterns to the degree of structural ordering in illite, providing a proxy for diagenetic and low-grade metamorphic transformations (Kübler, 1967).

The KI specifically measures the full width at half maximum (FWHM) of the 10 Å basal peak, expressed in degrees two-theta (2θ). Narrower peaks indicate more ordered crystalline structures, reflecting higher metamorphic grades or thermal maturity. Over time, the index has been calibrated against various metamorphic facies, enabling the delineation of zones such as the anchizone and epizone in sedimentary basins and orogenic belts. The measurement of FWHM at 10 Å was established by Kübler (1967) as an evolution of the previous measurement of the ratio between the 10 Å and 10.5 Å defined in his classical paper of Kubler (1964).

The crystallinity index or KI is directly related to the size and perfection of coherent scattering domains within the mineral's layered structure. Illite and related minerals typically exhibit basal spacings around 10 Å due to their layered structure. During metamorphism, dehydration and recrystallization processes promote better stacking and a reduction of structural defects, resulting in sharper peaks with smaller FWHM values (Moore and Reynolds, 1997). Considering this, the KI is an indirect but reliable measure of the mineral's structural evolution, capturing subtle changes in lattice parameters and stacking faults that are difficult to quantify by other methods. This sensitivity makes the KI indispensable for studying low-grade metamorphism as described by several authors (Campos et al. 2015, Frey and Robinson 1999, Lanson and Champion 1991, Pytte, 1982, Pytte and Reynolds, 1988).

The KI has been widely applied to characterize low-grade metamorphic environments, particularly in analyses of clay fractions isolated from sedimentary rocks and shales. For example, Warr and Cox (2016) utilized the KI to map metamorphic zones in New Zealand's South Island, correlating variations in crystallinity with thermal gradients and tectonic settings. Additionally, KI allows tracking the diagenetic to metamorphic transition, where illite progressively replaces smectite through illitization.

A significant advancement in KI application was demonstrating its correlation with vitrinite reflectance (Ro), a key parameter for assessing thermal maturity in sedimentary geology and petroleum system modeling. (Mählmann and Frey, 2012) demonstrated that KI values strongly correlate with vitrinite reflectance, enabling integrated reconstructions of burial and thermal histories. The index also serves as a valuable proxy in basin analysis and hydrocarbon exploration, where understanding the thermal evolution of source rocks is critical. By monitoring mineralogical transformations within the clay fraction, geoscientists can infer maximum paleotemperatures and assess organic matter maturation levels. These authors also conducted interlaboratory studies showing that the narrowing of the illite 10 Å basal peak (indicating increased crystallinity) is associated and mathematically correlated with increased vitrinite reflectance. This relationship positions the KI as a non-organic mineralogical proxy to qualitatively estimate the ranges of temperature reached by sedimentary rocks. Despite the fact of an extensive research on KI versus %Ro correlation, in the literature only scarce papers present validated datasets of this correlation, highlighting the relations proposed by Frey and Robinson (1999) and Mählmann and Frey (2012), presented in the Figure 31, which some mathematical regression can be applied in order to extend the correlation to another geological contexts.

Combining KI with vitrinite reflectance provides a more robust approach to reconstructing basin thermal histories, especially where vitrinite reflectance may be unreliable due to absence or degradation of organic material, although some revision and recommendations of inter-laboratory correlations were proposed to achieve an acceptable level of standardization for calibration and correlation between KI and %Ro (Mählmann and Frey, 2012, Warr and Mählmann, 2015). These standardized calibration procedures include the use of reference materials, establishing the Controlled Index of Crystallinity Scale (CIS), which improves reproducibility of results.

The analytical process of XRD analysis and the subsequent KI determination requires careful sample preparation of specific aliquots, especially the clay fraction. The clay fraction (<2 μm) is separated by sedimentation and often chemically treated to remove organic matter and iron oxides that interfere with diffraction patterns. Oriented mounts of the clay fraction on glass slides maximize basal reflection intensity and

minimize peak broadening caused by random particle orientation (Moore and Reynolds, 1997). The presence of mixed-layer clay minerals, such as illite-smectite, poses challenges in interpreting KI data. Techniques like ethylene glycol solvation and thermal treatments are employed to discriminate these phases and refine index calculations (Pytte and Reynolds,1988).

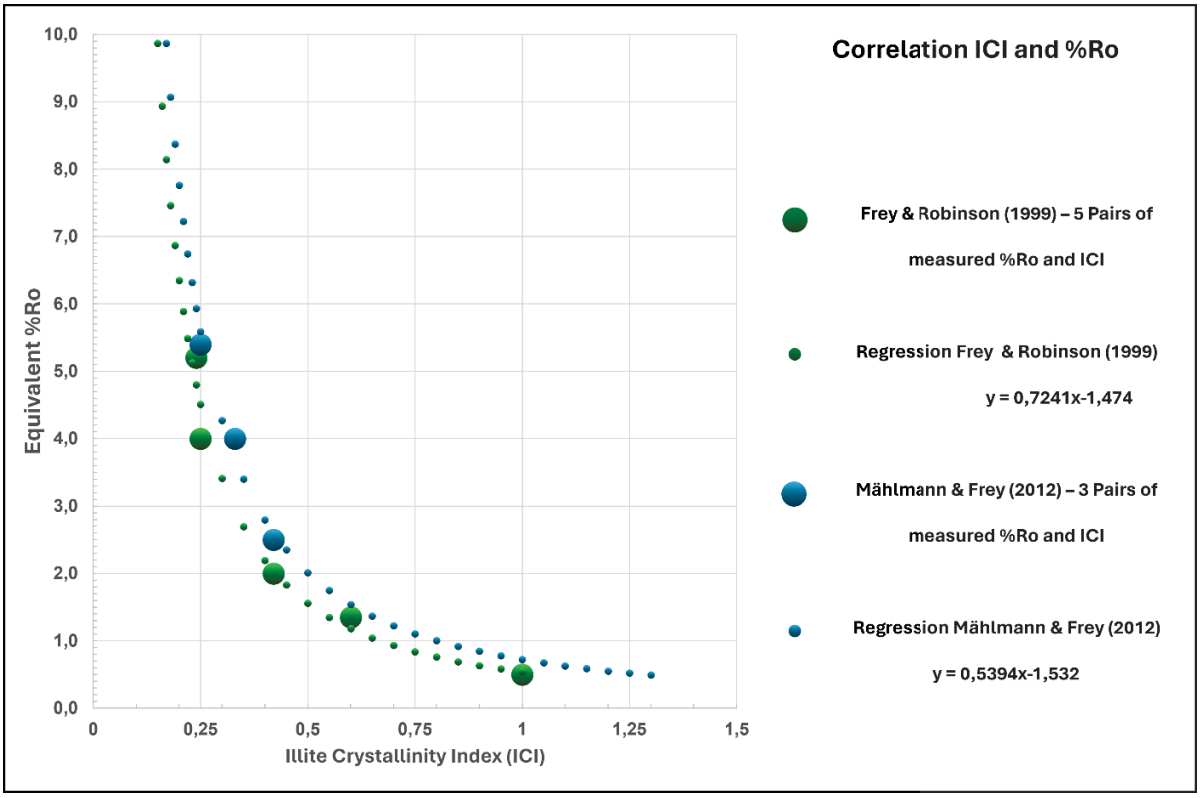

Figure 31 – Regression lines and equations from the relationship between Kubler Index or ICII (Illite Crystallinity Index) and percent of vitrinite reflectance from the data presented by Frey and Robinson, (1999) and Mählmann and Frey (2012).

3. DATASET AND METHODOLOGY

The dataset used in this study is summarized in the Figure 32, showing the location of the 2D and 3D petroleum system models, and the location of the wells A, B, C and D, which ones were used for vitrinite reflectance, compositional kinetics, XRD analyses and 1D PSM simulations.

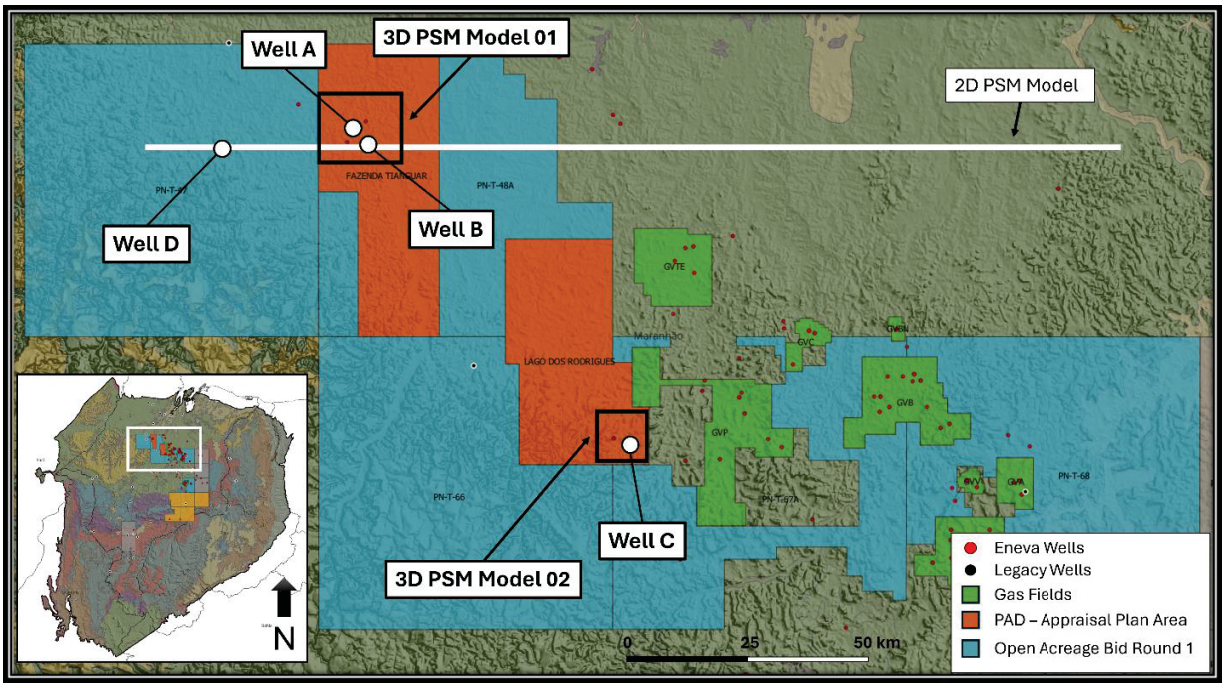

Figure 32 - Location of 3D, 2D and 1D PSM models used in this study. 3D SPM Model 01 and 02, the E-W line of 2D PSM model, and the 1D PSM models Well A, B and C. Additionally, the location of well B and D which were the selected wells to perform the study of compositional kinetics of the Pimenteiras formation is shown.

3.1. Analysis of Reflectance of Vitrinite

The visual analysis of kerogen and the determination of the vitrinite reflectance index was performed in by LCV/GeoLab Sur Laboratories, in Buenos Aires, Argentina and it was used a Carl Zeiss Axiomager A2m equipped with halogen and mercury sources. The measure plates were prepared in an epoxy base with a concentration of kerogen after dissolution in HCl and HF acids. The kerogen classification was complemented using microscopic analysis in palynologic type slabs.

A total of 54 samples (29 samples ate Well A, 14 samples at Well B and 11 samples at Well C) were analyzed for vitrinite reflectance index and the organic petrography and visual analysis of the kerogens.

3.2. Definition of compositional kinetic scheme from pimenteiras source rock and implementation on petromod

The determination of specific kinetic parameters for Pimenteiras formation was performed using two samples after a screening of 41 selected samples in the radioactive levels A, B, C, and D (Rodrigues, 1995) from wells B and D (Figure 33), in the north portion of the Parnaíba Basin, using the PhaseKinetic approach of di Primio and Horsfield, (2006).

The criteria for selecting the samples obey the following requirements:

- wells drilled with water base mud (WBM) to avoid contamination with organic fluids from drilling mud.
- Immature samples without the thermal effect of the magmatic intrusion, based on the initial screening of thermally mature samples using a previous 1D PSM thermal simulation.

Figure 33 – Photomosaic of sample selection for compositional kinetic analysis. A) Box with cuttings of Pimenteiras formation at the well 1- PA-1-MA; B) set of samples selected inside of each organic rich interval of the Pimenteiras fm. (A, B, C and D); C) detail of the selected sample at level A of the Pimenteiras formation, one of the selected samples for kinetic study.

The analytical program was performed in the laboratory of Geos4 in Michendorf, Germany and comprise the following workflow:

- TOC/Rock-Eval parameters –
- Petrographic maturity assignment in optical microscopy.
- Organofacies Type definition - Open-system pyrolysis-GC-FID.
- Bulk-kinetic modelling parameters - Source Rock Analyzer-FID.
- PhaseKinetic modelling parameters - MSSV – pyrolysis-GC-FID.

Pyrolysis was performed in Rock-Eval 6^{TM}. The analysis was performed in two steps: pyrolysis (conventional Rock Eval measurement) and oxidation (TOC determination). Pyrolysis: 300°C for 3 minutes then at 25°C/min. to 650°C (0 min.) and oxidation: 400°C (3 min.) at 25°C/min. to 850°C (5 min.).

Petrographic maturity was performed using Leica DM 4P microscope equipped with Hilgers FOSSIL MOT on 20 shale/sandstone cutting samples thin section, embedded in epoxy resin, and polished. The mean random reflectance was measured following standard procedures defined by Taylor et al. (1998). A synthetic reflectance standard (N-LASF46A: 1.311 %Rr) was applied. Reflectance measurements were performed on different types of vitrinite, bitumen and zooclasts (eg. graptolites and chitinozoa).

The thermovaporisation (free hydrocarbon) and the pyrolysis gas chromatography (petroleum types) were performed using the Quantum MSSV-2 Thermal Analysis System©. For the thermovaporisation milligram quantities of sample material were sealed in a glass capillary and heated to 300°C in the injector unit for 5 minutes. The tube was then cracked open using a piston device coupled with the injector, and the released volatile hydrocarbons analyzed by gas chromatography.

For the Pyrolysis gas the samples were heated in a flow of helium, and products released over the temperature range 300-600°C (40K/min) were focused using a cryogenic trap and then analyzed using a 50m x 0.32mm BP-1 capillary column equipped with a flame ionization detector. The GC oven temperature was programmed from 40°C to 320°C at 8°C/minute. Boiling ranges (C1, C2-C5, C6-C14, C15+) and individual compounds (n-alkenes, n-alkanes, alkylaromatic hydrocarbons, phenols and alkylthiophenes) were quantified by external standardisation using n-butane.

The bulk kinetic response was analyzed on twelve samples by non-isothermal open system pyrolysis at four different laboratory heating rates (0.7, 2.0, 5.0 and 15K/min) using an RE 6 and a Source Rock Analyzer®. The generated bulk petroleum formation curves serve as input for the bulk kinetic model consisting of an activation energy distribution and a single frequency factor (Figure 34). The selected samples for the bulk kinetic model and for the PhaseKinetic were the samples labelled 20189, from the Pimenteiras formation source rock interval A in Well B, at 2277 m, and the sample 20170 from Well D at 2034 m, in the source rock interval C.

For the PhaseKinetic the microscale sealed vessel pyrolysis (MSSV - Horsfield, 1989 a) was performed using the Quantum MSSV-2 Thermal Analysis System®. Milligram quantities of sample material were sealed in glass capillaries and artificially matured at

0.7K/min using a special MSSV prep-oven for the PhaseKinetics approach. The tubes were then cracked open using a piston device coupled with the injector, and the released products were swept into the GC using a flow of helium. An HP5890 II instrument was used for GC analysis (column: BP-1, 50 m length, i.d. 0.32 mm, film thickness 0.52 µm) with flame ionization detection. Individual compounds in the gas range (C1-C5), coarse boiling ranges (C1, C2-C5, C6-C14, C15+) and 25 pseudo-boiling ranges for each carbon number at and above C6 were quantified for the PhaseKinetics approach. Quantification was performed by external standardization using n-butane. Response factors for all compounds were assumed to be the same, except for methane whose response factor was 1.1.

The implementation of the analyzed kinetical scheme inside of the Petromod calculator Is done by the compilation of laboratory tables of energy of activation versus percent of a given component. Four different compositional schemes were defined in the PhaseKinetic study, such as black oil, two, four and fourteen compounds. The four compounds scheme (Methane, C2-C5, C6-C14 and C15+) was used in simulations to compare de effects of a generic kinetic scheme for a USA-Canada Devonian source rock (Woodford Shale – Hantschel and Kauerauf (2009).

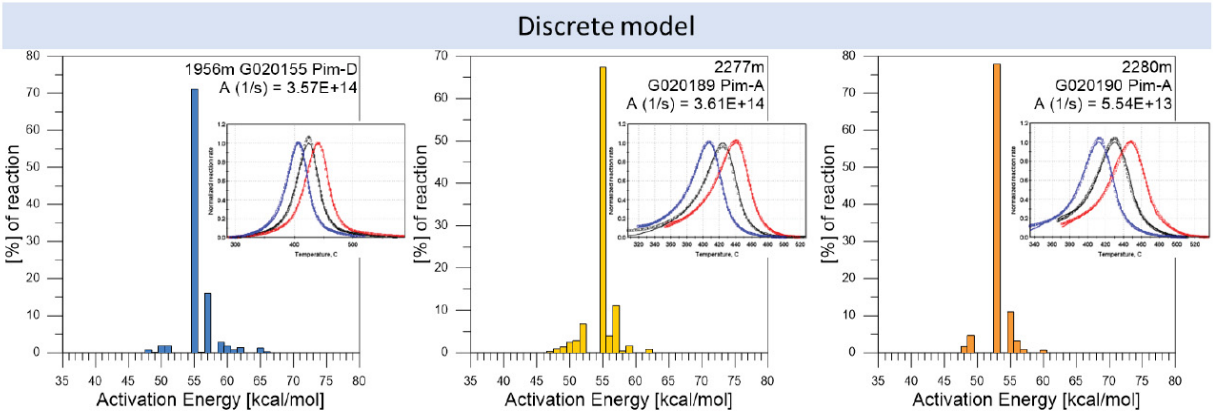

Figure 34 - Bulk kinetic parameters for three samples based on slow heating rates (0.7; 2.0; 5.0K/min) using discrete models. The sample 20189 (center) was the sample selected for PhaseKinetics. It is a sample of 2077 m (Pimenteiras SR A) from Well B.

3.3. X-Ray diffraction analysis

The X-Ray diffraction analysis was performed initially in three selected wells (Wells A, B and C) comprising 66 samples in Well A, 70 samples in Well B and 71 samples in well C. Most part of the samples are inside of Pimenteiras formation with few samples inside of Longá, Cabeças and Itaim formations (Table 2).

The samples include different sources, such as composed samples from well cuttings and samples collected from scratches from side well cores (SWCs).

Samples were analyzed into three different laboratories: the first set at Instituto LAMIR (Universidade Federal do Paraná – UFPR, Brazil), the second set at LCV/Geolab Sur in Buenos Aires, Argentina and the third set at Centro de Investigaciones Geológicas - Universidad de La Plata, Argentina. At the three laboratories the samples were analyzed in two distinct fractions: whole rock (powder) fraction and clay fraction. The clay fraction was analyzed in a natural untreated state, ethylene-glycolated state and heated at 550°C.

The samples processed in LAMIR were analyzed in a PanAnalytical EMPYREAN@ diffractometer, with a copper anode and energies of 40 kV and 30 mA using a step scan 0.017° and scan step time of 10,16 s, with a start position of 3.5085 (°2θ) to 69.97 (°2θ). The clay fraction was separated into two steps, the first, after centrifugation, to remove the coarse fraction and contaminants at the top of the mixture, and the second, after a second cycle of centrifugation, to collect the upper part of suspension, aiming to sample the preferred the *d*001 oriented clay mineral.

The second set of samples was processed in LCV/Geolab Sur, using a Phillips XPert MPD diffractometer with a copper anode and energies of 40 kV and 40 mA using a step scan 0.040 (°2θ) and scan step time of 1,00 s with variable scanning position angles.

The third set of samples, processed at CIG – UNLP, was analyzed using a Phillips XPert Pro diffractometer with a copper anode and energies of 40 kV and 40 mA using a step scan 0.030 (°2θ) and scan step time of 1,00 s with variable scanning position angles.

The separation of clay fraction in LCV and CIG-UNLP was performed after suspension in distillated water of the sample powder and ultrasonic vibration for 30 minutes to ensure the suspension of material fine than 4 microns. The natural clay sample is collected with a pipette in the upper part of the suspension, after the decantation

process, respecting Stokes Law parameters, assuring the preferential orientation of the clay minerals at the crystallographic plane *d*001. The Ethylene-Glycolated sample was obtained after explosion of 12 hours in the Ethylene-Glycol vapors, and the heated sample was obtained after 2 hours in an oven at 550°C (Figure 35).

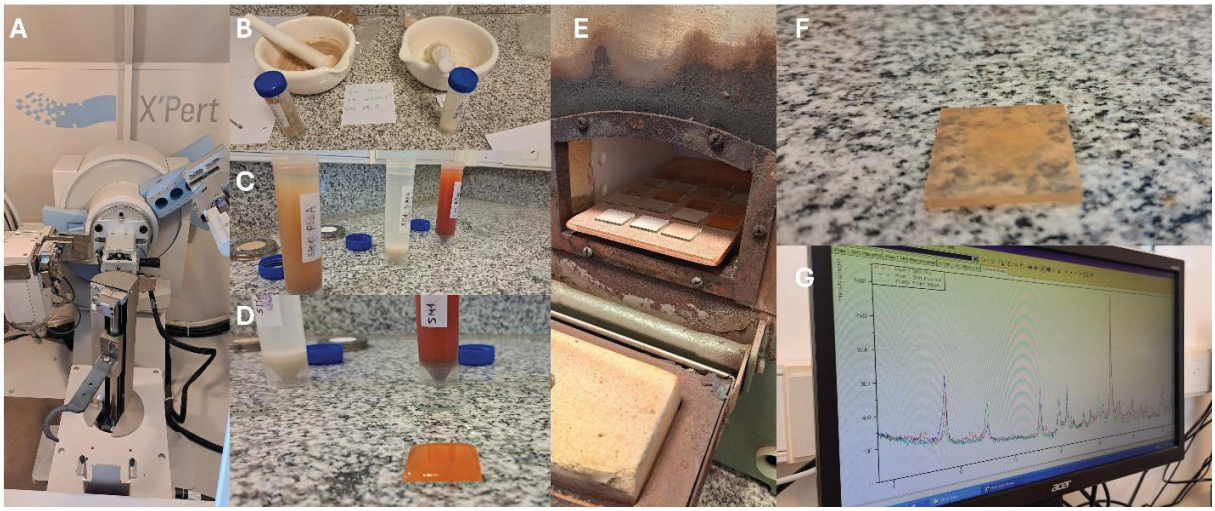

Figure 35 - Photomosaic of clay fraction sample preparation and analyses at CIG – UNPL laboratories, La Plata, Argentina. A – Diffractomer Phillips Xpert Pro; B - Sample crushing and homogenization; C - Decantation in tubes; D – Pipetting and glass base mounting of natural clay plate; E – Samples in the oven for two hours heating at 550°C; F – Dried natural clay fraction before analysis; G – Interface of Phillips Xpert Pro equipment during measuring process.

LAMIR, LCV and CIG equipment operates with the same wavelengths as follow: K Alpha1 1.54060 Â, K Alpha2 1,54443 Â, KBeta 1,39225 Â and the K Alpha2/ K Alpha1 ratio was 0,5. The details of the samples are presented in the table below:

#	Well	Top (MD)	Base (MD)	Av.Depth (MD)	TVD (m)	TVDSS (m)	Formation	Source	Laboratoty
1	Well A	1305	1314	1309,5	1227,50	-1221,50	Poti	Cuttings	CIG/UNPL
2	Well A	1323	1326	1324,5	1242,50	-1236,50	Poti	Cuttings	CIG/UNPL
3	Well A	1338	1341	1339,5	1257,50	-1251,50	Poti	Cuttings	CIG/UNPL
4	Well A	1353	1356	1354,5	1272,50	-1266,50	Poti	Cuttings	CIG/UNPL
5	Well A	1368	1371	1369,5	1287,50	-1281,50	Poti	Cuttings	CIG/UNPL
6	Well A	1383	1386	1384,5	1302,50	-1296,50	Longá	Cuttings	CIG/UNPL
7	Well A	1398	1401	1399,5	1317,50	-1311,50	Longá	Cuttings	CIG/UNPL
8	Well A	1413	1416	1414,5	1332,50	-1326,50	Longá	Cuttings	CIG/UNPL
9	Well A	1428	1431	1429,5	1347,50	-1341,50	Longá	Cuttings	CIG/UNPL
10	Well A	1443	1446	1444,5	1362,50	-1356,50	Longá	Cuttings	CIG/UNPL
11	Well A	1458	1461	1459,5	1377,50	-1371,50	Longá	Cuttings	CIG/UNPL
12	Well A	1473	1476	1474,5	1392,50	-1386,50	Longá	Cuttings	CIG/UNPL
13	Well A	1509	1512	1510,5	1428,50	-1422,50	Cabeças	Cuttings	CIG/UNPL
14	Well A	1524	1527	1525,5	1443,50	-1437,50	Cabeças	Cuttings	CIG/UNPL
15	Well A	1539	1542	1540,5	1458,50	-1452,50	Cabeças	Cuttings	CIG/UNPL
16	Well A	1554	1557	1555,5	1473,50	-1467,50	Cabeças	Cuttings	CIG/UNPL
17	Well A	1569	1572	1570,5	1488,50	-1482,50	Cabeças	Cuttings	CIG/UNPL
18	Well A	1581	1584	1582,5	1500,50	-1494,50	Cabeças	Cuttings	CIG/UNPL
19	Well A	1608	1611	1609,5	1527,50	-1521,50	Pimenteiras	Cuttings	CIG/UNPL
20	Well A	1623	1626	1624,5	1542,50	-1536,50	Pimenteiras	Cuttings	CIG/UNPL
21	Well A	1638	1641	1639,5	1557,50	-1551,50	Pimenteiras	Cuttings	CIG/UNPL
22	Well A	1653	1656	1654,5	1572,50	-1566,50	Pimenteiras	Cuttings	CIG/UNPL
23	Well A	1830	1833	1831,5	1749,50	-1743,50	Pimenteiras	Cuttings	CIG/UNPL
24	Well A	1899	1902	1900,5	1818,50	-1812,50	Pimenteiras	Cuttings	CIG/UNPL
25	Well A	1914	1917	1915,5	1833,50	-1827,50	Pimenteiras	Cuttings	CIG/UNPL
26	Well A	1929	1932	1930,5	1848,50	-1842,50	Pimenteiras	Cuttings	CIG/UNPL
27	Well A	1935	1935	1935,0	1853,00	-1847,00	Pimenteiras	SWC	LCV/Geolab Sur
28	Well A	1959	1962	1960,5	1878,50	-1872,50	Pimenteiras	Cuttings	CIG/UNPL
29	Well A	1968	1968	1968,0	1886,00	-1880,00	Pimenteiras	SWC	LCV/Geolab Sur
30	Well A	1974	1977	1975,5	1893,50	-1887,50	Pimenteiras	Cuttings	CIG/UNPL
31	Well A	1989	1992	1990,5	1908,50	-1902,50	Pimenteiras	Cuttings	CIG/UNPL
32	Well A	1998	1998	1998,0	1916,00	-1910,00	Pimenteiras	SWC	LCV/Geolab Sur
33	Well A	2004	2007	2005,5	1923,50	-1917,50	Pimenteiras	Cuttings	CIG/UNPL
34	Well A	2019	2022	2020,5	1938,50	-1932,50	Pimenteiras	Cuttings	CIG/UNPL
35	Well A	2025	2025	2025,0	1943,00	-1937,00	Pimenteiras	SWC	LCV/Geolab Sur
36	Well A	2034	2037	2035,5	1953,50	-1947,50	Pimenteiras	Cuttings	CIG/UNPL
37	Well A	2049	2049	2049,0	1967,00	-1961,00	Pimenteiras	SWC	LCV/Geolab Sur
38	Well A	2049	2052	2050,5	1968,50	-1962,50	Pimenteiras	Cuttings	CIG/UNPL
39	Well A	2064	2064	2064,0	1982,00	-1976,00	Pimenteiras	SWC	LCV/Geolab Sur
40	Well A	2064	2067	2065,5	1983,50	-1977,50	Pimenteiras	Cuttings	CIG/UNPL
41	Well A	2079	2082	2080,5	1998,50	-1992,50	Pimenteiras	Cuttings	CIG/UNPL
42	Well A	2082	2082	2082,0	2000,00	-1994,00	Pimenteiras	SWC	LCV/Geolab Sur
43	Well A	2094	2097	2095,5	2013,50	-2007,50	Pimenteiras	Cuttings	CIG/UNPL
44	Well A	2097	2097	2097,0	2015,00	-2009,00	Pimenteiras	SWC	LCV/Geolab Sur
45	Well A	2109	2112	2110,5	2028,50	-2022,50	Pimenteiras	Cuttings	CIG/UNPL
46	Well A	2115	2115	2115,0	2033,00	-2027,00	Pimenteiras	SWC	LCV/Geolab Sur
47	Well A	2124	2127	2125,5	2043,50	-2037,50	Pimenteiras	Cuttings	CIG/UNPL
48	Well A	2130	2130	2130,0	2048,00	-2042,00	Pimenteiras	SWC	LCV/Geolab Sur
49	Well A	2139	2142	2140,5	2058,50	-2052,50	Pimenteiras	Cuttings	CIG/UNPL
50	Well A	2154	2157	2155,5	2073,50	-2067,50	Pimenteiras	Cuttings	CIG/UNPL
51	Well A	2160	2160	2160,0	2078,00	-2072,00	Pimenteiras	SWC	LCV/Geolab Sur
52	Well A	2169	2172	2170,5	2088,50	-2082,50	Pimenteiras	Cuttings	CIG/UNPL
53	Well A	2184	2187	2185,5	2103,50	-2097,50	Pimenteiras	Cuttings	CIG/UNPL
54	Well A	2199	2202	2200,5	2118,50	-2112,50	Pimenteiras	Cuttings	CIG/UNPL
55	Well A	2202	2202	2202,0	2120,00	-2114,00	Pimenteiras	SWC	LCV/Geolab Sur
56	Well A	2214	2217	2215,5	2133,50	-2127,50	Pimenteiras	Cuttings	CIG/UNPL
57	Well A	2229	2229	2229,0	2147,00	-2141,00	Pimenteiras	SWC	LCV/Geolab Sur
58	Well A	2229	2232	2230,5	2148,50	-2142,50	Pimenteiras	Cuttings	CIG/UNPL
59	Well A	2244	2247	2245,5	2163,50	-2157,50	Itaim	Cuttings	CIG/UNPL
60	Well A	2259	2262	2260,5	2178,50	-2172,50	Itaim	Cuttings	CIG/UNPL
61	Well A	2274	2277	2275,5	2193,50	-2187,50	Itaim	Cuttings	CIG/UNPL
62	Well A	2289	2292	2290,5	2208,50	-2202,50	Itaim	Cuttings	CIG/UNPL
63	Well A	2304	2307	2305,5	2223,50	-2217,50	Itaim	Cuttings	CIG/UNPL
64	Well A	2319	2322	2320,5	2238,50	-2232,50	Itaim	Cuttings	CIG/UNPL
65	Well A	2334	2337	2335,5	2253,50	-2247,50	Itaim	Cuttings	CIG/UNPL
66	Well A	2349	2352	2350,5	2268,50	-2262,50	Itaim	Cuttings	CIG/UNPL
1	Well B	1350	1353	1351,5	1286,50	-1259,00	Poti	Cuttings	CIG/UNPL
2	Well B	1365	1368	1366,5	1301,50	-1273,00	Poti	Cuttings	CIG/UNPL
3	Well B	1380	1383	1381,5	1316,50	-1288,00	Poti	Cuttings	CIG/UNPL

4	Well B	1395	1398	1396,5	1331,50	-1303,00	Poti	Cuttings	CIG/UNPL
5	Well B	1410	1413	1411,5	1346,50	-1317,00	Poti	Cuttings	CIG/UNPL
6	Well B	1425	1428	1426,5	1361,50	-1332,00	Poti	Cuttings	CIG/UNPL
7	Well B	1440	1443	1441,5	1376,50	-1346,00	Poti	Cuttings	CIG/UNPL
8	Well B	1449	1461	1455,0	1426,28	-1361,28	Poti	Cuttings	LAMIR
9	Well B	1455	1458	1456,5	1391,50	-1361,00	Poti	Cuttings	CIG/UNPL
10	Well B	1470	1473	1471,5	1406,50	-1376,00	Poti	Cuttings	CIG/UNPL
11	Well B	1473	1482	1477,5	1447,75	-1382,75	Poti	Cuttings	LAMIR
12	Well B	1485	1488	1486,5	1421,50	-1391,00	Longá	Cuttings	CIG/UNPL
13	Well B	1500	1503	1501,5	1436,50	-1405,00	Longá	Cuttings	CIG/UNPL
14	Well B	1509	1521	1515,0	1484,84	-1419,84	Longá	Cuttings	LAMIR
15	Well B	1515	1518	1516,5	1451,50	-1420,00	Longá	Cuttings	CIG/UNPL
16	Well B	1530	1533	1531,5	1466,50	-1435,00	Longá	Cuttings	CIG/UNPL
17	Well B	1533	1548	1540,5	1509,37	-1444,37	Longá	Cuttings	LAMIR
18	Well B	1545	1548	1546,5	1481,50	-1449,00	Longá	Cuttings	CIG/UNPL
19	Well B	1560	1563	1561,5	1496,50	-1464,00	Longá	Cuttings	CIG/UNPL
20	Well B	1575	1578	1576,5	1511,50	-1479,00	Longá	Cuttings	CIG/UNPL
21	Well B	1590	1593	1591,5	1526,50	-1494,00	Longá	Cuttings	CIG/UNPL
22	Well B	1605	1608	1606,5	1541,50	-1508,00	Cabeças	Cuttings	CIG/UNPL
23	Well B	1620	1623	1621,5	1556,50	-1523,00	Cabeças	Cuttings	CIG/UNPL
24	Well B	1635	1638	1636,5	1571,50	-1538,00	Cabeças	Cuttings	CIG/UNPL
25	Well B	1650	1653	1651,5	1586,50	-1552,00	Cabeças	Cuttings	CIG/UNPL
26	Well B	1653	1662	1657,5	1624,33	-1559,33	Cabeças	Cuttings	LAMIR
27	Well B	1665	1668	1666,5	1601,50	-1567,00	Cabeças	Cuttings	CIG/UNPL
28	Well B	1680	1683	1681,5	1616,50	-1582,00	Cabeças	Cuttings	CIG/UNPL
29	Well B	1695	1698	1696,5	1631,50	-1597,00	Cabeças	Cuttings	CIG/UNPL
30	Well B	1827	1830	1828,5	1763,50	-1726,00	Pimenteiras	Cuttings	CIG/UNPL
31	Well B	1971	1974	1972,5	1907,50	-1866,00	Pimenteiras	Cuttings	CIG/UNPL
32	Well B	1971	1971	1971,0	1931,38	-1866,38	Pimenteiras	SWC	LCV/Geolab Sur
33	Well B	1995	1998	1996,5	1931,50	-1890,00	Pimenteiras	Cuttings	CIG/UNPL
34	Well B	2010	2013	2011,5	1946,50	-1904,00	Pimenteiras	Cuttings	CIG/UNPL
35	Well B	2019	2019	2019,0	1978,19	-1913,19	Pimenteiras	SWC	LCV/Geolab Sur
36	Well B	2021	2021	2021,0	1980,15	-1915,15	Pimenteiras	SWC	LCV/Geolab Sur
37	Well B	2022	2037	2029,5	1987,95	-1922,95	Pimenteiras	Cuttings	LAMIR
38	Well B	2025	2028	2026,5	1961,50	-1919,00	Pimenteiras	Cuttings	CIG/UNPL
39	Well B	2040	2043	2041,5	1976,50	-1934,00	Pimenteiras	Cuttings	CIG/UNPL
40	Well B	2055	2058	2056,5	1991,50	-1948,00	Pimenteiras	Cuttings	CIG/UNPL
41	Well B	2064	2088	2076,0	2033,86	-1968,86	Pimenteiras	Cuttings	LAMIR
42	Well B	2070	2073	2071,5	2006,50	-1963,00	Pimenteiras	Cuttings	CIG/UNPL
43	Well B	2085	2088	2086,5	2021,50	-1978,00	Pimenteiras	Cuttings	CIG/UNPL
44	Well B	2100	2103	2101,5	2036,50	-1992,00	Pimenteiras	Cuttings	CIG/UNPL
45	Well B	2112	2127	2119,5	2076,02	-2011,02	Pimenteiras	Cuttings	LAMIR
46	Well B	2115	2118	2116,5	2051,50	-2007,00	Pimenteiras	Cuttings	CIG/UNPL
47	Well B	2130	2133	2131,5	2066,50	-2022,00	Pimenteiras	Cuttings	CIG/UNPL
48	Well B	2145	2148	2146,5	2081,50	-2037,00	Pimenteiras	Cuttings	CIG/UNPL
49	Well B	2160	2163	2161,5	2096,50	-2051,00	Pimenteiras	Cuttings	CIG/UNPL
50	Well B	2175	2178	2176,5	2111,50	-2066,00	Pimenteiras	Cuttings	CIG/UNPL
51	Well B	2190	2193	2191,5	2126,50	-2081,00	Pimenteiras	Cuttings	CIG/UNPL
52	Well B	2205	2208	2206,5	2141,50	-2095,00	Pimenteiras	Cuttings	CIG/UNPL
53	Well B	2220	2223	2221,5	2156,50	-2110,00	Pimenteiras	Cuttings	CIG/UNPL
54	Well B	2235	2238	2236,5	2171,50	-2125,00	Pimenteiras	Cuttings	CIG/UNPL
55	Well B	2238	2262	2250,0	2204,67	-2139,67	Pimenteiras	Cuttings	LAMIR
56	Well B	2250	2253	2251,5	2186,50	-2140,00	Pimenteiras	Cuttings	CIG/UNPL
57	Well B	2265	2268	2266,5	2201,50	-2154,00	Pimenteiras	Cuttings	CIG/UNPL
58	Well B	2280	2283	2281,5	2216,50	-2169,00	Pimenteiras	Cuttings	CIG/UNPL
59	Well B	2289	2292	2290,5	2225,50	-2178,00	Pimenteiras	Cuttings	CIG/UNPL
60	Well B	2319	2322	2320,5	2255,50	-2207,00	Pimenteiras	Cuttings	CIG/UNPL
61	Well B	2325	2328	2326,5	2261,50	-2213,00	Pimenteiras	Cuttings	CIG/UNPL
62	Well B	2340	2343	2341,5	2276,50	-2228,00	Pimenteiras	Cuttings	CIG/UNPL
63	Well B	2355	2358	2356,5	2291,50	-2243,00	Pimenteiras	Cuttings	CIG/UNPL
64	Well B	2370	2373	2371,5	2306,50	-2257,00	Itaim	Cuttings	CIG/UNPL
65	Well B	2385	2388	2386,5	2321,50	-2272,00	Itaim	Cuttings	CIG/UNPL
66	Well B	2388	2397	2392,5	2344,08	-2279,08	Itaim	Cuttings	LAMIR
67	Well B	2400	2403	2401,5	2336,50	-2287,00	Itaim	Cuttings	CIG/UNPL
68	Well B	2415	2418	2416,5	2351,50	-2302,00	Itaim	Cuttings	CIG/UNPL
69	Well B	2430	2433	2431,5	2366,50	-2316,00	Itaim	Cuttings	CIG/UNPL
70	Well B	2445	2448	2446,5	2381,50	-2331,00	Itaim	Cuttings	CIG/UNPL
1	Well C	1305	1314	1309,5	1242,50	-1242,50	Poti	Cuttings	CIG/UNPL
2	Well C	1323	1332	1327,5	1260,50	-1260,50	Poti	Cuttings	CIG/UNPL
3	Well C	1341	1350	1345,5	1278,50	-1278,50	Poti	Cuttings	CIG/UNPL
4	Well C	1359	1368	1363,5	1296,50	-1296,50	Poti	Cuttings	CIG/UNPL

5	Well C	1509	1512	1510,5	1443,50	-1443,50	Poti	Cuttings	CIG/UNPL
6	Well C	1524	1527	1525,5	1458,50	-1458,50	Poti	Cuttings	CIG/UNPL
7	Well C	1539	1542	1540,5	1473,50	-1473,50	Poti	Cuttings	CIG/UNPL
8	Well C	1554	1557	1555,5	1488,50	-1488,50	Poti	Cuttings	CIG/UNPL
9	Well C	1590	1593	1591,5	1524,50	-1524,50	Poti	Cuttings	CIG/UNPL
10	Well C	1605	1608	1606,5	1539,50	-1539,50	Longá	Cuttings	CIG/UNPL
11	Well C	1620	1623	1621,5	1554,50	-1554,50	Longá	Cuttings	CIG/UNPL
12	Well C	1635	1638	1636,5	1569,50	-1569,50	Longá	Cuttings	CIG/UNPL
13	Well C	1650	1653	1651,5	1584,50	-1584,50	Longá	Cuttings	CIG/UNPL
14	Well C	1665	1668	1666,5	1599,50	-1599,50	Longá	Cuttings	CIG/UNPL
15	Well C	1680	1683	1681,5	1614,50	-1614,50	Longá	Cuttings	CIG/UNPL
16	Well C	1695	1698	1696,5	1629,50	-1629,50	Cabeças	Cuttings	CIG/UNPL
17	Well C	1710	1713	1711,5	1644,50	-1644,50	Cabeças	Cuttings	CIG/UNPL
18	Well C	1725	1728	1726,5	1659,50	-1659,50	Cabeças	Cuttings	CIG/UNPL
19	Well C	1740	1743	1741,5	1674,50	-1674,50	Cabeças	Cuttings	CIG/UNPL
20	Well C	1755	1758	1756,5	1689,50	-1689,50	Cabeças	Cuttings	CIG/UNPL
21	Well C	1770	1773	1771,5	1704,50	-1704,50	Cabeças	Cuttings	CIG/UNPL
22	Well C	1785	1788	1786,5	1719,50	-1719,50	Cabeças	Cuttings	CIG/UNPL
23	Well C	1800	1803	1801,5	1734,50	-1734,50	Cabeças	Cuttings	CIG/UNPL
24	Well C	1815	1818	1816,5	1749,50	-1749,50	Cabeças	Cuttings	CIG/UNPL
25	Well C	1821	1821	1821,0	1754,00	-1748,00	Cabeças	SWC	LCV/Geolab Sur
26	Well C	1830	1833	1831,5	1764,50	-1764,50	Pimenteiras	Cuttings	CIG/UNPL
27	Well C	1845	1848	1846,5	1779,50	-1779,50	Pimenteiras	Cuttings	CIG/UNPL
28	Well C	1860	1863	1861,5	1794,50	-1794,50	Pimenteiras	Cuttings	CIG/UNPL
29	Well C	1866	1866	1866,0	1799,00	-1793,00	Pimenteiras	SWC	LCV/Geolab Sur
30	Well C	1875	1878	1876,5	1809,50	-1809,50	Pimenteiras	Cuttings	CIG/UNPL
31	Well C	1890	1893	1891,5	1824,50	-1824,50	Pimenteiras	Cuttings	CIG/UNPL
32	Well C	1908	1911	1909,5	1842,50	-1842,50	Pimenteiras	Cuttings	CIG/UNPL
33	Well C	1917	1917	1917,0	1850,00	-1844,00	Pimenteiras	SWC	LCV/Geolab Sur
34	Well C	1923	1926	1924,5	1857,50	-1857,50	Pimenteiras	Cuttings	CIG/UNPL
35	Well C	1938	1941	1939,5	1872,50	-1872,50	Pimenteiras	Cuttings	CIG/UNPL
36	Well C	1953	1956	1954,5	1887,50	-1887,50	Pimenteiras	Cuttings	CIG/UNPL
37	Well C	1962	1962	1962,0	1895,00	-1889,00	Pimenteiras	SWC	LCV/Geolab Sur
38	Well C	1968	1971	1969,5	1902,50	-1902,50	Pimenteiras	Cuttings	CIG/UNPL
39	Well C	1983	1986	1984,5	1917,50	-1917,50	Pimenteiras	Cuttings	CIG/UNPL
40	Well C	1998	2001	1999,5	1932,50	-1932,50	Pimenteiras	Cuttings	CIG/UNPL
41	Well C	2007	2007	2007,0	1940,00	-1934,00	Pimenteiras	SWC	LCV/Geolab Sur
42	Well C	2013	2016	2014,5	1947,50	-1947,50	Pimenteiras	Cuttings	CIG/UNPL
43	Well C	2022	2022	2022,0	1955,00	-1949,00	Pimenteiras	SWC	LCV/Geolab Sur
44	Well C	2025	2028	2026,5	1959,50	-1959,50	Pimenteiras	Cuttings	CIG/UNPL
45	Well C	2061	2064	2062,5	1995,50	-1995,50	Pimenteiras	Cuttings	CIG/UNPL
46	Well C	2076	2079	2077,5	2010,50	-2010,50	Pimenteiras	Cuttings	CIG/UNPL
47	Well C	2088	2088	2088,0	2021,00	-2015,00	Pimenteiras	SWC	LCV/Geolab Sur
48	Well C	2091	2094	2092,5	2025,50	-2025,50	Pimenteiras	Cuttings	CIG/UNPL
49	Well C	2106	2109	2107,5	2040,50	-2040,50	Pimenteiras	Cuttings	CIG/UNPL
50	Well C	2124	2127	2125,5	2058,50	-2058,50	Pimenteiras	Cuttings	CIG/UNPL
51	Well C	2133	2136	2134,5	2067,50	-2067,50	Pimenteiras	Cuttings	CIG/UNPL
52	Well C	2172	2175	2173,5	2106,50	-2106,50	Pimenteiras	Cuttings	CIG/UNPL
53	Well C	2175	2175	2175,0	2108,00	-2102,00	Pimenteiras	SWC	LCV/Geolab Sur
54	Well C	2184	2187	2185,5	2118,50	-2118,50	Pimenteiras	Cuttings	CIG/UNPL
55	Well C	2199	2202	2200,5	2133,50	-2133,50	Pimenteiras	Cuttings	CIG/UNPL
56	Well C	2214	2217	2215,5	2148,50	-2148,50	Pimenteiras	Cuttings	CIG/UNPL
57	Well C	2229	2232	2230,5	2163,50	-2163,50	Pimenteiras	Cuttings	CIG/UNPL
58	Well C	2232	2232	2232,0	2165,00	-2159,00	Pimenteiras	SWC	LCV/Geolab Sur
59	Well C	2244	2247	2245,5	2178,50	-2178,50	Pimenteiras	Cuttings	CIG/UNPL
60	Well C	2247	2247	2247,0	2180,00	-2174,00	Pimenteiras	SWC	LCV/Geolab Sur
61	Well C	2259	2262	2260,5	2193,50	-2193,50	Pimenteiras	Cuttings	CIG/UNPL
62	Well C	2259	2259	2259,0	2192,00	-2186,00	Pimenteiras	SWC	LCV/Geolab Sur
63	Well C	2280	2283	2281,5	2214,50	-2214,50	Pimenteiras	Cuttings	CIG/UNPL
64	Well C	2295	2298	2296,5	2229,50	-2229,50	Pimenteiras	Cuttings	CIG/UNPL
65	Well C	2301	2301	2301,0	2234,00	-2228,00	Pimenteiras	SWC	LCV/Geolab Sur
66	Well C	2310	2313	2311,5	2244,50	-2244,50	Pimenteiras	Cuttings	CIG/UNPL
67	Well C	2325	2328	2326,5	2259,50	-2259,50	Pimenteiras	Cuttings	CIG/UNPL
68	Well C	2337	2337	2337,0	2270,00	-2264,00	Pimenteiras	SWC	LCV/Geolab Sur
69	Well C	2340	2343	2341,5	2274,50	-2274,50	Pimenteiras	Cuttings	CIG/UNPL
70	Well C	2355	2358	2356,5	2289,50	-2289,50	Pimenteiras	Cuttings	CIG/UNPL
71	Well C	2364	2364	2364,0	2297,00	-2291,00	Pimenteiras	SWC	LCV/Geolab Sur

Table 2 – Samples used in the X-Ray diffraction analysis with indication of the depths, formation, source of samples and laboratories used in the study

The initial interpretation of diffractograms was performed using the software HighScore Plus@ from PanAnalytical, and the recognizing of Illite phase was performed initially using the four samples (whole rock powder, natural clay, glycolated and heated) following the workflow proposed by USGS (USGS Clay mineral identification flow diagram - Figure 36) where illite is characterized by a peak in 10Â in an air dried sample, with no changes in the glycolated and heated diffractograms. The measure of the full width at half maximum intensity (FWHM) was also measured in the 10Â peak, manually inserted, after automatic correction of background in the Higscore Plus@ software. After the initial screening of the presence of a 10A peak phase, the data files were exported to be processed into the DecompXR software.

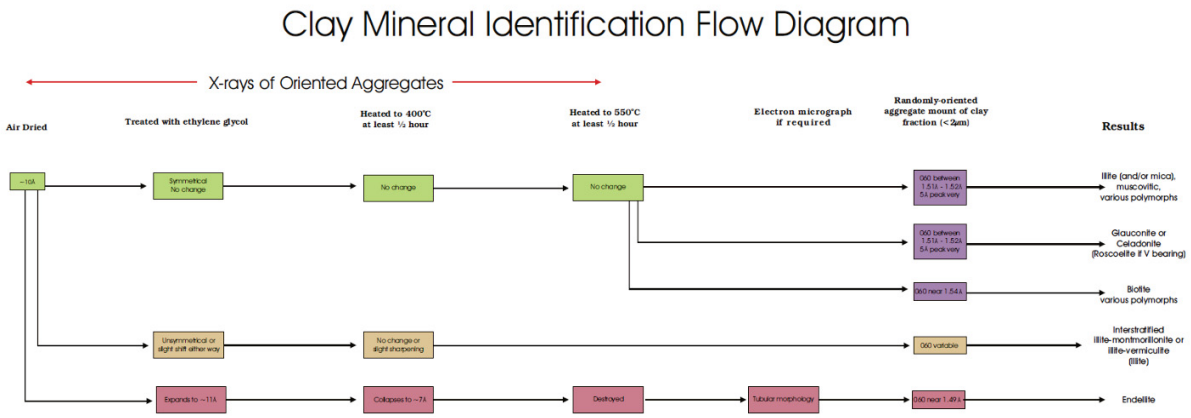

Figure 36 - USGS Clay mineral identification flow diagram for 10Â phase.

The conversion from measured illite crystallinity (FWHM) to percent of vitrinite reflectance %Ro using the exponential regression of the data presented by Frey and Robinson, (1999) and Mählmann and Frey, (2012), according to the Figure 31.

3.4. Spectral decomposition of illite peaks on XRD data

Spectral decomposition of the clay minerals was performed according to Lanson & Velte, (1992), Lanson (1997) and Lanson et al, (1998) procedures and was done in the reflection plane (d001) within the range of 3.5 to 10.5 °2θ CuKα; (25.2 to 8.2 Â).

The decomposed peaks (intensity, positions °2θ and FWHM) were calculated the software DecompXR (Beta Version 1.0.0.2) developed by Lanson (1997) using automatic fitting option and manually peak insertion and adjustment, especially in noisy samples. During the modeling and interpretation two main clay phases were considered: 1) Illite phases, near to 8,4 to 8,6 °2θ and, 2) muscovite or mica like phase (Lanson, 1997) near to 8,8 °2θ. In some samples a third and fourth phase was recognized near to 9,2 °2θ and was initially classified as Talc and chlorite, near to 6,2 °2θ (Figure 37).

The two main peaks, illite (authigenic formation, associated with metamorphism due to the magmatic intrusions) and detrital muscovite, associated with a previous phase of depositional micas, were studied and the FWHM was measured. The results of Kübler Index were firstly converted to equivalent in vitrinite (according to the regression established over the data presented by Mählmann and Frey (2012) and compared with measured vitrinite reflectance (%Ro) along the three wells. The KI and %Ro values were compared with modelled %Ro from 1D PSM model and were used to improve the thermal calibration of the models (Figure *38*). The full results of peak decomposition and the interpretation of the main clay mineral phases are presented in Appendix B.

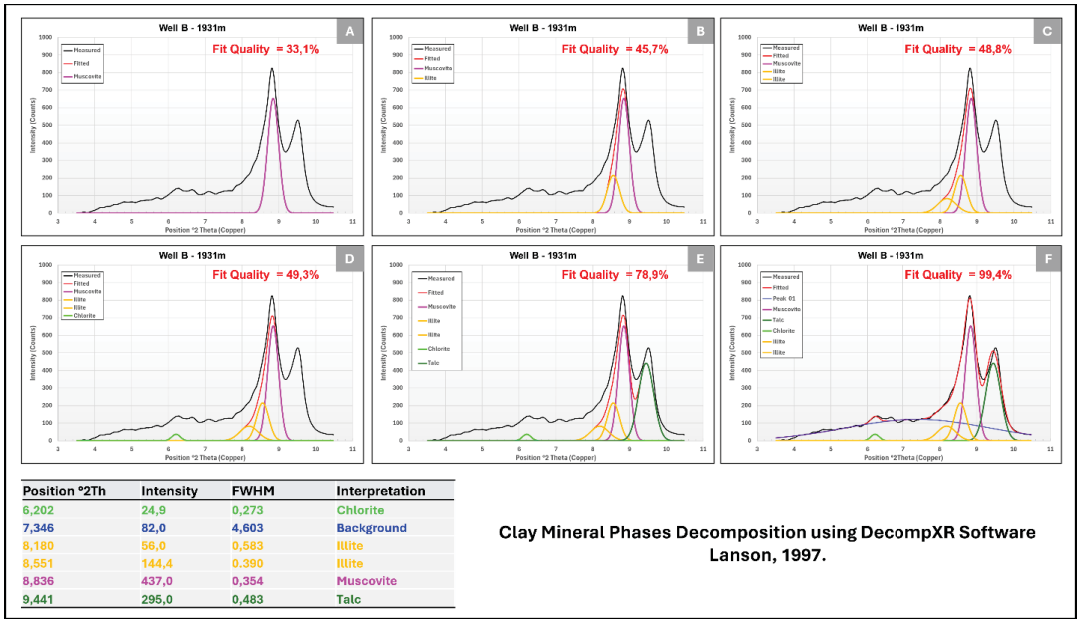

Figure 37 – Process of decomposition of X-Ray diffractogram into DecompXR software and interpretation of possible clay mineral phases. A) Mica-Like or Muscovite phase; B) and C) addition of Illite phases; D) Chlorite phase; E) Talc/Pyrophyllite and F) Final interpretation with insertion of a broad FWHM peak to correct background.

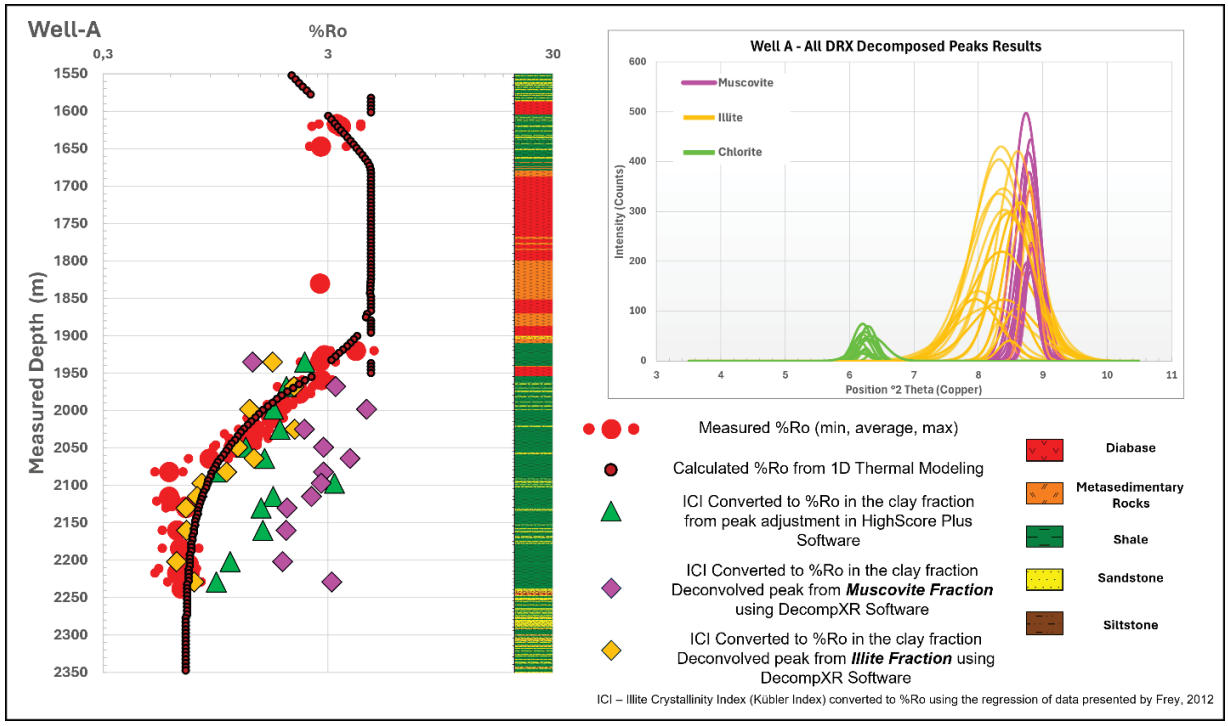

Figure 38 – Example of use of KI converted to %Ro and the comparison with measured %Ro along the interval of the Pimenteiras Formation at the well A, showing the preliminary results. Green triangles represent the first KI (converted to %Ro) measure at Highscore Plus Software@, the purple and yellow diamonds represent the KI (converted to %Ro) from decomposition at DecompRX software. The illite phase (yellow diamonds - authigenic formed) match with the measured vitrinite reflectance (red circles) while the detrital muscovite phases (purple diamonds) present a higher crystallinity. Conversion from KI to %Ro was performed using Mählmann and Frey (2012).

3.5. Petroleum systems modeling

The dataset of petroleum system modeling built for this work comprises (Figure 32):

- Two sets of three-dimensional models (3D PSM) in the northern part of the Parnaíba Basin.
- One set of two-dimensional model (2D PSM) along a E-W cross line in the central/north part of the basin.
- Three sets of one-dimensional (1D PSM) inside of the 3D models.

The 3D PSM models incorporates the 3D geological model (structural and stratigraphic framework), where a detailed seismic interpretation of the Meso

Devonian/Eo-Carboniferous sequence (from Cabeças to Itaim formations) was performed and a focused interpretation of the diabase sills in 2D seismic lines was integrated with impedance data from wells and seismic to propagate the 2D interpretation into the 3D geological models. It resulted in two 3D geological models, the first one, in the north part of the Figure 32 (3D PSM Model 01) and the second one (3D PSM Model 02) located in the south, both in the central part of the Parnaíba basin. The Figure 39 illustrates some of the steps in the workflow used to build the 3D models. These two models were converted into 3D PSM models and filled with the facies, reservoir, and source rock properties, already incorporating the new compositional kinetic parameters defined for the Pimenteiras Formation.

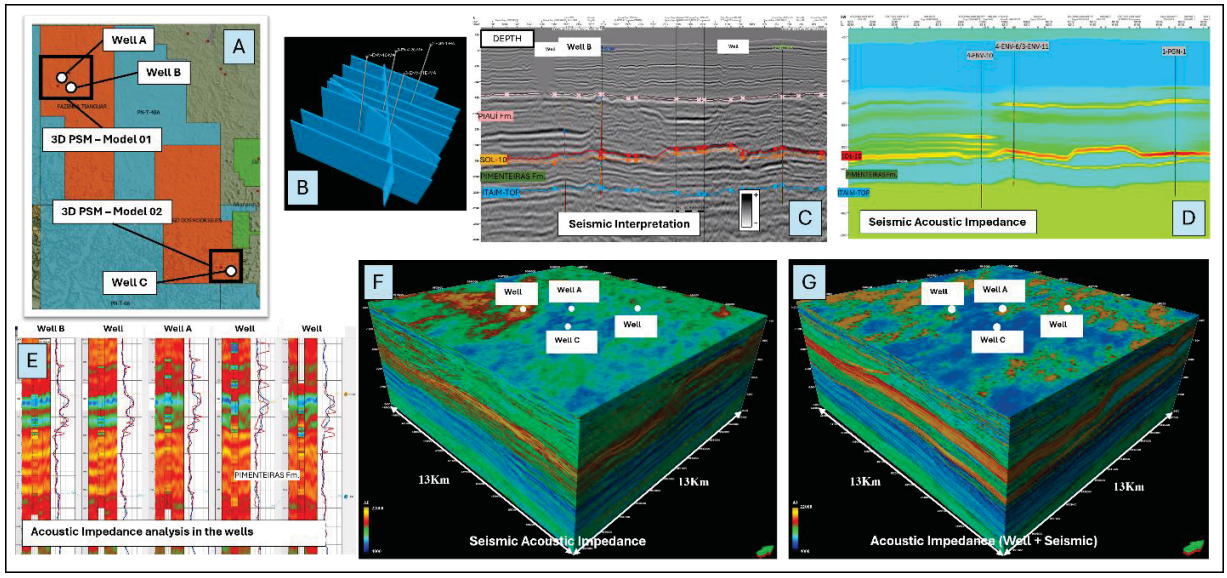

Figure 39 – Workflow of 3D Model Construction. A) Location of the two three-dimensional models and the 1D PSM models; B) seismic coverage at the 3D PSM Model 01; C) Example of a 2D seismic interpretation; D) Seismic acoustic impedance; E) Acoustic impedance from well analysis; F) Seismic acoustic impedance populated into the 3D geological model and G) Acoustic impedance into the 3D model from seismic plus well analysis

. The 2D PSM model consist in a E-W 2D depth seismic line, with 186 km, covering 2 distinct domains in the basin, the west part, where there is a decrease in the number and thickness of diabase sill intruded into the Pimenteiras formation and upper units and the east portion of the central part of the basin, with massive intrusion along Pimenteiras, Cabeças and Poti formations (Figure 40). The 2D section extends eastward near to the

main gas discoveries in the basin, the Parque dos Gaviões (Park of Hawks) cluster, encompassing 13 gas fields and more than 40 billion cubic meters of accumulated gas (already produced + certified reserves).

Additionally, three 1D PSM models were performed to provide thermal data for vitrinite (%Ro – Easy Ro Model - Sweeney and Burnham., 1990), smectite/illite ratio (Pytte and Reynolds, 1988) for comparison with the Kübler Index from DRX analysis (location of the 1D PSM models in the Figure 32). The one-dimensional models were built using detailed information from stratigraphy, including the well tops as well as all diabase sill intrusions interpreted by the drilling as shown in the Table 3, with the information from Well A model. The ages of the units and the main hiatus in the basin were incorporated according to the stratigraphic chart presented in Figure 4. These 1D model, were lately used to compare the results of modelled vitrinite reflectance with measurements of vitrinite reflectance and KI-Illite values converted to vitrinite reflectance.

Figure 41 show the example of Well A PSM model, with the results and calibration of temperature at the present-day and the burial history curves showing the evolution of temperature and calculated vitrinite reflectance over time.

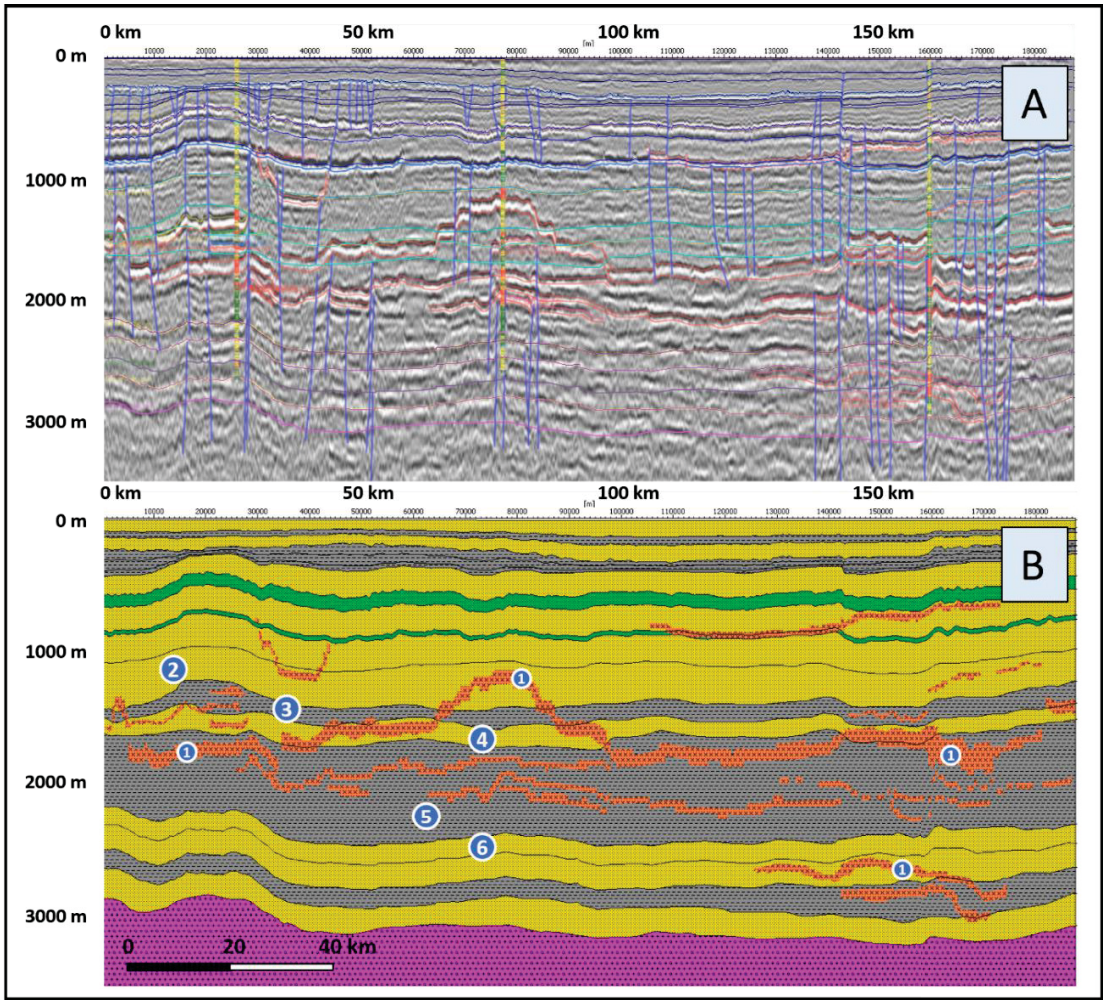

Figure 40 - 2D PSM Model. A) Depth converted seismic section (E-W Direction) with the interpretation of main horizons and faults; B) Petromod 2D PSM Model highlighting the Meso-Devonian/Eo Carboniferous sequence and the atypical petroleum system: 1) Diabase intrusive sill; 2) Poti Formation; 3) Longá Formation; 4) Cabeças Formation, 5) Pimenteiras Formation and 6) Itaim Formation.

Well A					
Age (Ma)	**Well Top/Horizon**	**Depth (TVDSS)**	**Thickness**	**Event Type**	**Layer Name**
0	HIA_RECENTE	-76	0	Hiatus	HIA_RECENTE
80	ITP	-76	130	Deposition	ITA
110	COD	54	226	Deposition	COD
115	COR	280	8	Deposition	COR
125	HIA_PSB	288	0	Hiatus	HIA_PSB
155	PSB	288	80	Deposition	PSB
200	HIA_SAM	368	0	Hiatus	HIA_SAM
220	SAM	368	58	Deposition	SAM
245	MOT	426	24	Deposition	MOT
260	PEF_01	450	244	Deposition	PEF_01
	SOL_PEF	694	5	Intrusion	SOL_PEF
280	PEF_02	699	41	Deposition	PEF_02
300	PIA_01	740	76	Deposition	PIA_01
	SOL_PIA	816	50	Intrusion	SOL_PIA
308	PIA_02	866	153	Deposition	PIA_02
315	HIA_POT	1019	0	Hiatus	HIA_POT
330	POT_01	1019	38	Deposition	POT_01
	SOL_POT	1057	10	Intrusion	SOL_POT
339	POT_02	1067	232	Deposition	POT_02
345	LON	1299	106	Deposition	LON
	SOL_LON	1405	16	Intrusion	SOL_LON
360	CAB_01	1421	85	Deposition	CAB_01
	SOL_CAB	1506	19	Intrusion	SOL_CAB
365	CAB_02	1525	5	Deposition	CAB_02
370	PIM_01	1530	76	Deposition	PIM_01
	SOL_PIM_01	1606	112	Intrusion	SOL_PIM_01
374	PIM_02	1718	53	Deposition	PIM_02
	SOL_PIM_02	1771	19	Intrusion	SOL_PIM_02
377	PIM_03	1790	13	Deposition	PIM_03
	SOL_PIM_03	1803	16	Intrusion	SOL_PIM_03
379	PIM_04	1819	41	Deposition	PIM_04
	SOL_PIM_04	1860	13	Intrusion	SOL_PIM_04
383	PIM_05	1873	287	Deposition	PIM_05
390	ITM	2160	140	Deposition	ITM
405	JAI	2300	150	Deposition	JAI
430	TIA	2450	250	Deposition	TIA
438	IPU	2700	100	Deposition	IPU
450	HIA_BAS	2800	0	Hiatus	HIA_BAS
550	BAS	2800	500	Deposition	BASEMENT
Total Sill Thickeness (m) (PIM Formation)			**160**		
Total Sill Thickeness (m)			**260**		

Table 3 - Example of input table of 1D PSM model (Well A) with the well tops/horizons, stratigraphic ages, depth, and thickness. The event type discriminates against Deposition, Hiatus and Intrusions. The total intrusive thickness in this well is 260 m.

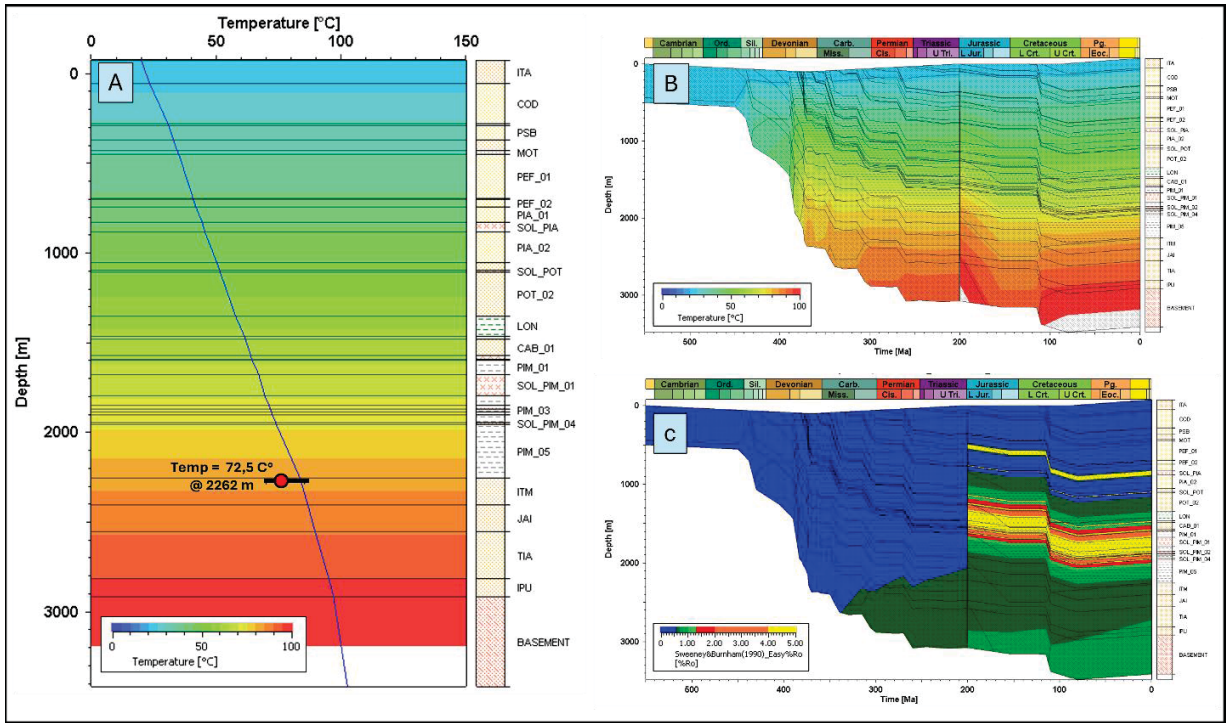

Figure 41 – 1D PSM Model (Well A) showing the present-day temperature, calibrated with bottom hole temperature data (A), and the burial history graphs for temperature (B) and vitrinite reflectance (C), using the Sweeney and Burnham (1990) model.

4. RESULTS

4.1. Vitrinite Reflectance Analysis

A total of 54 samples (29 samples at Well A, 14 samples at Well B and 11 samples at Well C) were analyzed for vitrinite reflectance index, organic petrography and visual analysis of the kerogens and the results are presented in Table 4.

Figure 42 shows some examples of high-quality samples from Well A (1968m) and Well C (1917m) each with approximately 30 measures and a reasonable concentration of measurements near the average values. The Figure 43 highlights the scattering of the reflectance values in some of the measures, with a high dispersion of minimum and maximum in two samples, at Well B (2061m, 11 measures) and Well A (2064m, five measurements).

The results of vitrinite reflectance were incorporated into the Petromod@ and used as primary input for thermal calibration and the comparison with the results of illite crystallinity, discussed in the results chapter.

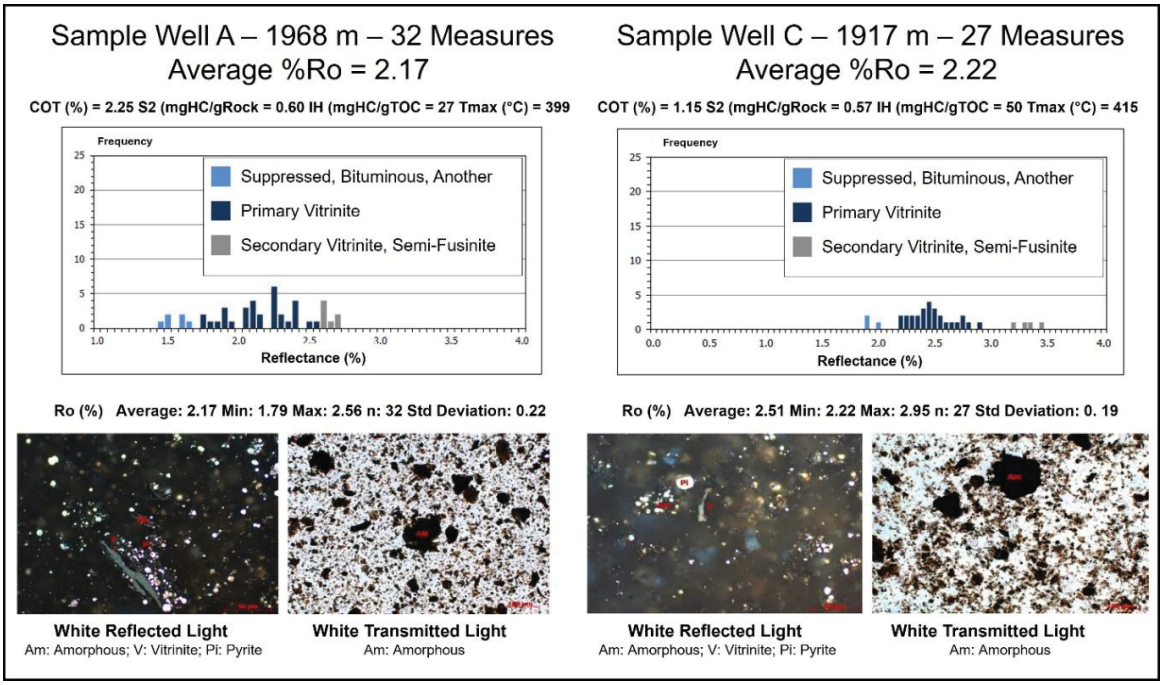

Figure 42 – Examples of vitrinite reflectance measurements procedure in two good quality samples. In the left, Well A at 1968 m, with 32 measures of primary vitrinite: In the right, Well C, 1917 m, with 27 measures of primary vitrinite.

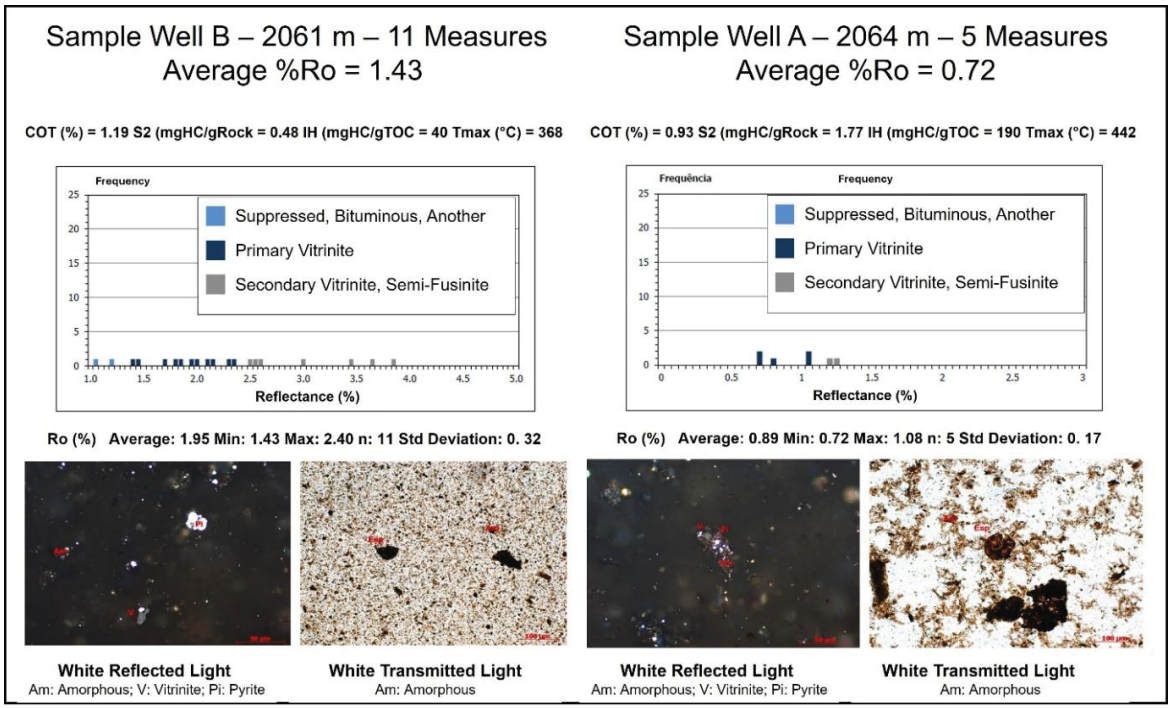

Figure 43 - Examples of vitrinite reflectance measurements procedure in two low quality samples. In the left, Well B at 2061 m, with 11 measures of primary vitrinite with high dispersion in the values: In the right, Well A, 2064 m, with five measures of primary vitrinite, showing the challenge in finding good quality measurements in some of the samples.

Well	Source	Depth (m)	%Ro	%Ro Min	%Ro Max	n	Std Dev.	Conf.	Amorphous		Liptinite						Vitr.	Inert.	Bit.	Contam.
									Fluor.	No Fluor.	Alg.	Esp.	Res.	Cut.	Liptdr.	Other				
Well A	Cu	1617	**3.28**	2.73	4.19	10	0.44	Low	Tr	90	-	-	-	-	Tr?	-	Tr	Tr	10	-
Well A	Cu	1620	**3.42**	2.54	4.20	12	0.48	Low	Tr	90	-	-	-	-	-	-	Tr	Tr	10	-
Well A	Cu	1647	**2.78**	2.48	3.62	9	0.34	Low	10	80	-	-	-	-	-	-	Tr	Tr	10	-
Well A	Cu	1830	**2.76**	2.75	2.77	2	0.02	Very Low	Tr	100	-	-	-	-	-	-	Tr	Tr	-	-
Well A	Cu	1920	**3.99**	3.07	4.80	3	0.87	Very Low	Tr	100	-	-	-	-	Tr?	-	Tr	Tr	-	-
Well A	Cu	1926	**2.89**	2.68	3.24	3	0.31	Very Low	Tr	100	-	-	-	-	-	-	Tr	Tr	-	-
Well A	Cu	1935	**2.76**	2.26	3.24	4	0.44	Very Low	100	Tr	-	-	-	-	-	-	Tr	Tr	Tr	-
Well A	Cu	1959	**2.80**	2.31	3.13	11	0.29	Low	100	Tr	-	-	-	-	-	-	Tr	Tr	Tr	-
Well A	Cu	1968	**2.17**	1.79	2.56	32	0.22	Medium	100	Tr	-	-	-	-	-	-	Tr	Tr	Tr	-
Well A	Cu	1977	**2.24**	1.88	2.51	33	0.18	Medium	95	Tr	-	-	-	-	-	-	5	Tr	-	-
Well A	Cu	1992	**1.88**	1.61	2.09	37	0.13	Medium	95	Tr	-	Tr	-	-	Tr	-	5	Tr	Tr	-
Well A	Cu	2010	**1.68**	1.31	1.90	35	0.16	Medium	100	Tr	-	Tr	-	-	Tr	-	Tr	Tr	Tr	-
Well A	Cu	2025	**1.42**	1.20	1.64	35	0.14	Medium	95	Tr	-	Tr	-	-	Tr	-	5	Tr	Tr	-
Well A	Cu	2031	**1.31**	1.04	1.59	20	0.18	Low	100	Tr	-	Tr	-	-	Tr	-	Tr	Tr	-	-
Well A	Cu	2037	**1.38**	1.09	1.63	38	0.13	Medium	100	Tr	-	Tr	-	-	Tr	-	Tr	Tr	-	-
Well A	Cu	2046	**1.24**	0.95	1.45	20	0.16	Low	100	Tr	-	Tr	-	-	Tr	-	Tr	Tr	-	-
Well A	Cu	2049	**1.14**	0.93	1.35	16	0.15	Med-Low	100	Tr	-	Tr	-	-	Tr	-	Tr	Tr	-	-
Well A	Cu	2064	**0.89**	0.72	1.08	5	0.17	Low	100	Tr	-	Tr	-	-	Tr	-	Tr	Tr	-	-
Well A	Cu	2082	**0.59**	0.51	0.68	11	0.06	Low	90	Tr	Tr	5	-	Tr	5	-	Tr	Tr	-	-
Well A	Cu	2115	**0.59**	0.57	0.59	3	0.01	Low	85	Tr	Tr	10	-	Tr	5	-	Tr	Tr	-	-
Well A	Cu	2121	**0.60**	0.52	0.69	7	0.06	Low	80	Tr	Tr	15	-	Tr	5	-	Tr	Tr	-	-
Well A	Cu	2130	**0.70**	0.57	0.79	27	0.06	Medium	85	Tr	Tr	10	-	Tr	5	-	Tr	Tr	-	-
Well A	Cu	2160	**0.64**	0.55	0.75	13	0.07	Medium	65	Tr	5	10	-	Tr	10	-	Tr	Tr	-	10
Well A	Cu	2184	**0.66**	0.55	0.80	20	0.08	Med-Low	65	Tr	10	10	-	Tr	10	-	Tr	Tr	-	5
Well A	Cu	2205	**0.72**	0.72	0.72	1	-	Med-Low	40	Tr	20	20	-	Tr	20	-	Tr	Tr	-	Tr
Well A	Cu	2211	**0.67**	0.53	0.78	12	0.09	Med-Low	55	Tr	15	15	-	Tr	15	-	Tr	Tr	-	Tr
Well A	Cu	2217	**0.64**	0.51	0.77	9	0.10	Med-Low	75	Tr	5	5	-	Tr	10	-	Tr	Tr	-	tr
Well A	Cu	2229	**0.68**	0.58	0.82	23	0.07	Med-High	90	Tr	5	5	-	Tr	5	-	Tr	Tr	-	-
Well A	Cu	2238	**0.67**	0.67	0.67	1	-	Med-Low	60	Tr	10	15	-	Tr	15	-	Tr	Tr	-	-
Well B	Cu	1665	**2.63**	1.97	3.29	11	0.49	Low	20	80	-	-	-	-	Tr?	-	Tr	Tr	-	-
Well B	Cu	1827	**2.83**	2.27	3.74	3	0.80	Very Low	20	80	-	-	-	-	-	-	Tr	Tr	-	Tr
Well B	Cu	1971	**2.66**	2.66	2.66	1	--	Very Low	Tr	100	-	-	-	-	-	-	Tr	Tr	-	Tr
Well B	Cu	1998	**2.04**	1.76	2.44	3	0.35	Very Low	10	90	-	-	-	-	Tr	-	Tr	Tr	-	-
Well B	Cu	2001	**2.26**	1.57	2.83	12	0.36	Low	30	70	-	-	-	-	-	-	Tr	Tr	-	-
Well B	Cu	2019	**2.14**	1.93	2.33	12	0.11	Low	30	70	-	-	-	-	-	-	Tr	Tr	-	-
Well B	Cu	2061	**1.95**	1.43	2.4	11	0.32	Low	40	60	-	-	-	-	Tr	-	Tr	Tr	-	-
Well B	Cu	2121	**1.12**	1.06	1.19	4	0.05	Low	100	Tr	-	Tr	-	-	Tr	-	Tr	Tr	-	-
Well B	Cu	2202	**0.84**	0.84	0.84	1	--	Low	100	Tr	-	Tr	-	-	Tr	-	Tr	Tr	-	-
Well B	Cu	2259	**0.56**	0.53	0.59	2	0.04	Low	75	Tr	5	10	-	-	10	-	Tr	Tr	-	-
Well B	Cu	2274	**0.67**	0.63	0.72	5	0.03	Low	80	Tr	Tr	10	-	-	10	-	Tr	Tr	-	-
Well C	Cu	1821	**1.47**	0.98	1.92	31	0.26	Medium	100	Tr	-	Tr?	-	-	Tr?	-	Tr	Tr	-	-
Well C	Cu	1886	**1.61**	1.13	1.93	34	0.20	Medium	100	Tr	-	Tr?	-	-	Tr?	-	Tr	Tr	-	-
Well C	Cu	1917	**2.51**	2.22	2.95	27	0.19	Medium	100	Tr	-	Tr?	-	-	Tr?	-	Tr	Tr	-	-
Well C	Cu	1962	**2.10**	1.59	2.49	29	0.29	Medium	100	Tr	-	Tr?	-	-	Tr?	-	Tr	Tr	Tr	-
Well C	Cu	2007	**2.30**	2.15	2.45	4	0.13	Very Low	50	50	-	-	-	-	Tr?	-	Tr	Tr	Tr?	-
Well C	Cu	2022	**2.26**	2.07	2.43	4	0.19	Very Low	50	50	-	-	-	-	-	-	Tr	Tr	Tr?	-
Well C	Cu	2088	**2.26**	1.97	2.68	6	0.26	Very Low	20	80	-	-	-	-	-	-	Tr	Tr	Tr?	-
Well C	Cu	2175	**2.61**	1.87	2.98	12	0.37	Low	20	80	-	-	-	-	-	-	Tr	Tr	-	-
Well C	Cu	2232	**2.17**	1.74	2.50	6	0.31	Low	70	30	-	-	-	-	-	-	Tr	Tr	-	Tr?
Well C	Cu	2247	**2.17**	1.47	2.46	6	0.38	Low	70	30	-	-	-	-	-	-	Tr	Tr	Tr	-
Well C	Cu	2259	**3.08**	2.79	3.37	2	0.41	Very Low	10	90	-	-	-	-	-	-	Tr	Tr	Tr	-
Well C	Cu	2301	**3.58**	3.03	3.94	4	0.39	Very Low	10	90	-	-	-	-	-	-	Tr	Tr	Tr	-
Well C	Cu	2337	**2.40**	2.40	2.40	1	-	Very Low	Tr	100	-	-	-	-	-	-	Tr	Tr	Tr	-
Well C	Cu	2364	**2.57**	2.39	2.76	2	0.26	Very Low	Tr	100	-	-	-	-	-	-	Tr	Tr	-	-

Table 4 – Measured values of vitrinite reflectance (%Ro, %Ro Min and %Ro Max) and visual analysis of kerogen in 54 samples at the wells A, B and C. Alg. = Alginite; Esp. = Esporinite; Res. = Resinite; Cut. = Cutinite; Liptdr. = Liptodetrinite; Vitr. = Vitrinite; Inert. = Inertinite; Bit. – Bitumen and Cont. = Contaminants

After an initial screening of thermal maturation in the sample selection, the 2D PSM model was carried out to validate the thermal scenario using the initial geochemical data such as pyrolysis, vitrinite, graptolite, and bitumen reflectance. The Figure 44 encompasses the integration of 2D PSM model and geochemical/maturity screening for the selection of the two Samples for Phase Kinetics analysis.

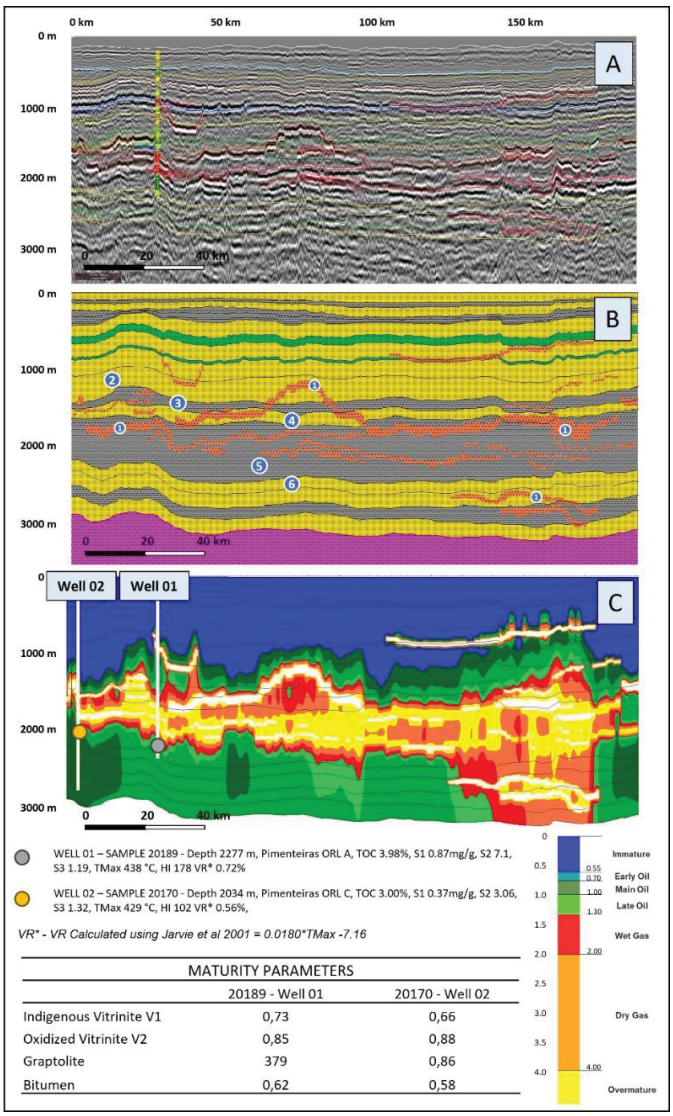

MATURITY PARAMETERS		
	20189 - Well 01	20170 - Well 02
Indigenous Vitrinite V1	0,73	0,66
Oxidized Vitrinite V2	0,85	0,88
Graptolite	379	0,86
Bitumen	0,62	0,58

Figure 44 2D PSM Model. (A) Depth converted seismic section (E-W Direction) with the interpretation of main horizons and faults; (B) Petromod 2D PSM Model highlighting the Meso-Devonian/Eo Carboniferous sequence and the atypical petroleum system: 1) Diabase intrusive sill; 2) Poti Formation; 3) Longá Formation; 4) Cabeças Formation, 5) Pimenteiras Formation and 6) Itaim Formation. (C) Calculated Vitrinite reflectance along the 2D Model, indicating the position of the wells 01 and 02 and the samples 20170 and 20189, with the geochemical and maturity parameters used to selection for phase kinetics. VR* values were initially calculated using TMax Jarvie et al. (2001) and later were compared with vitrinite, grapholite and bitumen reflectance.

4.2. Organofacies, Compositional Kinetics and Phase Behavior Results

The analytical results (and later implementation of the analyzed kinetical scheme inside of the Petromod calculator) was done by the compilation of laboratory tables of energy of activation versus the percentage of a given component, as exemplified in Table 5 and Table *6*, respectively. The black oil, oil and gas, four compounds and fourteen compounds kinetic parameters for organic-rich levels A (Sample 20189, well B at 2,277m) and C (Sample 20170, well D at 2,034 m), is shown graphically in Figure 45 and Figure 46.

Well	Sample	kcal/mol	C1	C2-5	C6-14	C15+
Well 01	20189	45	0,00	0,00	0,00	0,00
Well 01	20189	46	0,00	0,00	0,00	0,00
Well 01	20189	47	0,00	0,00	0,00	0,00
Well 01	20189	48	0,00	0,00	0,00	0,00
Well 01	20189	49	0,00	0,00	0,00	0,00
Well 01	20189	50	0,00	0,00	0,00	0,00
Well 01	20189	51	0,00	0,00	0,00	0,00
Well 01	20189	52	100,00	100,00	100,00	100,00
Well 01	20189	53	0,00	0,00	0,00	0,00
Well 01	20189	54	0,00	0,00	0,00	0,00
Well 01	20189	55	0,00	0,00	0,00	0,00
Well 01	20189	56	0,00	0,00	0,00	0,00
Well 01	20189	57	0,00	0,00	0,00	0,00
Well 01	20189	58	0,00	0,00	0,00	0,00
Well 01	20189	59	0,00	0,00	0,00	0,00
Well 01	20189	60	0,00	0,00	0,00	0,00
Well 01	20189	61	0,00	0,00	0,00	0,00
Well 01	20189	62	0,00	0,00	0,00	0,00
Well 01	20189	63	0,00	0,00	0,00	0,00
Well 01	20189	64	0,00	0,00	0,00	0,00
Well 01	20189	65	0,00	0,00	0,00	0,00
Well 01	20189	66	0,00	0,00	0,00	0,00
Well 01	20189	67	0,00	0,00	0,00	0,00
Well 01	20189	68	0,00	0,00	0,00	0,00
Potential (%)			**9,19**	**14,97**	**28,95**	**46,90**

Table 5 - Four components compositional scheme table for the sample 20189, from the Pimenteiras formation source rock interval A in Well 01, at 2277 m showing the energy of activation values in kcal/mol versus the percentual amount of each compound.

Well	Sample	kcal/mol	C1	C2-5	C6-14	C15+
Well 02	20170	45	0,00	0,00	0,00	0,00
Well 02	20170	46	0,00	0,00	0,00	0,00
Well 02	20170	47	0,04	0,09	0,12	1,12
Well 02	20170	48	0,16	0,33	0,45	4,31
Well 02	20170	49	0,23	0,48	0,66	6,27
Well 02	20170	50	0,42	0,87	1,21	11,47
Well 02	20170	51	0,49	1,02	1,42	13,48
Well 02	20170	52	5,13	7,01	7,06	7,31
Well 02	20170	53	0,00	0,00	0,00	0,00
Well 02	20170	54	0,00	0,00	0,00	0,00
Well 02	20170	55	55,29	73,60	71,48	55,96
Well 02	20170	56	5,64	4,91	4,30	0,07
Well 02	20170	57	25,99	9,32	10,59	0,00
Well 02	20170	58	0,94	0,34	0,38	0,00
Well 02	20170	59	3,73	1,34	1,52	0,00
Well 02	20170	60	0,00	0,00	0,00	0,00
Well 02	20170	61	0,00	0,00	0,00	0,00
Well 02	20170	62	1,95	0,70	0,79	0,00
Well 02	20170	63	0,00	0,00	0,00	0,00
Well 02	20170	64	0,00	0,00	0,00	0,00
Well 02	20170	65	0,00	0,00	0,00	0,00
Well 02	20170	66	0,00	0,00	0,00	0,00
Well 02	20170	67	0,00	0,00	0,00	0,00
Well 02	20170	68	0,00	0,00	0,00	0,00
Potential (%)			**13,95**	**16,42**	**55,92**	**13,71**

Table 6 - Four components compositional scheme table for the sample 20170, from the Pimenteiras formation source rock interval C in Well 02, at 2034 m showing the energy of activation values in kcal/mol versus the percentual amount of each compound.

The analysis of kinetics of the Pimenteiras Formation ORL A at Well B and ORL C at Well D led to some important achievements in understanding the process of transformation of the Type II marine kerogen in petroleum. Optical microscopy of source rock organic matter revealed that the Alginite is an important part of the maceral assemblage with a significant contribution of amorphous organic matter and traces of vitrinite (Mahlstedt and Horsfield, 2023). Pyrolysate composition is indicative of marine algal material, especially the smooth decrease of concentrations of straight alkyl-chain homologues with increasing carbon-atom number and the absence of maxima in the wax-region, characteristic of selectively preserved lacustrine algal material (Figure 47), Horsfield (1989a, 1990).

Organic matter dominated by selectively preserved algal material comprises homogeneous kerogen usually characterized by very narrow activation energy (Ea) distributions with a single dominant generation potential between 50 and 55 kcal/mol (Figure 47 B), (Mahlstedt and Horsfield, 2023). Thus, hydrocarbons generation from Pimenteiras SR Level C (sample 20170) can be described by a single Ea at 52 kcal/mol responsible for 100% of the bulk kerogen-to-petroleum-conversion reaction, in contrast, the Pimenteiras SR Level A (sample 20189) has one dominant Ea centered at 55 kcal/mol which accounts for “only” ~70% of the bulk reaction leaving potential for minor Ea´s distributed between 50 and 60 kcal/mol (Figure 48).

A comparison of the transformation ratio rate versus temperature curves for the Pimenteiras samples and Woodford Shales (Devonian from the USA and Canada) is shown in Figure 48. The kinetics of the Pimenteiras samples are generally slower than those of the classical Type II marine kinetic scheme available in commercial packages. The temperatures required for the onset and end of hydrocarbon generation (indicated by the temperature at 10% and 90% of TR respectively) in the samples of the Pimenteiras range from 120-140°C and 140-170°C, respectively, while the Woodford shale generates petroleum (10-90% TR) over a broader temperature interval of 60°C between 100 and 160°C (Figure 48).

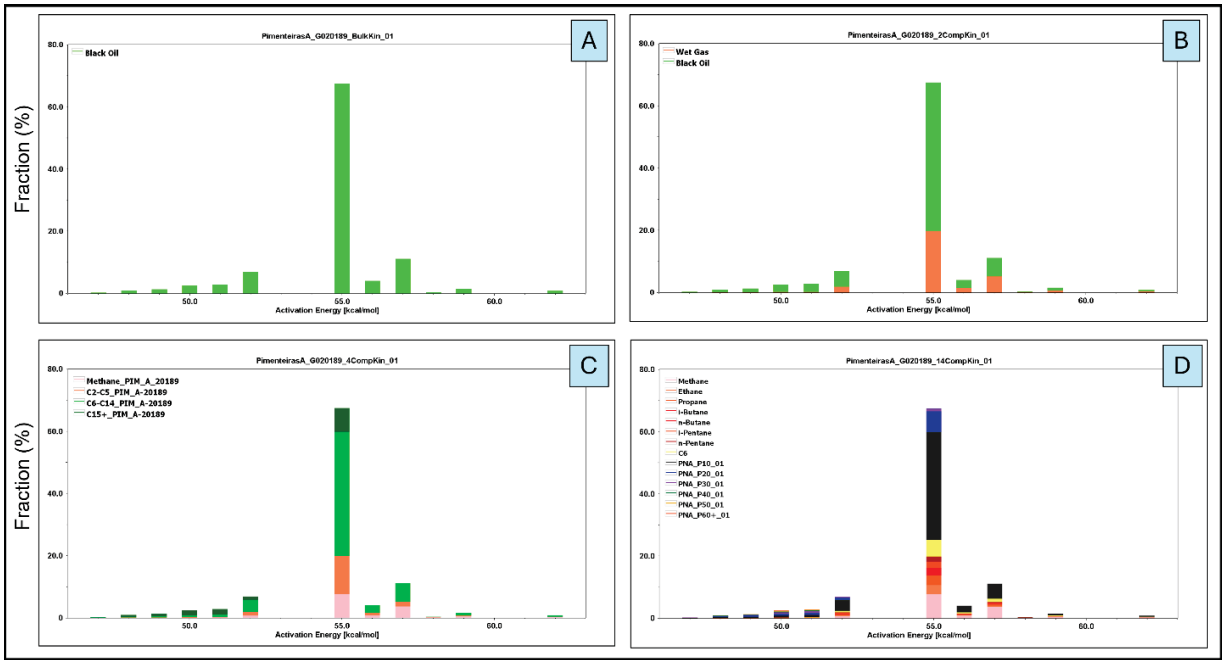

Figure 45 – Compositional scheme for the black oil (A), two components (B), four components (C) and fourteen components (D) for the sample 20189, from the Pimenteiras Formation source rock interval A in Well B, at 2277 m.

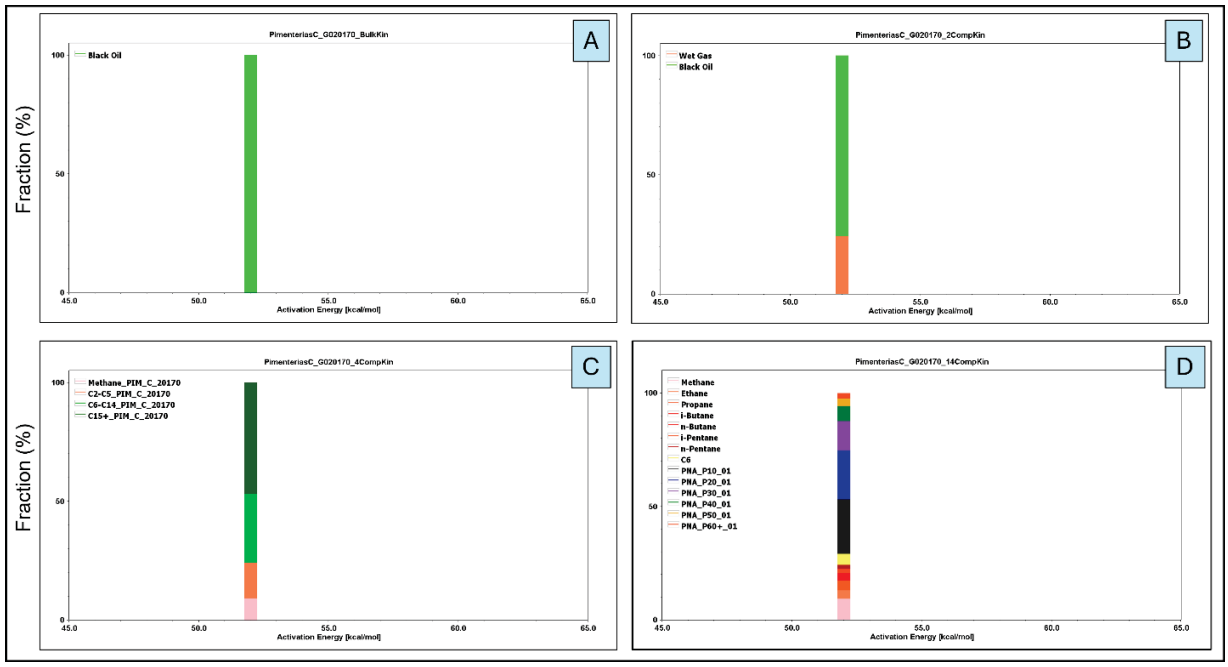

Figure 46 – Compositional scheme for the black oil (A), two components (B), four components (C) and fourteen components (D) for the sample 20170, from the Pimenteiras Formation source rock interval C in Well D, at 2034 m.

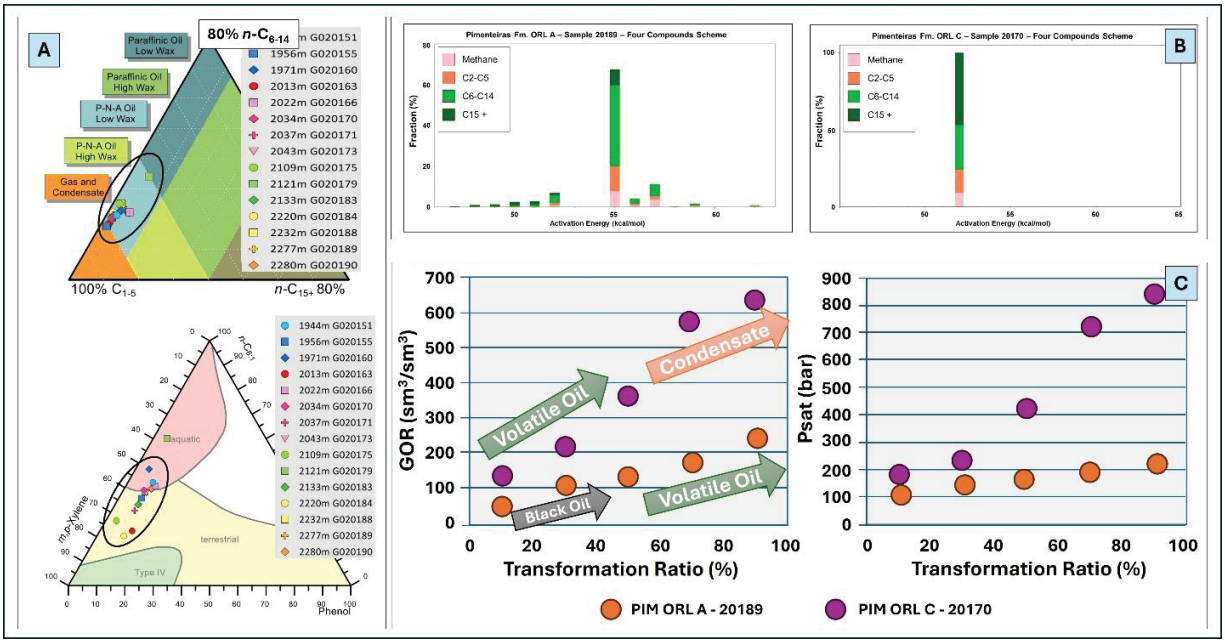

Figure 47 - Organofacies, kinetics and phase behavior for samples 20189 (ORL A – Well B) and 20170 (ORL C – Well D) showing the petroleum type of samples into the gas/condensate field (A – Horsfield (1989a)), the narrow distribution of activation energies for samples 20189 and 20170, between 50 to 60 kcal/mol (B), and the impact of these petroleum type and kinetic parameters on phase composition (C).

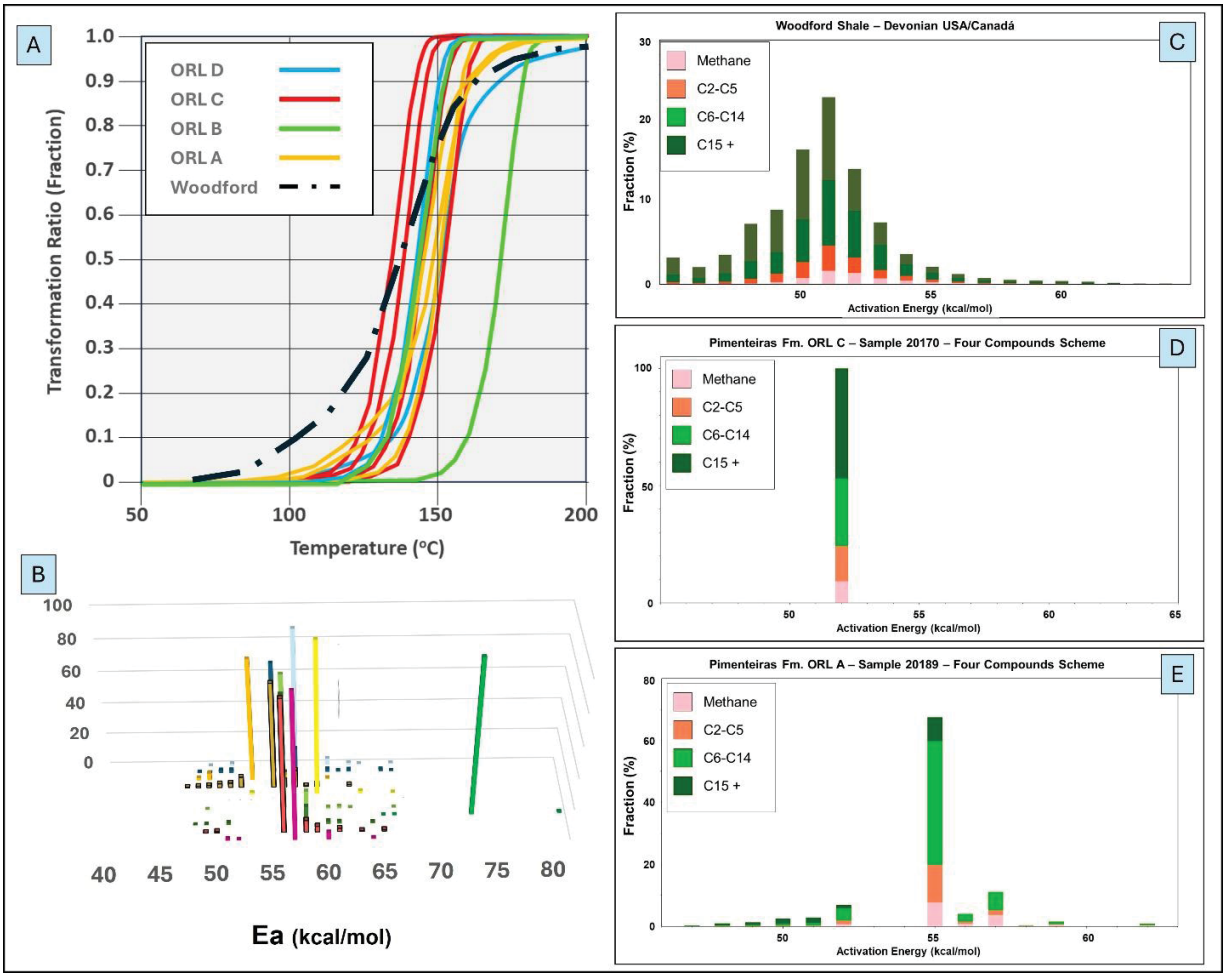

Figure 48 Kinetic Results A) Comparison of transformation ratio curves between the Pimenteiras Formation and Woodford Shale, calculating using heating rates of 3k/My (Devonian from USA/Canada – Hantschel and Kauerauf 2009). B) Bulk kinetic curves for several samples from Pimenteiras Formation showing a narrow interval of activation energies (between 55 to 60 kcal/mol); Comparison of four compounds kinetic schemes for: C) Woodford Shale; D) Pimenteiras level C; and E) Pimenteiras level A.

4.3. XRD Analysis, Kubler Index and Esquevin Index Results

The results of the analysis of XRD data, focusing on the recognizing of Illite and Muscovite phases in the natural clay faction, and the measurement of the FWHM, or Kubler Index at the 10Â peaks of decomposed diffractogram are presented in the Table 7. The results of calculation of the equivalent of vitrinite reflectance (%Ro) using the equations presented in the Figure 31 is presented to both mineral phases.

The Table 7 also presents the values of measurements of the intensity of illite/muscovite peaks on the crystallographic planes *d*001 and *d*002 of the Smectite/Illite/Muscovite, respectively the peaks at 10Â and 5Â in the clay fraction diffractogram. Finally, the calculated results of the Esquevin index are also presented in the table below.

#	Well	Av.Depth (MD)	Formation	Source	KI Illite	%Ro Illite	KI Muscovite	%Ro Muscovite	Intensity 10Â	Intensity 5Â	Esquevin Index	Remarks
1	Well A	1309,5	Poti	Cuttings	1,10	0,67	0,43	1,96	126,00	48,00	0,38	
2	Well A	1324,5	Poti	Cuttings	0,85	0,89	0,34	2,60	75,00	35,00	0,47	
3	Well A	1339,5	Poti	Cuttings	N/A	N/A	0,21	4,52	33,00	15,00	0,45	Noisy
4	Well A	1354,5	Poti	Cuttings	0,64	1,25	0,35	2,48	58,00	32,00	0,55	
5	Well A	1369,5	Poti	Cuttings	0,68	1,16	0,33	2,65	27,00	18,00	0,67	
6	Well A	1384,5	Longá	Cuttings	0,81	0,94	0,35	2,52	89,00	36,00	0,40	
7	Well A	1399,5	Longá	Cuttings	0,81	0,95	0,31	2,86	192,00	73,00	0,38	
8	Well A	1414,5	Longá	Cuttings	0,78	0,98	0,55	1,48	244,00	70,00	0,29	
9	Well A	1429,5	Longá	Cuttings	0,76	1,02	0,33	2,67	192,00	63,00	0,33	
10	Well A	1444,5	Longá	Cuttings	0,71	1,10	0,37	2,32	194,00	60,00	0,31	
11	Well A	1459,5	Longá	Cuttings	0,78	0,99	0,18	5,18	241,00	69,00	0,29	
12	Well A	1474,5	Longá	Cuttings	0,61	1,32	0,23	4,05	253,00	66,00	0,26	
13	Well A	1510,5	Cabeças	Cuttings	0,55	1,49	0,49	1,67	69,00	24,00	0,35	
14	Well A	1525,5	Cabeças	Cuttings	0,59	1,35	0,51	1,63	135,00	33,00	0,24	
15	Well A	1540,5	Cabeças	Cuttings	0,61	1,32	0,28	3,21	128,00	47,00	0,37	
16	Well A	1555,5	Cabeças	Cuttings	0,41	2,04	0,34	2,58	100,00	32,00	0,32	
17	Well A	1570,5	Cabeças	Cuttings	0,46	1,82	0,39	2,19	141,00	57,00	0,40	
18	Well A	1582,5	Cabeças	Cuttings	0,39	2,20	0,35	2,48	129,00	49,00	0,38	
19	Well A	1609,5	Pimenteiras	Cuttings	0,32	2,70	0,33	2,63	279,00	90,00	0,32	
20	Well A	1624,5	Pimenteiras	Cuttings	0,37	2,34	0,28	3,15	278,00	66,00	0,24	
21	Well A	1639,5	Pimenteiras	Cuttings	0,32	2,77	0,36	2,43	259,00	92,00	0,36	
22	Well A	1654,5	Pimenteiras	Cuttings	0,33	2,69	0,33	2,66	420,00	126,00	0,30	
23	Well A	1831,5	Pimenteiras	Cuttings	0,31	2,84	0,31	2,84	288,00	77,00	0,27	
24	Well A	1900,5	Pimenteiras	Cuttings	0,28	3,15	0,20	4,68	189,00	68,00	0,36	
25	Well A	1915,5	Pimenteiras	Cuttings	0,30	2,92	0,29	3,12	310,00	103,00	0,33	
26	Well A	1930,5	Pimenteiras	Cuttings	0,55	1,46	0,39	2,17	207,00	63,00	0,30	
27	Well A	1935,0	Pimenteiras	SWC	0,49	1,70	0,58	1,38	1110,00	285,00	0,26	
28	Well A	1960,5	Pimenteiras	Cuttings	0,36	2,44	0,27	3,35	104,00	49,00	0,47	
29	Well A	1968,0	Pimenteiras	SWC	0,40	2,12	0,28	3,24	537,00	139,00	0,26	
30	Well A	1975,5	Pimenteiras	Cuttings	0,37	2,34	0,28	3,21	97,00	46,00	0,47	
31	Well A	1990,5	Pimenteiras	Cuttings	0,39	2,21	0,35	2,48	144,00	96,00	0,67	
32	Well A	1998,0	Pimenteiras	SWC	0,60	1,34	0,21	4,45	729,00	180,00	0,25	
33	Well A	2005,5	Pimenteiras	Cuttings	0,38	2,28	0,28	3,17	149,00	66,00	0,44	
34	Well A	2020,5	Pimenteiras	Cuttings	0,43	1,98	0,22	4,19	143,00	40,00	0,28	
35	Well A	2025,0	Pimenteiras	SWC	0,40	2,13	0,37	2,35	273,00	67,00	0,25	
36	Well A	2035,5	Pimenteiras	Cuttings	0,40	2,11	0,35	2,52	63,00	28,00	0,44	
37	Well A	2049,0	Pimenteiras	SWC	0,66	1,19	0,31	2,87	345,00	105,00	0,30	
38	Well A	2050,5	Pimenteiras	Cuttings	0,62	1,29	0,31	2,81	88,00	39,00	0,44	
39	Well A	2064,0	Pimenteiras	SWC	0,57	1,41	0,24	3,76	644,00	189,00	0,29	
40	Well A	2065,5	Pimenteiras	Cuttings	0,57	1,42	0,31	2,86	132,00	50,00	0,38	
41	Well A	2080,5	Pimenteiras	Cuttings	0,73	1,06	0,21	4,35	126,00	38,00	0,30	
42	Well A	2082,0	Pimenteiras	SWC	0,73	1,06	0,31	2,87	743,00	235,00	0,32	
43	Well A	2095,5	Pimenteiras	Cuttings	0,66	1,19	0,26	3,50	82,00	42,00	0,51	
44	Well A	2097,0	Pimenteiras	SWC	0,90	0,84	0,30	2,93	646,00	192,00	0,30	
45	Well A	2110,5	Pimenteiras	Cuttings	1,14	0,64	0,24	3,74	56,00	29,00	0,52	
46	Well A	2115,0	Pimenteiras	SWC	0,95	0,79	0,34	2,53	680,00	206,00	0,30	
47	Well A	2125,5	Pimenteiras	Cuttings	1,19	0,61	0,31	2,87	120,00	36,00	0,30	
48	Well A	2130,0	Pimenteiras	SWC	1,05	0,70	0,43	1,97	553,00	157,00	0,28	
49	Well A	2140,5	Pimenteiras	Cuttings	0,92	0,82	0,43	1,96	57,00	35,00	0,61	
50	Well A	2155,5	Pimenteiras	Cuttings	0,95	0,79	0,32	2,77	88,00	32,00	0,36	
51	Well A	2160,0	Pimenteiras	SWC	1,04	0,71	0,43	1,95	841,00	241,00	0,29	
52	Well A	2170,5	Pimenteiras	Cuttings	1,23	0,58	0,36	2,37	125,00	39,00	0,31	
53	Well A	2185,5	Pimenteiras	Cuttings	1,07	0,69	0,35	2,52	71,00	23,00	0,32	
54	Well A	2200,5	Pimenteiras	Cuttings	1,06	0,69	0,27	3,28	104,00	52,00	0,50	
55	Well A	2202,0	Pimenteiras	SWC	1,14	0,64	0,44	1,88	700,00	218,00	0,31	
56	Well A	2215,5	Pimenteiras	Cuttings	1,07	0,69	0,44	1,92	110,00	39,00	0,35	
57	Well A	2229,0	Pimenteiras	SWC	0,98	0,76	0,29	3,12	490,00	121,00	0,25	
58	Well A	2230,5	Pimenteiras	Cuttings	0,99	0,75	0,38	2,26	117,00	40,00	0,34	
59	Well A	2245,5	Itaim	Cuttings	N/A	N/A	N/A	N/A	N/A	N/A	N/A	Noisy
60	Well A	2260,5	Itaim	Cuttings	N/A	N/A	N/A	N/A	N/A	N/A	N/A	Noisy
61	Well A	2275,5	Itaim	Cuttings	N/A	N/A	N/A	N/A	N/A	N/A	N/A	Noisy
62	Well A	2290,5	Itaim	Cuttings	N/A	N/A	N/A	N/A	N/A	N/A	N/A	Noisy
63	Well A	2305,5	Itaim	Cuttings	N/A	N/A	N/A	N/A	N/A	N/A	N/A	Noisy
64	Well A	2320,5	Itaim	Cuttings	N/A	N/A	N/A	N/A	N/A	N/A	N/A	Noisy
65	Well A	2335,5	Itaim	Cuttings	N/A	N/A	N/A	N/A	N/A	N/A	N/A	Noisy
66	Well A	2350,5	Itaim	Cuttings	N/A	N/A	N/A	N/A	N/A	N/A	N/A	Noisy
1	Well B	1351,5	Poti	Cuttings	0,83	0,93	0,35	2,49	88	30	0,34	
2	Well B	1366,5	Poti	Cuttings	0,92	0,82	0,35	2,44	100	42	0,42	
3	Well B	1381,5	Poti	Cuttings	0,64	1,24	0,22	4,19	62	25	0,40	

4	Well B	1396,5	Poti	Cuttings	0,88	0,86	0,36	2,42	68	33	0,49	
5	Well B	1411,5	Poti	Cuttings	1,04	0,71	0,42	2,01	220	77	0,35	
6	Well B	1426,5	Poti	Cuttings	0,90	0,84	0,39	2,17	351	131	0,37	
7	Well B	1441,5	Poti	Cuttings	0,86	0,88	0,41	2,08	662	293	0,44	
8	Well B	1455,0	Poti	Cuttings	0,91	0,83	0,26	3,56	150	60	0,40	
9	Well B	1456,5	Poti	Cuttings	0,91	0,83	0,35	2,47	672	274	0,41	
10	Well B	1471,5	Poti	Cuttings	0,58	1,38	0,44	1,88	404	141	0,35	
11	Well B	1477,5	Poti	Cuttings	0,71	1,10	0,26	3,45	263	71	0,27	
12	Well B	1486,5	Longá	Cuttings	0,67	1,18	0,45	1,87	601	206	0,34	
13	Well B	1501,5	Longá	Cuttings	0,57	1,40	0,40	2,13	254	74	0,29	
14	Well B	1515,0	Longá	Cuttings	0,74	1,05	0,23	3,95	200	77	0,39	
15	Well B	1516,5	Longá	Cuttings	0,78	0,99	0,37	2,34	490	195	0,40	
16	Well B	1531,5	Longá	Cuttings					88	25	0,28	very noisy
17	Well B	1540,5	Longá	Cuttings	0,68	1,15	0,17	5,79	200	56	0,28	
18	Well B	1546,5	Longá	Cuttings	0,69	1,13	0,19	4,93	329	96	0,29	
19	Well B	1561,5	Longá	Cuttings	0,67	1,18	0,50	1,65	288	72	0,25	
20	Well B	1576,5	Longá	Cuttings	0,59	1,35	0,25	3,59	310	82	0,26	
21	Well B	1591,5	Longá	Cuttings	0,57	1,41	0,43	1,98	187	60	0,32	
22	Well B	1606,5	Cabeças	Cuttings	0,57	1,43	0,39	2,19	233	67	0,29	
23	Well B	1621,5	Cabeças	Cuttings	0,54	1,52	0,40	2,13	189	44	0,23	noisy
24	Well B	1636,5	Cabeças	Cuttings	0,53	1,54	0,38	2,27	173	48	0,28	
25	Well B	1651,5	Cabeças	Cuttings	0,49	1,70	0,32	2,77	690	215	0,31	
26	Well B	1657,5	Cabeças	Cuttings	0,41	2,08	0,23	4,09	332	99	0,30	
27	Well B	1666,5	Cabeças	Cuttings	0,48	1,73	0,28	3,26	826	278	0,34	
28	Well B	1681,5	Cabeças	Cuttings	0,40	2,15	0,28	3,20	981	264	0,27	
29	Well B	1696,5	Cabeças	Cuttings	0,28	3,18	0,28	3,18	678	227	0,33	only 1 Phase
30	Well B	1828,5	Pimenteiras	Cuttings	0,32	2,75	0,32	2,75	377	103	0,27	
31	Well B	1972,5	Pimenteiras	Cuttings	0,26	3,47	0,26	3,47	944	347	0,37	
32	Well B	1971,0	Pimenteiras	SWC	0,39	2,19	0,35	2,44	919	180	0,20	
33	Well B	1996,5	Pimenteiras	Cuttings	0,29	3,10	0,29	3,10	217	76	0,35	
34	Well B	2011,5	Pimenteiras	Cuttings	0,46	1,83	0,26	3,51	231	67	0,29	
35	Well B	2019,0	Pimenteiras	SWC	0,56	1,43	0,26	3,53	762	175	0,23	
36	Well B	2021,0	Pimenteiras	SWC	0,40	2,15	0,26	3,50	632	155	0,25	
37	Well B	2029,5	Pimenteiras	Cuttings	0,57	1,40	0,18	5,41	204	74	0,36	
38	Well B	2026,5	Pimenteiras	Cuttings	0,32	2,74	0,31	2,81	326	101	0,31	
39	Well B	2041,5	Pimenteiras	Cuttings	0,58	1,39	0,34	2,54	385	120	0,31	
40	Well B	2056,5	Pimenteiras	Cuttings	0,45	1,85	0,27	3,33	276	86	0,31	
41	Well B	2076,0	Pimenteiras	Cuttings	0,46	1,81	0,16	6,08	142	53	0,37	
42	Well B	2071,5	Pimenteiras	Cuttings	0,68	1,16	0,27	3,32	69	40	0,58	
43	Well B	2086,5	Pimenteiras	Cuttings	0,54	1,51	0,22	4,13	135	55	0,41	
44	Well B	2101,5	Pimenteiras	Cuttings	0,37	2,34	0,31	2,83	161	63	0,39	
45	Well B	2119,5	Pimenteiras	Cuttings	0,65	1,21	0,31	2,82	212	88	0,42	
46	Well B	2116,5	Pimenteiras	Cuttings	0,77	1,00	0,26	3,54	537	187	0,35	
47	Well B	2131,5	Pimenteiras	Cuttings	0,83	0,92	0,29	3,13	439	146	0,33	
48	Well B	2146,5	Pimenteiras	Cuttings	0,60	1,34	0,29	3,10	260	80	0,31	
49	Well B	2161,5	Pimenteiras	Cuttings	0,89	0,85	0,29	3,12	191	57	0,30	
50	Well B	2176,5	Pimenteiras	Cuttings	0,76	1,02	0,28	3,25	286	91	0,32	
51	Well B	2191,5	Pimenteiras	Cuttings	0,94	0,79	0,31	2,82	173	61	0,35	
52	Well B	2206,5	Pimenteiras	Cuttings	0,79	0,97	0,33	2,69	153	44	0,29	
53	Well B	2221,5	Pimenteiras	Cuttings	0,76	1,01	0,27	3,41	282	104	0,37	
54	Well B	2236,5	Pimenteiras	Cuttings	0,89	0,85	0,32	2,70	180	63	0,35	
55	Well B	2250,0	Pimenteiras	Cuttings	0,96	0,78	0,21	4,45	170	60	0,35	
56	Well B	2251,5	Pimenteiras	Cuttings	0,78	0,98	0,26	3,48	255	96	0,38	
57	Well B	2266,5	Pimenteiras	Cuttings	0,85	0,90	0,38	2,25	104	46	0,44	
58	Well B	2281,5	Pimenteiras	Cuttings	0,84	0,91	0,33	2,68	258	84	0,33	
59	Well B	2290,5	Pimenteiras	Cuttings	0,83	0,92	0,30	3,01	66	27	0,41	
60	Well B	2320,5	Pimenteiras	Cuttings	0,91	0,82	0,25	3,68	150	45	0,30	
61	Well B	2326,5	Pimenteiras	Cuttings	0,96	0,77	0,34	2,59	70	45	0,64	very noisy
62	Well B	2341,5	Pimenteiras	Cuttings	0,83	0,92	0,32	2,78	107	48	0,45	
63	Well B	2356,5	Pimenteiras	Cuttings	0,86	0,88	0,39	2,18	55	18	0,33	
64	Well B	2371,5	Itaim	Cuttings	0,74	1,06	0,40	2,14	71	40	0,56	
65	Well B	2386,5	Itaim	Cuttings					77	24	0,31	very noisy
66	Well B	2392,5	Itaim	Cuttings	0,93	0,81	0,28	3,17	234	66	0,28	
67	Well B	2401,5	Itaim	Cuttings	0,70	1,11	0,43	1,93	88	33	0,38	
68	Well B	2416,5	Itaim	Cuttings	0,84	0,91	0,18	5,31				very noisy
69	Well B	2431,5	Itaim	Cuttings								
70	Well B	2446,5	Itaim	Cuttings	0,64	1,25	0,39	2,19	55	36	0,65	
1	Well C	1309,5	Poti	Cuttings	0,51	1,62	0,29	3,11	137	43	0,31	
2	Well C	1327,5	Poti	Cuttings	0,45	1,87	0,23	4,07	372	115	0,31	
3	Well C	1345,5	Poti	Cuttings	0,37	2,34	0,27	3,28	144	41	0,28	
4	Well C	1363,5	Poti	Cuttings	0,34	2,54	0,35	2,50	28	35	1,25	10Ã very low

5	Well C	1510,5	Poti	Cuttings	0,23	3,95	0,25	3,73	70	29	0,41	5Ã very low
6	Well C	1525,5	Poti	Cuttings	0,24	3,78	0,28	3,17	88	27	0,31	5Ã very low
7	Well C	1540,5	Poti	Cuttings	0,29	3,13	0,26	3,56	75	24	0,32	
8	Well C	1555,5	Poti	Cuttings	0,37	2,36	0,37	2,36	58	31	0,53	
9	Well C	1591,5	Poti	Cuttings	0,36	2,40	0,26	3,47	52	30	0,58	10Ã/5Â low
10	Well C	1606,5	Longá	Cuttings	0,41	2,05	0,24	3,82	97	34	0,35	
11	Well C	1621,5	Longá	Cuttings	0,39	2,22	0,31	2,80	114	59	0,52	
12	Well C	1636,5	Longá	Cuttings	0,38	2,24	0,34	2,56	123	52	0,42	
13	Well C	1651,5	Longá	Cuttings	0,45	1,88	0,29	3,11	107	52	0,49	
14	Well C	1666,5	Longá	Cuttings	0,50	1,66	0,31	2,80	123	65	0,53	
15	Well C	1681,5	Longá	Cuttings	0,42	2,01	0,41	2,06	81	37	0,46	
16	Well C	1696,5	Cabeças	Cuttings	0,54	1,52	0,33	2,69				10Ã/5Â low
17	Well C	1711,5	Cabeças	Cuttings								10Ã/5Â low
18	Well C	1726,5	Cabeças	Cuttings	0,44	1,93	0,39	2,20	90	30	0,33	
19	Well C	1741,5	Cabeças	Cuttings	0,50	1,64	0,45	1,86	69	24	0,35	
20	Well C	1756,5	Cabeças	Cuttings	0,52	1,56	0,24	3,78	54	25	0,46	
21	Well C	1771,5	Cabeças	Cuttings					39	30	0,77	10Ã/5Â low
22	Well C	1786,5	Cabeças	Cuttings	0,51	1,62	0,30	2,94	35	64	1,83	
23	Well C	1801,5	Cabeças	Cuttings	0,47	1,75	0,28	3,17	45	38	0,84	
24	Well C	1816,5	Cabeças	Cuttings	0,57	1,43	0,22	4,31	58	39	0,67	10Ã/5Â low
25	Well C	1821,0	Cabeças	SWC	0,63	1,25	0,25	3,61	69	26	0,38	
26	Well C	1831,5	Pimenteiras	Cuttings	0,59	1,36	0,21	4,47	98	70	0,71	
27	Well C	1846,5	Pimenteiras	Cuttings	0,52	1,59	0,32	2,72	63	31	0,49	
28	Well C	1861,5	Pimenteiras	Cuttings	0,49	1,68	0,29	3,06	79	32	0,41	
29	Well C	1866,0	Pimenteiras	SWC	0,47	1,77	0,29	3,08	105	38	0,36	
30	Well C	1876,5	Pimenteiras	Cuttings	0,49	1,70	0,27	3,33	148	67	0,45	
31	Well C	1891,5	Pimenteiras	Cuttings	0,45	1,85	0,29	3,12	255	99	0,39	
32	Well C	1909,5	Pimenteiras	Cuttings	0,49	1,69	0,31	2,89	357	133	0,37	
33	Well C	1917,0	Pimenteiras	SWC	0,48	1,72	0,23	4,01	307	86	0,28	
34	Well C	1924,5	Pimenteiras	Cuttings	0,48	1,74	0,31	2,86	261	96	0,37	
35	Well C	1939,5	Pimenteiras	Cuttings	0,45	1,85	0,38	2,26	142	56	0,39	
36	Well C	1954,5	Pimenteiras	Cuttings	0,54	1,50	0,23	4,03	131	44	0,34	
37	Well C	1962,0	Pimenteiras	SWC	0,43	1,94	0,24	3,80	96	40	0,42	
38	Well C	1969,5	Pimenteiras	Cuttings	0,43	1,94	0,41	2,09	179	68	0,38	
39	Well C	1984,5	Pimenteiras	Cuttings	0,49	1,70	0,34	2,55	161	51	0,32	
40	Well C	1999,5	Pimenteiras	Cuttings	0,43	1,94	0,35	2,44	235	75	0,32	
41	Well C	2007,0	Pimenteiras	SWC	0,53	1,53	0,34	2,55	184	56	0,30	
42	Well C	2014,5	Pimenteiras	Cuttings	0,40	2,12	0,39	2,16	140	31	0,22	
43	Well C	2022,0	Pimenteiras	SWC	0,43	1,96	0,38	2,26	548	150	0,27	
44	Well C	2026,5	Pimenteiras	Cuttings	0,41	2,07	0,36	2,37	241	62	0,26	
45	Well C	2062,5	Pimenteiras	Cuttings	0,33	2,64	0,36	2,42	400	119	0,30	
46	Well C	2077,5	Pimenteiras	Cuttings	0,43	1,96	0,40	2,11	219	57	0,26	
47	Well C	2088,0	Pimenteiras	SWC	0,54	1,52	0,46	1,79	163	40	0,25	
48	Well C	2092,5	Pimenteiras	Cuttings	0,36	2,38	0,30	2,95	188	64	0,34	
49	Well C	2107,5	Pimenteiras	Cuttings	0,36	2,38	0,30	3,01	352	116	0,33	
50	Well C	2125,5	Pimenteiras	Cuttings	0,35	2,47	0,32	2,79	352	90	0,26	
51	Well C	2134,5	Pimenteiras	Cuttings	0,35	2,48	0,34	2,56	193	58	0,30	
52	Well C	2173,5	Pimenteiras	Cuttings	0,41	2,05	0,26	3,50	263	83	0,32	
53	Well C	2175,0	Pimenteiras	SWC	0,38	2,23	0,25	3,61	294	86	0,29	
54	Well C	2185,5	Pimenteiras	Cuttings	0,37	2,30	0,28	3,18	130	30	0,23	
55	Well C	2200,5	Pimenteiras	Cuttings	0,39	2,18	0,38	2,27	514	133	0,26	
56	Well C	2215,5	Pimenteiras	Cuttings	0,41	2,06	0,29	3,07	412	117	0,28	
57	Well C	2230,5	Pimenteiras	Cuttings	0,34	2,53	0,31	2,86	356	99	0,28	
58	Well C	2232,0	Pimenteiras	SWC	0,50	1,64	0,24	3,80	311	81	0,26	
59	Well C	2245,5	Pimenteiras	Cuttings	0,39	2,21	0,27	3,38	211	60	0,28	
60	Well C	2247,0	Pimenteiras	SWC	0,35	2,46	0,22	4,15	248	54	0,22	
61	Well C	2260,5	Pimenteiras	Cuttings	0,37	2,33	0,29	3,06	328	99	0,30	
62	Well C	2259,0	Pimenteiras	SWC	0,37	2,34	0,25	3,71	346	112	0,32	
63	Well C	2281,5	Pimenteiras	Cuttings	0,33	2,64	0,33	2,66	279	78	0,28	
64	Well C	2296,5	Pimenteiras	Cuttings	0,36	2,43	0,32	2,72	254	99	0,39	
65	Well C	2301,0	Pimenteiras	SWC	0,37	2,34	0,36	2,41	226	61	0,27	
66	Well C	2311,5	Pimenteiras	Cuttings	0,35	2,50	0,34	2,58	171	57	0,33	
67	Well C	2326,5	Pimenteiras	Cuttings	0,35	2,47	0,30	2,92	227	76	0,33	
68	Well C	2337,0	Pimenteiras	SWC	0,40	2,10	0,28	3,22	267	86	0,32	
69	Well C	2341,5	Pimenteiras	Cuttings	0,36	2,39	0,28	3,16	318	124	0,39	
70	Well C	2356,5	Pimenteiras	Cuttings	0,32	2,78	0,32	2,73	449	148	0,33	
71	Well C	2364,0	Pimenteiras	SWC	0,33	2,67	0,20	4,62	274	74	0,27	

Table 7 - Results of Kubler index for Illite and Muscovite Phase at decomposed peaks measured at natural clay fraction, conversion from KI to equivalent %Ro, Intensity measured at 10Â and % Â peaks and Esquevin Index for the 207 samples analyzed at wells A, B and C.

The semi-quantitative results of the XRD data from total powder and clay fractions were also calculated and are presented in the Figure 49, Figure 50 and Figure 51.The XRD results were analyzed using a semi-quantitative approach following the minerals present in the whole rock carried out from the intensity of the main peak for each mineral (Schultz, 1964 modified with own standards - Moore and Reynolds, 1997). The estimation of the mineralogical components has a methodological error ca. 10%. The crystallinity of clay minerals was deduced from the shape and sharpness of the XRD peaks (Brindley and Brown, 1980). The semi-quantitative estimations of the relative concentrations of clay minerals were based on the peak area method following the methodology from Biscaye (1965). The response of mineral species to sedimentation depends on the form of the particles (Pierce, 1969); for that reason, each mineral proportion is not directly proportional to the defined areas. The relative percentages of each clay mineral were determined by applying empirical factors (Moore and Reynolds, 1997).

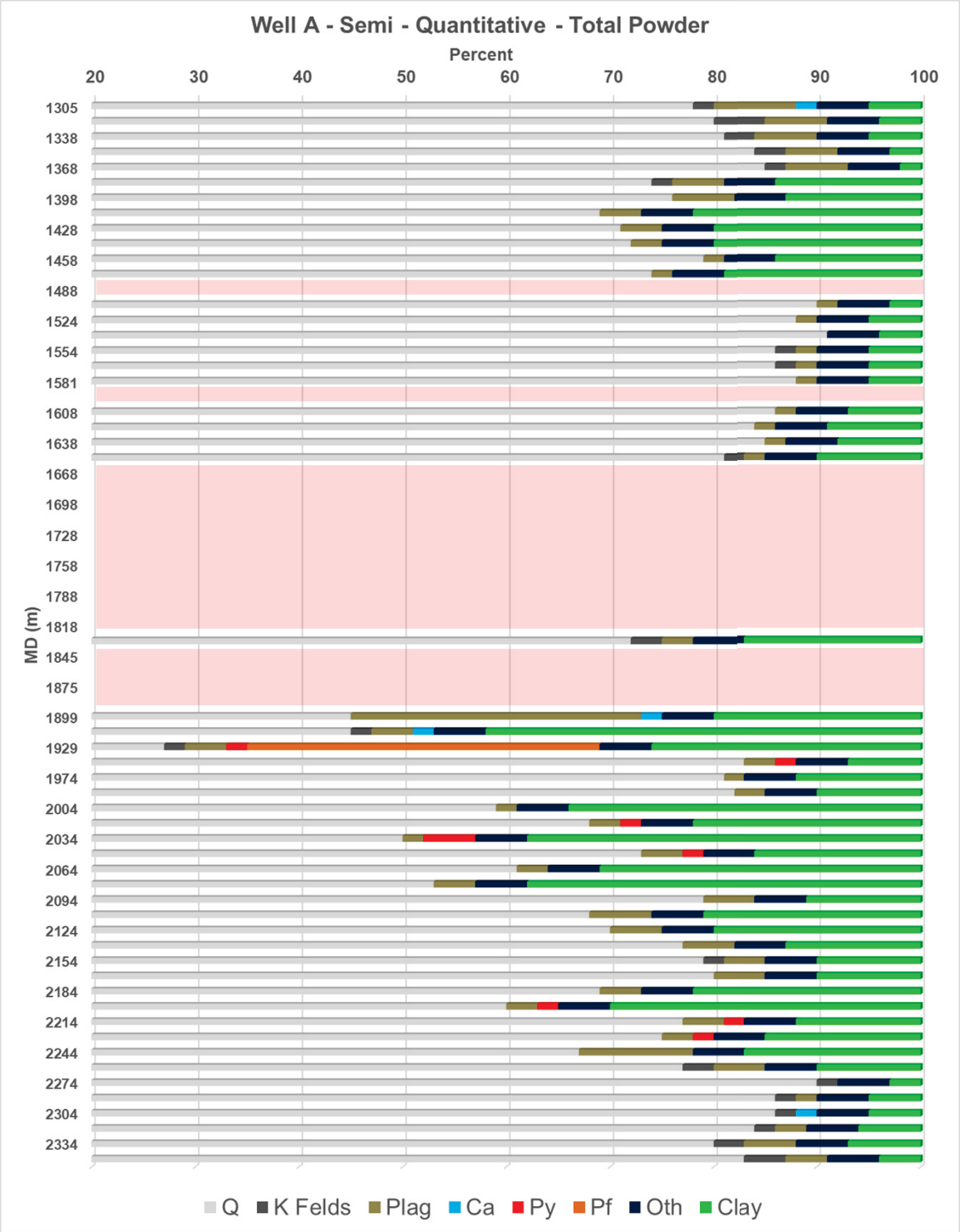

Figure 49 - Semi quantitative results from total powder and clay fractions from well A samples. Legend for total powder fraction: Qz= quartz, K Felds= K Feldspars, Plag= Plagioclase, Ca= Calcite, Dol= Dolomite, Sid= Siderite, Py= Pyrite, Pf= Pyrophyllite, Oth= Others, Clay= Clay. Legend for clay fraction: I/M= Illite or Mica, I/S Interstratified Illite-Smectite, Sm= Smectite, Cl= Chlorite, K= Kaolinite.

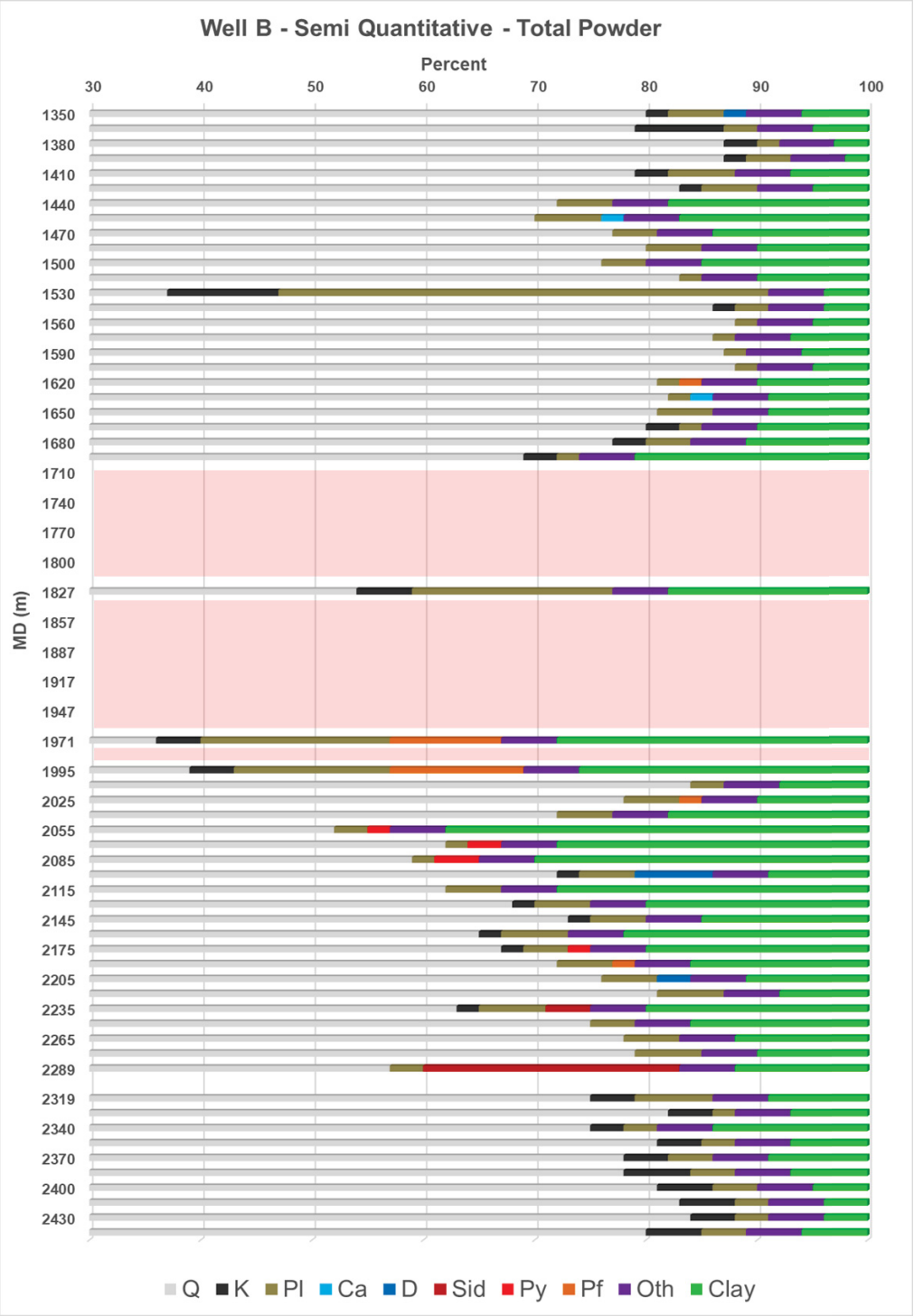

Figure 50 - Semi quantitative results from total powder and clay fractions from well B samples. Legend for total powder fraction: Qz= quartz, K Felds= K Feldspars, Plag= Plagioclase, Ca= Calcite, Dol= Dolomite, Sid= Siderite, Py= Pyrite, Pf= Pyrophyllite, Oth= Others, Clay= Clay. Legend for clay fraction: I/M= Illite or Mica, I/S Interstratified Illite-Smectite, Sm= Smectite, Cl= Chlorite, K= Kaolinite.

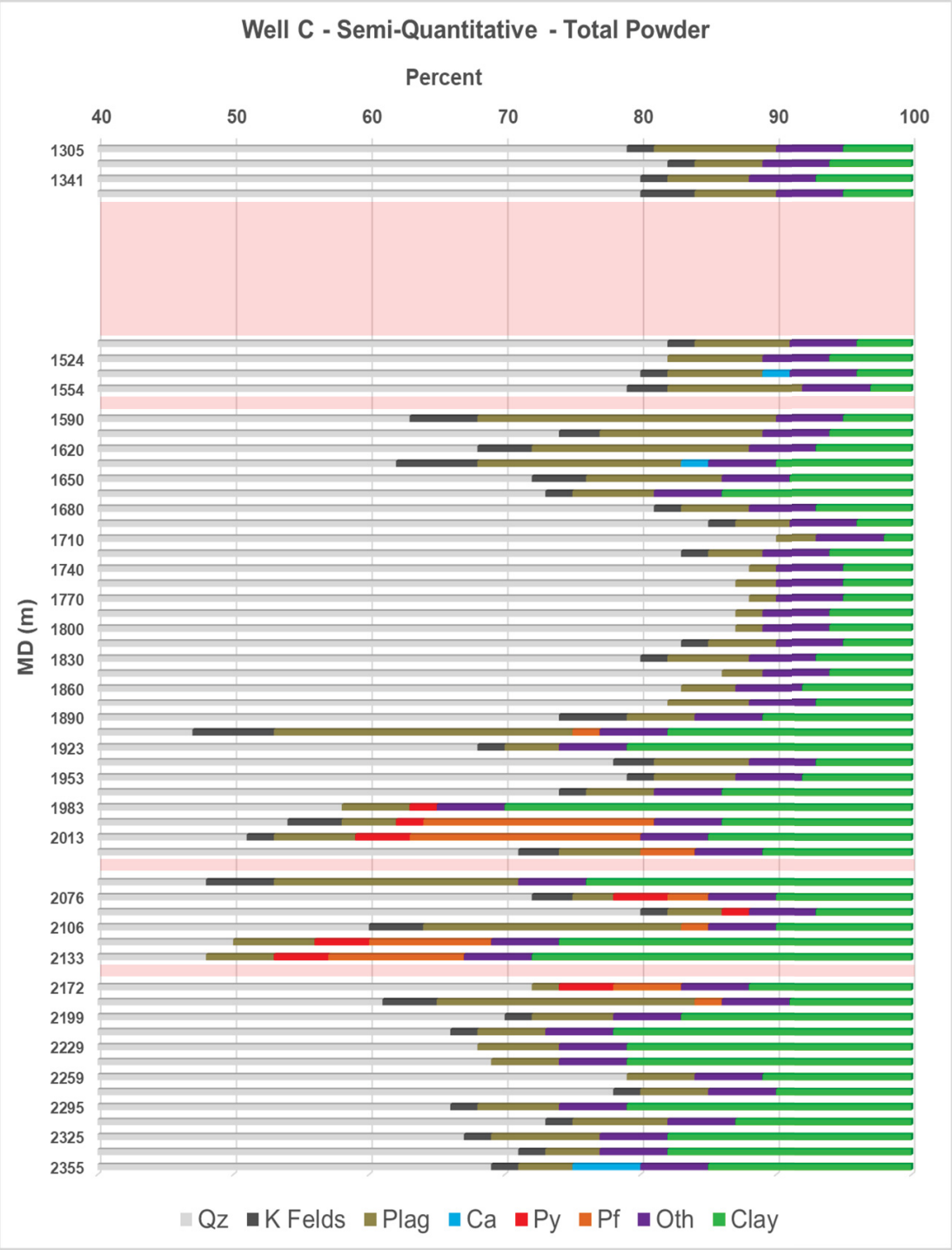

Figure 51 - Semi quantitative results from total powder and clay fractions from well C samples. . Legend for total powder fraction: Qz= quartz, K Felds= K Feldspars, Plag= Plagioclase, Ca= Calcite, Py= Pyrite, Pf= Pyrophyllite, Oth= Others, Clay= Clay. Legend for clay fraction: I/M= Illite or Mica, I/S Interstratified Illite-Smectite, Sm= smectite, Cl= Chlorite, K= Kaolinite.

4.4. Petroleum System Modeling Results

4.4.1. Impacts of PSM results due to implementation of compositional kinetics scheme for Pimenteiras Formation

The analysis of kinetics of the Pimenteiras Formation organic rich levels A (Well B) and C (Well D) lead to some important achievements to understand the process of transformation of the Type II marine kerogens in petroleum. The analysis of kerogens revealed that the part composition of the maceral assemblage is an *algae* called alginite with significant contribution of amorphous organic matter and traces of vitrinite.

This singles algae contribution led to a very narrow distribution of the activation energies, between 50 to 55 kcal/mol, with a single peak of the generation, as show in the Figure 48 E. The Pimenteiras SR Level C has a single peak at 52kcal/mol (Figure 48- D), while the Pimenteiras SR Level A has a distribution between 50 to 60, with main peak centered at 55 kcal/mol (Figure 48 - E). The transformation ratio versus temperature curves of the Pimenteiras samples are in general less reactive in comparison with classical Type II marine kinetics from Woodford Shales (Devonian of USA/Canada) for example, a common kinetics available in commercial packages (Figure 48 A).

The new compositional kinetic, for primary cracking, for the Pimenteiras formation was tested by Lopes and Mio, (2023) and Mio et al., (2023) in 2D PSM models and shows relevant differences in hydrocarbon column height and in the predicted composition of expected hydrocarbons in PSM simulations (Figure 52).

The results were fully implemented in high resolution 3D PSM model 01 (100x100m of grid cell size - Figure *32*) and the simulations shows the strong impact of the use of new kinetic parameters on source rock maturation (Figure *53*). The transformation ratio at the three organic-rich levels in the model (Pimenteiras SR´s A, B and C) are significantly less evolved when compared with the model ran with the Woodford Shale kinetics, especially in the lower levels (SR A and B) that are far from the diabase intrusions. This effect is caused by the differences in reactivity (Activation Energies - Ea´s) showed in the Figure 48, considering the kinetic parameters for the two analyzed samples.

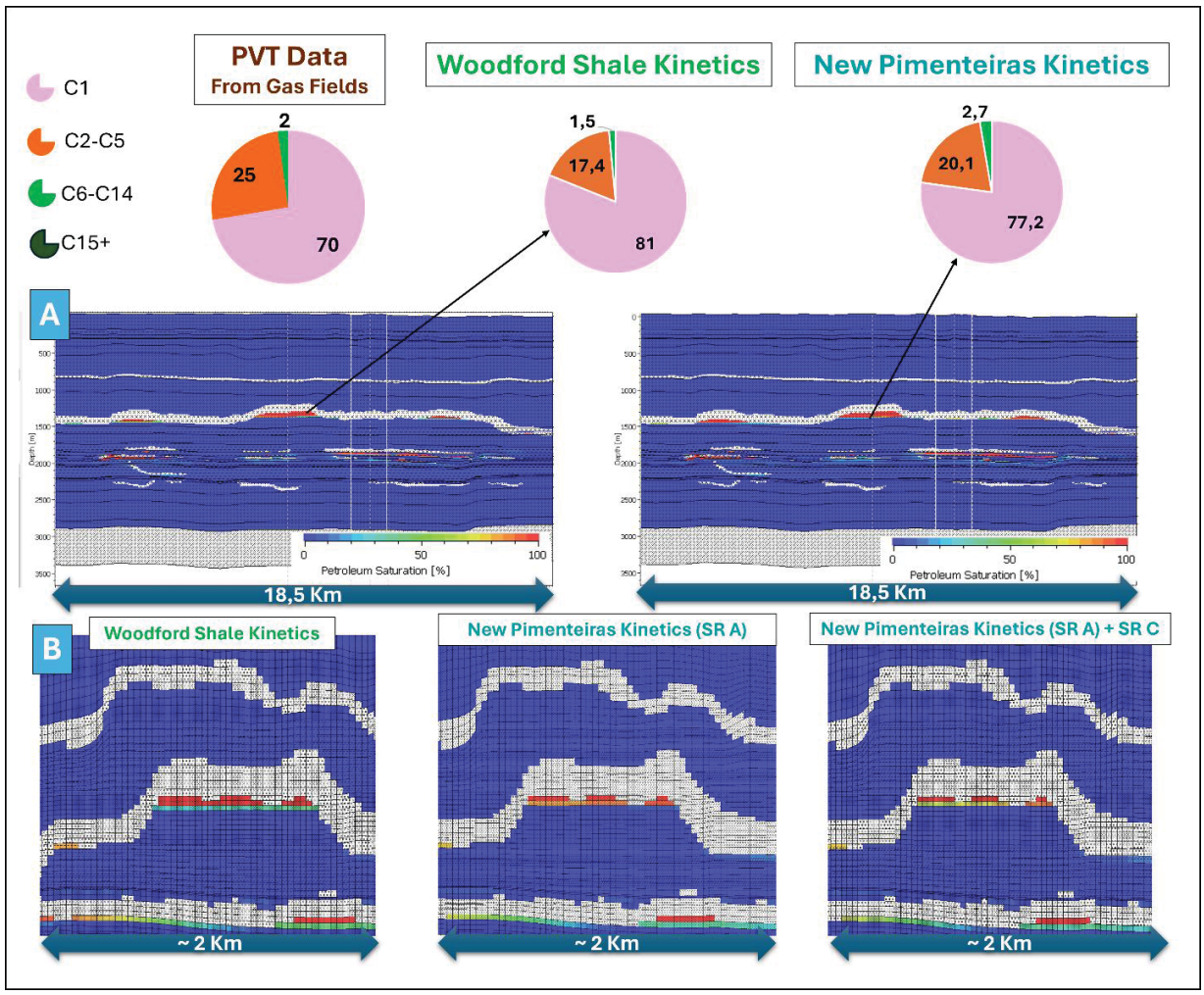

Figure 52 – Implementation of kinetic parameters of the Pimenteiras formation into 2D PSM. A) Impacts on hydrocarbon composition prediction in a 2D model ran with Woodford Shale Kinetic (left), and Pimenteiras Formation Kinetic (right) with composition close to the PVT data from the fields (adapted from Lopes and Mio, 2023). B) Impact in hydrocarbon column height and composition of expected accumulations in the PSM 2D model in the northern part of the Parnaíba Basin (Figure 32), adapted from Mio et al., (2023).

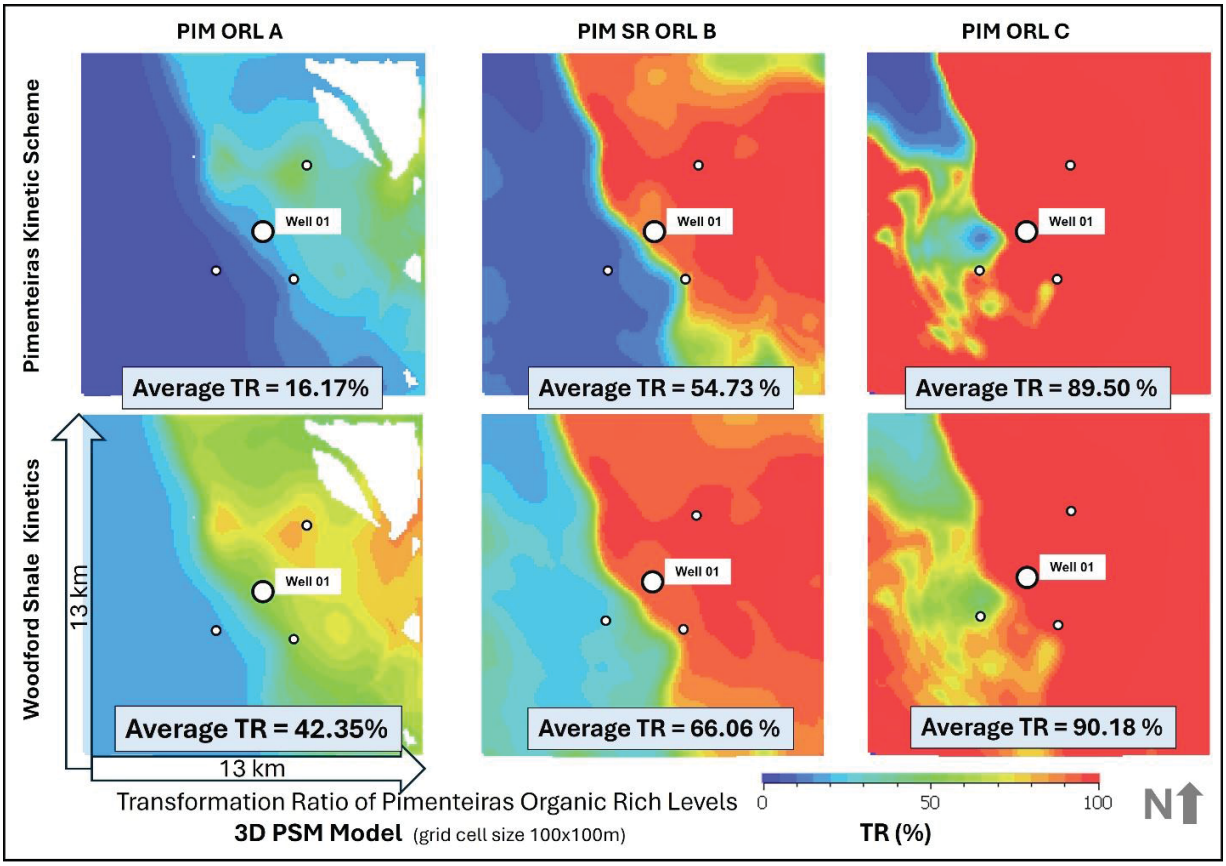

Figure 53 – Impact of the use of distinct kinetics scheme on **Transformation Ratio** of source rock in the 3D PSM (Model 01). Upper line: using the new kinetic parameters for the Pimenteiras formation and the impact at SR level A (left), SR Level B (middle) and SR Level C (right); Lower Line using classical Woodford Shale Kinetics from Petromod library.

4.4.2. Smectite to Illite calculation in PSM Models

After the incorporation of the new acquired data od vitrinite reflectance, 54 samples on the wells A, B and C (Table 1), the 1D PSM model were thermally calibrated and some results of Smectite-to-illite transformation became available to be discussed. Since the PSM models incorporate the temperature and pressure conditions of any point in the basin all along the basin evolution it is possible to incorporate any algorithm which calculation depends on these values.

Petromod@ incorporates two different models of illite to smectite transformations and the more robust is the model proposed by Pytte, (1982) and Pytte and Reynolds,

(1988) who described a sixth order kinetic reaction incorporating both, the time-temperature variations and the chemical equilibrium between K and Na (Equation 8).

Considering that one of the objectives of this research is to recognize and define an inorganic paleothermometer, in the range of the anqui-metamorphism, it is important to define if the Pimenteiras Formation and surrounding formations have reached the minimum conversion rate of detrital smectite into the diagenetic and/or metamorphic illite.

The 1D PSM simulations at wells A, B and C, show that Pimenteiras formation is entirely inside of a range of more than 80% of I/S conversion (Figure 54). The analysis of the complete profile vs depth indicates that part of conversion is due to burial (from surface to 1500m in wells A and B and from surface to 500 m in well C) while part of the conversion is related to diabase intrusions.

In well C, the configuration of positioning and thickness lead to more than 75% of I/S conversion from 500 m to below and there is no tendency to return to the burial trend at the bottom of the well, since there is a series of intrusions inside of the Pimenteiras Formation at this well (Figure 54).

In wells A and B, there is a gradual increase in I/S until the 1500m, where the intrusive sills became thick, inside of the Pimenteiras Formation. From 2000 m towards the bottom of the wells it is possible to note a decrease in I/S and the tendency of the profile to return to the burial trend.

The same exercise was done into a highly refined 3D PSM model (3D PSM Model 01 – 100x100m of grid cell size) where the vitrinite reflectance data was also incorporated and the previous 1D PSM thermal calibration was applied in the model. The same thermal parameters were used in the setup, including basal heat flow, boundary conditions, thermal properties, and age of the intrusions.

The results of 3D PSM (Figure *55*) demonstrates that the Pimenteiras Formation encompasses enough smectite to illite conversion (more than 80%) enabling the use of the Illite Crystallinity Index or Kubler Index (Kubler, 1964) as a potential paleo thermometer to be used in conjunction with vitrinite reflectance data.

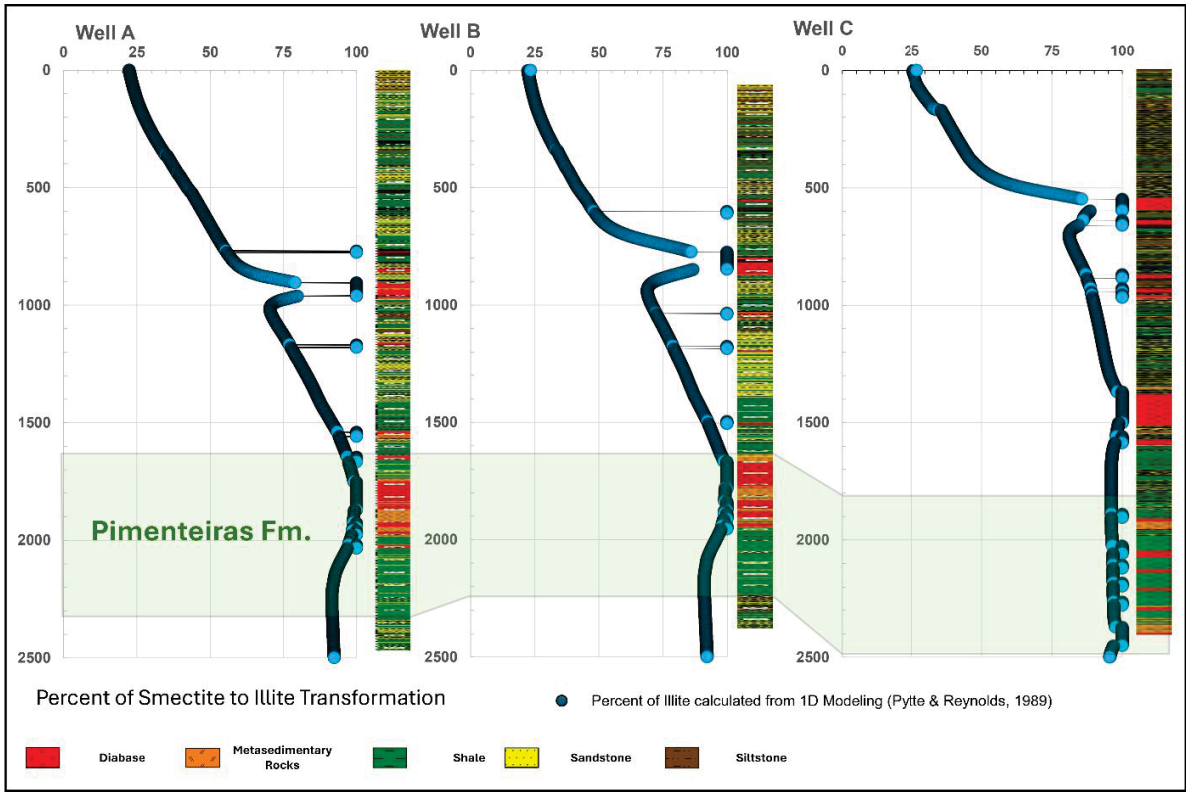

Figure 54 – Percent of smectite to illite conversion along the three studied wells, performed through 1D PSM in Petromod@ using the sixth order kinetics scheme proposed by Pytte and Reynolds (1988). The whole Pimenteiras Formation is inside a range of more than 80% of I/S conversion rate.

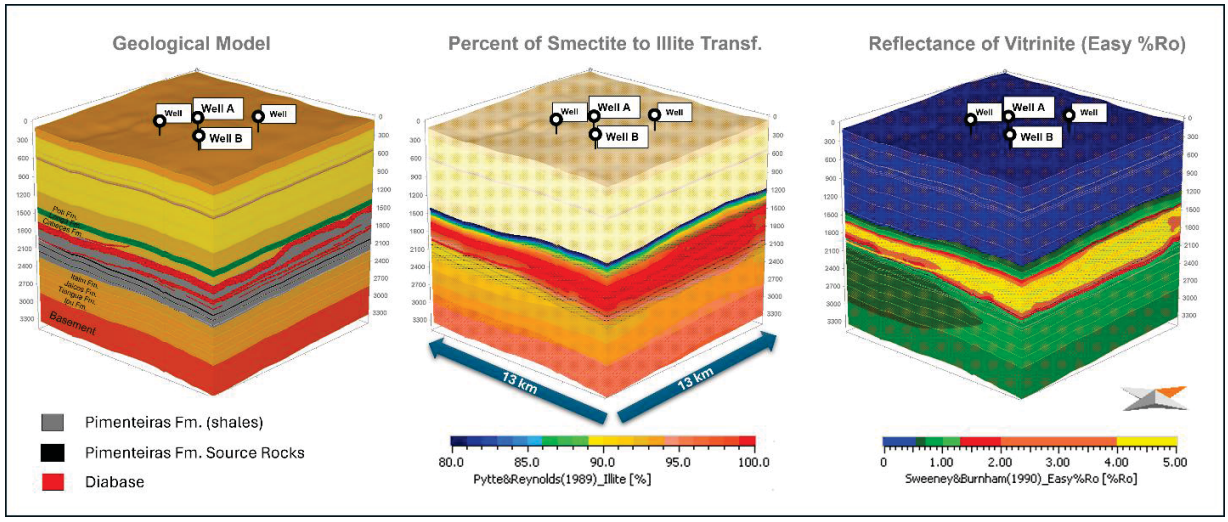

Figure 55 – 3D PSM Model 01 with the calculation of percent for smectite to illite transformation (Pytte and Reynolds, (1988) and the reflectance of vitrinite (Easy %Ro).

5. DISCUSSION

5.1. The characterization of organofacies and the implication of the kinetic parameters on the Pimenteiras Formation.

Optical microscopy revealed that alginite is one of the predominant maceral in all samples investigated, together amorphous O.M.. The presence of selectively preserved algal organic matter is the cause for Ea distributions to be dominated by a single potential that accounts for at least 70% of the bulk reaction in all cases. Such narrow Ea distributions are classically associated with homogenous, lacustrine source rocks, but marine alginites also often show this feature, e.g., the Ordovician Goldwyer Formation, Austrália, whose sequence I is characterized by the presence of large fractions of selectively preserved lipids derived from *Gloeocapsomorpha prisca (G. prisca)* Johnson et al. (2020). Other examples of narrow Ea´s for Type II marine source rocks are presented by Peters et al. (2006) The systematics of physical properties as determined by the PhaseKinetics approach are also in line with marine Type II kerogen containing source rocks in that pyrolysis products are much more gas prone than the typical waxy decomposition products of lacustrine algal derived kerogens and in that GOR and Psat values gradually increase with increasing maturation level (Figure 47).

Cumulative fluids generated from sample 20189 fall within the black oil class over the primary kerogen conversion range up to the conversion level TR 50%. Values indicating the beginning of volatile oil (Psat > 200 bars and GOR > 160 Sm3/Sm3) are reached at TR 70%. GOR and Psat values gently evolve from ~50 Sm3/Sm3 and ~100 bar at 10% TR to ~175 Sm3/Sm3 and ~190 bar at 70% TR. At 90% TR the cumulative GOR and Psat quickly reach values of ~250 Sm3/Sm3 and ~220 bar (Mahlstedt and Horsfield, 2023). Taking instantaneous compositions into account, i.e., compositions generated between two TR levels calculated simply by subtraction of yields of the lower TR experiment from yields of the higher TR experiment, volatile oil is generated already from 30% TR on onwards over the entire primary kerogen conversion range (Figure 47). In contrast to the original PhaseKinetics approach published by di Primio and Horsfield (2006), these instantaneous yields are used to build all compositional models as

prediction of the physical properties of expelled and cumulatively reservoired fluids is improved especially at higher thermal maturity levels.

The evolution of the physical properties of fluids generated from sample 20170 is more extreme. Cumulative fluids fall into the black oil class only at the conversion level TR 10%, into the volatile oil class from 30 to 50% TR, and into the condensate class exceeding 70% TR. Taking instantaneous compositions into account condensate is generated already from 30% TR on onwards over the entire primary kerogen conversion range (Figure 47), (Mahlstedt and Horsfield, 2023). This evolution is not in concordance with the samples mixed base low wax oil generation potential under open-system pyrolysis GC conditions and does not reproduce the natural behavior of typical marine Type II kerogen containing organic matter. There is some evidence though that generation of CO2 or H2O from the decomposition of mineral matter (e.g., siderite or smectite) leads to oxidation and aromatization of primarily generated organic compounds and finally to the formation of char and gas under the closed-system MSSV-pyrolysis conditions. The relevance of these interactions in a geological context is nevertheless completely unclear (Mahlstedt and Horsfield, 2023).

Thus, a compositional kinetic model was developed using the cumulative pyrolysate composition at 30% TR (prior to the severe impact of secondary reactions induced by mineral matter decomposition) to populate the single activation energy potential of the samples kinetic scheme (Figure 47). In the PhaseKinetics approach cumulative yields are used to populate the first potential of the Ea distribution and instantaneous compositions for each subsequent potential. As only one potential is present in the case of the Pimenteiras sample 20170, the cumulative composition is justified.

5.2. The implementation of the Pimenteiras kinetics and the comparison of modeling results with the Woodford Shale kinetics.

The atypical petroleum system of the Parnaíba Basin encompasses a significant number of uncertainties that must be appropriately managed to avoid a low level of predictability in these studies. Recent research on important parameters such as tectonics and basin evolution (Daly et al. 2018; Watts et al. 2018) the age, composition, and thermal properties of magmatism (Aragão, 2020; Heilbron et al. 2018; Lopes, 2019; Lopes et al. 2021; Miranda, 2014 and Miranda et al. 2016), thermal calibration parameters (Mio, 2022 and Mio et al. 2023) and specific kinetic definition (Lopes and Mio, 2023 and Mio et al. 2023) have been developed in the Parnaíba Basin and has contributed to reducing of the number of unknowns and the level of uncertainty in the numerical simulations.

In the Parnaíba Basin, previous petroleum system evaluation and modeling studies were carried out mainly focusing on the impact of heat transfer throughout the basin and in the mechanisms of magma emplacement (i.e., age, composition and sequence of magma emplacement (Aragão, 2020; Lopes et al. 2021; Michelon, 2020; Milani and Zalán 1999; Miranda et al. 2016 and 2018). These petroleum system modeling studies considered generic kinetic parameters, such as those by Pepper and Corvi (1995) and the Woodford Shale (Hantschel and Kauerauf, 2009) as analogous to the Devonian source rocks.

Preliminary results of the new compositional kinetics for the Pimenteiras Formation, using the analysis from the sample 20189 (kinetic parameters of ORL A – Well B), were initially tested by Lopes and Mio (2023) and Lopes et al. (2021) in 2D PSM models in the central part of the Parnaíba Basin. These tests revealed significant differences in hydrocarbon column height and the predicted composition of hydrocarbons in PSM simulations. These authors assumed the kinetic parameters of sample 20189 into the A, B, C, and D ORL´s in these studies, and tested the impact at a known gas field with a methane gas content of 70%. The results show that the predicted content of C1 was reduced from 81%, using Woodford Shale kinetics to 77% with the new kinetics (Figure 52). The predicted column heights changed from about 30 m using Woodford Shale to

around 10 m using the Pimenteiras kinetic parameters. The results are much closer to the gas composition of the field.

In this study, the definition of a consistent and more precise kinetic scheme for the Devonian Pimenteiras formation (organic-rich levels A, B, C, and D), was supported by the FSM and implemented into a 3D PSM simulator. Numerical modeling simulations demonstrate a significant impact when comparing the use of the Devonian Shale generic kinetic library (e.g., Woodford Shale) and the Pimenteiras kinetics, as observed in Table 8. This is evident not only in the lateral variation of maturity but also in the vertical distribution of maturity and hydrocarbon generation. Simulation Scenarios A and B are presented int the Figure 56.

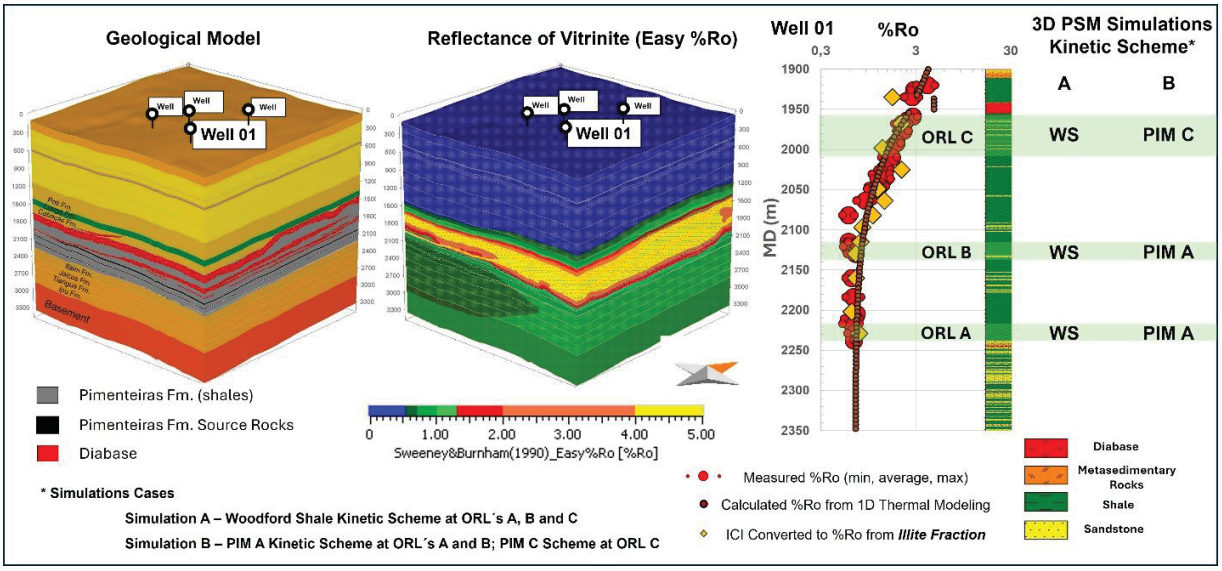

Figure 56 - Experimental design of the 3D Petroleum System Modeling simulations showing the geological model used (left), the three-dimensional result of the predicted vitrinite reflectance (center) and the detail of the Well 01 ORL´s A, B and C, coupled with thermal calibration using vitrinite data and illite crystallite index. Experiments A and B employed different kinetics assignments as described in the text, and their results were compared.

The coupled effect of the: 1) the differences in the compounds generated in each activation energy classes (Figure 48) and, 2) substantial differences in the maturity of the source rock due to the distance between the ORL´s to the heating source (diabase sills) (Figure *53* and Figure 56), will lead to significant differences in several parameters and outputs of petroleum system modeling. Important differences in timing and amount of

source rock maturation are expected as well as in the type, phase and quantities of predicted hydrocarbons.

In this study, the analysis focused specifically on the impact of kinetic scheme specifically defined for the Pimenteiras Formation on transformation ratio of organic matter on the masses of generated hydrocarbons and the distribution of these masses along the area of the 3D model for each modeled organic-rich interval.

The area of the 3D PSM model is situated north of the Parnaíba Basin and has been explored for conventional oil and gas, resulting in several discoveries. It is important to note that interest in the unconventional production of shale oil and gas has recently been on the rise despite the unclear legislative regulations governing this exploration method in Brazil. This area has a significant change in the sill intrusion configuration from east to west. In the eastern part, where the well is located, a massive intrusion of diabase sill occurs at the top and middle of the Pimenteiras Formation, near to ORL´s D and C, in contrast, in the west, the sills are more concentrated near the top (ORL D -Figure 44 and Figure 56).

This configuration and the resulting distance from the thermal source led to a decrease in the hydrocarbon transformation ratio of ORL´s B and A. The further the source rock is from the thermal influence of the diabase sills, the fewer hydrocarbons are generated from the source rock. This effect is evidenced in the transformation ratio of the source rock, as shown in Figure *53*, where in the northeast area ORL´s C and B are almost 100% transformed, while in the southwest area, ORL C is less transformed with a lower transformation ratio, and ORL´s B and A are nearly immature.

The numerical results presented in the Table 8 show percentage differences of -61.8% -17.2 % and -0.8 % when comparing the average transformation ratio of the Pimenteiras kinetics with Woodford for ORL´s A, B, and C, respectively. At the level of ORL C, the difference of -0.8 % can be considered negligible since the source rock is almost totally transformed (90.18 % versus 89.50 % of average TR). However in ORL A, at the base of the Pimenteiras Formation and far from the heating source the differences are significant, with 42.35 % of average TR using Woodford versus 16.17 % using the

Pimenteiras kinetics, resulting in a total difference of -61.8% between the modeled scenarios (Table 8 and Figure *53*).

These results indicate that the source rock, located far from the heating source, did not reach sufficient conditions for the generation and expulsion of hydrocarbons when modelled with a most precise kinetic scheme. Additionally, the southwest part of the 3D PSM exhibits TR values near zero at ORL´s A and B, showing adequate generation conditions only in ORL C (Figure *53*). The differences in transformation ratio directly reflect on the hydrocarbon's masses generated and their different compounds. Additional simulations were carried out using 4 Compounds kinetic parameters and the generated masses were grouped in Gas (Methane + C1 to C5 Compounds), Oil (C6 toC15 and C15+) and Bulk (Oil + Gas) products. The bulk composition masses (Table 8 and Figure 57) show results consistent with the transformation ratios for ORL´s A, B, and C. For ORL A, the total generated masses for oil and gas were 3.82 MM tons using the Woodford Shale compared to 1.28 MM tons using the Pimenteiras kinetics, representing a decrease of 66.8 % in the expected potential of generated hydrocarbons. This trend of variation in potential between Scenario A and B is similar for the generated masses of oil (Figure 58 and Table 8). Comparing the masses from the Woodford scenario to the Pimenteiras scenario, differences of -70.3%, -36.9% and -23.2% were observed for ORL´s A, B, and C, represented by oil masses of 3.29, 11.35 and 42.94 MM tons using the Woodford kinetics and 0.98, 7.16 and 32.99 MM tons with the Pimenteiras kinetics.

Parameter	Organic Rich Level	Scenario A PIM *	Scenario B WS *	Diff (%)**
Transformation Ratio (%)	ORL A	16,17	42,35	-61,8
	ORL B	54,73	66,06	-17,2
	ORL C	89,50	90,18	-0,8
Bulk Generated Masses (Oil + Gas) along the 3D PSM Model (MM Tons)	ORL A	1,28	3,82	-66,6
	ORL B	10,99	13,65	-19,5
	ORL C	51,83	52,44	-1,2
Bulk Generated Masses (Oil + Gas) (Tons per sqkm)	ORL A	7555,00	22610,00	-66,6
	ORL B	65050,00	80808,00	-19,5
	ORL C	306674,00	310343,00	-1,2
Generated Masses of Gas along the 3D PSM Model (MM Tons)	ORL A	0,22	0,52	-58,8
	ORL B	2,70	2,30	17,3
	ORL C	10,50	9,49	10,6
Generated Masses of Gas (Tons per sqkm)	ORL A	1275,00	3095,00	-58,8
	ORL B	15955,00	13598,00	17,3
	ORL C	62183,00	56205,00	10,6
Generated Masses of Oil along the 3D PSM Model (MM Tons)	ORL A	0,98	3,29	-70,2
	ORL B	7,16	11,35	-36,9
	ORL C	32,99	42,94	-23,2
Generated Masses of Oil (Tons per sqkm)	ORL A	5809,00	19514,00	-70,2
	ORL B	42436,00	67209,00	-36,9
	ORL C	195197,00	254138,00	-23,2

* PIM - Pimenteiras Fm. Kinetic Scheme - WS - Woodford Shale Kinetic Scheme

** (PIM/WS)-100%

Table 8 - Differences in 3D PSM simulations results using the Woodford Shale and Pimenteiras kinetic schemes for transformation ratio, generated masses of oil and gas and oil+gas (bulk) for the organic rich levels A, B and C of the Pimenteiras Formation, Parnaíba Basin. Values are presented in Million of Tons for the whole area of the 3D PSM (169 sqkm) and in tons per square kilometer. Transformation ratio is expressed as the average along the whole model (100x100 m cell size – totalizing 17100 cells per interval).

The results from compositional simulations also revealed significant differences in the masses of generated gas (Table 8 and Figure 59). For the basal level OLR A, the differences are -55.8 % (0.51 MM tons for Woodford versus 0,22 MM tons for Pimenteiras), consistent with the transformation ratio and bulk generated masses.

However, for the ORL´s B and C there is an inversion in the potential, with Pimenteiras Scenario contributing with more amount than Woodford Scenario, showing a positive difference of 17.3 % for ORL B and 10.6 % for ORL C (2.3 and 9.49 MM Tons for B and C from Woodford versus 2.7 and 10.50 MM tons from Pimenteiras). This difference is mainly due to the variation in the main activation energy peak from 52 kcal/mol at Pimenteiras ORL C to 55 kcal/mol for Pimenteiras ORL A, associated with the distance from the heating source and a higher GOR of the main Ea potential of the Pimenteiras compositional kinetics compared to the Woodford kinetic potentials.

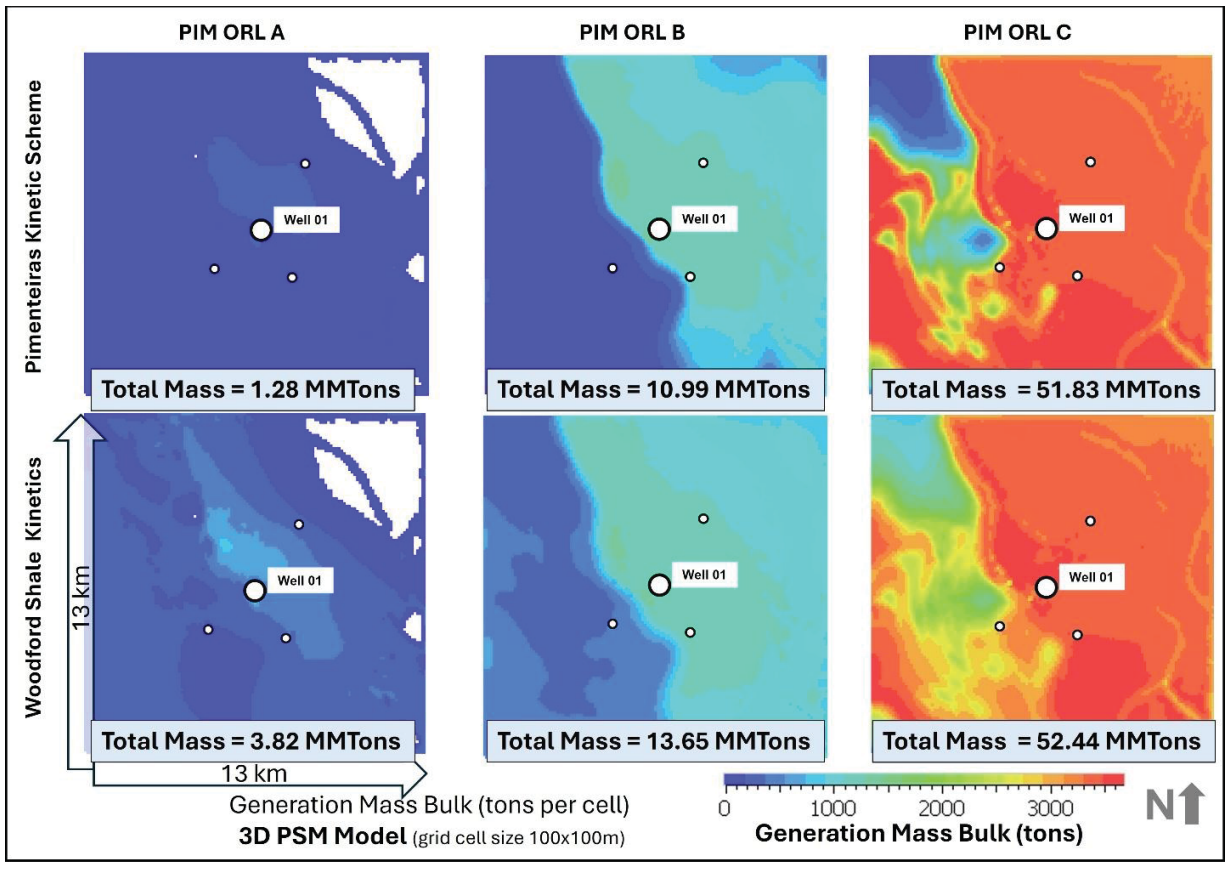

Figure 57 - Simulation results of generation mass of oil + gas (bulk generation) in the 3D PSM. Upper line: using the new kinetic parameters for the Pimenteiras formation and the impact at ORL A (left), ORL B (middle) and ORL C (right); Lower Line using Woodford Shale Kinetics from Petromod library (Hantschel and Kauerauf, 2009).

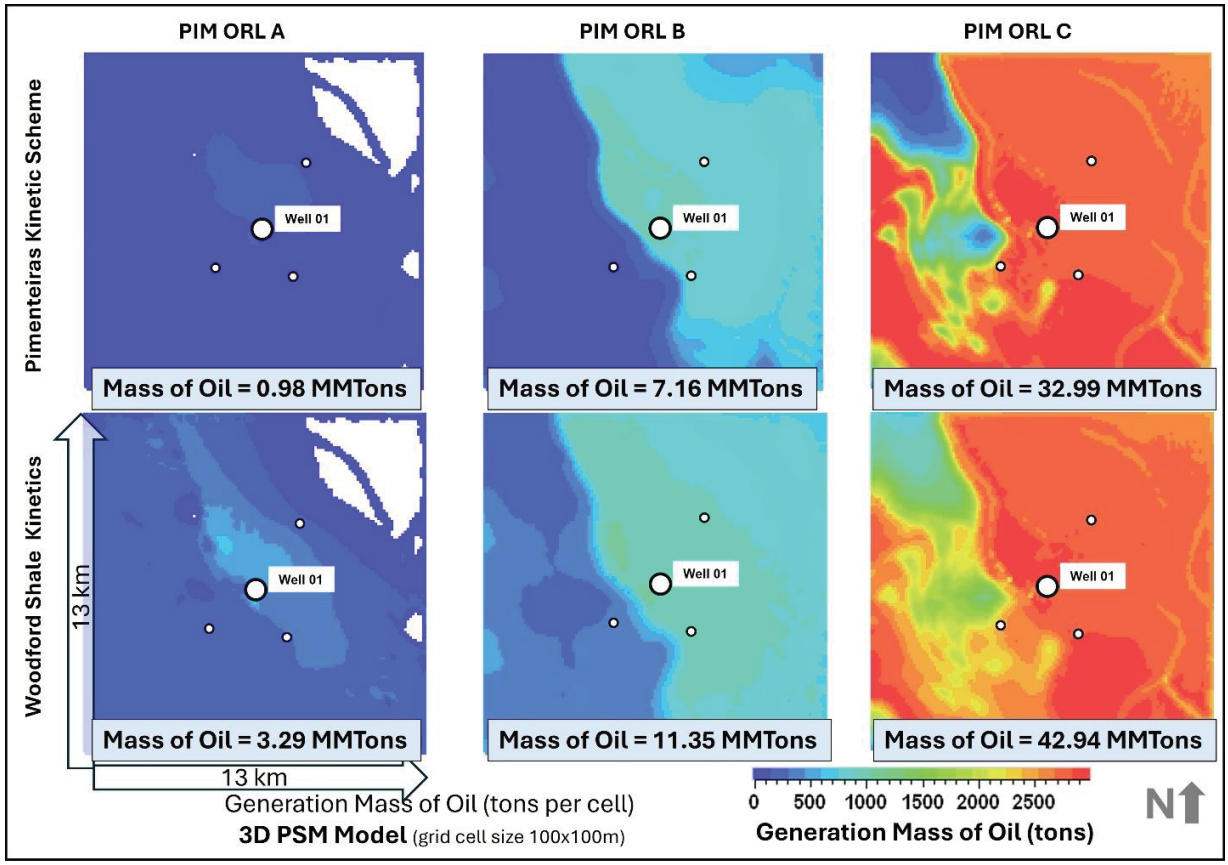

Figure 58 - - Simulation results of generation mass of oil in the 3D PSM. Upper line: using the new kinetic parameters for Pimenteiras formation and the impact at ORL A (left), ORL B (middle) and ORL C (right); Lower Line using Woodford Shale Kinetics from Petromod library (Hantschel and Kauerauf, 2009).

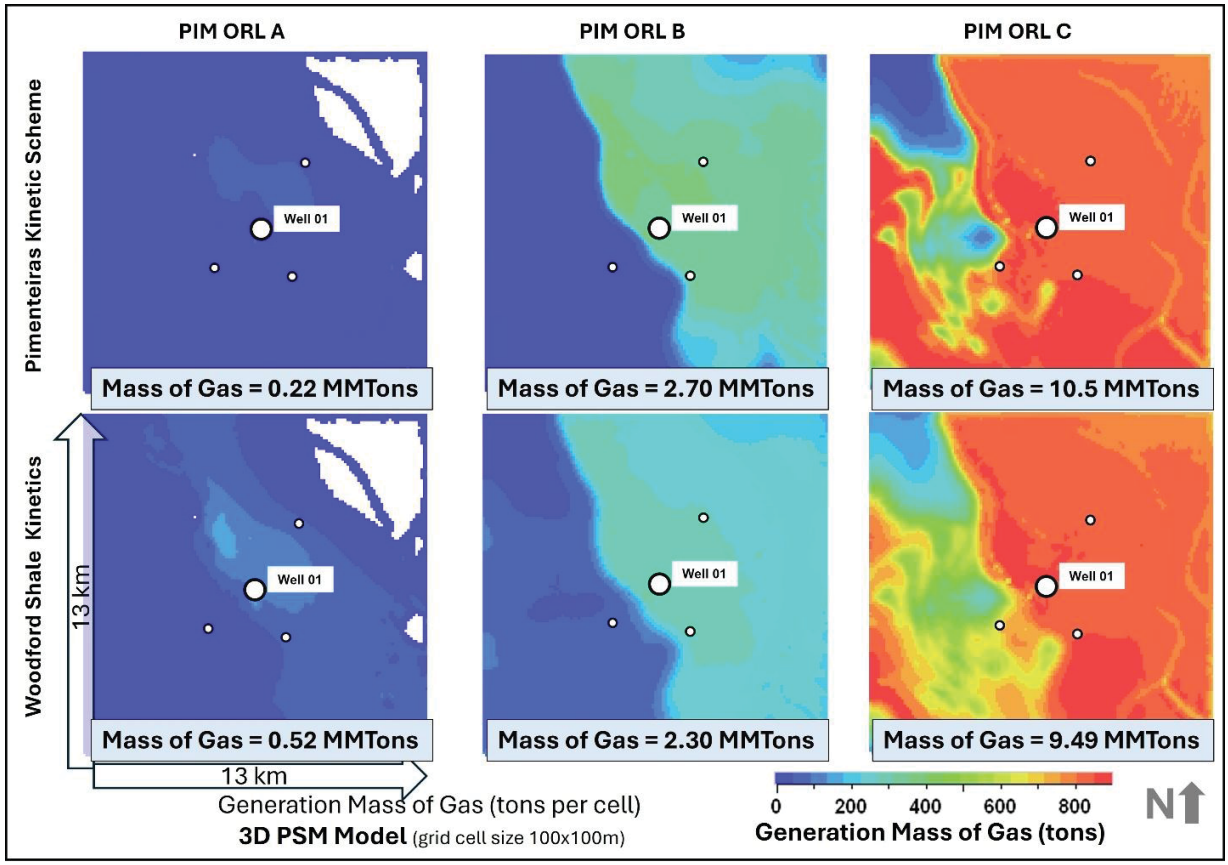

Figure 59 - Simulation results of generation mass of gas in the 3D PSM. Upper line: using the new kinetic parameters for Pimenteiras formation and the impact at ORL A (left), ORL B (middle) and ORL C (right); Lower Line using Woodford Shale Kinetics from Petromod library (Hantschel and Kauerauf, 2009).

5.3. The use of Kubler Index from decomposed Illite fraction as support of the reflectance of vitrinite in the atypical petroleum systems modeling.

The use of variation of clay mineral crystallinity has been extensively used to determine a certain grade of metamorphism on metasedimentary rocks since the first establishment in 1964 and 1967 in the classic papers of Bernard Kubler (Kubler 1964 and Kübler (1967), who stated *" Qualitatively, the crystalline structures become purified, their X diffractions diagrams become more complete and their streak profile becomes more tapered"*. During the early diagenesis, initial smectite, detrital or from volcanic glass origin, undergoes progressively transformation to illite in temperatures near to 90 °C (Frey and Robinson, 1999). During the late diagenesis to early anchizone, thin packets of bedding-parallel authigenic illite are gradually replaced by larger crystals of muscovite. These crystals of muscovite continue to evolve into larger and mature muscovite in response to a continuous increase in temperature and pressure (Frey and Robinson, 1999).

The process of smectic/illite/muscovite transformation from diagenesis to epizone was fully described in literature along the time(Brigatti and Guggenheim, 2002; Ferreiro Mählmann et al. 2024; Frey and Robinson, 1999; Guggenheim et al. 1995; Johnson et al. 2020; Mählmann and Frey, 2012; Mullis et al. 2017; Stern et al. 1991; Warr and Ferreiro Mählmann, 2015a and 2015b), including the recognizing on XRD diffractogram patterns, the standardization of Kubler Index measurements, and the correlation with organic matter thermal parameters as vitrinite reflectance and bitumen reflectance.

The techniques of low-grade metamorphism recognizing and quantification were extensively studied in the Alps areas, a regional diagenesis to low-medium grade of metamorphism, by authors as Frey and Robinson (1999), Kubler (1964), Kübler (1967), Mählmann and Frey (2012), Mullis et al. (2017), Stern et al. (1991) Warr and Ferreiro Mählmann (2015a), and extended for other author to different areas and geological contexts as Campos et al. (2015), Elizabeth Garduño-Martínez et al. (2015), Pytte (1982), Pytte and Reynolds (1988) and Santos (2017).

The process of conversion of smectite into illite from the point of view of kinetic process, using pressure and temperature variations along the time was better explored and described by Pytte (1982), e Pytte and Reynolds (1988) and Reynolds (1980). These authors described a continuous process of transformation of I/S pairs to pure illite phase. And these authors introduce the use of illite crystalline in contact metamorphism settings.

The challenge of quantification of this process on XRD data consists of the separation of the intermediate phases from the end members (smectite, illite and muscovite) at the main peak of illite/muscovite micas at ~10Â (~ 8.8 °2θ), since during this kinetic transformation different stages/phases can coexist. The most relevant advances in that field of research were made by Lanson (1997), Lanson et al. (1998), Lanson and Champion (1991) and Lanson and Velte (1992). Lanson and Velte (1992), studying clay diagenetic evolution in the Paris Basin, developed a technique of decomposition of X-Ray diffraction patterns to better measure the KI at each of I/S or pure illite/muscovite phase, through a software called DecompXR, where it is possible to load XRD diffractogram data into the interest interval (in this study from 3.5 to 10.5 °2θ), adding manually some predicted peak phases (eg. illite, chlorite, muscovite, pyrophyllite, talc) and perform an automatic adjustment of the decomposed peaks with measured data.

In the present research work, the peaks of the 207 samples (Table 2) were decomposed into de interval from 3,5 to 10 of clay fraction diffractogram using the DecompXR software Lanson and Velte (1992), the Kubler Index (Full width at half maximum – FWHM, Kübler, 1967) was measured on the peaks of illite and muscovite phases. These values of KI were converted to equivalent vitrinite reflectance using an exponential adjustment of the KI-Ro pairs (Ki-Ro Illite and KI-Ro Muscovite) proposed by Mählmann and Frey (2012), as shown in Figure 31. The Kübler Index values of converted equivalent vitrinite reflectance (Ki-Ro Illite and KI-Ro Muscovite) were compared with the measured vitrinite reflectance (Table 4) and with the calculated vitrinite reflectance (From 1D PSM – Easy Ro - Sweeney et al. 1995). Figure 60 shows the comparison between the XRD decomposed phase of illite, converted to equivalent vitrinite (KI-Ro Illite), yellow diamonds in the graph, with measured range of vitrinite (minimum, average and maximum - red circles) showing a good correlation along the profile of well A. The points of illite

show the increase of thermal stress and consequently increase in values of measured vitrinite and 1D PSM calculated %Ro (small dark red points) nearby to diabase intrusions. The values of calculated vitrinite at 1300m are around 0.7 %Ro increasing to 4.0 %Ro in the top of the diabase main sill (~1680m), this tendency is followed by the measure vitrinite and illite KI-Ro from illite. The whole interval from 1680 to 1900 m, is intruded by several diabase sills, and the calculated vitrinite reaches the maximum of 4.0 (threshold of Petromod calculation). From the 1900m to the bottom of the well A there is a decrease of thermal stress, and the tendency of all thermal parameters returns to a “burial” pattern. The data of measured vitrinite shows the return of the curve to values of vitrinite around 0.7-0.8 %Ro, followed by the calibrated results of modelled %Ro and for the values of the illite phase equivalent vitrinite (KI-Ro Illite). In the top right of Figure 60 the results of all decomposed peaks for illite, muscovite and chlorite are presented. The smectite/illite and muscovite peaks are in the interval from 8.0 to 8.6 (°2θ position), showing differences in height and width of peaks, indicating continuous changes in crystalline reorganization of I/S pairs (Pytte, 1982; Pytte and Reynolds, 1988). The peaks classified as muscovite phase are well centered between 8.75 to 8.8 (°2θ position), presenting the highest intensity and sharpness, while the illite peaks are less developed in terms of intensity and sharpness, with values of °2θ from 8.6 to 8.7.

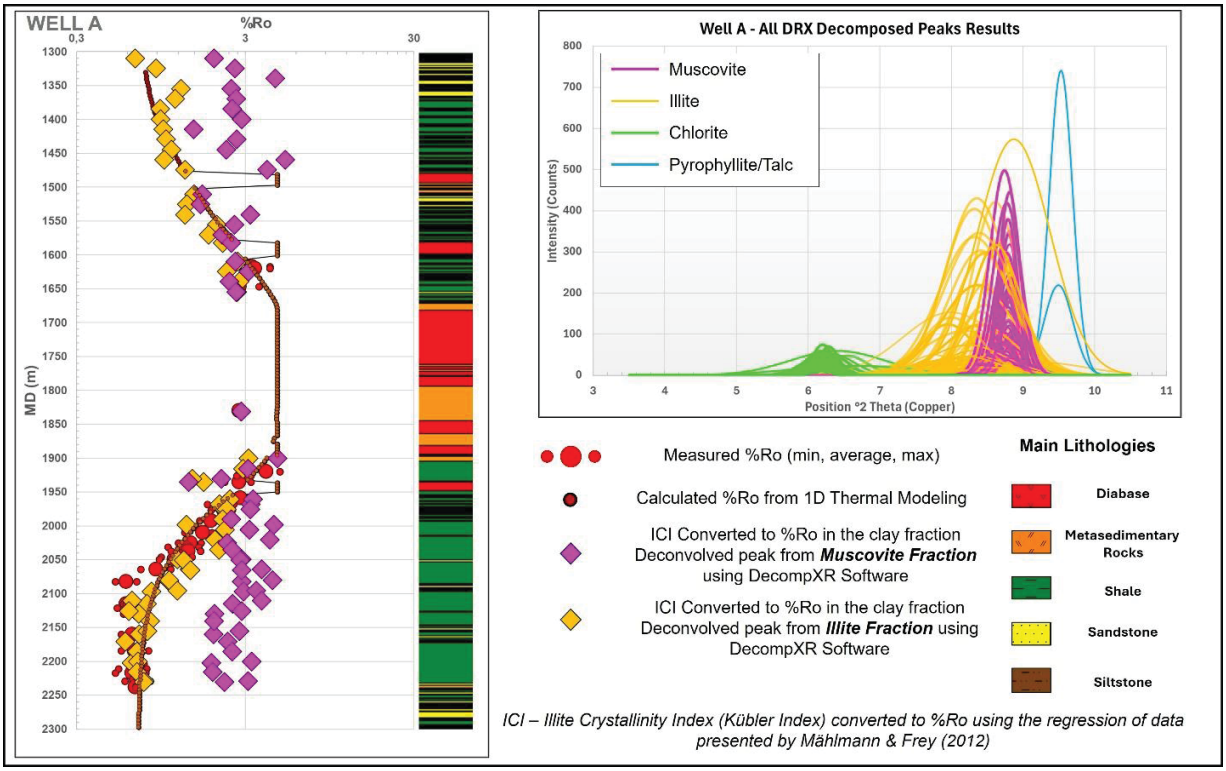

Figure 60 - Correlation between measured vitrinite (red points), simulation results of reflectance of vitrinite (small continuous points and line) and the equivalent reflectance of vitrinite from Kubler Index from Illite (yellow diamonds) and Muscovite (purple diamonds) fractions at Well A. At the top right the summary diffractogram of the decomposed phases results from 66 samples analyzed

The muscovite phase converted to equivalent vitrinite (KI-Ro Muscovite- purple diamonds -Figure 60) presents a straight line all along the profile, interpreted as an indication of detrital nature with a constant rate of crystallinity, inherent to the source area metamorphism level.

The results of KI-Ro Illite from well A were also compared with the results of modelled Smectite-to-Illite conversion, using the algorithm from Pytte and Reynolds (1988) and the maximum temperature reached in the past (Figure 61). Is it possible to note the correlation between the vitrinite trend (measured, calculated from 1D PSM and from KI) and the increase of the rate of smectite/illite conversion, coherent with maximum past temperatures. From depth of 1300 m to the top of main intruded interval (~1650 m) the conversion rates increase from 85% to 100%, decreasing from 100% at the base of the intrusion to 92% at 2150 m, returning to a burial trend with a decrease of gradient towards the base of the well. This turning point is reached when maximum past

temperatures reduce from 335°C (at the base of the thicker diabase intrusion, at 1905 m) to 155 °C.

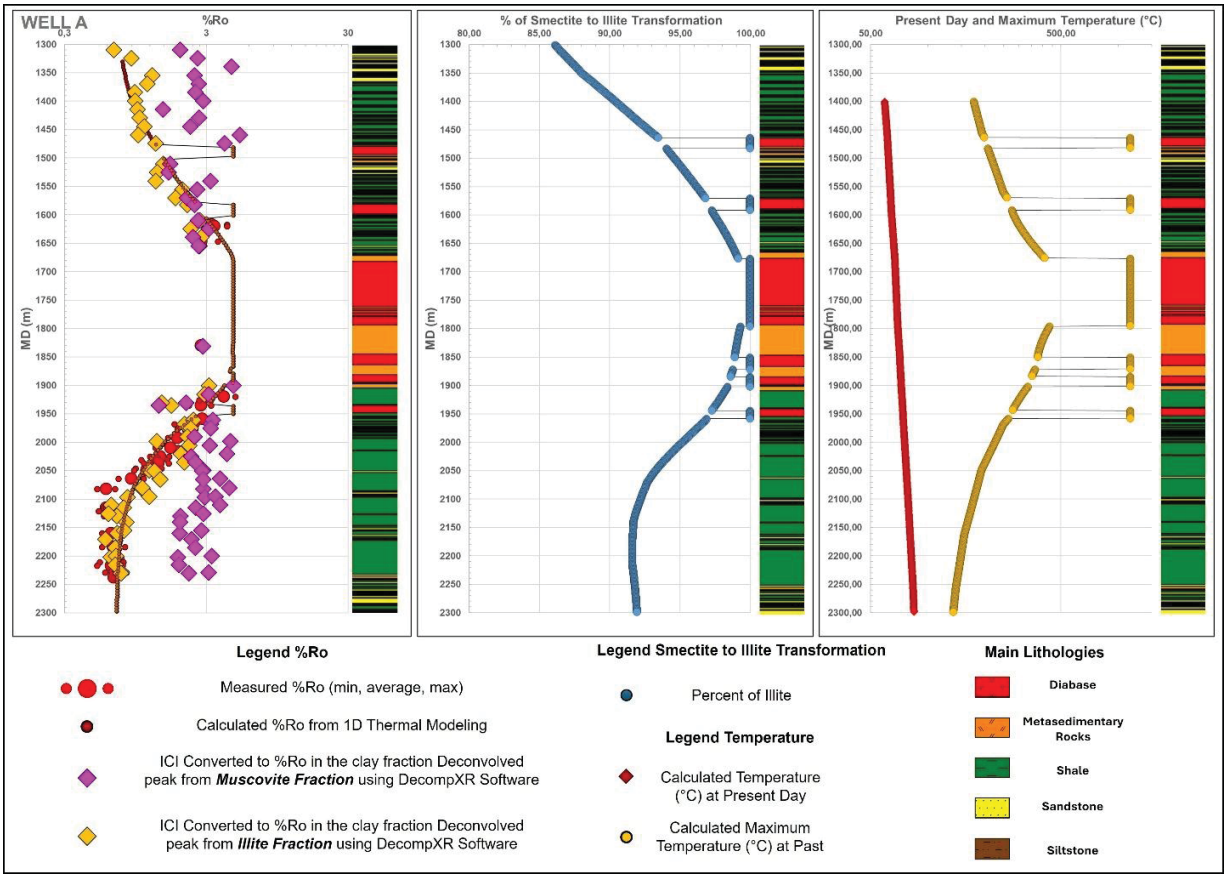

Figure 61 - Correlation between measured vitrinite and simulation results of reflectance of vitrinite (left), percent of illite to smectite transformation (center) and present day and maximum past temperatures from 1D modelling (right), at Well A.

Well B presents similar diabase intrusions settings, with a major intrusion from 1600m to around 1900 m (Figure 62). The KI-Ro Illite matches very well with the calculated %Ro, calibrated with measured %Ro data. At the base of the well, there is an increase in the trend of KI-Ro Illite, probably due to an intrusion which was not drilled by the well. The KI-Ro Muscovite runs almost as a straight line along the well, in a range of %Ro greater than 3.0 (average of 3,07 % Ro – with a maximum of 5.31 %Ro). In the top right of Figure 62, the results of all decomposed peaks for illite, muscovite and chlorite are presented.

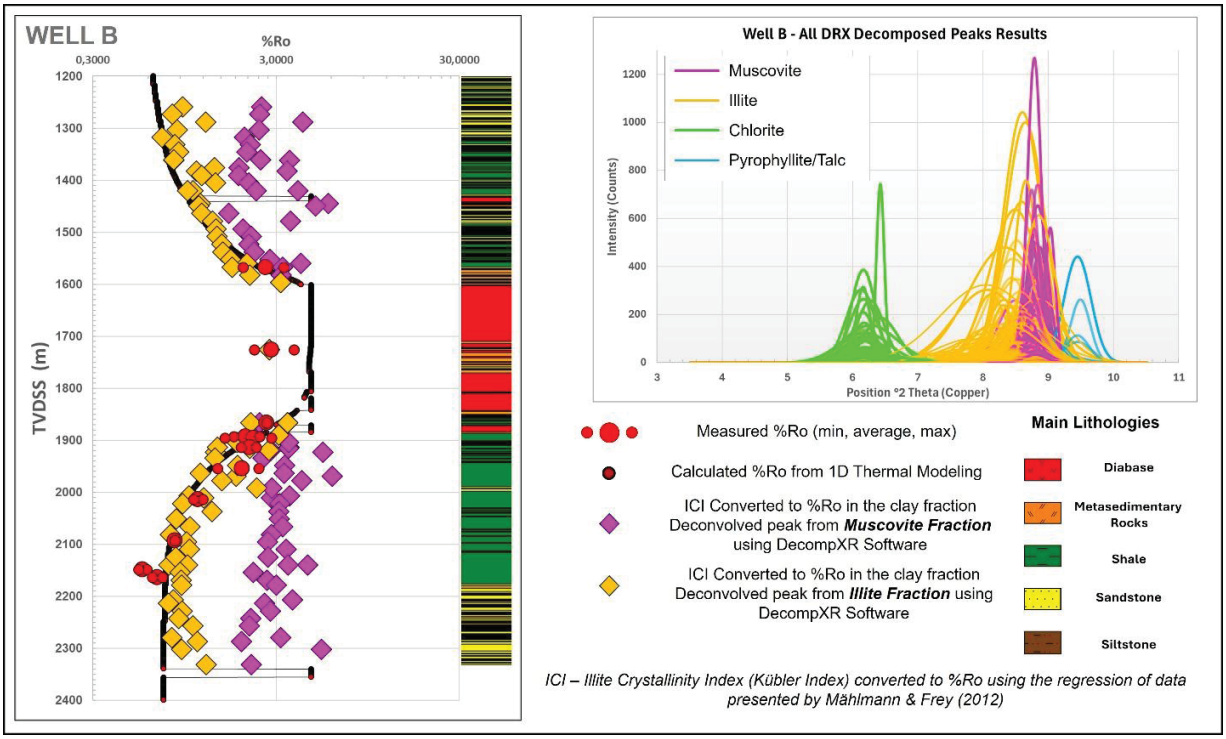

Figure 62 – Correlation between measured vitrinite (red points), simulation results of reflectance of vitrinite (small continuous points and line) and the equivalent reflectance of vitrinite from Kubler Index from Illite (yellow diamonds) and Muscovite (purple diamonds) fractions at Well B. At the top right the summary diffractograms of the decomposed phases results from 66 samples analyzed.

The results of smectite-to-illite conversion (Figure 63) are consistent with the measured KI-Ro Illite along the well, increasing from 82% of transformation at 1200 m, reaching 100% at the top of the main intrusion at ~1600 m. From the base of the diabase's (~1900 m) the calculated conversion rate reduces to 92% at the turning point in 2100 m, returning to the "burial" positive gradient (Figure 63 - center). The modelled past maximum temperatures reached 369 °C at 1600 m (top of diabase´s) and 298 °C at 1883 m (base of the intrusions - Figure 63, right).

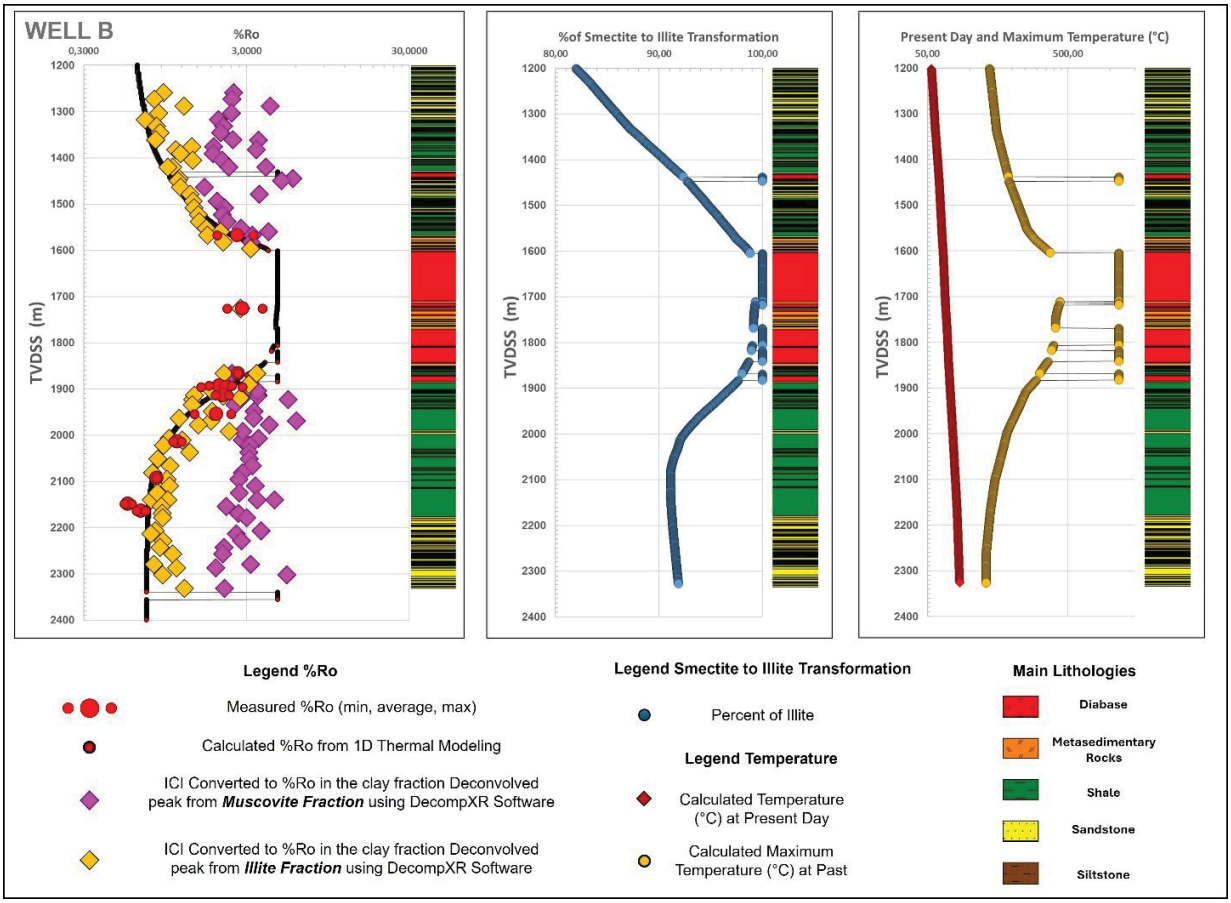

Figure 63 -Correlation between measured vitrinite and simulation results of reflectance of vitrinite (left), percent of illite to smectite transformation (center) and present day and maximum past temperatures from 1D modelling (rigth), at the Well B.

The well C presents a diabase intrusion at the top of the studied profile, from around 1380 m to 1500 m, and the KI-Ro Illite presented good correspondence with modelled vitrinite from 1D PSM as well as with the measured vitrinite reflectance points (Figure 64). The values of KI-Ro Illite range from 1.25 to 3.95 %Ro (average 2.10 %Ro). The KI-Ro Muscovite present values ranging from 1.79 to 4.62 %Ro, average (3.02 %Ro), showing a slight increase in the values towards the bottom of the profile (Figure 64).

The decomposed diffractograms (Figure 64) show the high level of crystallinity of Illite and Muscovite phases (high intensity and narrowing of the peaks) and the presence of a phase around 9.5 (°2θ), interpreted as extensive appearance of pyrophyllite, as shown in the semi-quantitative interpretation of XRD data (Figure 51). The data from Well

C was more challenging in recognizing and separating the Illite and Muscovite phase, due to the advanced smectite-to-Illite conversion rate, as demonstrated in the profile of the Figure 65, where the calculated values of conversion are greater than 95% along all studied interval, leading to a coexistence of high evolved I/S pairs with muscovite phases. (Figure 54 and Figure 65).

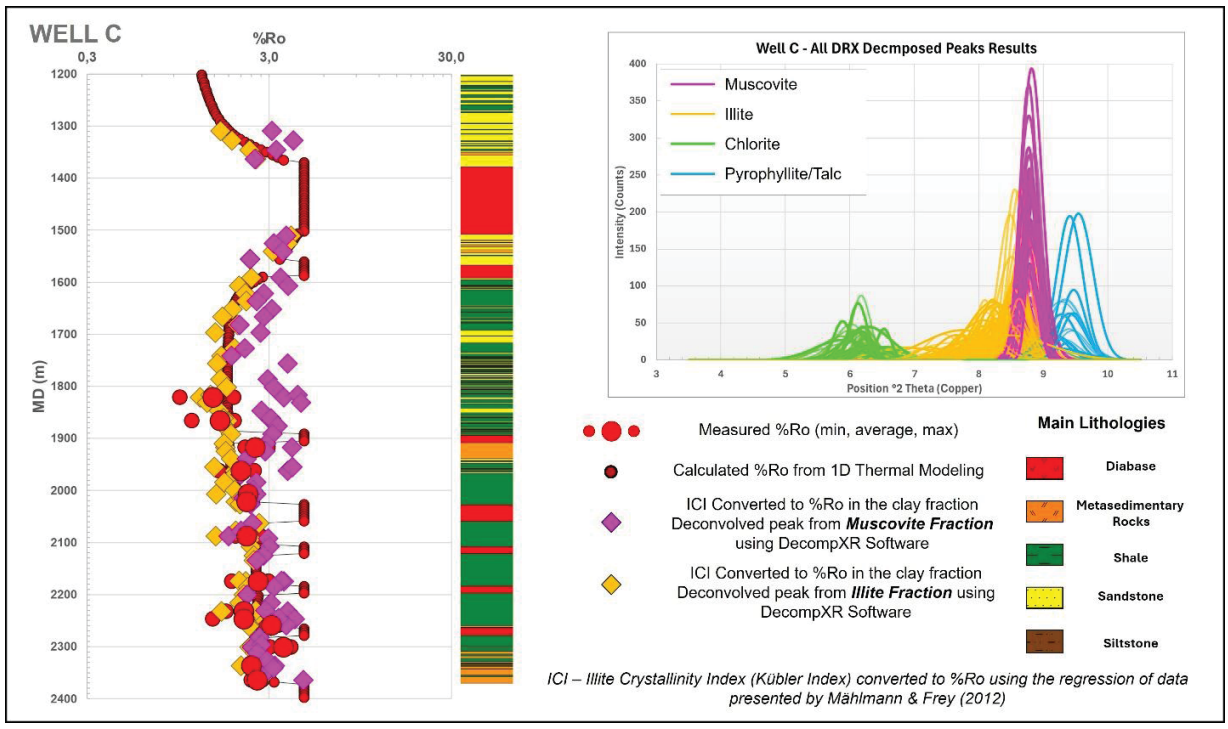

Figure 64 - Correlation between measured vitrinite (red points), simulation results of reflectance of vitrinite (small continuous points and line) and the equivalent reflectance of vitrinite from Kubler Index from Illite (yellow diamonds) and Muscovite (purple diamonds) fractions at Well C. At the top right the summary diffractograms of the decomposed phases results from 66 samples analyzed.

The maximum temperatures in the past from results of 1D PSM show values of 339 °C at the top of the main intrusion (1369 m) and 370 °C at the base of diabase interval (1504 m - Figure 65). In contrast with wells A and B, where the maximum past temperatures tend to decrease to low values with the distance of main diabase intrusion, reaching 136 °C at 2298 m in the well A (at the TD of the well - Figure 61) and 130 °C at 2325 m at well B (TD of the well - Figure 63), in the Well C, the maximum past temperature are always above 230 °C from 1700 m to 2300 m increasing to 312 °C at the base of the well. This continuous profile of high past temperatures is due to the presence of minor diabase intrusions along the profile, holding high thermal stress.

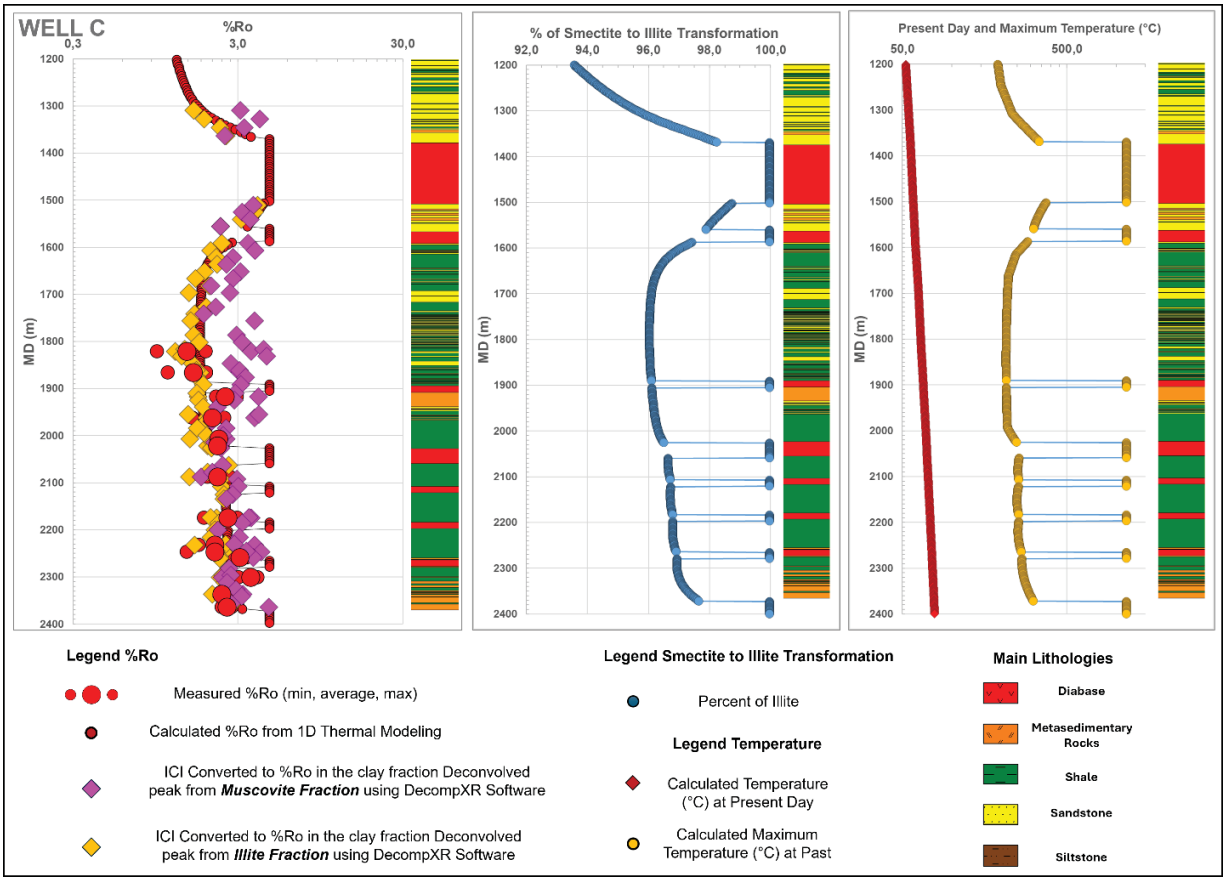

Figure 65 - Correlation between measured vitrinite and simulation results of reflectance of vitrinite (left), percent of illite to smectite transformation (center) and present day and maximum past temperatures from 1D modelling (rigth), at the Well C.

The results of comparison between Ki-Ro Illite, measured vitrinite reflectance and calculated vitrinite reflectance from 1D PSM along the wells A, B and C demonstrates good correlation between the inorganic and organic thermal parameters, in the ranges of thermal maturation from 0.3 %Ro to around 4.0 %Ro, a common range in the atypical petroleum system in igneous-sedimentary basins as Parnaíba basin.

The values of KI-Ro Illite range from 0.58 to 3.15 %Ro (Well A), from 0.31%Ro to 3.47 %Ro (Well B) and from 1.25 %Ro to 3.95 %Ro (Well C). And the values of measured Ki to illite phase range from 0.28 Δ°2θ to 1.23 Δ°2θ (Well A) from 0.26 Δ°2θ to 1.04 Δ°2θ (Well B) and from 0.23 Δ°2θ to 0.63 Δ°2θ (Well C), reliable with authigenic formation, in a wide range, from low-grade diagenesis, through high-grade diagenesis, low-grade and high-grade anchizone, reaching the epizone, showing an continuous increase in

crystallinity (not linearly positive with depth) due to the thermal influence of burial and contact metamorphism.

The values of KI-Ro Muscovite range from 1.38 %Ro to 5.18 %Ro (Well A), from 1.65 %Ro to 6.08 %Ro (Well B) and from 1,79 to 4.62 %Ro (Well C) while the values of measured KI to Muscovite phase range from 0.18 ∆°2θ to 0.58 ∆°2θ (Well A), 0.16 ∆°2θ to 0.50 ∆°2θ (Well B) and 0.20 ∆°2θ to 0.46 ∆°2θ (Well C), consistent with a detrital inherited phase from terranes with variable metamorphic ranges, mainly from anchizone to epizone.

5.4. Analysis of Esquevin index results versus Kubler Index, the Anchimetamorphic zone and Epizone characterization at the analyzed wells.

The use of the Kubler Index (Kübler,1967) together Esquevin Index (Esquevin, 1969) is an important tool evaluate the effects of evolution of metamorphism, together with the changes in chemical composition of clay minerals (Pamoukaghian, 2012; Peral, 2008 and Poiré, 1984) in sedimentary and low metamorphic sequences. The diagram presented in the Figure 66 is classical view of these two parameters, where in the X axis is plotted the Esquevin Index (ratio between intensity of *d*001 and *d*002 of illite reflection in clay fraction), with the chemical ranges of Mg Illite (Esquevin Index < 0.25) and Al Illite (Esquevin Index > 0.40). Along Y axis is plotted the measured Kübler Index, with the limits of diagenesis (KI > 0.42 ∆°2θ), anchizone (KI between 0.42 ∆°2θ and 0.25 ∆°2θ) and epizone (KI < 0.25 ∆°2θ), those zones, originally defined by Kübler (1967) and revised by Mählmann and Frey (2012), Warr and Ferreiro Mählmann (2015a, 2015b).

Figure 66, show that the composition of both illite and muscovite phases, from most samples, falls inside of the intermediate chemical composition field, without a clear tendency, even with the increase of crystallinity. In the three wells, some of the samples present a more aluminous character, although, again, it is not possible to define a specific trend. In terms of crystallinity, all the muscovite phases are inside of the anchizone, with few samples reaching the epizone field.

The illite phase samples at Well A presents a dispersion of level of crystallinity consistent with the thermal maturity observed along the profiles (Figure 54, Figure 60 and

Figure 61), and few samples reaching the field of anchizone. Similar tendency of increasing maturity is observed in the Well B, with samples ranging from low crystallinity, and few samples reaching the anchizone field, in accordance with the maturity, smectite-to-illite conversion and maximum past temperature profiles, as observed in the Figure 54, Figure 62, Figure 63. The Well C presents a more evolved crystallinity, with all samples reaching at least the high-grade diagenesis zone (KI < 1.0 ∆°2θ - Ferreiro Mählmann et al. 2024) and a significant number of samples reaching the anchizone field. It can be explained since the thermal status reached by Well C led to a high smectite-to-illite conversion (above 95%), improving the crystallinity of authigenic illite phase near to the detrital muscovite.

This is also evidenced in the semi-quantitative interpretation of total powder and clay fraction from XRD data, where in the Well C, there is a decreasing of I/S contend, the appearance of pyrophyllite, and the increase in chlorite contend, if compared with the semi-quantitative analysis from wells A and B, where the relative quantity of I/S is greater than well C, and less percentage of I/M is found (Figure 49, Figure 50 and Figure 51). The Figure 67 presents the comparison between KI vs Esquevin Index plots with vertical profiles of maturity and smectite-to-illite conversion, at wells A, B and C.

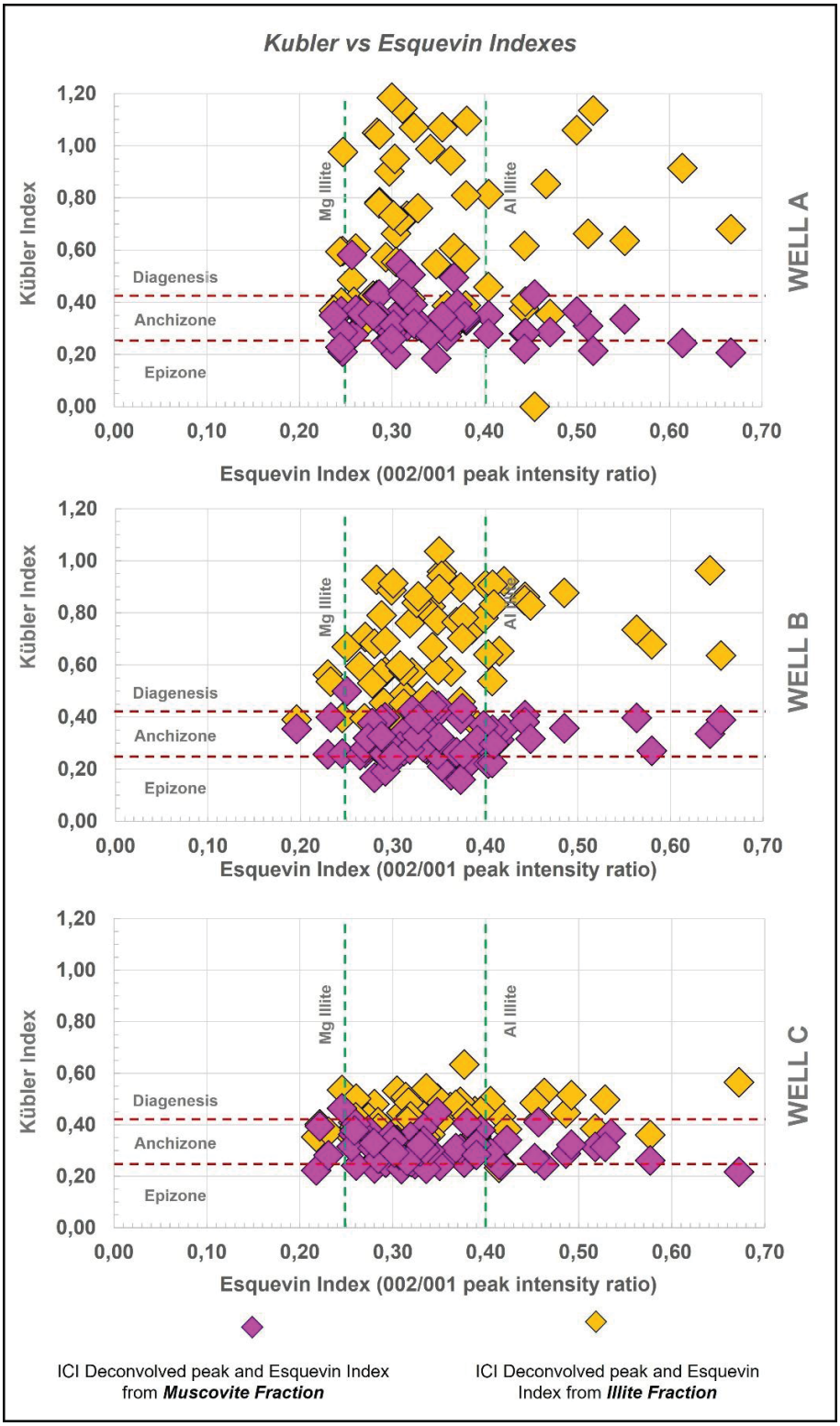

Figure 66 – Plot of crystallinity (Kubler Index) vs chemistry of illite (Esquevin Index) from wells A (top), B (center) and C (bottom)

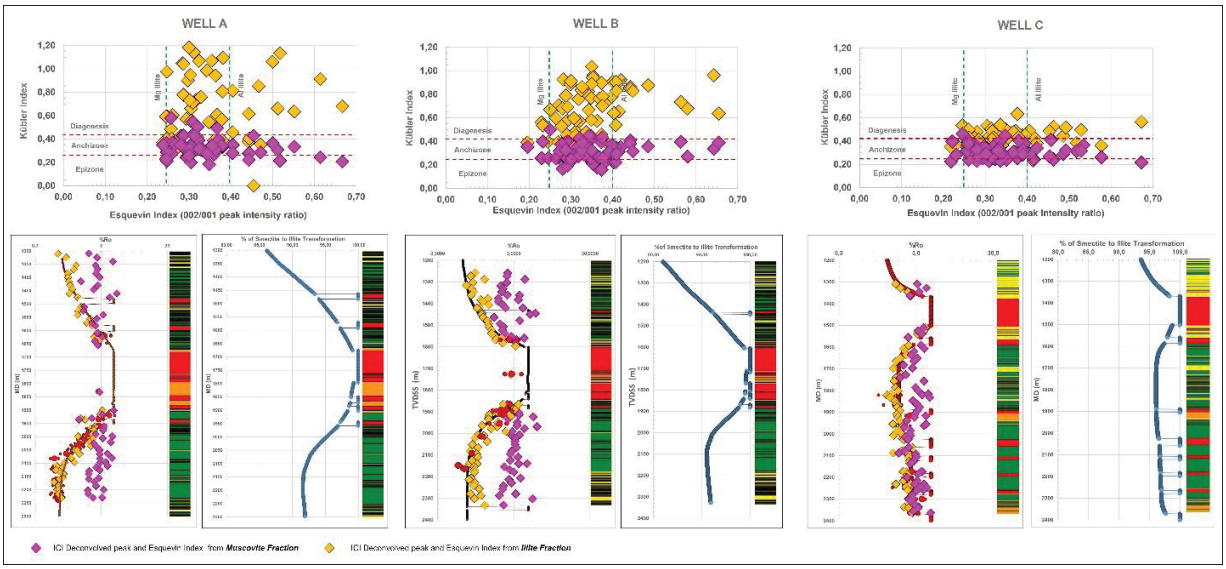

Figure 67 – Comparison between KI vs Esquevin Index plots with vertical profiles of maturity and smectite-to-illite conversion, at the wells A, B and C.

5.5. Correlation between Kubler Index and Vitrinite and the Anchimetamorphic zone and Epizone characterization at the analyzed wells.

The final hypothesis proposed for investigating in this research is the correlation between the Kübler Index (KI) and Vitrinite Reflectance (%Ro) in an atypical petroleum system context, specifically in the igneous-sedimentary settings found in the Parnaiba Basin. The comparison with previous studies, which were performed in regional metamorphism contexts, as described by authors as Ferreiro Mählmann (2012), Kubler (1964), Kübler (1967), Mählmann and Frey (2012), Mullis et al. (2017), Warr and Ferreiro Mählmann (2015a, 2015b), was also a commitment of this work, as well as the validation of this correlation or proposal of new correlation parameters.

To achieve this objective and to perform this comparison, a set of 37 pairs of measured vitrinite reflectance and Kubler Index data into the Meso-Devonian Eo-Carboniferous sequence of the Parnaíba Basin were used, according to the Table 9. The values of Kübler Index were calculated for both phases, illite and muscovite, and mathematical correlations were performed to compare the data.

#	Well	Av.Depth (MD)	Formation	KI Illite	%Ro Illite	KI Muscovite	%Ro Muscovite	%Ro Av.	%Ro Min	%Ro Max	%Ro n
1	Well A	1831,5	Pimenteiras	0,31	2,84	0,31	2,84	2,76	2,75	2,77	2
2	Well A	1935,0	Pimenteiras	0,49	1,70	0,58	1,38	2,76	2,26	3,24	4
3	Well A	1960,5	Pimenteiras	0,36	2,44	0,27	3,35	2,80	2,31	3,13	11
4	Well A	1968,0	Pimenteiras	0,40	2,12	0,28	3,24	2,17	1,79	2,56	32
5	Well A	2025,0	Pimenteiras	0,40	2,13	0,37	2,35	1,42	1,20	1,64	35
6	Well A	2050,5	Pimenteiras	0,62	1,29	0,31	2,81	1,14	0,93	1,35	16
7	Well A	2064,0	Pimenteiras	0,57	1,41	0,24	3,76	0,89	0,72	1,08	5
8	Well A	2082,0	Pimenteiras	0,73	1,06	0,31	2,87	0,59	0,51	0,68	11
9	Well A	2115,0	Pimenteiras	0,95	0,79	0,34	2,53	0,59	0,57	0,59	3
10	Well A	2130,0	Pimenteiras	1,05	0,70	0,43	1,97	0,70	0,57	0,79	27
11	Well A	2160,0	Pimenteiras	1,04	0,71	0,43	1,95	0,64	0,55	0,75	
12	Well A	2185,5	Pimenteiras	1,07	0,69	0,35	2,52	0,66	0,55	0,80	20
13	Well A	2229,0	Pimenteiras	0,98	0,76	0,29	3,12	0,68	0,58	0,82	23
14	Well B	1666,5	Cabeças	0,48	1,73	0,28	3,26	2,63	1,97	3,29	11
15	Well B	1828,5	Pimenteiras	0,32	2,75	0,32	2,75	2,83	2,27	3,74	3
16	Well B	1972,5	Pimenteiras	0,26	3,47	0,26	3,47	2,66	2,66	2,66	1
17	Well B	1996,5	Pimenteiras	0,29	3,10	0,29	3,10	2,04	1,76	2,44	3
18	Well B	2019,0	Pimenteiras	0,56	1,43	0,26	3,53	2,14	1,93	2,33	12
19	Well B	2119,5	Pimenteiras	0,65	1,21	0,31	2,82	1,12	1,06	1,19	4
20	Well C	1821,0	Cabeças	0,63	1,25	0,25	3,61	1,47	0,98	1,92	31
21	Well C	1866,0	Pimenteiras	0,47	1,77	0,29	3,08	1,61	1,13	1,93	34
22	Well C	1917,0	Pimenteiras	0,48	1,72	0,23	4,01	2,51	2,22	2,95	27
23	Well C	1962,0	Pimenteiras	0,43	1,94	0,24	3,80	2,10	1,59	2,49	29
24	Well C	2007,0	Pimenteiras	0,53	1,53	0,34	2,55	2,30	2,15	2,45	4
25	Well C	2022,0	Pimenteiras	0,43	1,96	0,38	2,26	2,26	2,07	2,43	4
26	Well C	2088,0	Pimenteiras	0,54	1,52	0,46	1,79	2,26	1,97	2,68	6
27	Well C	2173,5	Pimenteiras	0,41	2,05	0,26	3,50	2,61	1,87	2,98	12
28	Well C	2175,0	Pimenteiras	0,38	2,23	0,25	3,61	2,61	1,87	2,98	12
29	Well C	2230,5	Pimenteiras	0,34	2,53	0,31	2,86	2,17	1,74	2,50	6
30	Well C	2232,0	Pimenteiras	0,50	1,64	0,24	3,80	2,17	1,74	2,50	6
31	Well C	2245,5	Pimenteiras	0,39	2,21	0,27	3,38	2,17	1,47	2,46	6
32	Well C	2247,0	Pimenteiras	0,35	2,46	0,22	4,15	2,17	1,47	2,46	6
33	Well C	2260,5	Pimenteiras	0,37	2,33	0,29	3,06	3,08	2,79	3,37	2
34	Well C	2259,0	Pimenteiras	0,37	2,34	0,25	3,71	3,08	2,79	3,37	2
35	Well C	2301,0	Pimenteiras	0,37	2,34	0,36	2,41	3,58	3,03	3,94	4
36	Well C	2337,0	Pimenteiras	0,40	2,10	0,28	3,22	2,40	2,40	2,40	1
37	Well C	2364,0	Pimenteiras	0,33	2,67	0,20	4,62	2,57	2,39	2,76	2

Table 9 – Pairs of measured reflectance of vitrinite and Kubler Index from Illite and Muscovite decomposed phases, at the wells A, B and C.

Initially, the data from 37 pairs were, compared with the exponential trend lines for the 5 pairs of KI-Ro published from Frey and Robinson (1999), and for the three selected pairs from Mählmann and Frey (2012), (the last one was used to convert and obtain Ki-Ro Illite and Ki-Ro Muscovite values as presented in the Figure 60**Erro! Fonte de r eferência não encontrada.** to Figure 65. The correlations, equations of exponential adjustments and r2 correlation coefficients are presented in Figure 68. It is possible to note that authigenic illite phase is consistent with the literature correlations, and the regression equation presented a r2 coefficient of 0.58. However, as expected, the detrital phases of muscovite did not present a consistent correlation between crystallinity and vitrinite reflectance, with a coefficient of correlation of 0.03 (Figure 68).

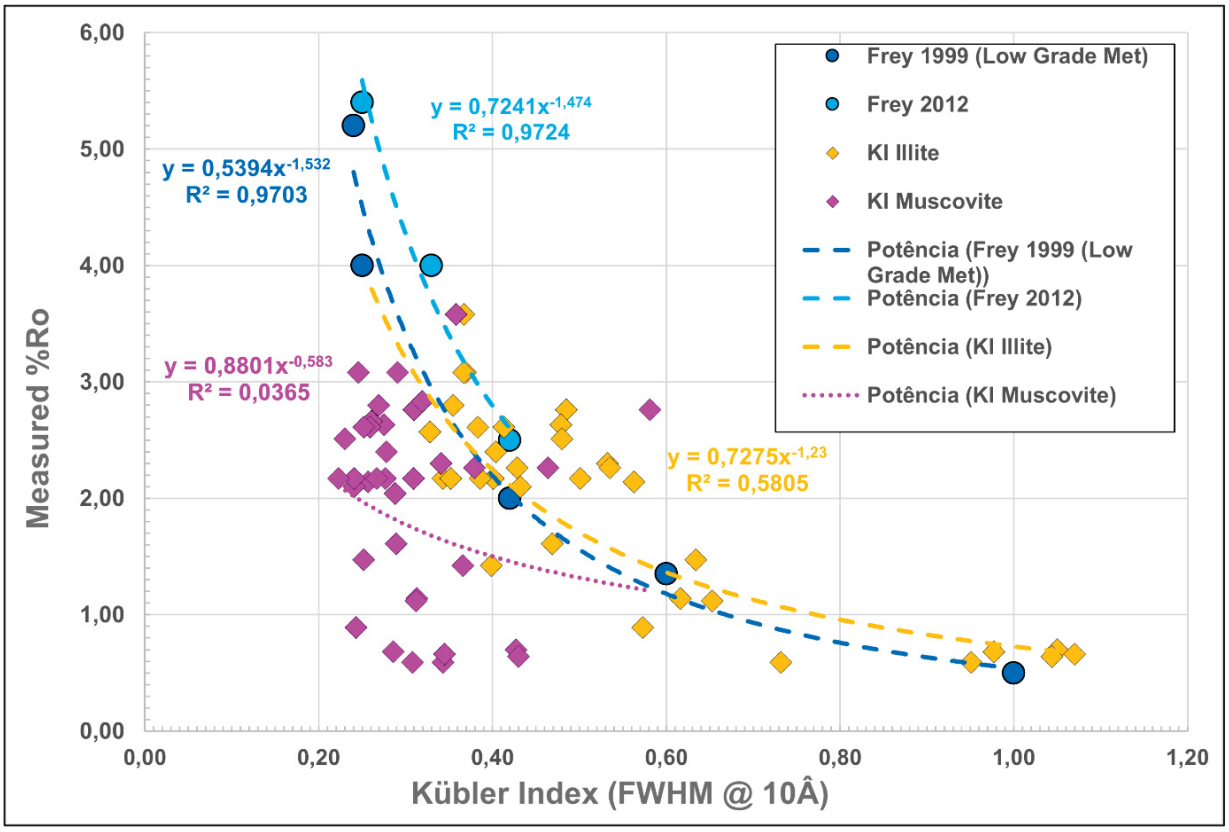

Figure 68 – Correlation between 37 pairs of measured vitrinite reflectance and Kübler Index (KI) measured for Illite (yellow) and Muscovite (purple) phases. The results are compared with the pairs of KI-Ro from Frey and Robinson (1999) e Mählmann and Frey (2012) reference points and their respective correlation using an exponential regression.

Finally, the KI-Ro pairs were plotted in the graph proposed by Ferreiro Mählmann et al. (2024), based on hundreds of samples from Alps, from dozens of PhD thesis studying regional metamorphism (Figure 69).

The plot of Ki-Ro Illite samples falls inside of the range of Orogenic Diagenesis and Metamorphism, between the interval of Low and High Geothermal intervals proposed by these authors. In terms of crystallinity and maturity, most of the samples are within high-grade diagenesis, low-grade anchizone and high-grade anchizone with a few samples falling into epizone range. The exponential adjustments of KI-Ro Illite pairs provided a correlation equation to be used in contact metamorphism settings, in igneous sedimentary basins, where the KI = 0.7399 Ro $^{-0,604}$, proposed in this research as an alternative to use

in this specific geological setting as an alternative to regional metamorphism contexts equations.

In contrast and as expected, most part of Ki-Ro Muscovite pairs fall outside of the main orogenic diagenesis and metamorphism trend proposed by Ferreiro Mählmann et al. (2024). Most samples are within low-grade and high-grade anchizone, with only a few in the epizone. The correlation factor calculated for KI-Ro Muscovite phase is very low, at 0.04, indicating no correlation with contact metamorphism in the atypical petroleum system of the Pimenteiras Formation, Parnaíba Basin, NE Brazil, and supporting the hypothesis of a detrital contribution from source areas.

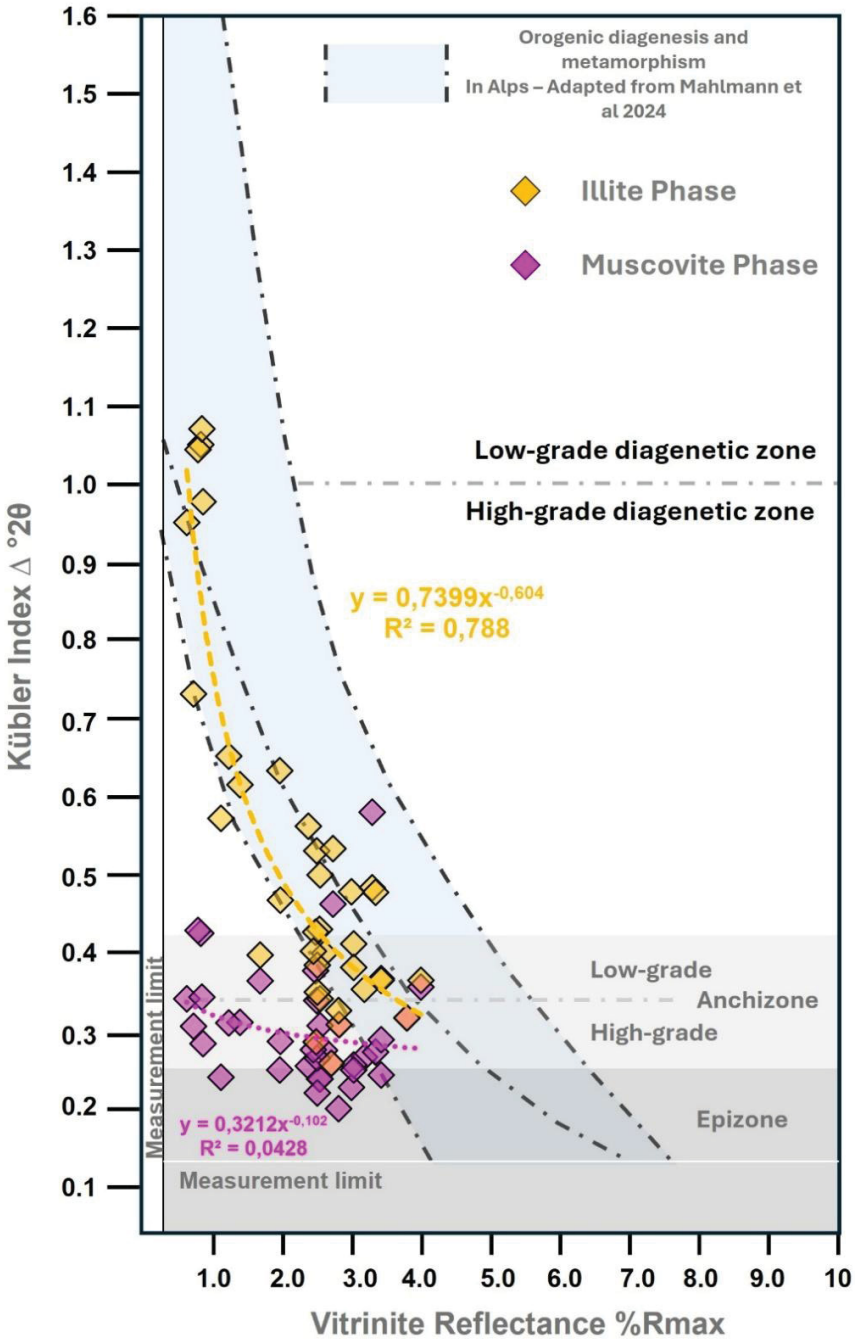

Figure 69 – Plot of 37 pairs of measured vitrinite reflectance and Kübler Index (KI) measured for Illite (yellow) and Muscovite (purple) phases into the pathway of diagenesis-metamorphism proposed by Ferreiro Mählmann et al. (2024) for regional metamorphism in the Alps, showing the Illite phase data match inside the range of orogenic diagenesis-metamorphism, while the Muscovite phase data did not match, indicating a detrital origin.

6. SCIENTIFIC CONTRIBUTIONS

Two scientific papers were produced as a result of the main outcomes of this integrated research project. The first one, entitled "**Compositional Kinetic Scheme for the selected organic-rich levels in the Pimenteiras Formation, Devonian of the Parnaíba Basin – Implications for Atypical Petroleum Systems Modeling**", presents the main results of compositional kinetic parameters of the Pimenteiras Formation, the sample screening, the analytical process, implementation, testing and results of this new scheme into the 3D Petroleum System Modeling. This paper was submitted to the **Marine and Petroleum Geology** journal in April of 2025, and until the moment of writing of this thesis, it is in the process of peer review.

The second paper, entitled "**The integration of Kubler Index and reflectance of vitrinite as thermal calibration parameters in the numerical modelling of the atypical petroleum system of the Pimenteiras Formation, Devonian of Parnaíba Basin, NE – Brazil**" debates the use of Kubler Index (KI) as support for vitrinite reflectance in atypical petroleum system. It describes the process of spectral decomposition of Illite and Muscovite phases on XRD data, the calculation of KI at illite phase, the conversion of KI to equivalent vitrinite, the applicability of this data on thermal calibration and the estimation of the range of contact metamorphism on igneous-sedimentary contexts. The paper is planned to be submitted to the **Natural Resources Research** journal or equivalent, when the internal revision is finished.

Compositional Kinetic Scheme for the selected organic-rich levels in the Pimenteiras Formation, Devonian of the Parnaíba Basin – Implications for Atypical Petroleum Systems Modeling

Eduardo de Mio [a,b] *, Henrique A. Lopes [a], Fernando Bastos Aragão [a], Manuela Yebra de Lima e Silva. [a], Nicolaj Mahlsted [c], Brian Horsfield [c], Frederico Silveira de Miranda [a], Diogo Michelon [a], Cassia Lima Cardozo [a], Anelize Manuela Bahniuk Rumbelsperger [b] ,L eonardo Fadel Cury [b].

[a] ENEVA, Board of Exploration and Low Carbon Technologies - Praia de Botafogo, 501 Torre Corcovado, sala 404 B. Rio de Janeiro (RJ) – Brazil Zip Code: 22.250-040

[b] LAMIR Institute, UFPR – Universidade Federal do Paraná, Centro Politécnico, Curitiba, Brazil; lamir@ufpr.br

[c] Geos4 GmbH - Peter-Huchel-Chaussee, 88 14552 - Michendorf - Germany - Phone +49 (0)33205 2 38 61 - info@geos4.de

ABSTRACT

Kinetics analysis is key to evaluating petroleum systems as they control hydrocarbon generation conditions, masses, composition and phases. In frontier basins, using kinetics from analogous source rocks introduces a high uncertainty in petroleum system evaluation. Source rock kinetics may differ within the same basin due to variations in depositional environment and composition. This study integrates new Rock-Eval, organic petrography, thermovaporisation, pyrolysis gas chromatography and bulk and compositional phase kinetics data with forward stratigraphic modeling (FSM) and petroleum system modelling (PSM) to improve the understanding of the Meso-Devonian Eo-Carboniferous atypical petroleum system of Parnaíba Basin, NE of Brazil. The analytical program was performed over 41 samples from four Organic Rich Levels (ORL´s) of Devonian Pimenteiras Formation Shales. Two samples were selected to execute Compositional Phase Kinetics analysis in organic rich levels (ORL) A and C. Alginite is the dominant maceral in more than twenty samples followed by, vitrinite, zooclasts, amorphous organic matter and bituminite. Vitrinite, graptolite and bitumen reflectance values range from 0.6 to 0.8% (%Ro). Phase kinetics results showed a narrow activation energy distribution (between 50-56 kcal/mol) in line with a homogeneous kerogen structure. The analysis of pyrolysate corroborates the deposition of algal/bacterial organic matter in a dominantly marine Type II kerogen environment. The stratigraphic analysis and FSM results indicate potential for extrapolating the kinetic scheme for selected ORL´s along the basin. These kinetic schemes were assigned to the 3D PSM simulator and compared with simulations using the Woodford Shale kinetic scheme. Differences of -66,6 %, -19,5 % and -0,8 % respectively for ORL´s A, B and C in generated petroleum masses, indicate significant effect of the kinetic scheme on PSM prediction. In conclusion, local kinetic analysis is essential for properly evaluating a petroleum system and minimizing exploratory uncertainties; its homogeneous composition and depositional environment support that the same kinetics can be extrapolated over a large area within a basin.

Keywords: 1; Parnaíba Basin 2; Atypical Petroleum System 3; Compositional Kinetics 4; Petroleum System modeling (PSM) 5; Forward Stratigraphic Modeling (FSM);

The integration of Kubler Index and vitrinite reflectance as thermal calibration parameters in the numerical modelling of the atypical petroleum system of Pimenteiras Formation, Devonian of Parnaíba Basin, NE – Brazil

Eduardo de Mio [a,b], Henrique A. Lopes [a], Lilian Souza da Silveira [a], Guilherme Fedalto [b], Larissa da Rocha Santos [a], Daniel Poiré [c], Luis Vigiani [c], Anelize Manuela Bahniuk Rumbelsperger [b] , Leonardo Fadel Cury [b].

[a] ENEVA, Board of Exploration and Low Carbon Technologies - Praia de Botafogo, 501 Torre Corcovado, sala 404 B. Rio de Janeiro (RJ) – Brazil Zip Code: 22.250-040

[b] LAMIR Institute, UFPR – Universidade Federal do Paraná, Centro Politécnico, Curitiba, Brazil; lamir@ufpr.br

[c] Centro de Investigaciones Geologicas – CIG – Universidad Nacional de La Plata - UNPL

ABSTRACT

Reflectance of vitrinite is the most common thermal calibration parameter in sedimentary basins, to evaluate and reconstruct the thermal history, although, factors as the scarcity of particles in devonian or older sediments and the high thermal stress reached in the igneous sedimentary petroleum systems lead to significant challenges in modeling process. This study integrates new Rock-Eval and organic petrography in addition to extensive X-Ray diffraction analysis (XRD) to improve the understanding of the Meso-Devonian Eo-Carboniferous atypical petroleum system of Parnaíba Basin, NE of Brazil. The analytical program was performed over 54 samples of vitrinite reflectance (%Ro) and 207 samples of XRD, from three selected wells in the central part of the basin, covering the entire Meso-Devonian Eo-Carboniferous sequence. Spectral decomposition on 10Â peak (*d001* position) was carried out in XRD data to separate diagenetic/anqui-metamorphic smectite/illite (I/S) phase from the metamorphic detrital muscovite phase. The Kubler Index, KI, (FWHM – expressed as °Δ *2θ*) was measured in the Illite phase, converted to equivalent %Ro and compared with the results of calculated %Ro along the three sets of 1D Petroleum System Models (PSM), originally calibrated with measured %Ro and the conversion ratio of smectite to illite was also calculated along these models. The Esquevin Index (ratio of d002/d001 reflections) was calculated and compared with KI along the profiles. The results demonstrate good correlation between KI (from Illite phase) with measured %Ro, allowing the use of KI for thermal calibration and indicating a progressive conversion of I/S (KI values from 1,23 to 0,23 °Δ *2θ*), from diagenesis zone, through anchizone, reaching the epizone, nearby to igneous intrusions. The muscovite phase KI values range from 0,58 to 0,16 °Δ *2θ,* corroborating the detrital nature of this phase, and does not correlate with calculated and measured %Ro, however, it is possible to note a progressive increase in metamorphism along the wells, suggesting that muscovite phase could have been recrystallized during the magmatic event. Finally, 37 pairs of KI vs %Ro were compared of literature data and showing reasonable correlation with pairs obtained in regional metamorphic contexts and validating the use of KI as an additional thermal proxy in contact metamorphism along atypical petroleum systems.

Keywords: 1; Kubler Index 2; Reflectance of Vitrinite 3; Atypical Petroleum System 4; Smectite/Illite conversion 5; Parnaíba Basin

7. CONCLUSIONS AND FINAL REMARKS

The main outcomes of this research highlighted the requirement and importance of specific improvements in PSM process, in atypical petroleum systems, in igneous-sedimentary basins, a context where paleo temperatures and pressures led the sedimentary sequences in ranges of late diagenesis, anchizone and epizone conditions.

In this context, the definition of a specific kinetic scheme for source rock transformation and the use of an inorganic thermal calibration parameter enhances the method by reducing uncertainties, culminating in more precise predictions of hydrocarbons products. These statements are especially valid in the Parnaíba Basin, where the atypical Meso-Devonian Eo-Carboniferous is responsible for dozens of natural gas accumulations.

The results of research can be grouped into three main lines:

New Geochemical Data – Pyrolysis, Organic Petrography and Vitrinite Reflectance Analysis

- The result of organic petrography shows that alginite is one of the dominant macerals in all ORL´s in the Pimenteiras Formation, together with amorphous organic matter and contributions from vitrinite, zooclasts, and bituminite. The pyrolysates of all analyzed samples are dominated by gas compounds and the petroleum-type organofacies plot within the paraffinic-naphthenic-aromatic (P-N-A) low wax petroleum type, a trend typically observed in source rocks containing marine Type II kerogens.
- Measured vitrinite reflectance data analysis demonstrates the scarcity of particles in the Devonian Pimenteiras Formation, the variable quality of the samples and the fingerprint of thermal stress due to the magmatism along the 3 studied wells. The average measured wells range from 0.56 to 3.99 %Ro and the maximum values ranges from 0.59 to 4.8 %Ro, highlighting the dispersion along vertical profiles, as result of heating during the emplacement of diabase sills.

Kinetics of Pimenteiras Formation and Implementation into 3D PSM

- The MSSV Pyrolysis results indicated a very narrow distribution of activation energies, concentrated between 50 and 55 kcal/mol, with one dominant potential accounting for at least 70% of the bulk reaction. The Pimenteiras ORL C displays a single peak at 52kcal/mol, while the Pimenteiras ORL A shows a distribution of activation energies between 50 and 60 kcal/mol, with the main peak centered at 55 kcal/mol. These results align with the predominance of selectively preserved algal organic matter, alginite, as determined through organic petrography.
- The comparison of the Pimenteiras ORL´s A and C kinetics, established in this research, with the Devonian Woodford shale kinetics in the 3D PSM model reveals significant differences in the average transformation ratio, which ranged from -0.8 % at ORL C, near the heating source, to -61.8 % at the basal ORL A. Differences were also noted in the bulk generated masses (Oil + Gas), with values of -66.6 %, -19.5 % and -1.2 % for ORL´s A, B, and C, respectively, when comparing simulations scenarios A and B. An inversion in the trends of this variation was also noted in the generated masses of gas versus oil, highlighting the importance of a compositional kinetic scheme in predicting phase and composition in atypical petroleum system modeling. The individual contributions of each organic-rich level will lead to hydrocarbon accumulation (or an expectation for in situ generation in the case of an unconventional approach) that will be controlled in terms of phase, composition, and percentage of trap filling by the correct kinetic input and appropriated thermal calibration of the numerical models. As consequence, hydrocarbon volumes generated and thermal maturation predictions from standard kinetic data, compared to the one presented in this work will have an important impact in the understanding of exploration potential of the Parnaiba Basin

XRD data Analysis, Decomposition and KI versus Ro Correlation

- The analyses of extensive dataset of X-Ray diffraction date demonstrates that the Kübler Index of decomposed illite phase, converted to equivalent vitrinite (KI-Ro Illite) presented good correlation with measured vitrinite reflectance and the 1D PSM calculated vitrinite along the three studied wells, demonstrating the equilibrium between two distinct kinetic processes in contact metamorphism settings. The KI from decomposed phase of muscovite, converted to vitrinite (Ki-Ro Muscovite) presents a straight pattern along the vertical profiles, interpreted as the fingerprint of the regional metamorphism at source area and a detrital characteristic of this mineral phase. The 3D PSM simulation results of smectite-to-Illite conversion are consistent with the amounts of I/S, illite and muscovite phases observed in XRD data along the 3 studied wells, and with the semi-quantitative interpretation of total powder and clay fractions.
- The Kübler Index from decomposed phase of Illite can be used as an inorganic thermal calibration parameter in atypical petroleum system, as support to measured vitrinite reflectance. The analysis of 207 XRD samples of clay fraction demonstrates correlation with the limits of Orogenetic Diagenesis and Metamorphism proposed by Ferreiro Mählmann et al. (2024) in regional metamorphism settings in the extensively studied area in the Alps, and a specific correlation equation for use in contact metamorphism settings in igneous sedimentary basins is proposed, where the KI = 0.7399 Ro $^{-0,604}$. This correlation equation was based on 37 pairs of measured vitrinite vs Kübler Index from Illite fraction. A calibrated Kübler Index has also a great potential to be used in PSM to evaluate the potential for hydrocarbon exploration of older stratigraphic intervals with scarcity of vitrine reflectance data, opening a new frontier for hydrocarbon exploration in the Paleozoic/older basins.

Finally, it is important to emphasize that the integration of the advancements achieved in this study, such as a dedicated kinetic model for source rock thermal maturation and the application of an alternative inorganic thermal calibration parameter, combined with conventional vitrinite reflectance measurement offers a more rigorous and

coherent methodological framework for petroleum system modeling in geologically complex settings as atypical petroleum systems. Nonetheless, critical sources of uncertainty, including the chronology and emplacement dynamics of igneous intrusions, compositional heterogeneity of magmatic bodies, and advective-convective components of heat transfer require further investigation, given their potential to significantly influence the thermal history prediction in numerical modeling.

REFERENCES

ABRAKASA, S.; KOUADIO, K. E.; ESSIAGNE, F.-H.; OURA, E. L. A Probable Connection between a Bitumen Sample from the Western Niger Delta and Isan Well Sample from the Lower Cretaceous (Neocomian) Shale. Open Journal of Geology, v. 12, n. 12, p. 1081–1092, 2022.

ALLEN, P. A.; ALLEN, J. R. Basin Analysis. Second Edition ed. Blackwell Publishing, 2005.

ALMEIDA, F. F. M.; CARNEIRO, C. D. . R. Inundações marinhas fanerozóicas no Brasil e recursos minerais associados. In: V. Mantesso-Neto; A. Bartonelli; C. D. R. Carneiro; B. B. Brito Neves (Orgs.); Geologia do Continente Sul-Americano: Evolução da obra de Fernando Flávio Marques de Almeida. p.43–58, 2004. Beca Editora.

ARAGÃO, F. B. Implicações do magmatismo na geração e migração de hidrocarbonetos na Bacia do Parnaíba, Brasil, a partir de modelagem 1D de sistemas petrolíferos., 2020. Rio de Janeiro: Faculdade de Geologia da Universidade do Estado do Rio de Janeiro.

BARBOSA, É. N.; CÓRDOBA, V. C.; DO CARMO SOUSA, D. Evolução estratigráfica da Sequência Neocarbonífera-Eotriássica da Bacia do Parnaíba, Brasil. Brazilian Journal of Geology, v. 46, n. 2, p. 181–198, 2016.

BEHAR, F.; KRESSMANN, S.; RUDKIEWICZ, J. L.; VANDENBROUCKE, M. Experimental simulation in a confined system and kinetic modelling of kerogen and oil cracking. Organic Geochemistry, v. 19, n. 1–3, p. 173–189, 1992.

BEHAR, F.; UNGERER, P.; KRESSMANN, S.; RUDKIEWICZ, J. L. Thermal Evolution of Crude Oils in Sedimentary Basins: Experimental Simulation in a Confined System and Kinetic Modeling. Revue de l'Institut Français du Pétrole, v. 46, n. 2, p. 151–181, 1991.

BEHAR, F.; VANDENBROUCKE, M.; TANG, Y.; MARQUIS, F.; ESPITALIE, J. Thermal cracking of kerogen in open and closed systems: determination of kinetic parameters and stoichiometric coefficients for oil and gas generation. Organic Geochemistry, v. 26, n. 5–6, p. 321–339, 1997.

BISCAYE, P. E. Mineralogy and sedimentation of recent deep-sea clay in the Atlantic Ocean and adjacent seas and oceans. Geological Society of America Bulletin, v. 76, p. 803–832, 1965.

BRIGATTI, M. F.; GUGGENHEIM, S. Mica Crystal Chemistry and the Influence of Pressure, Temperature, and Solid Solution on Atomistic Models. Reviews in Mineralogy and Geochemistry, v. 46, n. 1, p. 1–97, 2002.

BRINDLEY, G. W.; BROWN, G. Crystal Structures of Clay Minerals and their X-Ray Identification. Mineralogical Society of Great Britain and Ireland, 1980.

BRITO NEVES, B. B.; FUCK, R. A.; CORDANI, U. G.; THOMAZ, A. Influence of basement structures on the evolution of the major sedimentary basins of Brazil: a case of tectonic heritage. Journal of Geodynamics, v. 1, p. 495–510, 1984.

BUECKER, C.; RYBACH, L. A simple method to determine heat production from gamma logs. Marine and Petroleum Geology, v. 13, p. 373–377, 1996.

CAMPOS, L. F. B.; GUIMARÃES, E. M.; GRUDKA BARROSO, R. H.; GOMES, A. W. Influence of pressure and temperature in the illite crystallinity in Proterozoic sequences: North of Distrito Federal and Goiás, Brasil. Brazilian Journal of Geology, v. 45, n. 3, p. 383–398, 2015. Sociedade Brasileira de Geologia.

CANELAS, D. Modelagem 2D de Sistemas Petrolíferos de um seção em águas ultra profunda na Bacia da Foz do Amazonas., 2020. Niteroi: Universidade Federal Fluminense.

DE CASTRO, D. L.; FUCK, R. A.; PHILLIPS, J. D.; et al. Crustal structure beneath the Paleozoic Parnaíba Basin revealed by airborne gravity and magnetic data, Brazil. Tectonophysics, v. 614, p. 128–145, 2014.

CORDANI, U. G.; D'AGRELLA- FILHO, M. S.; BRITO NEVES, B. B.; TRINDADE, R. . I. F. Tearing up Rodinia: the Neoproterozoic paleogeography of South American Cratonic Fragments. Terra Nova, v. 15, p. 315–380, 2003.

CRUZ, E. M. A.; CÓRDOBA, V. C.; SOUSA, D. DO C. Análise Estratigráfica Da Sequência Siluriana Da Bacia Do Parnaíba, Nordeste Do Brasil. Geosciences = Geociências, v. 38, n. 1, p. 33–49, 2019.

CULLITY, B. D.; STOCK, S. R. Elements of X-Ray Diffraction. 3rd ed. 2001.

DALY, M. C.; ANDRADE, V.; BAROUSSE, C. A.; et al. Brasiliano crustal structure and the tectonic setting of the Parnaíba basin of NE Brazil: Results of a deep seismic reflection profile. Tectonics, v. 33, n. 11, p. 2102–2120, 2014.

DALY, M. C.; FUCK, R. A.; JULIÀ, J.; MACDONALD, D. I. M.; WATTS, A. B. Cratonic basin formation: A case study of the Parnaíba Basin of Brazil. Geological Society Special Publication, v. 472, n. 1, p. 1–15, 2018.

DELANEY, P. T. Fortran 77 programs for conductive cooling of dikes with temperature-dependent thermal properties and heat cristallisation. Computers and Geosciences, v. 14, p. 181–212, 1988.

DUTTA, N. C. Shale compaction, burial diagenesis, and geopressures: A dynamic model, solution and some results. In: J. Burrus (Org.); Thermal Modeling in Sedimentary Basins. p.149–172, 1986. Paris: Tecnip.

EIRAS, J. E.; WANDERLEY FILHO, J. R. Sistemas Petrolíferos ígneo-Sedimentares. 2o Congresso Brasileiro de P&D Em Petróleo & Gás. Anais... , 2003. Rio de Janeiro.

ELIZABETH GARDUÑO-MARTÍNEZ, D.; PI PUIG, T.; SOLÉ, J.; MARTINI, M.; RENÉ ALCALÁ-MARTÍNEZ, J. K-Ar illite-mica age constraints on the formation and reactivation history of the El Doctor fault zone, central Mexico. 2015.

ESPITALIÉ, J.; UNGERER, P.; IRWIN, I.; MARQUIS, F. Primary cracking of kerogens. Experimenting and modelling C1, C2–C5, C6–C15 and C15+ classes of hydrocarbons formed. Organic Geochemistry, v. 13, n. 4–6, p. 893–899, 1988.

ESQUEVIN, J. Influence de la composition chimique des illites sur leur cristallinité: Bull. Centre de Recherches de Pau . Bull. Centre de Recherches de Pau, p. 147–153, 1969.

DELLA FÁVERA, J. C. Tempestitos da bacia do Parnaíba: um ensaio holístico, 1990. Porto Alegre: Instituto de Geociências.

FERRAZ, N. C.; CÓRDOBA VALÉRIA CENTURION; SOUZA, D. DO C. Análise Estratigráfica Da Sequência Mesodevoniana-Eocarbonífera Da Bacia Do Parnaíba, Nordeste Do Brasil. Geosciences = Geociências, v. 36, n. 1, p. 154–172, 2017.

FERREIRO MÄHLMANN, R.; RAHN, M.; POTEL, S.; NGUYEN-THANH, L.; PETSCHICK, R. Determination of a normal orogenic palaeo-geothermal gradient with clay mineral and organic matter indices: a review. Swiss Journal of Geosciences, v. 117, n. 1, 2024. Birkhauser.

FREY, M.; ROBINSON, DOUG. Low-grade metamorphism. Blackwell Science, 1999.

GIACOVAZZO, C.; MONACO, H. L.; VITERBO, D.; et al. Fundamentals of Crystallography. 2nd ed. Oxford, 2002.

GÓES, A. M. O.; FEIJÓ, F. J. Bacia do Parnaíba. Boletim de Geociências da Petrobras., v. 8, p. 57–68, 1994.

GÓES, A. M. O.; SOUZA, J. M. P.; TEIXEIRA, L. B. Estágio exploratório e perspectivas petrolíferas da bacia do Parnaíba. Boletim de Geociências da Petrobras, v. 4, p. 55–94, 1990.

GUGGENHEIM, STEPHEN; MARTIN, R. T.; ALIETTI, A.; et al. Definition of clay and clay mineral: Joint report of the AIPEA nomenclature and CMS nomenclature committees. Clays and Clay Minerals, 1995. Clay Minerals Society.

HANTSCHEL, T.; KAUERAUF, A. I. Fundamentals of Basin and Petroleum Systems Modeling. First Edition ed. Berlin: Springer-Verlag, 2009.

HEILBRON, M.; GUEDES, E.; MANE, M.; et al. Geochemical and temporal provinciality of the magmatism of the eastern Parnaíba Basin, NE Brazil. Geological Society Special Publication, v. 472, n. 1, p. 251–278, 2018.

HORSFIELD, B. Practical criteria for classifying kerogens: Some observations from pyrolysis-gas chromatography. Geochimica et Cosmochimica Acta, v. 53, n. 4, p. 891–901, 1989a.

HORSFIELD, B. Practical criteria for classifying kerogens: Some observations from pyrolysis-gas chromatography. Geochimica et Cosmochimica Acta, v. 53, n. 4, p. 891–901, 1989b.

HORSFIELD, B. Evaluating kerogen type according to source quality, compositional heterogeneity and thermal lability. In: Elsevier (Org.); Proceedings of the 7th International Palynological Congress: Part II. Anais... . p.357–365, 1990. Amsterdam.

JARVIE, D. M.; CLAXTON, B. L.; HENK, F.; BREYER, J. T. Oil and shale gas from the Barnett Shale, Fort Worth Basin, Texas. AAPG Bulletin, v. 88, p. 100, 2001.

JOHNSON, L. M.; REZAEE, R.; SMITH, G. C.; et al. Kinetics of hydrocarbon generation from the marine Ordovician Goldwyer Formation, Canning Basin, Western Australia. International Journal of Coal Geology, v. 232, p. 103623, 2020.

KUBLER, B. Les Argiles. Indicateurs de métamorphisme. Revue de L'Institute Français du Pétrole, p. 1093–1112, 1964.

KÜBLER, B. Quantitative evaluation of crystallinity by X-ray diffraction: illite crystallinity, a new method for determining the degree of metamorphism. Journal of Sedimentary Petrology, v. 37, n. 3, p. 975–988, 1967.

LANSON, B. Decomposition of experimental x-ray diffraction patterns (profile fitting): A convenient way to study clay minerals. Clays and Clay Minerals, v. 45, n. 2, p. 132–146, 1997. Clay Minerals Society.

LANSON, B.; CHAMPION, D. The I/S-to-illite reaction in the late stage diagenesis. American Journal of Science, v. 291, n. 5, p. 473–506, 1991.

LANSON, B.; VELDE, B.; MEUNIER, A. Late-stage diagenesis of illitic clay minerals as seen by decomposition of X-ray diffraction patterns: Contrasted behaviors of sedimentary basins with different burial histories. Clays and Clay Minerals, v. 46, n. 1, p. 69–78, 1998. Clay Minerals Society.

LANSON, B.; VELTE, B. Decomposition of X-Ray diffraction patterns: a convenient way to describe comlex I/S diagenetic evolution. Clay and Clay Minerals, v. 40, n. 6, p. 629–643, 1992.

LARTER. Some pragmatic perspectives in source rock geochemistry. Marine and Petroleum Geology, v. 5, p. 194–204, 1988.

LOPES, H. A. Efeitos geoquímicos , mineralógicos e petrofísicos de soleiras máficas em rochas reservatório siliciclásticas da Bacia do Parnaíba : implicações para o sistema petrolífero Efeitos geoquímicos , mineralógicos e petrofísicos de soleiras máficas em rochas re. , p. 128, 2019.

LOPES, H. A.; ARAGÃO, F. B.; MIO, E. Atypical Petroleum System Modelling - Improving Intrusion Emplacement Mechanisms into PSM flow. Petroleum Systems Techology Days. Anais... , 2021. Aachen.

LOPES, H. A.; MIO, E. The importance of using local kinetics on modelling Petroleum Systems: Parnaiba Basin Atypical Petroleum System case study. In: ALAGO (Org.); XVI Latin American Congress on Organic Geochemistry. Anais... , 2023. Aracaju.

MAGOON, L. B.; BEAUMONT, E. A. Petroleum Systems. Exploring for Oil and Gas Traps. p.1–33, 1998.

MÄHLMANN, R. F.; FREY, M. Standardisation, calibration and correlation of the Kübler-index and the vitrinite/bituminite reflectance: An inter-laboratory and field related study. Swiss Journal of Geosciences, v. 105, n. 2, p. 153–170, 2012.

MAHLSTEDT, N.; HORSFIELD, B. Organic petrography and petroleum generation characteristics for Pimenteiras Formation (Devonian shale) samples from two wells in the Parnaiba Basin, Brazil. Michendorf, 2023.

MICHELON, D. Interpretação sísmica e geocronólogica do magmatismo na porção centro-norte da Bacia do Parnaíba, Brasil. Rio de Janeiro, 2020.

MILANI, E. J.; ZALÁN, P. V. An outline of the geology and petroleum systems of the Paleozoic interior basins of South America. Episodes, v. 22, n. 3, p. 199–205, 1999. International Union of Geological Sciences.

MIO, E. Reconstrução da História Térmica em Bacias Sedimentares: Utilização da cristalinidade da Ilita como geotermômetro auxiliar e refinamento da contribuição radiogênica de sedimentos utilizado dados de gamma-ray espectral - Exemplo da Bacia do Parnaíba. 25 Seminário da Pos Graduação em Geologia da UFPR . Anais... , 2022.

MIO, E.; LOPES, H. A.; MICHELON, D.; et al. Improvements in Atypical Petroleum System Modelling in Parnaiba Basin, NE Brazil. 84th EAGE Annual Conference & Exhibition. Anais... , 2023. Viena: EAGE.

MIRANDA, F. S. Caracterização geológica da Formação Pimenteiras como potencial reservatório do tipo shale-gas (Devoniano da Bacia do Parnaíba)., 2014. Rio de Janeiro: Universidade do Estado do Rio de Janeiro.

MIRANDA, F. S.; CUNHA, P. R. C.; CALDEIRA, J. L.; ARAGÃO, F. B.; MICHELON, D. The Atypical Igneous-sedimentary Petroleum Systems of the Parnaíba Basin: Seismic, Well-logs and Analogues. AAPG International Conference and Exhibition. Anais... . p.220, 2016. Barcelona.

MIRANDA, F. S.; VETTORAZZI, A. L.; CUNHA, P. R. D. C.; et al. Atypical igneous-sedimentary petroleum systems of the Parnaíba Basin, Brazil: Seismic, well logs and cores. Geological Society Special Publication, v. 472, n. 1, p. 341–360, 2018.

MOORE, D. M.; REYNOLDS, R. C. X-Ray Diffraction and the Identification and Analysis of Clay Minerals. 2nd ed. Oxford: Oxford University Press, 1997.

MULLIS, J.; MÄHLMANN, R. F.; WOLF, M. Fluid inclusion microthermometry to calibrate vitrinite reflectance (between 50 and 270 °C), illite Kübler-Index data and the diagenesis/anchizone boundary in the external part of the Central Alps. Applied Clay Science, v. 143, p. 307–319, 2017. Elsevier Ltd.

OLIVEIRA, D. C.; MOHRIAK, W. U. Jaibaras through: an important element in the early tectonic evolution of the Parnaíba interior sag basin, Northern Brazil. Marine and Petroleum Geology, v. 20, p. 351–383, 2003.

PAMOUKAGHIAN, K. Sedimentología y Estratigrafía de la Formación Piedras de Afilar, Terreno Tandilia, Uruguay, 2012. La Plata: Universid Nacional de La Plata.

PEPPER, A. S.; CORVI, P. Simple Kinetic model of petroleum formation. Part I: oil and gas generation from kerogen. Marine and Petroleum Geology, v. 12, n. 3, p. 291–319, 1995.

PERAL, L. E. G. PETROLOGIA Y DIAGENESIS DE LAS UNIDADES SEDIMENTARIAS PRECAMBRICAS DE OLAVARRIA, PROVINCIA DE BUENOS AIRES, 2008. Ph Thesis, La Plata: Universid Nacional de La Plata.

PETERS, K. E.; WALTERS, C. C.; MANKIEWICZ, P. J. Evaluation of kinetic uncertainty in numerical models of petroleum generation. AAPG Bulletin, v. 90, n. 3, p. 387–403, 2006.

PETERS, K. E.; WALTERS, C. C.; MOLDOVAN, J. M. The Biomarker Guide, volume 1 and 2. Second Edition ed. Cambridge: Cambridge University Press, 2005.

PETERS, T.; WARD, C. R. Applications of X-ray Diffraction in Clay Mineral Studies. In: F. ; T. B. K. G. ; L. G. BERGAYA (Org.); Handbook of Clay Science. 2nd ed, 2010. Amsterdam: Elsevier.

PIERCE, J. W.; SIEGEL, F. R. Quantification in Clay Mineral Studies of Sediments and Sedimentary Rocks. SEPM Journal of Sedimentary Research, v. Vol. 39, p. 187–193, 1969.

POIRÉ, D. G. Mineralogía y sedimentología de la Formación Sierras Bayas en el Núcleo Septentrional de las sierras ho¬mónimas, partido de Olavarría, provincia de Buenos Aires. Facultad de Ciencias Naturales y Museo, Universidad Nacional de La Plata, 1984. Doctoral Thesis, La Plata: Universidad Nacional de La Plata.

POR KIA, J.; MIO, E. Pore pressure prediction using 2D Basinmodeling technique. Earth and Environmental Science ,. Anais... , 2022. IOP Conference Series.

PORTO, A.; CARVALHO, C.; LIMA, C.; et al. The Neoproterozoic basement of the Parnaíba Basin (NE Brazil) from combined geophysical-geological analysis: A missing piece of the western Gondwana puzzle. Precambrian Research, v. 379, p. 106784, 2022.

PORTO, A.; DALY, M. C.; LA TERRA, E.; FONTES, S. The pre-Silurian Riachão basin: A new perspective on the basement of the Parnaíba basin, NE Brazil. Geological Society Special Publication, v. 472, n. 1, p. 127–145, 2018.

DI PRIMIO, R.; HORSFIELD, B. From petroleum-type organofacies to hydrocarbon phase prediction. AAPG Bulletin, v. 90, n. 7, p. 1031–1058, 2006.

PYTTE, A. M. The kinetics of the smectite to illite reaction in contact metamorphic shales., 1982. Hannover: Dartmouth College.

PYTTE, A. M.; REYNOLDS, R. C. The thermal transformation of smectite to illite. In: N. D. Naeser; T. H. McCulloh (Orgs.); Thermal History of Sedimentary Basins. p.133–140, 1988. Springer-Verlag.

REYNOLDS, R. C. Interstratified clay minerals. In: G. W. Brindley; G. Brown (Orgs.); Crystal Structures of the Clay Minerals and their X-Ray identification. p.1–495, 1980. London: Mineralogical Society.

RODRIGUES, R. A. Geoquímica Orgânica na bacia do Parnaíba, 1995. Porto Alegre: Instituto de Geociências,.

RYBACH, L. W¨armeproduktionsbestimmungen an Gesteinen der Schweizer Alpen (Determinations of heat production in rocks of the Swiss Alps), Beitr¨age zur Geologie der Schweiz. Geotechnische Serie, v. 41, p. 43, 1973.

SANTOS, L. R. METAMORFISMO DE BAIXO GRAU NAS ROCHAS METASSEDIMENTARES TERRÍGENAS DA FORMAÇÃO CAPIRU – REGIÃO DO MORRO GRANDE, COLOMBO – PR, 2017. Curitiba: Universidade Federal do Paraná.

SCHULTZ, L. G. Quantitative interpretation of mineralogical composition from X-ray and chemical data for the Pierre Shale. United States Geological Survey Professional Paper, v. 391, n. C, 1964.

SILVA, M. A. Difração de Raios X Aplicada à Caracterização de Materiais. Revista Brasileira de Ensino de Física, v. 34, n. 3, p. 1–10, 2012.

SOARES, J. E. P.; STEPHENSON, R.; FUCK, R. A.; et al. Structure of the crust and upper mantle beneath the Parnaíba Basin, Brazil, from wide-angle reflection–refraction data. Geological Society, London, Special Publications, v. 472, n. 1, p. 67–82, 2018.

STERN, W. B.; MULLIS, J. R. M.; FREY, M. Deconvolution of the first “illite” basal reflection. Schweizerische mineralogische und petrographische Mitteilungen, v. 71, p. 453–462, 1991.

SWEENEY, J. . J.; BURNHAM., A. K. Evaluation of a simple model of vitrinite reflectance based on chemical kinetics. AAPG Bulletin, v. 74, p. 1559–1570, 1990.

SWEENEY, J. J.; BRAUN, L. R.; BURNHAN, A. K. Chemical kinetic model of hydrocarbon generation, expulsion, and destruction applied to the Maracaibo Basin, Venezuela. AAPG Bulletin, v. 79, p. 1515–1532, 1995.

TAYLOR, G. H.; TEICHMÜLLER, M.; DAVIS, A.; et al. Organic Petrology. Berlin: Gebrüder Borntraeger, 1998.

TEGELAAR, E. W.; NOBLE, R. A. Kinetics of hydrocarbon generation as a function of the molecular structure of kerogen as revealed by pyrolysis-gas chromatography. Organic Geochemistry, v. 22, n. 3–5, p. 543–574, 1994.

TISSOT, B. P.; WELTE, D. H. Petroleum formation and occurrence. Second Edition ed. Berlin: Springer-Verlag, 1984.

TOZER, B.; WATTS, A. B.; DALY, M. C. Crustal structure, gravity anomalies, and subsidence history of the Parnaíba cratonic basin, Northeast Brazil. Journal of Geophysical Research: Solid Earth, v. 122, n. 7, p. 5591–5621, 2017.

TURCOTTE, D. L.; SCHUBERT, G. Geodynamics. Second Edtion ed. Cambridge, 2002.

UNGERER, P.; BURRUS, J.; DOLIGEZ, B.; CHENET, P. Y.; BESSIS, F. Basin evaluation by integrated two–dimensional modeling of heat transfer, fluid flow, hydrocarbon gerneration and migration. AAPG Bulletin, v. 74, p. 390–335, 1990.

VANDENBROUCKE, M.; BEHAR, F.; RUDKIEWICZ, J. L. Kinetic modelling of petroleum formation and cracking: implications from the high pressure/high temperature Elgin Field (UK, North Sea). Organic Geochemistry, v. 30, n. 9, p. 1105–1125, 1999.

VAZ, P. T.; REZENDE, N. G. A. M.; WANDERLEY FILHO, J. R.; SILVA TRAVASSOS, W. A. Bacia do parnaíba. Boletim de Geociencias da Petrobras, v. 15, n. 2, p. 253–263, 2007.

WAPLES, D. W. Time and temperature in petroleum formation: application of Lopatin’s method to petroleum exploration. AAPG Bulletin, v. 64, p. 916–926, 1980.

WARR, L. N.; FERREIRO MÄHLMANN, R. Recommendations for Kübler Index standardization. Clay Minerals, v. 50, n. 3, p. 283–286, 2015a. Mineralogical Society.

WARR, L. N.; FERREIRO MÄHLMANN, R. Recommendations for Kübler Index standardization. Clay Minerals, v. 50, n. 3, p. 283–286, 2015b. Mineralogical Society.

WATTS, A. B.; TOZER, B.; DALY, M. C.; SMITH, J. A comparative study of the Parnaíba, Michigan and Congo cratonic basins. Geological Society Special Publication, v. 472, n. 1, p. 45–66, 2018.

YOUNG, C. G. K. Estratigrafia de alta resolução da Formação Pimenteira (Devoniano, bacia do Parnaíba)., 2006. Rio de Janeiro: Instituto de Geociências, Universidade Federal do Rio de Janeiro.

YUKLER, M. A.; CORNFORD, C.; WELTE, D. Simulation of geologic, hydrodynamic, and thermodynamic development of a sediment basin – a quantitative approach. In: U. Rad; W. B. F. Rian (Orgs.); Initial Reports of the Deep Sea Drilling Project,. p.761–771, 1979.

8. APPENDIX A – 1D PSM Input Tables

Well C					
Age (Ma)	Well Top/Horizon	Depth (TVDSS)	Thickness (m)	Event Type	Layer Name
0	HIA_ITP	-61	0	Hiatus	HIA_ITP
90	ITP	-61	62	Deposition	ITP
100	COD	1	52	Deposition	COD
110	COR	53	49	Deposition	COR
155	PSB	102	7	Deposition	PSB
200	HIA_SAM	109	0	Hiatus	HIA_SAM
220	SAM	109	205	Deposition	SAM
245	MOT_01	314	174	Deposition	MOT_01
	SOL_MOT_01	488	48	Deposition	SOL_MOT_01
248	MOT_02	536	42	Deposition	MOT_02
	SOL_MOT_02	578	20	Deposition	SOL_MOT_02
250	PEF_01	598	210	Deposition	PEF_01
280	SOL_PEF	808	15	Deposition	SOL_PEF
281	PEF_02	823	43	Deposition	PEF_02
283	SOL_PEF_02	866	16	Deposition	SOL_PEF_02
285	PEF_03	882	12	Deposition	PEF_03
290	SOL_PEF_03	894	10	Deposition	SOL_PEF_03
300	PIA	904	264	Deposition	PIA
330	POT_01	1168	138	Deposition	POT_01
340	SOL_POT_01	1306	131	Deposition	SOL_POT_01
341	POT_02	1437	59	Deposition	POT_02
348	SOL_POT_02	1496	26	Deposition	SOL_POT_02
349	POT_03	1522	3	Deposition	POT_03
350	LON	1525	101	Deposition	LON
360	CAB	1626	129	Deposition	CAB
370	PIM_01	1755	70	Deposition	PIM_01
372	SOL_PIM_01	1825	14	Deposition	SOL_PIM_01
374	PIM_02	1839	121	Deposition	PIM_02
376	SOL_PIM_02	1960	32	Deposition	SOL_PIM_02
378	PIM_03	1992	49	Deposition	PIM_03
380	SOL_PIM_03	2041	13	Deposition	SOL_PIM_03
382	PIM_04	2054	63	Deposition	PIM_04
384	SOL_PIM_04	2117	13	Deposition	SOL_PIM_04
385	PIM_05	2130	68	Deposition	PIM_05
386	SOL_PIM_05	2198	13	Deposition	SOL_PIM_05
387	PIM_06	2211	94	Deposition	PIM_06
388	SOL_PIM_06	2305	20	Deposition	SOL_PIM_06
389	PIM_07	2325	59	Deposition	PM_07
390	ITM	2384	150	Deposition	ITM
405	JAI	2534	150	Deposition	JAI
430	TIA	2684	250	Deposition	TIA
438	IPU	2934	100	Deposition	IPU
550	TOP_BSM	3034	500	Deposition	TOP_BSM
Total Sill Thickeness (m) (PIM Formation)			**105**		
Total Sill Thickeness (m)			**371**		

Table 10 Input table of 1 PSM model for Well B with the well tops/horizons, stratigraphic ages, depth, and thickness. The event type discriminates among Deposition, Hiatus and Intrusions. The total intrusive thickness in this well is 371 m.

9. APPENDIX B – DRX Decomposition Charts

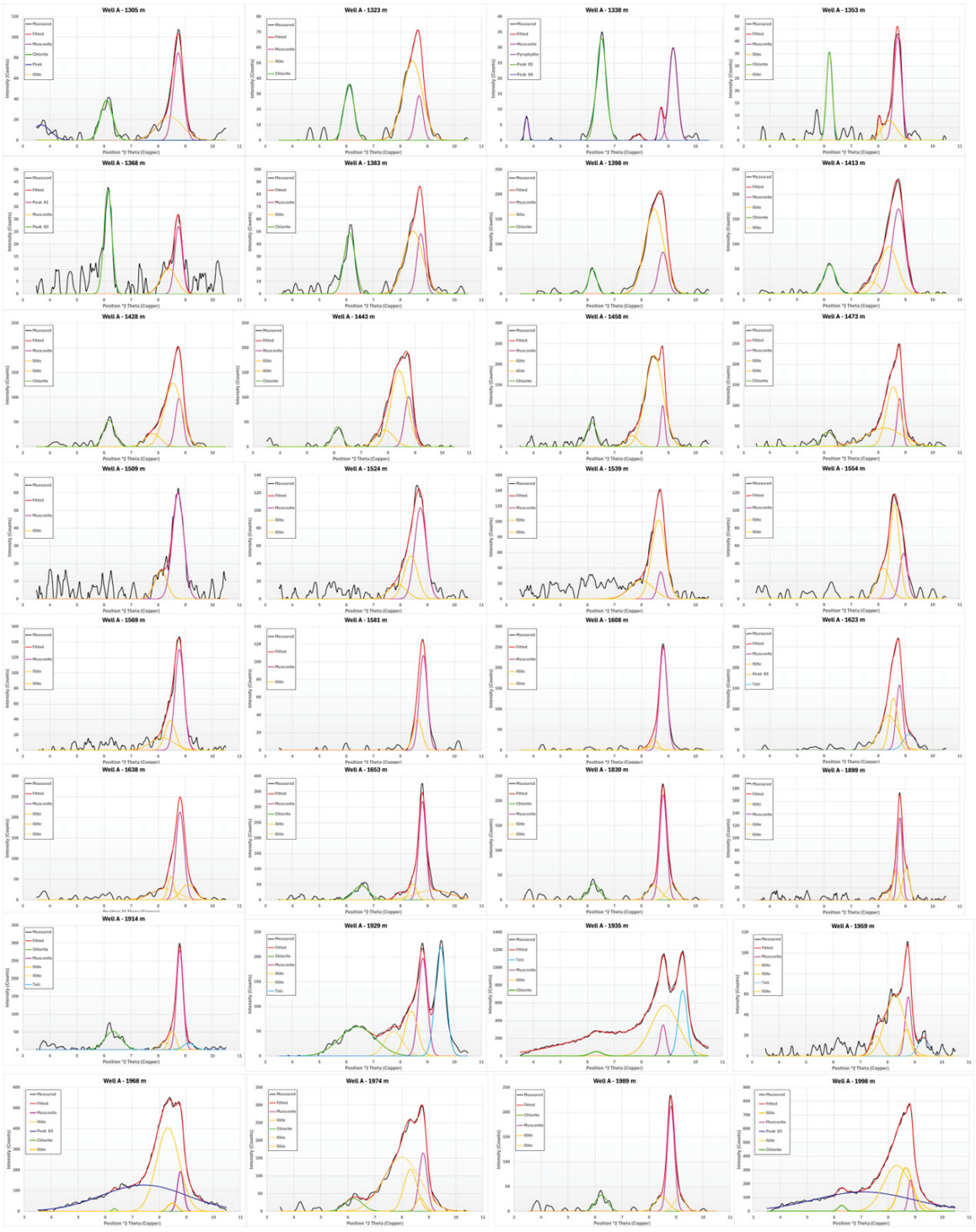

XRD Decomposition chart of the Well A (depths from 1305m to 1998 m), with interpretation, showing the measured XRD profile (black), the interpreted clay mineral phases (orange=Illite; pink=Muscovite; light green=Chlorite; blue=Pyrophyllite/Talc) and the fitted profile (red).

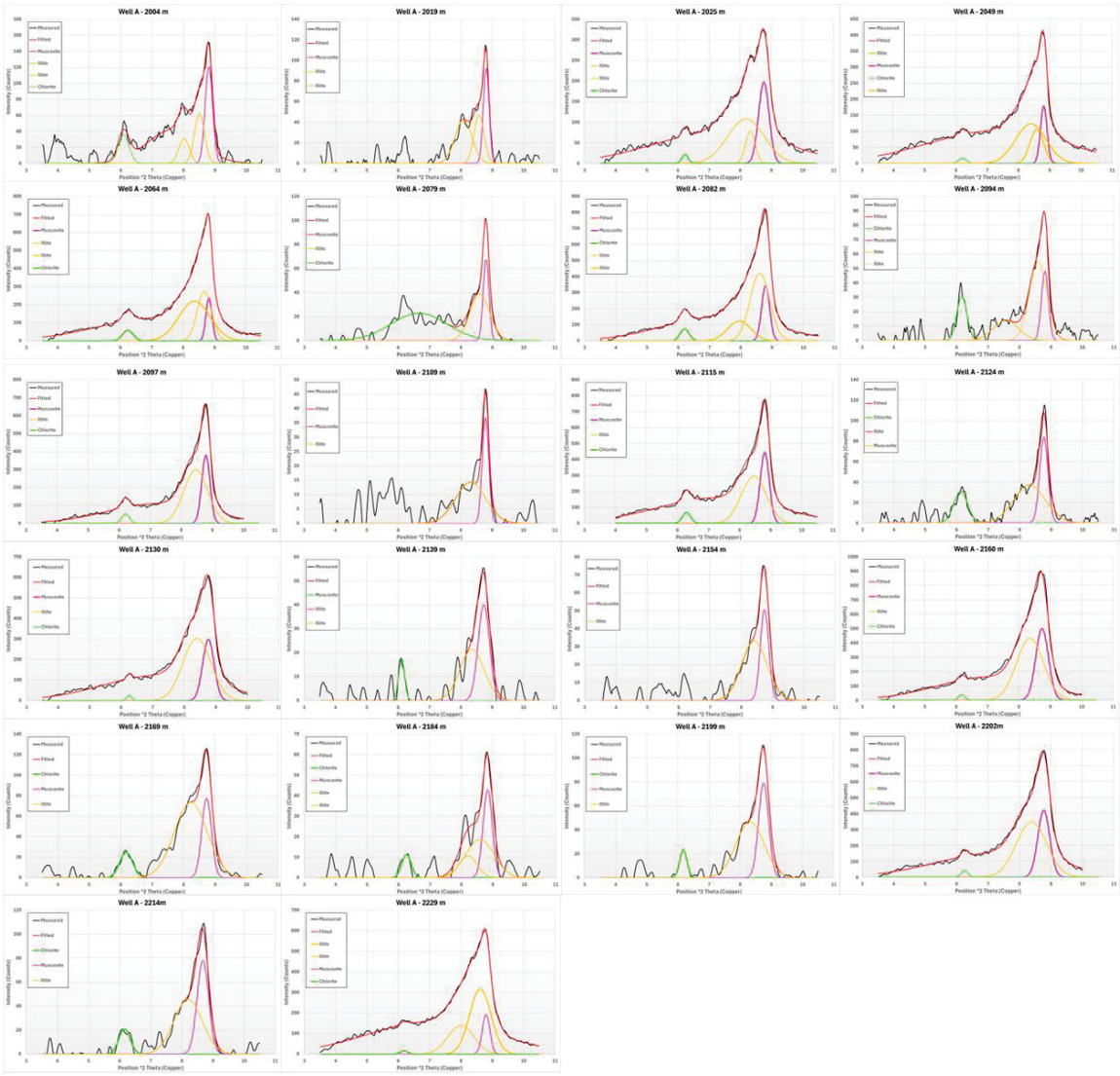

XRD Decomposition chart of the Well A (depths from 2004 m to 2229 m), with interpretation, showing the measured XRD profile (black), the interpreted clay mineral phases (orange=Illite; pink=Muscovite; light green=Chlorite; blue=Pyrophyllite/Talc) and the fitted profile (red).

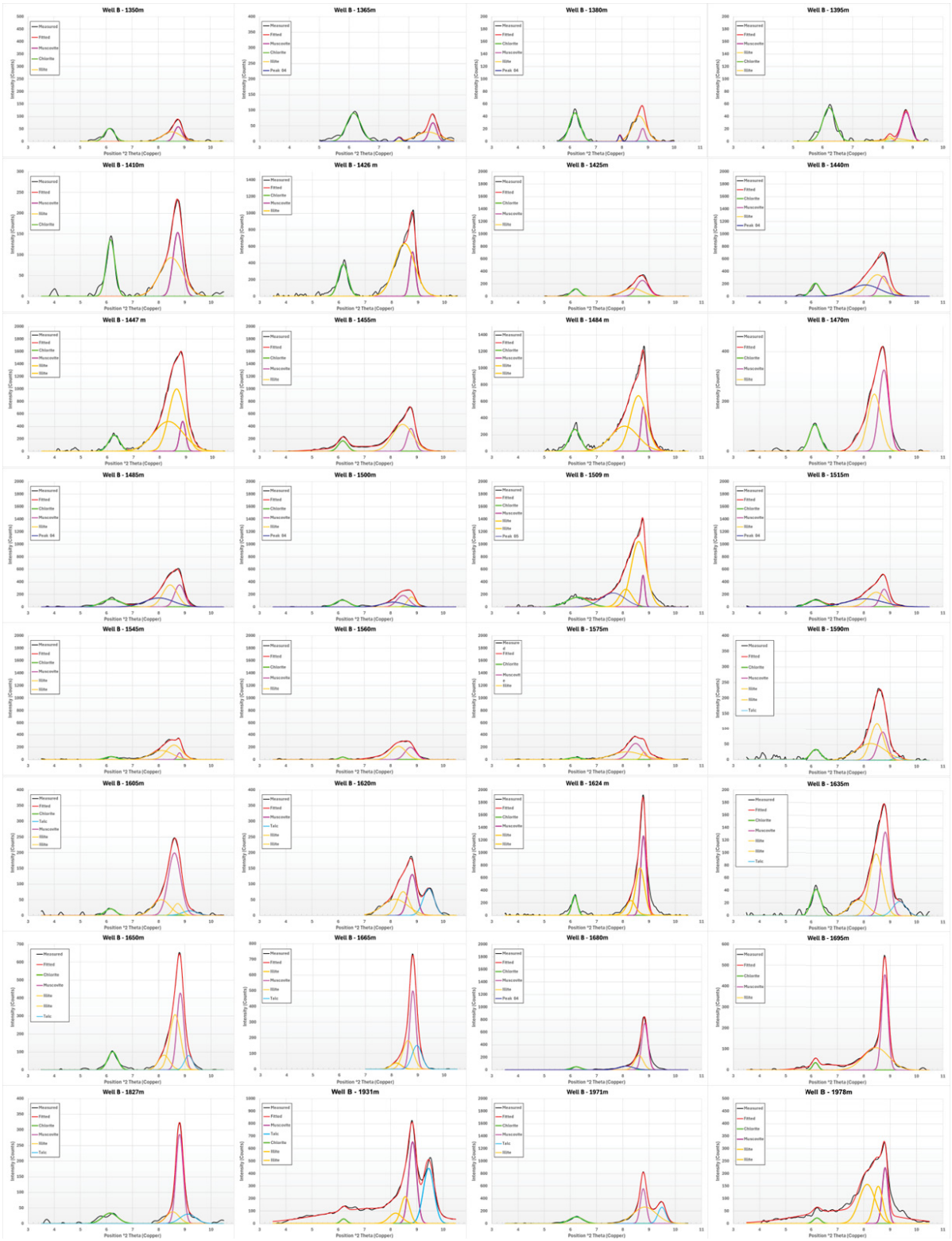

XRD Decomposition chart of the Well B (depths from 1350m to 1978m), with interpretation, showing the measured XRD profile (black), the interpreted clay mineral phases (orange=Illite; pink=Muscovite; light green=Chlorite; blue=Pyrophyllite/Talc) and the fitted profile (red).

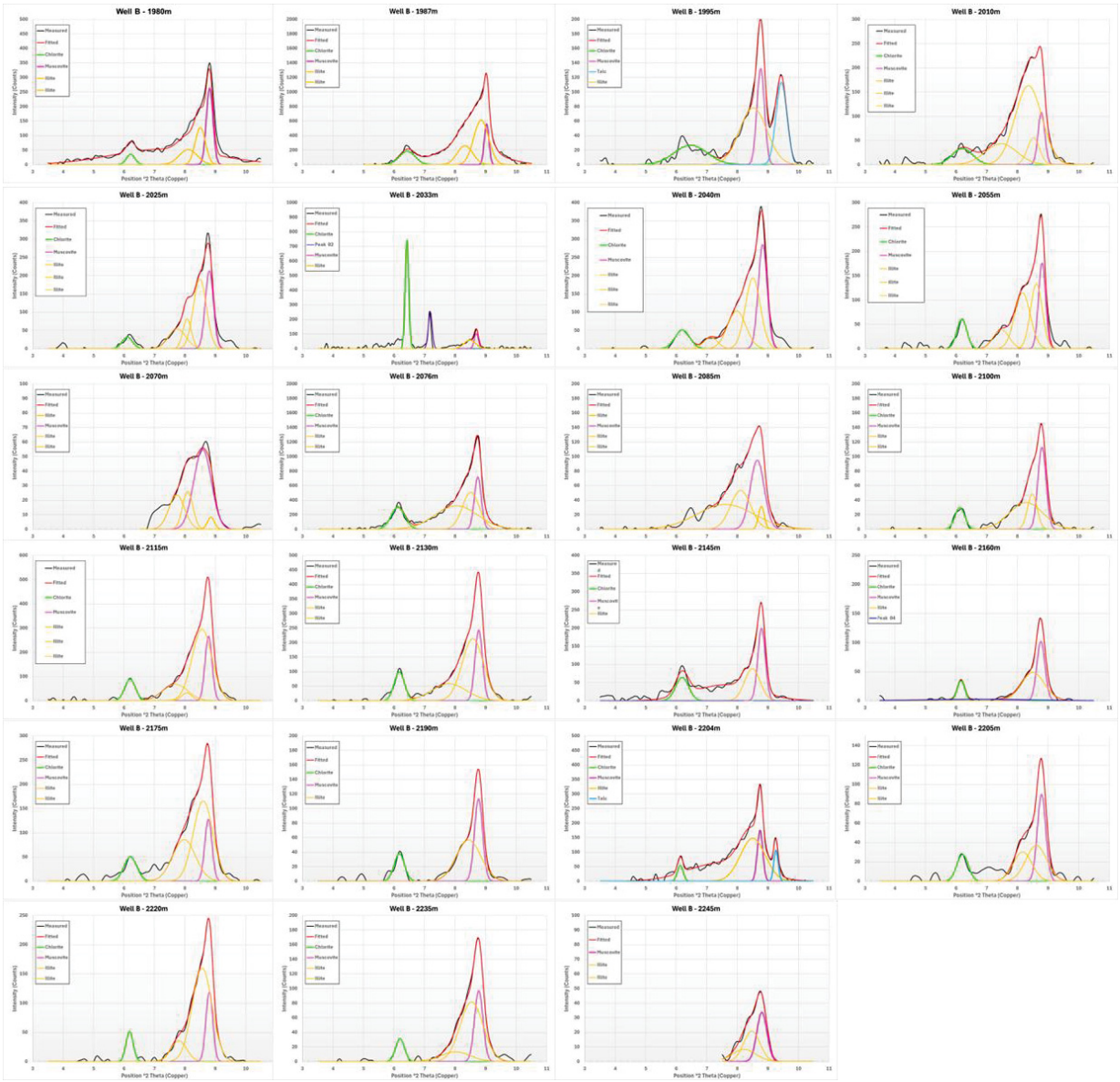

XRD Decomposition chart of the Well B (depths from 1980m to 2245m), with interpretation, showing the measured XRD profile (black), the interpreted clay mineral phases (orange=Illite; pink=Muscovite; light green=Chlorite; blue=Pyrophyllite/Talc) and the fitted profile (red).

XRD Decomposition chart of the Well C (depths from 1305m to 1938m), with interpretation, showing the measured XRD profile (black), the interpreted clay mineral phases (orange=Illite; pink=Muscovite; light green=Chlorite; blue=Pyrophyllite/Talc) and the fitted profile (red).

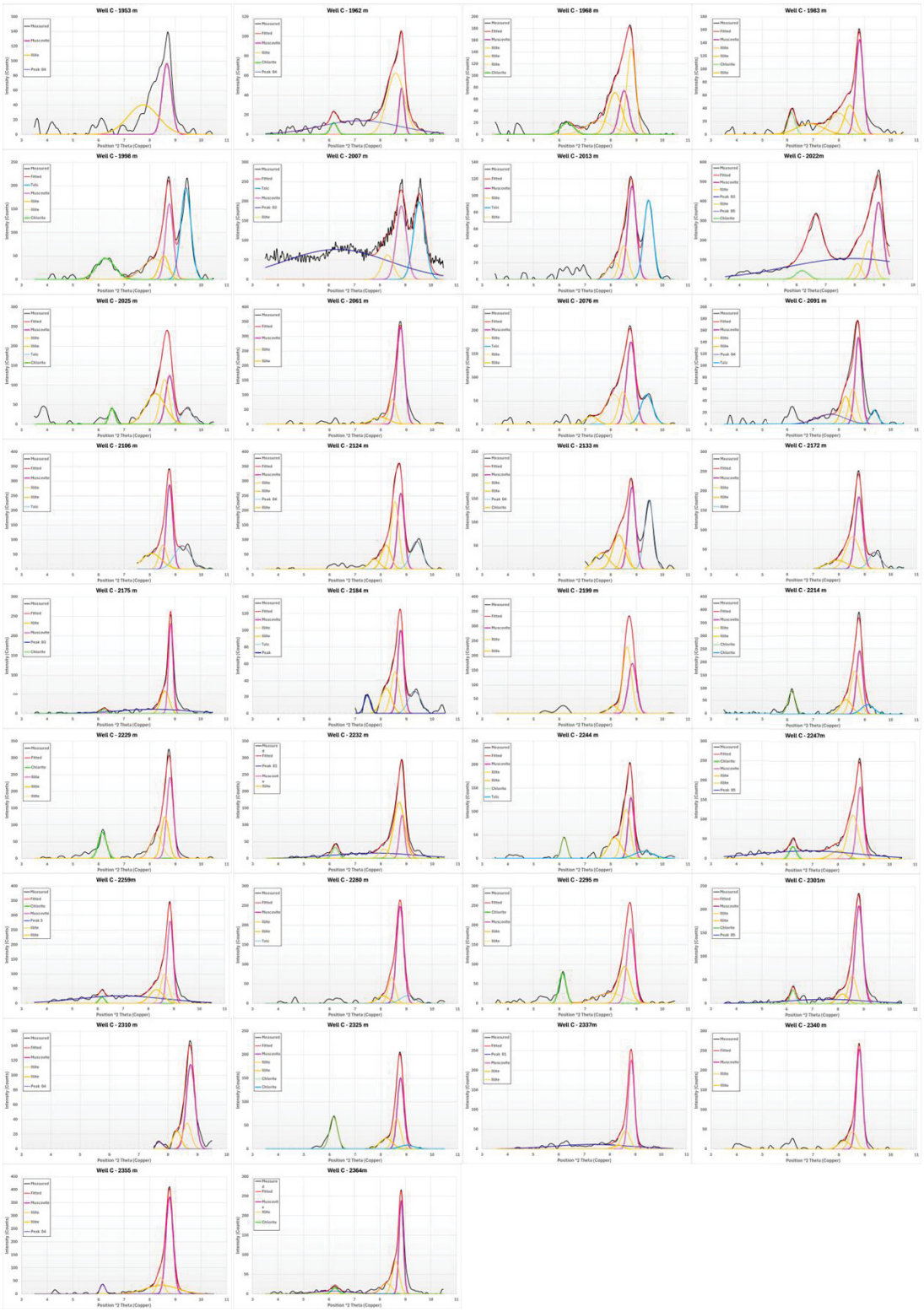

XRD Decomposition chart of the Well C (depths from 1953m to 2364m), with interpretation, showing the measured XRD profile (black), the interpreted clay mineral phases (orange=Illite; pink=Muscovite; light green=Chlorite; blue=Pyrophyllite/Talc) and the fitted profile (red).